Scholars' Mine

Doctoral Dissertations   Student Theses and Dissertations

Fall 2018

Discrete element and artificial intelligence modeling of rock properties and formation failure in advance of shovel excavation

Muhammad Waqas

Recommended Citation

DISCRETE ELEMENT AND ARTIFICIAL INTELLIGENCE MODELING OF ROCK

PROPERTIES AND FORMATION FAILURE IN ADVANCE OF SHOVEL

EXCAVATION

by

MUHAMMAD WAQAS

A DISSERTATION

Presented to the Faculty of the Graduate School of the

MISSOURI UNIVERSITY OF SCIENCE AND TECHNOLOGY

In Partial Fulfillment of the Requirements for the Degree

DOCTOR OF PHILOSOPHY

in

MINING ENGINEERING

2018

Approved by:

Samuel Frimpong, Advisor
Grzegorz Galecki, Co-Advisor
Lana Alagha
Kwame Awuah-Offei
K. Chandrashekhara

ABSTRACT

Rock tests are performed before the start of every mining or civil engineering project as part of a detailed feasibility study. The feasibility study is costly and it comprises drilling, sample collection, sample handling and laboratory testing. Numerical modeling techniques, such as Particle Flow Code (PFC), can be used to provide reliable estimates of rock strength values. The numerical models for unconfined compressive strength (UCS), direct tension, and Brazilian tests were developed in PFC, and validated using data from literature. A particle size range of 3-5 mm with $D_{max}/D_{min} = 1.67$ gave the best results. The numerical errors were in the range of 6-22% for UCS, 21-80% for direct tension, and 5-10% for Brazilian tests. About 1,800 confined compression tests were also performed in PFC to obtain formation material properties. However, the PFC algorithm takes a very long computational time to complete the process, and thus, there is a need for more efficient and faster methods. In this research, the author uses artificial intelligence methods including, Artificial Neural Network, Mamdani Fuzzy Logic, and Hybrid neural Fuzzy Inference System (HyFIS) to solve this problem. These methods, along with the Multiple Linear Regression method, were used for the predictive analysis. Based on R^2 and RMSE statistics for the testing phase, HyFIS is the best predictive model. This study is the first attempt to develop self-learning artificial intelligent models for predicting formation material properties. In addition, this research study investigates the shovel excavation process using the discrete element technique in PFC to examine the shovel digging phase. The shovel excavation simulator provides a tool for optimizing strategies for maximizing its performance that provides a major breakthrough in the shovel excavation frontier.

ACKNOWLEDGMENTS

TABLE OF CONTENTS

LIST OF ILLUSTRATIONS

LIST OF TABLES

1. INTRODUCTION

The United States is among the major mineral producing countries and exports several mineral commodities to other countries. Mineral commodities serve as the backbone of the U.S. economy. The estimated value of U.S. minerals in 2016 was $108.9 billion. These minerals were processed into $706 billion secondary products which were used by construction and manufacturing companies to add $2,780 billion to the U.S. gross domestic product (GDP) value of 18,860 billion (U.S. Geological Survey, 2017). Therefore, the economy of the United States largely depends on key minerals, coal, aggregates and stone production. A total of 71% of metals, 95% of non-metals, and 67% of coal (CDC, 2015, 2015a; EPA, 2005), are actively being extracted with surface mining technology. This research is carried out to improve the efficiency of surface mining operations. This section provides the research background, recognizing the problems and the possible solution, research objectives, scope or limitations of the research, research methodology used to tackle the problems, expected industrial and scientific contributions, and the dissertation's structure.

1.1. RESEARCH BACKGROUND

In surface mining operations, shovel excavation and loading are the dominant methods with cable shovel being one of most important heavy equipment for mine production operations. Electric rope shovel, with its long service life, high productivity, low energy consumption and high maintainability, is always preferred to the hydraulic excavator for surface mining operations with high productivity (Wei and Gao, 2012). A

total of 2,700 units of electric rope shovels are active worldwide including 1,850 units of 20 metric ton or larger (parkerbaymining.com). Caterpillar and KOMATSU are the chief electric shovel manufacturers worldwide. These companies are producing bigger and bigger electric shovels over the years, and the current size ranges from 15 to 122.7 metric tons (17 to 135 tons) (mining.komatsu/surface-mining/electric-rope-shovels). This increase in size results in a number of problems related to shovel dipper and teeth interaction with the formation.

The cable shovel is composed of front-end, lower and upper assembly and its nomenclature is presented in Figure 1.1 (Raza and Frimpong, 2017). The lower assembly comprises crawler shoes and propel drive system, which help in moving during the operation. The upper assembly is the controlling assembly and it comprises the operator's cabinet, electronic control cabinet, swing and hoist control machinery. The front-end assembly comprises rope, crowd machinery, boom, dipper handle and dipper, which interacts with the formation during shovel operation.

One of the critical components of an electric rope shovel is the dipper-teeth component, the weakest chain in the system availability. Roy et al. (2001) showed that dipper-related problems were found to be the second highest contributor in shovel breakdown time as compared to other subsystems as illustrated in Figure 1.2. It was also found out that the dipper-related problems in terms of frequencies were the highest contributor towards shovel breakdown as compared to other subsystems as illustrated in Figure 1.3. These breakdowns can result in higher maintenance, production and repair costs, increased downtimes, reduced availability, utilization and efficiency, and hence reduction in profit.
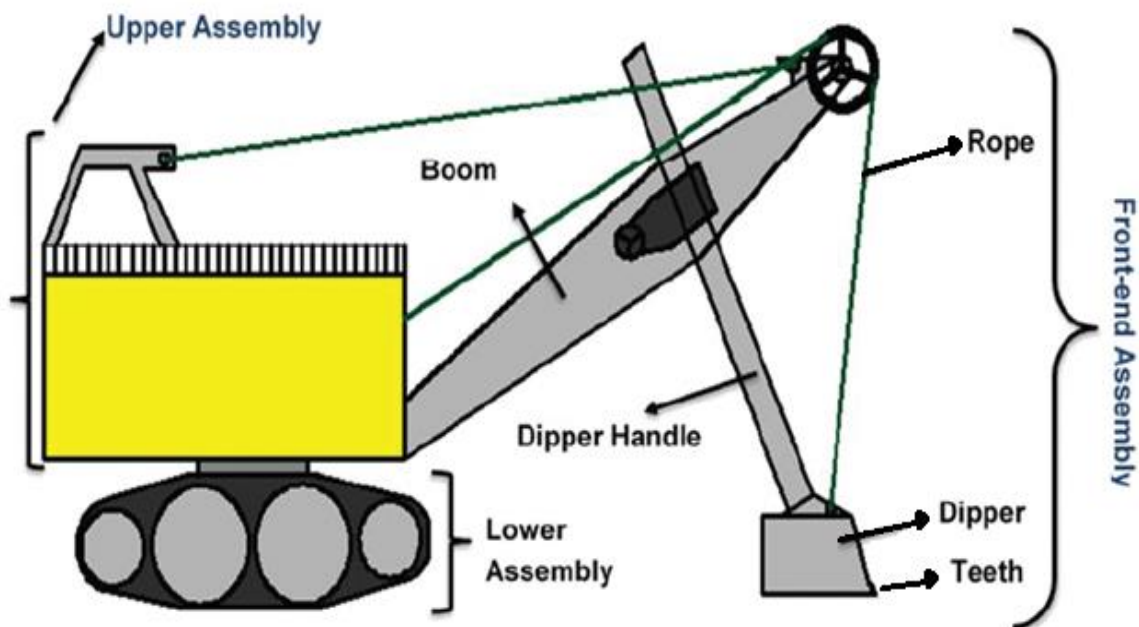
Figure 1.1. Electric rope shovel assemblies (Raza and Frimpong, 2013)

Shovel working cycle consists of penetrating, digging, swinging, dumping and propelling. An efficient digging methodology can increase productivity, and reduce the operating and maintenance costs. Hustrulid (1999) also showed that an efficient excavation technique results in an efficient mining process because ore and waste extraction is mainly done by the loading equipment. One percent improvement in excavation efficiency can save millions of dollars and increase the profitability of a mine. Hence, it is required to study the factors affecting the excavator performance, monitor and work towards improving equipment performance.
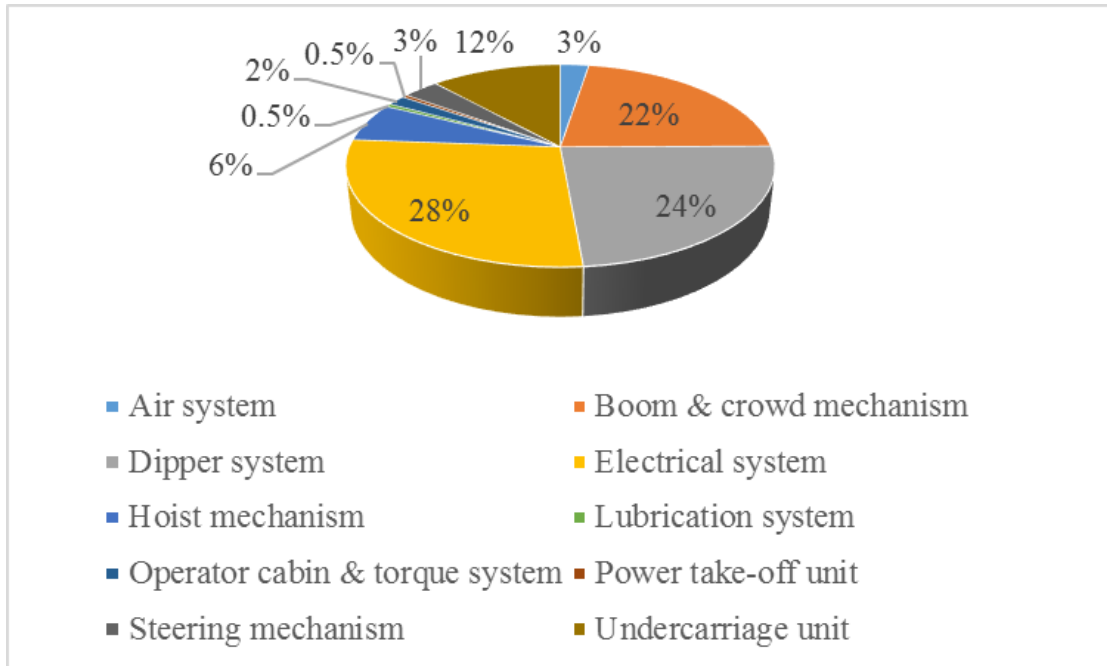
Figure 1.2. Shovel breakdown times w.r.t. different subsystems (Roy et al., 2001)
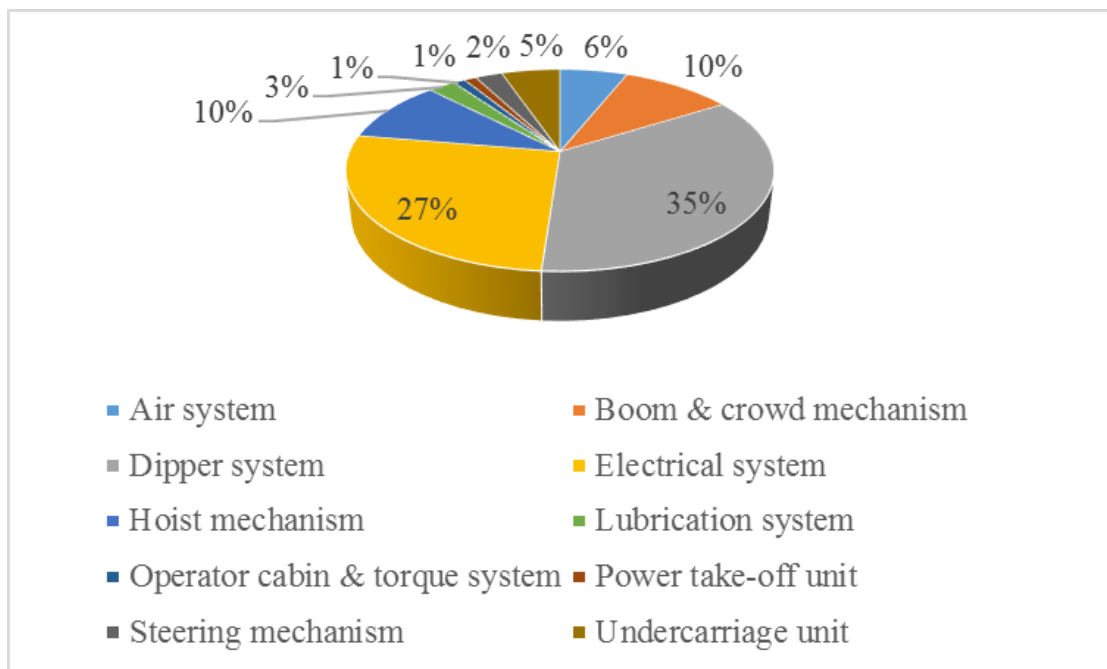
Figure 1.3. Shovel breakdown frequencies w.r.t. different subsystems (Roy et al., 2001)

1.2. PROBLEM STATEMENT

Rock tests are performed before the start of every mining or civil engineering project for the purpose of feasibility studies. It results in huge costs, comprising drilling, sample collection, sample handling and finally laboratory testing. Unconfined compressive strength (UCS), direct tension, and indirect Brazilian tests are common laboratory tests. According to GEOLABS (2018), a UCS test costs $73 and an indirect Brazilian tensile strength test costs $86. According to Standard Laboratories. (2016), a UCS test costs $78 and an indirect Brazilian tensile strength test costs $35.50. In the idealized world of numerical models, these tests are possible and provide reliable estimates of rock strength values. Experimental methods require a lot of resources, time and cost, whereas numerical methods save time and resources, hence are less costly.

The Particle Flow Code (PFC) offers a general purpose Discrete Element Modeling (DEM) framework, and can be used to perform the above mentioned rock tests to determine the rock strength values. A combination of both laboratory and numerical rock tests can be performed to lower the costs. Different researchers have developed rock test models in the past using PFC, but according to the author's knowledge, no one have followed ISRM (1978a, b), ISRM (1979a, b), ASTM-D3967 (2008), and ASTM-D4543 (2008) standards. For the Brazilian tensile strength tests, it is recommended by these standards to have a sample that has a thickness to diameter ratio of 0.5. Potyondy and Cundall (2004), and Coetzee and Els (2009a) have used cuboid samples for their rock test models. The size of the sample is expected to have an effect on the results of these numerical rock tests. It is expected to get reasonably accurate rock strengths values that will save lot of time and money resources, especially for the feasibility studies.

PFC, being a discrete element code takes a lot of time to complete the numerical tests as well as it has high initial cost. There is a need to look for an alternative. Artificial intelligence models can be a possible alternative to PFC. Artificial Neural Network (ANN), Mamdani Fuzzy Logic (MFL), Hybrid neural Fuzzy Inference System (HyFIS), along with the Multiple Linear Regression (MLR) methods will be developed and tested. Initially, the numerical rock tests will be done in PFC. Eighty percent data of these test results will be used as input to train these AI models, and the remaining twenty percent data will be used to test the performance of these AI models. If any of these AI models can serve as an alternative, this will help in reducing the computational cost.

The mining industry uses capital-extensive and large-capacity equipment like shovels for material excavation and haulage. During formation excavation, there are significant inconsistencies in formation hardness as illustrated in Figure 1.4 (a) and (b), which result in fluctuating mechanical energy input and stress loading of teeth of shovel dipper. It is nearly impossible for an operator to have an exact knowledge of the material to be encountered during each of the digging phases and modify the digging trajectory accordingly. Tactical improvements in the digging efficiency of the cable shovel have involved improving the operator preferences and practices. Automating the operator's duties can be an excellent alternative to a strenuous task of improving the operator efficiencies.

A trend towards developing bigger shovel dippers is found and the biggest shovel dipper to date can carry more than 122 metric tons per pass. The increase in size has resulted in many challenges regarding the stresses on these shovels during excavation. The shovel dipper, teeth, and lips are directly in contact with the formation during the digging

cycle. The dipper bears the dynamic weight and impact forces, while teeth and lips bear the fatigue, impact and dynamic resistive forces. Tooth breakage or failures can occur due to these high dynamic forces. Because of the sizes and the amount of excavated material per pass, these forces can cause component failures due to wear and tear and hence need to be addressed appropriately. It took four days to replace a tooth set costing around $3,000 at the Morenci mine (Knights, 2009). Also, a cost of $41,368 was estimated due to the unplanned change-out of the tooth set. The broken teeth can also be transported into the crushers causing crusher breakdowns.
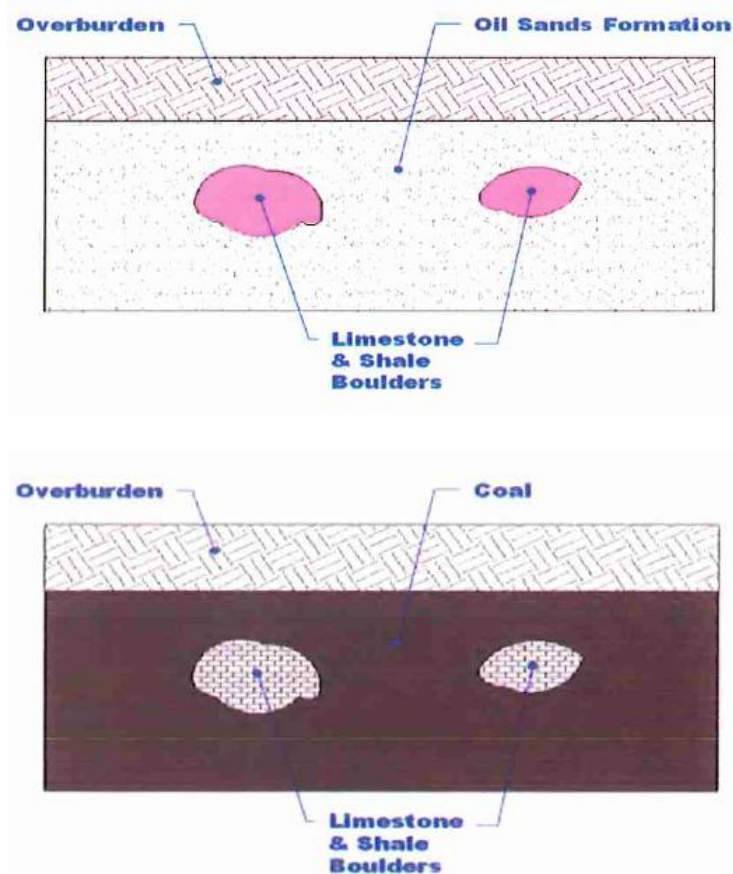
Figure 1.4. Formation with random occurrences of boulders in oil sands and coal

Therefore, understanding the shovel digging phase is very important in achieving production efficiencies. With the advent of intelligent shovel excavation (ISE) technology by Frimpong and Hu (2008), proper and accurate modeling of formation can be done. In the last phase of this study, DEM analysis in PFC will be done to observe the behavior of discrete formation particles in front of the shovel dipper. The numerical simulations will be performed in PFC3D to observe the behavior of granular material flow into the shovel dipper. This will allow engineers to select optimum strategies to maximize excavation performance.

1.3. RESEARCH OBJECTIVES

The primary goal of this research is to numerically model the material formations by using PFC, and to look for an alternative of PFC rock mechanics tests. The main components of this primary objective include the following:

- To develop and calibrate the numerical models for some of the common rock mechanics tests including unconfined compression, direction tension, and indirect Brazilian tests;

- To obtain some of the selected properties of rock formations;

- To develop and test some of the most common artificial intelligence models for the prediction of the properties of rock formations;

- To modify a 3D virtual prototype of an industry standard cable shovel dipper (P&H 4800-XPC) for offline simulations; and

- To develop a 3D model in PFC for shovel digging phase to observe the behavior of material flow into the dipper.

1.4. SCOPE OF THE RESEARCH

This research is limited to the development of numerical models for unconfined compressive strength (UCS), direct tension, and indirect Brazilian tests. Other rock mechanics tests can also be performed and validated. This study is limited to measure some selected formation properties that include resilient modulus, Young's modulus, Poisson's ratio, shear modulus, and friction coefficient. Hence, the developed AI models can only predict these properties but the approach can be extended to measure and predict more properties.

The research work is limited to the shovel excavation technology but can be extended to other earth excavation equipment involving digging and cutting. The work is primarily focused on the digging phase of the shovel excavation process. The research is concerned with developing the computer-aided solutions for the shovel digging problems. Numerical experiments are done but no physical experiments have been carried out in this study. Experimental results of previous researchers are used for validating the results of numerical experiments.

1.5. RESEARCH METHODOLOGY

A thorough literature review has been carried out to determine the knowledge extent in the field of rock mechanics testing, formation excavations, dynamic and numerical modeling, virtual prototyping, and artificial intelligence modeling with primary focus on shovel excavation. Numerical models for the rock mechanics tests are developed in PFC. Virtual laboratory test simulations are done by writing FISH scripts in PFC3D software.

Machine learning/Artificial intelligence approach is used to develop the Artificial Neural Network (ANN), Mamdani Fuzzy Logic (MFL), and Hybrid neural Fuzzy Inference System (HyFIS) models. The multiple linear regression (MLR) method is also used for the predictions, as it is one of the most commonly used methods for the predictive analysis. Once the HyFIS has been recognized as the best predictor, it is further used on eight datasets to check its prediction capability.

Industry scale dipper model of P&H 4800-XPC generated in SolidWorks by (Wardeh and Frimpong, 2016) is imported in Rhino 5. The full-scale mining bench model is also generated in Rhino 5 and imported into PFC3D. Virtual prototyping and DEM analysis of shovel excavation cycle are carried out in PFC3D software. Results are analyzed with conclusions and recommendations for advancing knowledge and frontiers in shovel formation excavation.

1.6. EXPECTED INDUSTRIAL AND SCIENTIFIC CONTRIBUTIONS

The developed numerical models for the rock mechanics tests are expected to give reasonably accurate rock strengths values that will save lot of time and money resources, especially for the feasibility studies.

This study is the first attempt to develop self-learning artificial intelligent models for the prediction of the formation material properties. These AI models especially, HyFIS can be used to predict the desired properties with reasonable accuracy. It is further expected that the HyFIS can be used as a replacement for the PFC rock tests. This is the first attempt to look for an AI model as a replacement to PFC rock mechanics tests. This will allow researchers to use a cheap software, still getting comparable results. The system consisting

of artificial intelligence model, capable of predicting the formation material properties, will allow engineers to save time, money and resources.

For the first time, DEM simulations for P&H 4800-XPC in PFC3D were performed to simulate, study and analyze the cable shovel digging phase. The developed simulator model can compare the performance of different excavation variables, and allow engineers to select optimum strategies to maximize excavation performance.

1.7. DISSERTATION'S STRUCTURE

The dissertation is divided into eight sections. Section 1 provides the research background, problem statement and the possible solution, research methodology to tackle the problem with expected contributions. Section 2 includes the detailed and critical literature review of the formation excavation science and engineering. The review is divided into four tiers: description of in-situ material properties, formation excavation modeling with primary focus on shovel excavation, numerical modeling, and artificial intelligence modeling. Section 3 describes the details of the Discrete Element Method (DEM) and Particle Flow Code (PFC) software. Section 4 presents the formation material modeling and calibration carried out in PFC. Section 5 covers the artificial intelligence modeling with emphasis on the Artificial Neural Network (ANN), Mamdani Fuzzy Logic (MFL), and Hybrid neural Fuzzy Inference System (HyFIS) methods. Section 6 gives the details of virtual prototyping and shovel dipper filling. Section 7 provides the analysis and discussions of the results. Section 8 contains the conclusions and the possible recommendations for the future work.

2. LITERATURE REVIEW

This section includes the detailed and critical literature review of the formation excavation science and engineering. The review is divided into four tiers: description of in-situ material properties, formation excavation modeling with primary focus on shovel excavation, numerical modeling, and artificial intelligence modeling. At the end, the summary of the literature review is presented.

2.1. UNIQUE BEHAVIOR OF ROCKS AND SOILS

From the engineering point of view, rock can be defined as a material with very strong molecular and internal cohesive forces, which bind the constituents together. Soil, on the other hand, can be defined as loose agglomerate of minerals and organic matter (Holtz et al., 2011). As rocks and soils are made up of some constituents, generally they have voids which are filled with water, air, organic material or some other impurities. The interaction between different constituents, physical and chemical changes in water and air cause the rocks and soils to develop their unique properties. These properties make them behave very differently in in-situ conditions as compared to laboratory conditions.

Properties of rocks and soils can change very drastically even after a distance of some millimeters. They are heterogeneous in nature rather than homogeneous. They are also non-linear materials as their stress-strain curves are not linear. Their engineering properties are different in different directions, i.e., they are anisotropic. Also, they have very good memory, i.e., they can remember the stresses which have been imposed on them in the past. Their heterogeneous nature, non-linear behavior, anisotropic condition and their

good memory make them very complex engineering material (Holtz et al., 2011). As a result, it is required to understand their engineering properties in detail to determine their unique behavior.

2.2. PROPERTIES OF ROCKS AND SOILS

Humans use rocks and soils for different purposes, especially as construction materials and as foundation for engineering structures. Rocks contain discontinuities like folds, faults, joints, shearing zones and bedding planes, which make them behave differently from many other engineering materials (Zhang, 2016). The difference between intact rock and rock mass should be understood. Intact rock is a continuum solid made up of different minerals whereas the rock mass is the in-situ medium made up of different intact rock blocks, which are separated by different discontinuities and is shown in Figure 2.1. Intact rock properties are affected by the alignment of minerals present and the bonding of minerals with each other. On the other hand, the rock mass is discontinuous and is often heterogeneous and anisotropic in nature, which makes it difficult to determine its properties (Zhang, 2016).

A soil mass is mostly made up of solid particles. These solids are not tightly packed and there are a lot of void spaces as well which are often filled with water and air. So, a soil mass consists of all the three states of matter. If these solid particles are observed at the microscopic level, each particle will have some contact with other particles. Contact forces are produced between a particle and its neighbors due to the weight of the overlapping particles. These forces hold the solids particles in their places and are responsible for the strength of soils.
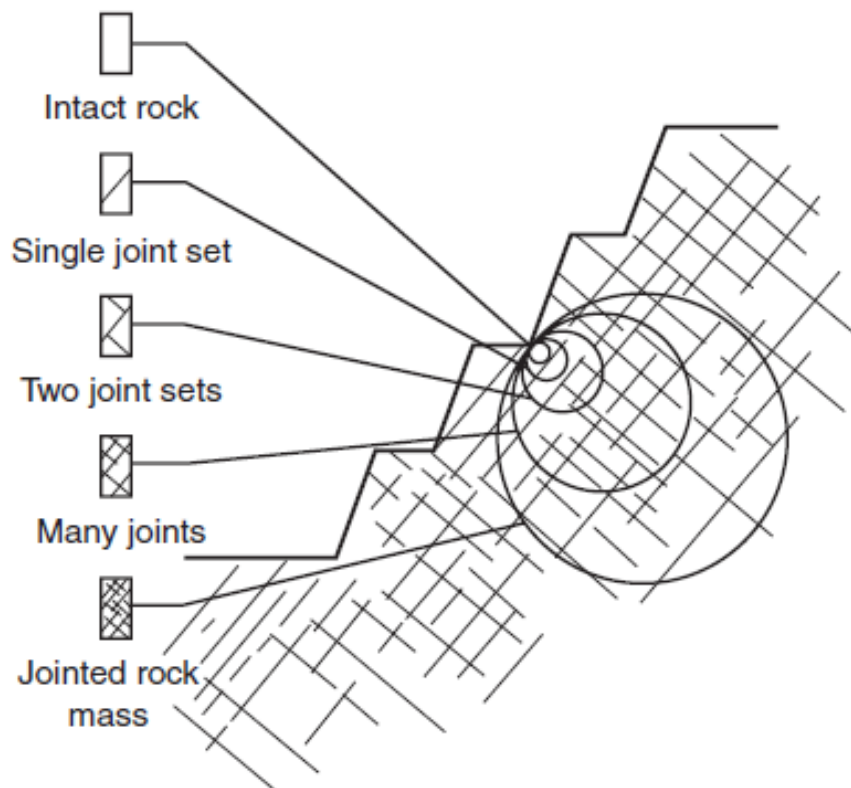
Figure 2.1. Difference between intact rock and rock mass (Wyllie et al., 2004)

Soils can be classified as cohesive or non-cohesive depending upon their behavior in dry or wet conditions. The soils are said to be cohesive if the particles can stick together irrespective of being wet or dry. Cohesion is a material property, which is dependent upon the distribution of soil particles. Cohesive soils contain a lot of fine particles especially clay particles which can stick together, even without the presence of water. On the other hand, non-cohesive soils are deficient in having a particular amount of fine particles. Although, these particles can stick together in the presence of water but, as soon as the water goes off, they disintegrate into different particles. These are known as non-cohesive

or cohesion-less soils (Johnson and Degraff, 1988). Rocks and soils exhibit a wide range of properties due to the presence of different minerals and structures. Some of these properties are easy to determine and they are known as index properties (Goodman, 1989).

2.2.1. Void Ratio. The void ratio (e) is defined as the ratio of the volume of the voids to the volume of the solids. It is a dimensionless quantity and is usually presented as a fraction. The value of the void ratio can range in between 0 to ∞ (Holtz et al., 2011). The void ratio is the most important parameter, which affects the strength of rock/soil.

2.2.2. Degree of Saturation. Degree of saturation (S) is defined as the ratio of the volume of water to the volume of voids. It represents how much percentage of voids in a rock/soil is filled with water. It is usually represented as a percentage and it ranges from dry to fully saturated rock/soil (Holtz et al., 2011).

2.2.3. Water Content. Water content (w) is defined as the ratio of the mass of water to the dry mass of solids and is usually represented as a percentage. The samples are normally dried in an oven to get dry mass. Water content in organic soils can be determined but they should be dried at low temperatures to avoid destruction of organic matters. Water content is one of the major factors, which can result in the reduction of rock/soil strength. The more the water content, the lower will be the strength and more likely it will fail easily. Due to the presence of different amount of water content in the same rock/soil, there will be a big difference between their properties (Brown and Frimpong, 2012).

2.2.4. Porosity. Porosity (n) is defined as the ratio of the volume of voids/pores to the total volume of rock/soil. It is a dimensionless quantity and is usually represented as a fraction or percentage. Porosity serves as an accurate index of rock/soil quality as it has a huge impact on the strength of rock/soil. The higher the porosity, the lower will be the

strength. Porosity varies considerably for different rock/soil types due to several natural, physical, chemical and geological processes. It changes considerably even for the same rock/soil type due to change in depth, pressure, temperature, grain shape and grain size distribution. Alramahi et al. (2005) found that when using well-graded grains for a quartz core, smaller porosity values were obtained, while when using poorly graded grains, higher porosity values were obtained. The values of porosity can be determined by following ways; from density, from water content when saturated in water, mercury content when saturated in mercury, from solid volume and pore air volume (Goodman, 1989).

Soils normally have higher values of porosities as compared to rocks. The porosity values for sand and clay are normally found in between 25-50%. On the other hand, the porosity values for fractured basalt and karstic limestone are normally found in between 5-50% and the porosity values for dense crystalline rocks are in between 0-5% (Wyllie et al., 2004).

2.2.5. Density, Unit Weight, and Specific Gravity. Density (ρ) is a vital element in almost all the phase relations for rock/soil. The density of a rock/soil is defined as mass per unit volume. Sometimes the words like dry, saturated, submerged or buoyant, total, wet, moist or bulk are used with the density to explain the different conditions of rock/soil. Dry density (ρ_d) is defined as the mass of dry rock/soil per unit total volume. The dry density can be used to estimate the degree of compaction of rocks/soils when some mechanical energy is being imposed on them. The saturated density (ρ_{sat}) is defined as the mass of saturated rock/soil per unit total volume and is used when 100% voids of rock/soil are filled with water. The density of water is subtracted from the saturated density of rock/soil, to obtain the submerged, effective or buoyant density (ρ_b). Submerged or buoyant

density is usually dependent upon the temperature as the water density is dependent upon the temperature. Total, wet, moist or bulk density (ρ_t) is defined as the total mass of partially saturated or saturated rock/soil per unit total volume.

Unit weight (γ) is defined as the ratio of the weight of the material to the volume of the material. Just similar to density, the words like dry, saturated, submerged or buoyant, total, wet, moist or bulk are used with the unit weight to explain the different conditions of rock/soil. By simply multiplying the different densities with acceleration due to gravity (g), we can get the corresponding unit weights.

The specific gravity (S.G.) is defined as the ratio of the unit weight of rock/soil to the unit weight of water at 4^0 C. The numerical values of density and specific gravity for a particular rock/soil are almost the same but the only difference is that the specific gravity is a dimensionless quantity.

2.2.6. Shear Strength. Shear strength of a rock/soil is defined as the maximum or ultimate shear stresses that rock/soil can withstand without failing. The terms 'peak shear strength and residual shear strength' are also used in literature. Peak shear strength is defined as maximum shear strength along a failure surface whereas residual shear strength is defined as very low strength remaining on the surface after large displacement. The shear strength of a rock/soil is a measure of the stability of the rock/soil under numerous stress conditions (Brown and Frimpong, 2012). So, the shear strength of rock/soil mass and discontinuities are required to be determined accurately as it is the most important and critical parameter for any engineering project.

The factors that affect the shear strength of discontinuities include surface roughness, the shape of the surface, the rock on the surface and the infilling material.

Spacing and surface conditions of discontinuities, compressive strength and friction angle of intact rocks are some of the factors that affect the shear strength of jointed rock masses (Wyllie et al., 2004). The peak shear strength of rock/soil can be explained by the Coulomb (1776) as illustrated in Equation (2.1); τ is the shear strength of rock/soil, σ is the normal stress, c is the cohesion and ϕ is the friction angle.

$$\tau = c + \sigma \tan \phi \qquad\qquad (2.1)$$

Rocks and soils show both frictional and cohesive attitude at measureable values of normal stresses (De Blasio, 2011). The cohesion and friction angle are the strength parameters. These are not in-built material properties but are dependent upon the conditions. Cohesion is defined as the shear resistance at zero normal stress. Soils usually have lower cohesion values as compared to rocks. Cohesion values of soils are normally in the order of few kPa whereas rocks have thousands of times larger cohesion values as compared to soils (De Blasio, 2011). Friction angle is defined as resistance to sliding between the grains due to interlocking of rock/soil grains. Inter-granular friction is the cause of shear strength in non-cohesive soils while internal friction and cohesion are the cause of shear strength in cohesive soils (Brown and Frimpong, 2012).

The shear strength of rock/soil can be determined by different methods and techniques. As far as the drainage conditions are the same, all the methods gave the same shear strength values (Osman, 1964a). He tried different methods which were mainly classified into three categories; direct, compression and torsional tests. Rock/soils exhibit a lot more engineering properties, which are not the scope of this study.

2.3. FORMATION EXCAVATION MODELING

The basic earthmoving process consists of penetration, cutting, and excavation (Blouin et al., 2001; Lipsett and Moghaddam, 2011). Figure 2.2 (a) presents the penetration action, which is defined as the insertion of a cutting tool into soil/rock. Figure 2.2 (b) presents the cutting action, which is the lateral movement by the cutting tool. The tool usually moves at some angle to the horizontal (inclined) and moves forward at a certain depth while maintaining a constant speed and the inclination (rake) angle. The forward movement of the tool (normally following a curvilinear path) to fill the bucket to the maximum capacity is known as loading/excavation as shown in Figure 2.2 (c).

The significant excavation forces in any machine-formation interactions include the breakout, cutting, and formation resistant forces (Frimpong et al., 2005). The breakout force is the force provided by the machine for cutting the material and is dependent upon machine weight, power output, and tractive effort. The force present at the soil-tool interface is called the cutting force and is dependent on the tool, soil, soil-tool and operating parameters. The force imposed by the formation on the cutting tool is known as formation
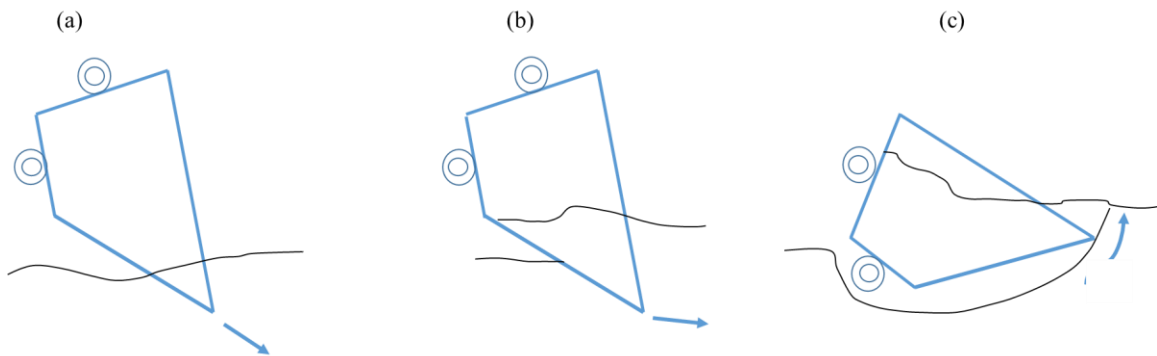
Figure 2.2. Fundamental earthmoving actions (a) Penetration (b) Cutting (c) Loading (Excavation) (reproduced after Blouin et al., 2001)

resistive force and is dependent on the engineering properties, geology and post-tectonic deformation characteristics and hydrogeology of the formation. In order to remove the material from its original location, the breakout force should be larger than the resistive forces. The formation resistive forces experienced by the cutting tool lays the foundation of the theory of cutting resistance on excavation machines (Awuah-Offei, 2006). The detailed understanding of the working environment, soil, cutting tool and soil-tool parameters are required for the required performance.

With the complex nature of soil-tool interaction modeling, limited research has been done in this area. Hemami (1994) showed that the behavior of the material during excavation is not yet well understood and this is valid still today. In the past, studies on soil-tool interaction modeling considered the evaluation of the different forces under varying condition. Three main types of soil-tool interaction modeling methods are found in the literature; analytical, experimental and numerical methods.

Coulomb (1773) was the first to present a noteworthy theoretical model for describing soil failure and soil shear strength/resistive forces. He concluded that the peak shear strength of soil can be presented as a combination of cohesive and frictional components as illustrated by Equation (2.1). It is assumed till today that the soil follows Coulomb criteria and fails along shearing. Mohr (1914) presented a graphical technique (Mohr circle of stress) and mathematical equations to determine the stress condition at a point in equilibrium for any kind of material. Both the criterion can be combined into mathematical equations as illustrated by Equation (2.2) (Holtz et al., 2011; McKyes, 1985; Raza, 2016).

$$\sigma_n = \frac{\sigma_1 + \sigma_3}{2} + \left(\frac{\sigma_1 - \sigma_3}{2}\right) \cos 2\theta$$

(2.2)

$$\tau = \left(\frac{\sigma_1 - \sigma_3}{2}\right) \sin 2\theta$$

$$q_u = cN_c + qN_q + 0.5\gamma'BN_\gamma \qquad\qquad (2.3)$$

Based on passive earth pressure theory, illustrated by Equation (2.3), Terzaghi (1943) presented a theory for determining the ultimate bearing capacities of soils for shallow foundations. N_c, N_q and N_γ are bearing capacity factors and are dependent upon the internal friction angle (ϕ) of soil. Payne (1956) discovered the relationship between the physical properties of soil and the forces caused by narrow vertical tine. He performed a lot of qualitative experiments to produce different soil failure shapes and concluded that the soil failure done by narrow tools is totally different as done by wide tools. Based on Coulomb's failure criteria, he proposed a model on the forces developed on wedge formed in front of a cutting tool. The major assumption of this model was that the soil failure along the soil-soil plane is governed by the Coulomb's Equation (2.1). The process of calculating the forces on the tool was tedious and time consuming.

Osman (1964b) was probably the first author who found similarities between Terzaghi's (1943) bearing capacity model and the mechanics of earth movement. He used a wide cutting blade to present a theoretical model for determining different parameters. The blade movement was considered perpendicular to the length on three different soil types to make it a simple 2D model. He verified his quantitative theoretical model and presented the experimental results. He concluded that an earth-moving problem can be

described by Equation (2.4), which he found after the dimensional analysis. This equation describes that force on the cutting blade is dependent on different parameters. Equation (2.5) can be written in dimensionless form as in Equation (2.6). He also concluded that a small change in cohesion or friction angle will result in increased cutting force.

$$P = f\,(c,\,\phi,\,\delta,\,c_a,\,z,\,\gamma,\,\alpha,\,q) \tag{2.4}$$

$$\frac{P}{\gamma z^2} = f\left(\frac{c}{\gamma z}\,,\delta,\phi,\frac{c_a}{\gamma z}\,,\alpha,\frac{q}{\gamma z}\right) \tag{2.5}$$

Reece (1964) suggested that all the soil forces can be combined into a single equation and presented the fundamental equation of earth-moving mechanics (Equation (2.6)). Equation (2.6) can be used to determine the force required to fail any mass of soil. For two dimensional cases, the same equation can be modified to Equation (2.7). He also presented the similarities between his equation and Terzaghi's (1943) bearing capacity model equation. He was unable to validate his equation mathematically but with the help of simple examples, he tried to develop the importance of his proposed equation.

$$P = cz^2 N_c + \gamma z^3 N_\gamma + qz^2 N_q + c_\alpha z^2 N_\alpha \tag{2.6}$$

$$P = czN_c + \gamma z^2 N_\gamma + qzN_q + c_\alpha zN_\alpha \tag{2.7}$$

Hettiaratchi et al. (1966) verified the Reece (1964) equation and presented many charts to determine the N-factor values. Reece (1964) assumed that Equation (2.7) is only

valid if the variables like γ, c, c_α and q, do not affect the failure surface and N-factors values but Hettiaratchi et al. (1966) showed that these N-factors and failure surface are dependent on these variable. They presented that these N-factors values are not constant for any given conditions or geometry, and hence their use can result in some degree of error, although they finally concluded that the errors encountered by making the Reece (1964) assumption will be very small for all practical examples and hence can be neglected.

Based on the Mohr-Coulomb criteria, Thakur and Godwin (1990) studied the tip effect by using a 20-guage rotating wire. The conditions were almost similar to that of a blade working in frictional soils. The major assumption was that the tip of the wire has high strength and is not extendable. They concluded that the soil can fail in two modes, which occur at the same time. First, a passive general shear failure zone towards the free curved face of a previous cut and a local shear failure zone towards the un-deformed soil. The conclusions drawn from this study form the basis to understand the mechanics of different rotary machines.

Qinsen and Shuren (1994) developed a 2D formation resistive force model for a bulldozer blade. They found the resultant forces acting on the soil wedge in advance of the blade, which were further resolved into horizontal and vertical forces. The analytical model was verified experimentally with reasonably good results. The model was further used to observe the effects of blade velocity, tool depth, and the soil density on the forces. The results showed that soil density and tool depth affect both the mean and fluctuating amplitudes of force on the bulldozer blade, but the velocity affects the force on the blade only when high (above 0.3 m/s) (Qinsen and Shuren, 1994). The tool depth and soil density both affected the forces on the blade (Qinsen and Shuren, 1994).

McKyes and Ali (1977) proposed that a 3D model can predict the resistive forces and the volume of the soil more accurately in advance of a narrow cutting tool. They modeled soil failure pattern and the crescent radius as a function of the soil properties and the cutting tool. The soil failure pattern was also modeled as a function of the failure angle, considering a straight line failure plane (i.e. the path of least resistance).

Another 3D force prediction model for narrow cutting tools was developed by Godwin and Spoor (1977). They worked with two different soil types assuming that these soils are homogeneous, isotropic and will follow Mohr-Coulomb failure criteria. They proposed that the soil failure occurs in two zones, crescent failure zone (above a certain critical depth) and lateral failure zone (below critical depth), as illustrated in Figure 2.3. They concluded that for small aspect ratios (working depth/width ratio), only the crescent failure zone is found while for large aspect ratios, both the failure zones will be observed. They also produced mathematical equations to determine the critical depth and found that the critical depth is inversely proportional to rake angle given a fixed aspect ratio. It was also found that the critical depth increases with increasing tool width and soil friction angle for a particular rake angle.

Perumpral et al. (1983) proposed that the forces on the sides of the soil wedge play a vital role in the soil cutting process and were modeled instead of the forces on the failure crescent. They were able to determine all the forces on the soil wedge by applying the limit equilibrium analysis technique and using the path of least resistance approach. They were unable to determine to soil failure angle accurately.

Swick and Perumpral (1988) modified Perumpral et al. (1983) model to observe soil behavior under dynamic conditions. The new model included shear rate effects on soil
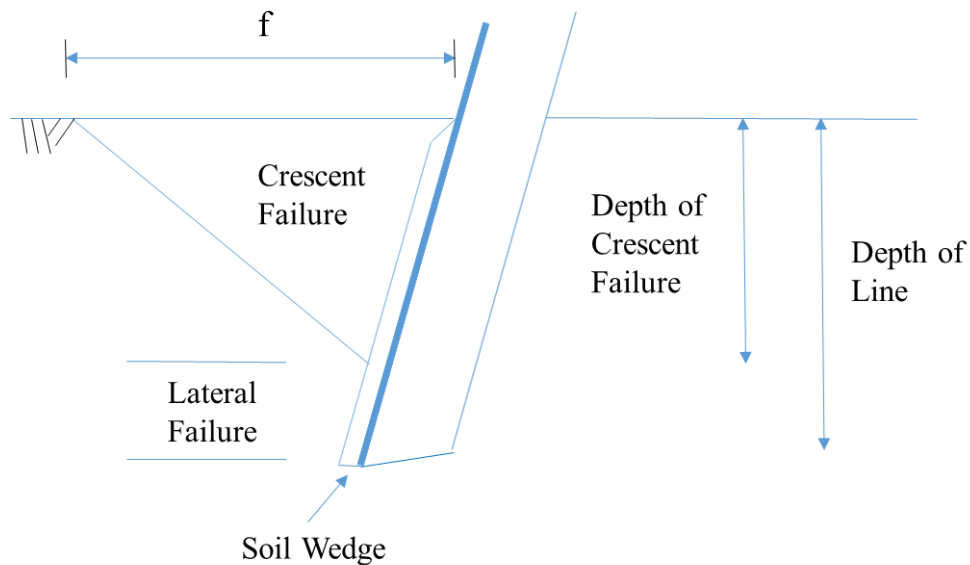
Figure 2.3. Soil failure pattern (reproduced after Godwin and Spoor, 1977)

shear strength and soil-metal friction parameters, which were missing in the earlier model. For validation purposes, they performed tests on artificial soil for four tool speeds, four tool widths, three tool angles and three tool depths (resulted in 144 combinations) to see effects on cutting resistance offered by soil. They found that internal friction angle, soil-tool interaction angle, adhesion and cohesion do not depend on shear rate. The resulting model outputs were close enough to the experimental results. A model to predict the soil trajectory on a moldboard plow surface was developed by Suministrado et al. (1990a). They performed many experiments to assess their model predictions. These soil trajectory models were further used by Suministrado et al. (1990b) to develop a 3D model for determining the soil reaction forces. The method of trial wedges was used to determine the failure plane angle. Experiments were carried out for the assessment of the 3D model and were successful.

The limiting stress condition of the Coulomb's material and ignorance of the dynamic effects by the passive earth theory were criticized by Dechao and Yusu (1991). These assumptions are valid for soils having a definite failure profile but cannot be applied to flow failure soils. The principle of virtual power in plasticity theory was used to determine the resistive forces. The forces from soil deformation were also taken into consideration. The validation of the model was done experimentally. The passive earth theory and other related models assumed the instantaneous soil failure along the failure plane. This may be applicable to plastic soils, but not for all soils. In some cases, failure starts and progresses from the tip of the cutting tool.

According to Alekseeva et al. (1985), Dombrovskii and Pankratov (1961) suggested that the tangential force to soil digging (P), is the sum of three constituent forces: a soil's resistance to cutting, the tool's frictional resistance with soil, resistance to movement of the drag prism ahead of the tool, and the soil movement inside the dipper/bucket as illustrated in Equation (2.8). They combined all the resistance and cutting forces and proposed a simplified relation in Equation (2.9). Experiments were performed on different soil types to determine the values of k and k_1.

$$P = \mu_1 \, N' + \varepsilon \, (1 + q_n) \, B_v \, k_n + kwd \qquad (2.8)$$

$$P = k_1 \, wd \qquad (2.9)$$

The universal earthmoving equation (Equation (2.3)), based on the passive earth pressure theory, was stretched to buckets by sub-dividing the bucket into its individual

components (like sidewalls, blade, and the backside of the bucket) by Balonev (1983). According to Balonev (1983), the total resistance on the bucket is the sum of the resistances on the individual components as in Equation (2.10). f_1 is the cutting resistance of the flat trenching blade with a sharp edge; f_2 is the additional resistance due to the wear of the edge, f_3 is the resistance offered by the two side walls, and f_4 is the resistance due to friction of the sides.

$$P = f_1 + f_2 + f_3 + f_4 \qquad (2.10)$$

Zelenin et al. (1985) performed a lot of experiments for cutting the frozen soil. The digging resistance was divided into the cutting resistance (P) on the teeth and the filling resistance (W). They developed an empirical model, as illustrated in Equation (2.11) to determine the cutting resistance offered by the unfrozen soil on a bucket without teeth. They proposed that the bucket with teeth diminishes the participation of side walls during the soil cutting process as illustrated in Equation (2.12). C_o is defined as the number of impacts required to sink a cylindrical tip in a standardized test by 10 cm^5; z is the coefficient that considers the effect of cutting blade on the force; w is the tool/dipper width; and d is the depth of tool/dipper into the bench. They developed a graph to determine the 'z' values, which are dependent upon 'w' and, 'd'. From that graph, it was seen that the 'z' values increase as the 'd' values decrease. The 'z' values were obtained for d = 0.25 - 0.5 m and are presented in Table 2.1. The 'z' values are also dependent upon the ratio a/b ('a' is the spacing between the teeth and 'b' is the width of a tooth), and are presented in Table 2.2.

$$P = 10C_0 d^{1.35}(1 + 2.6w)(1 + 0.0075\beta')(1 \pm s)V\mu \qquad (2.11)$$

$$P = 10C_0 d^{1.35}(1 + 2.6w)(1 + 0.0075\beta')z \qquad (2.12)$$

Table 2.1. Dependence of coefficient 'z' on depth and width of cutting tool

Width of tool/dipper (m)	0.25 – 0.5	0.5 – 0.75	0.75 – 1.0	1.0 – 1.25
Coefficient 'z' values	0.55 – 0.75	0.63 – 0.78	0.69 – 0.8	0.71 – 0.82

Table 2.2. Dependence of coefficient 'z' on a/b (Zelenin et al., 1985)

Ratio a/b	a = b	a = 2b – 3b	a = 4b	a = 5b
'z' values	1.2	1	1.1	1.25

Zelenin et al. (1985) further developed their model to determine the filling resistance force as illustrated in Equation (2.13). They sub-divided the filling resistance into two components: the force developed by the drag prism of the soil in front of the bucket (P_n), and the force developed by the chip itself which enters the bucket (longitudinal compression, R). The factors affecting these two forces have been incorporated into the filling resistance model. The 'R' force is proportional to the cross-section of the stratum being excavated and the specific resistance of the given stratum to longitudinal

compression. Being a strength parameter, it depends on the soil being excavated by the excavator. According to Zelenin et al. (1985), these forces are available for graders and dragline buckets having teeth but are not available for shovel dippers having teeth. The teeth break the soil in advance of the dipper movement and hence, drag prism force is absent as illustrated in Equation (2.12). The study was limited because experimentations were carried out on smaller buckets, but the present day dipper is large enough to carry payloads of greater than 100 tons.

$$W = P_n + R = g \, q \, \gamma \, \tan \rho + FK_{comp} \tag{2.13}$$

To automate the loading process of the Load-Haul-Dump (LHD) loader, Hemami et al. (1994) proposed a model comprising of six forces ($f_1 - f_6$) that should be overcome for successful excavation (Figure 2.4). These forces can be explained as follows:

- f_1: The force necessary to overwhelm the payload weight

- f_2: The resistive force from the formation as a result of material movement

- f_3: The frictional force generated due to the sliding of the material inside the dipper

- f_4: The resistance to cutting at the dipper teeth

- f_5: The inertial force generated by the excavated material inside the dipper

- f_6: The required force to move the unfilled dipper

All the forces in Hemami et al. (1994) model are dynamic, except f_6. The point of application and the magnitude of f_1 force change at each time step during the whole excavation process. They used position, velocity, orientation of the bucket, and the geometric configuration to model the force f_1. The geometric configuration used to

determine the material's center of mass inside the bucket, is not applicable to current dippers. Because the current dippers are more of a rectangular shape, compared to the triangular bucket considered by Hemami et al. (1994). According to Hemami et al. (1994), if a proper dipper trajectory is selected, the force f_2 can be taken equal to zero. The forces f_3 and f_4 were combined into a single force and can be determined by Zelenin et al. (1985) approach (Equation (2.12)). The force f_5 is dependent on the dipper's acceleration and the force f_6 is known beforehand.
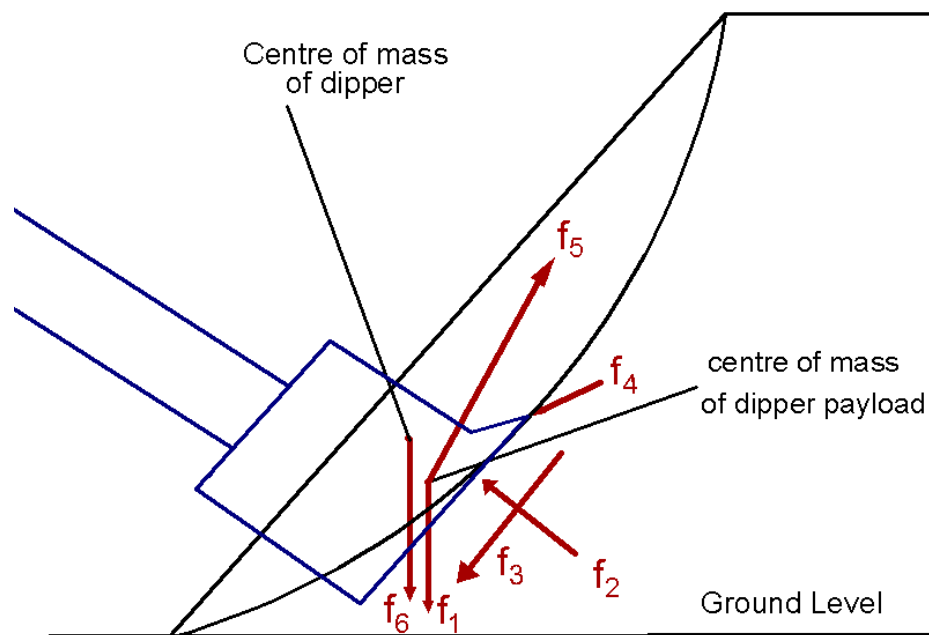
Figure 2.4. Forces on a shovel dipper during a loading cycle (Hemami et al., 1994)

Takahashi et al. (1998) presented somewhat similar model to Hemami et al. (1994) to determine the formation resistive forces for a Load-Haul-Dump loader and for a wheel

loader. They proposed five resistive forces (F_1 - F_5), merging f_6 and f_1 forces of Hemami et al. (1994) model. The force f_6 shouldn't be modeled as part of force f_1 or f_5 as the point of application is not concentric. The forces of Takahashi et al. (1998) model are shown in Figure 2.5, and are explained as follows:

- F_1: The gravitational force of the bucket and soil/rocks in the bucket

- F_2: The force acting on the bucket bottom when it pushes the rock pile

- F_3: The frictional force between the bucket and rock pile

- F_4: The cutting force acting on the edge of the bucket

- F_5: The force required to move the rocks inside the bucket
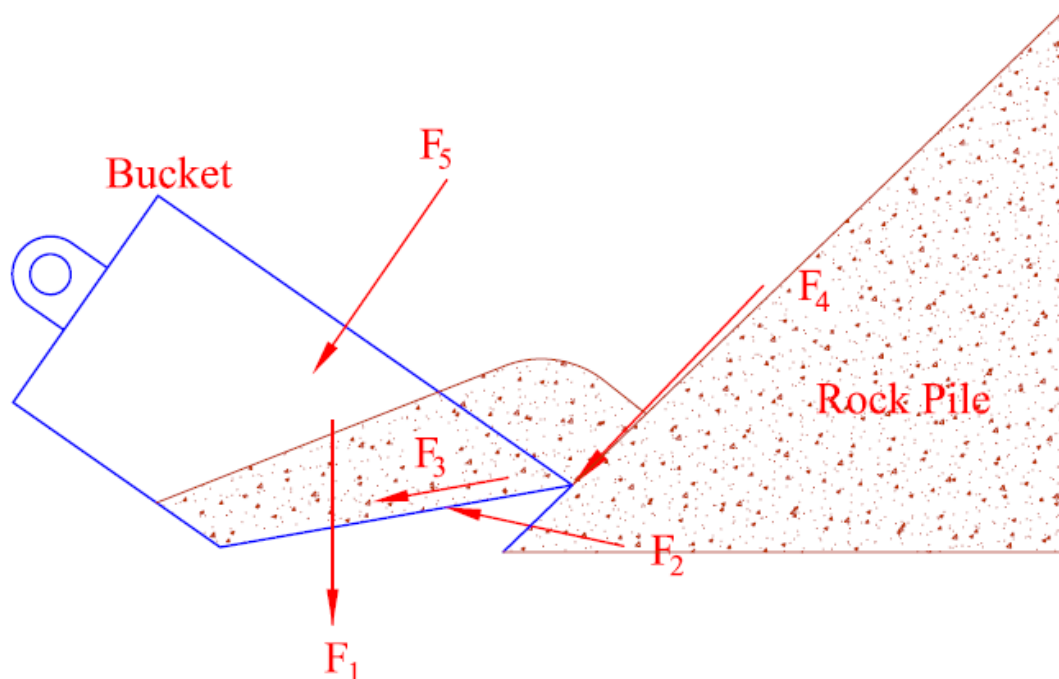
Figure 2.5. Forces on an excavator bucket during a loading cycle (Takahashi et al., 1998)

The forces F_1 and F_3 were determined geometrically using the soil properties and bucket orientation. The forces F_2 and F_5 were determined in a similar manner using the approach of Hemami et al. (1994). The force balanced equations were solved using the static earth pressure on the soil particles to determine the F_4 force. To verify the empirical model, small-scale testing was done, limited to the lower penetration rates.

A model to determine the six forces similar to the Hemami et al. (1994) model was proposed by Awuah-Offei and Frimpong (2004), Awuah-Offei (2006), and Awuah-Offei et al., (2009). The area (A_c) of the excavated material can be calculated using the geometry in Figure 2.6 and is illustrated in Equation (2.14). The initial coordinates of the dipper tip when it contacts the soil are x_0 and y_0, and x_t is the coordinate of the dipper tip after a time 't'. Once, all the points on the dipper trajectory are known, the area under the trajectory curve can be calculated by the integral term.

$$A_c = (x_t - x_0)y_0 + \frac{1}{2}(x_t - x_0)^2 \tan r - \int_{x_0}^{x_t} f(x)dx \qquad (2.14)$$

$$f_1 = A_c \omega \rho g \qquad (2.15)$$

The force f_1 was modeled as a dynamic force and is illustrated in Equation (2.15). The forces f_2 and f_5 were determined in a similar manner using the approach of Hemami et al. (1994). Based on the Balovnev (1983) model, the forces f_3 and f_4 were modeled. As the shovel dipper moves into the formation, the forces on the dipper were determined using a numerical model created in Matlab/Simulink. The model did not consider the forces for the individual joints and links.
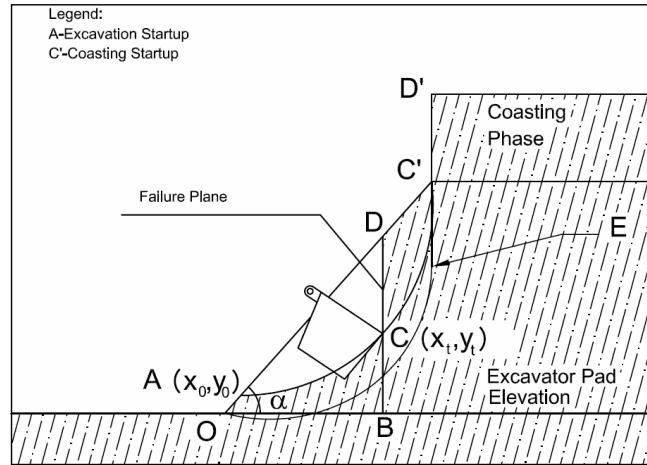
Figure 2.6. A 2D model of formation excavation (Awuah-Offei, 2006)

Raza and Frimpong (2017) used the Awuah-Offei (2006) model of the payload force to determine the dynamic force f_1 (material weight). A specified curved trajectory was assumed, which is illustrated by the quadratic Equation (2.16). The force f_6 (dipper weight) was determined continuously throughout the whole simulation. Both the f_1 and f_6 forces were determined at specific time intervals and were plotted as shown in Figure 2.7. By using the Zelenin et al. (1985) model (Equation (2.12)), the forces f_3 and f_4 were determined by combining them into a single force, which was further resolved into its normal and tangential components. The model gave reasonably accurate results.

$$y = 0.9927x^2 - 22.557x + 117.68 \qquad (2.16)$$

Although previous models do not solve the excavation problems completely, they can be used as guidelines for the current research to achieve novel results. This study is an attempt to advance the body of knowledge and frontiers in formation excavation science.
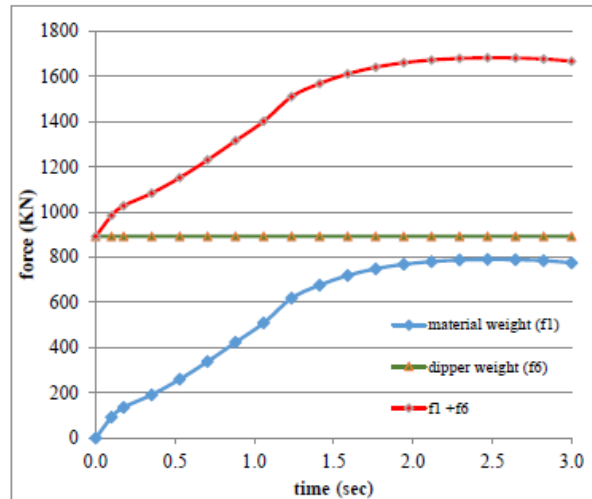
Figure 2.7. Determination of payload and dipper weight (Raza, 2016)

2.4. NUMERICAL MODELING

The requirement for soil cutting models that allow for progressive soil failure prompted the use of numerical methods in soil-tool interaction modeling. Before the development of electronic technology, engineering problems were modeled and solved in their simplified form. Due to the development of the computer technology in the last three and half decades, engineering problems are solved with ease with the help of numerical methods. The use of numerical methods became popular due to following reasons:

- Numerical methods can be utilized for sensitivity analysis to observe the effects of different parameters, hence to determine the most critical parameter.

- Experimental methods require a lot of resources in terms of time and cost. On the other hand, numerical methods save time and resources, hence are less costly.

- All the desired parameters can be used in mathematical models of physical processes and can be easily solved with the help of numerical methods.

- Due to the complicated terrains and heterogeneous properties of formations, many practical problems are difficult to model and solve by analytical methods, hence requiring a rigorous numerical method.

Finite element method (FEM) and Discrete element method (DEM) are the two main numerical methods used in the areas of soil-tool interaction and failure mechanism.

2.4.1. Finite Element Method. Soils are usually considered to be continuum media for the better performance of FEM. To date, very less research has been done for soil-tool interaction studies using FEM techniques. Yong and Hanna (1977) were the first to apply FEM technique to observe the soil-cutting process in front of the cutting tool, and to predict the displacement and stresses during the process. A 2D model of soil failure was developed by using plane-strain analysis while stress-strain relations were determined experimentally. They were able to validate their numerical results of resultant forces and failure pattern. In an application of drag-cutters and drag-bits for rock cutting, FEM was used to determine the resistive forces (Xiang and Saperstein, 1988). The study also predicted the failure zone for various stress applications. Kushwaha and Shen (1995) applied FEM to solve the dynamic equation of soil-tool interaction. Rosa and Wulfsohn (1999) used FEM to develop a constitutive model for high-speed cutting tools.

To observe the soil-tool interaction, a 3D FEM was used by Chi and Kushwaha (1991) using the approach of Yong and Hanna (1977). Stress-strain relations were determined by performing a series of triaxial tests. These relations were used as an input to the FEM model to determine the Poisson's ratio and soil-metal friction. A 3D FEM model was developed for the interaction of a subsoiler (having a chisel point) with non-homogenous sandy loam soil (Mouazen and Nemenyi, 1999). The effect of cutting edge

geometry of a 400 mm wide experimental sweep on the horizontal and vertical force components was studied by Fielke (1999). Plouffe et al. (1999) engaged a 3D FEM to simulate forces functional on a moldboard plow during an operation.

FEM works well when the medium is continuous, that is one of the biggest deficiency of the method and it cannot be applied to soils accurately. That is why an approach was required that can capture the deformation pattern while maintaining the discrete nature of the soils.

2.4.2. Discrete Element Method. Discrete element method (DEM) is one of the main numerical methods for modeling soil-tool interaction and failure mechanism studies and has gained great popularity in recent years. The DEM concept was first introduced by Cundall (1971) for rock mechanics analysis. Cundall and Strack (1979) extended the DEM use for the analysis of forces and motion in 2D discrete discs assemblies. The main objective of this fundamental research was to prove that DEM technique can accurately and realistically determine the behavior of discs assemblies. In DEM, the particle to particle interaction and particle to wall interaction can be seen as a short time problem as the equilibrium conditions changes at each time step. By determining the movement of each particle, a series of calculations was done to determine the displacements and contact forces at equilibrium.

The velocity and acceleration during each time step were assumed constant. The other assumption was that the disturbance could travel to next disc only in a single time step. So the time step should be chosen small enough to incorporate that assumption. Different properties were tested to see the effect on the contact forces. The following conclusions were made; (i) damping has no effect on equilibrium contact force; and (ii)

shear stiffness (k_s), normal stiffness (k_n) and friction angle have a huge impact on discs assemblies' behavior. Their model regenerated the stress-strain behavior of granular assemblies but underestimated the repose angle. The major limitation of the model presented was that it dealt with dry assemblies and total contact forces only.

Tanaka et al. (2000) used Cundall and Strack (1979) DEM to develop a mechanical model for analyzing the discontinuous nature of soil. They performed an experiment in which a metal bar was tried to penetrate the soil mass and determined the deformation and resistive forces on the bar. They found that the soil near the bar moved downward as the bar was also moving down. The simulation was done to check the validity of the model. The effect of the friction coefficient between particle and wall was simulated as shown in Figure 2.8. It was found that the deformation near the bar is directly proportional to the coefficient of friction. Experimental results matched with simulation results to some accuracy at only one value of coefficient of friction. To overcome these problems, they performed an experiment by using alumina balls instead of soil. They were successful in getting the desired deformations but still failed to get comparable resistive forces.

$(\mu_w = 0.0)$ $(\mu_w = 0.25)$ $(\mu_w = 0.5)$ $(\mu_w = 0.75)$
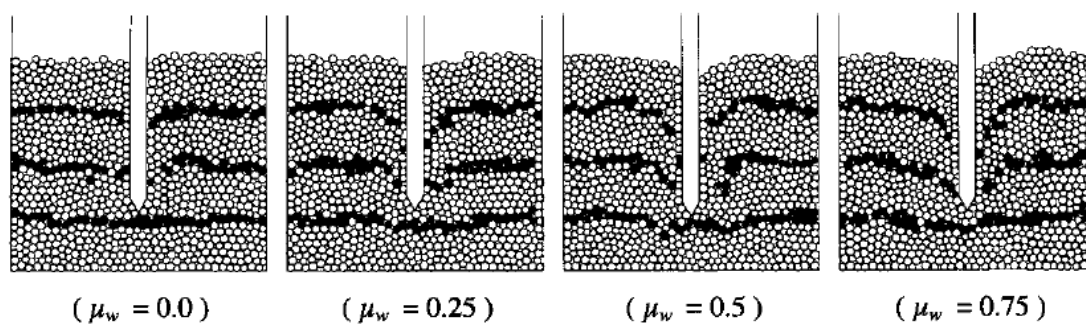
Figure 2.8. The effect of the friction coefficient (Tanaka et al., 2000)

Momozu et al. (2002) introduced the concept of soil clod and developed a modified DEM model. Simulations were performed and the results showed promising deformation patterns but the model failed to account for resistive forces. Furthermore, a single blade was used for the simulation rather than a full shovel dipper (Figure 2.9). Ai et al. (2011) then proposed a modification in the Cundall and Strack (1979) DEM model and included the elastic-plastic spring-dashpot elements to account for rolling friction and rolling resistance (Figure 2.10).

Rasimarzabadi and Joseph (2016) investigated the filling of a shovel dipper using PFC2D. Experiments were performed by using two cube root scaled models (1:32 and 1:20) of the 44m^3 dipper by moving them through angular crushed limestone placed in a bin. Filling procedure of the dipper was calibrated but the material properties were not calibrated accurately (Rasimarzabadi, 2016). DEM simulations of dipper having teeth and without teeth were also conducted to examine their influence.
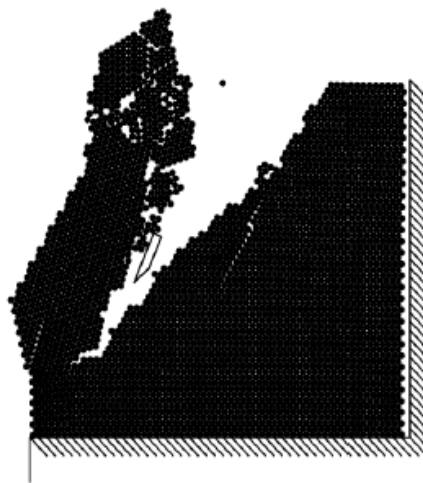
Figure 2.9. Simulated cutting process (Momozu et al., 2002)
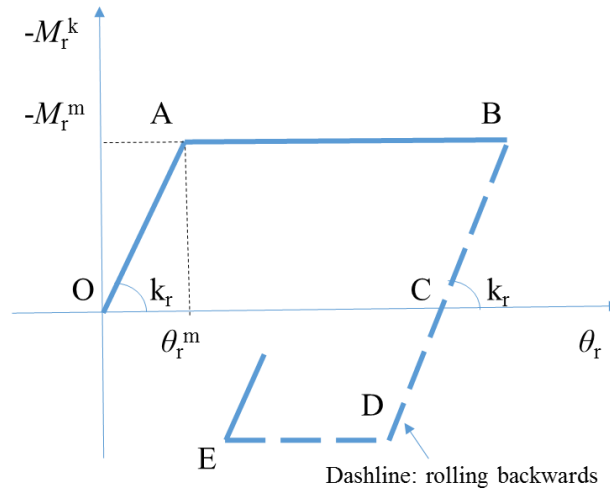
Figure 2.10. Spring torque of elastic-plastic spring-dashpot model (Ai et al., 2011)

2.5. MULTIPLE LINEAR REGRESSION

A multiple linear regression (MLR) model is the advanced form of simple linear regression (SLR) model (Tranmer and Elliot, 2008). There are 'p-1' independent variables in MLR, and the relationship between the independent variables and the dependent variable (y_i) is given by Equation (2.17). β_0 is the intercept, β_1-β_{p-1} are the coefficients relating the independent variables to the dependent variable, and 'e_i' is the error. The coefficients (β_k) are also known as partial regression coefficients (Eberly, 2007). The least square criterion is used for estimating MLR as given by Equation (2.18). Standard errors depend on the mean square error (s^2) with 'n-p' degrees of freedom, and is given by Equation (2.19).

$$y_i = \beta_0 + \beta_1 x_{i,1} + \beta_2 x_{i,2} + \ldots\ldots + \beta_{p-1} x_{i,p-1} + e_i \qquad (2.17)$$

$$\sum_{i=1}^{n} (y_i - (\beta_0 + \beta_1 x_{i,1} + \beta_2 x_{i,2} + \ldots\ldots + \beta_{p-1} x_{i,p-1}))^2 \qquad (2.18)$$

$$s^2 = \frac{1}{n-p}\sum_{i=1}^{n}(y_i - \hat{y}_i)^2 \qquad (2.19)$$

An ANOVA table is developed having the sum of squares (SS), degrees of freedom, and F-test. The coefficient of multiple determination (R^2) is defined as the ratio of the SS of the model to the SS (total). R^2 measures the variation in y linked with p-1 predictors with values between 0 and 1. With an increase in SS (model), R^2 increases but for the non-significant predictors, there is a little increase in R^2. It is not mandatory that the best model will have the highest R^2 value. Therefore, adjusted R^2 is mostly used in MLR analysis. The adjusted R^2 is calculated by using the mean squares instead of SS and is illustrated in Equation (2.20). The root mean square error (RMSE) is another important parameter that shows the capability of the model predictions and can be determined by using the Equation (2.21).

$$R_a^2 = 1 - \frac{mean\ square(error)}{mean\ square(total)} \qquad (2.20)$$

$$RMSE = \sqrt{\frac{\sum_{i=1}^{n}(y_i - \hat{y}_i)^2}{n}} \qquad (2.21)$$

2.6. ARTIFICIAL INTELLIGENCE

Artificial intelligence (also known as machine intelligence) is the intelligence shown by machines. Artificial Neural Network (ANN), Mamdani Fuzzy Logic (MFL), and Hybrid neural Fuzzy Inference System (HyFIS) are some of the important artificial intelligence (AI) models.

2.6.1. Artificial Neural Network. An ANN is a complex network that works similar to a human brain (Wang, 2003). According to Shanmuganathan (2016), the human brain is much more complicated, as there are still many unknown cognitive functions. However, the main characteristics common to both natural and artificial networks are learning and adaption, generalization, enormous parallelism, robustness, information storage and processing.
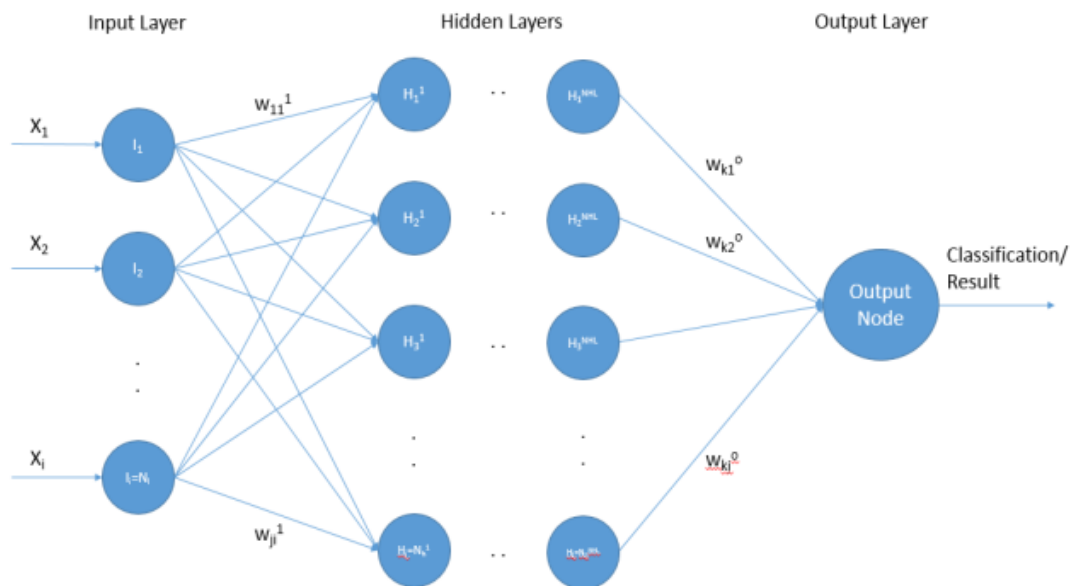
Figure 2.11. A multi-hidden layered neural network (Ali and Frimpong, 2018)

An ANN consists of an input layer, hidden layers (one or more), and an output layer and as illustrated in Figure 2.11. Every layer in an ANN consists of neurons (also called as nodes) that process the data. Different numeric numbers, known as 'weights' connects

these neurons within the layers. As the connections exist between the neurons, the neural networks are also known as connectionist models (Kasabov, 1996). The neurons in the input layer accept the data and forward it to the hidden layer. The data is processed and the weights are assigned by the neurons in the hidden and output layers. A bias is also added to each neuron in hidden and output layers to obtain non-zero outputs. The output O_k, of kth neuron in a single hidden layer is given by the Equation (2.22). σ is the activation/transfer function, the number of input neurons is denoted by n, the weights by w_{kj}, inputs by I_j, and bias of the hidden layer by B_k.

$$O_k = \sigma(\textstyle\sum_{j=1}^{n} w_{kj} I_j + B_k) \tag{2.22}$$

An ANN model is developed in two phases: feedforward phase and gradient descent based error backpropagation phase. The steps discussed earlier are completed in phase one while in phase two, ANN decision parameters are adjusted to optimize the problem and to get desired results. The error contribution of each neuron is determined, and by adjusting the weights and bias of the neurons, errors are brought within a specified tolerance. Ali and Frimpong (2018) discussed the detailed mathematical modeling of the two phases for an ANN model having multiple hidden layers.

2.6.2. Mamdani Fuzzy Logic. Zadeh (1965a) first used the fuzzy logic term when he proposed his fuzzy set theory. Fuzzy logic uses the concept of fuzzy set in which the truth-values of variables range between 0 (completely false) and 1 (completely true). MFL is one of the first control systems that were developed using fuzzy set theory and is the most commonly used fuzzy logic models. Mamdani and Assilian (1975) proposed the

famous MFL model, while they were trying to synthesize a combination of linguistic rules during a combination of a boiler and a steam engine. They used the concept of Zadeh (1973b), who proposed the fuzzy algorithms for complex systems and decision processes.

In MFL, a set of linguistic rules are expressed in such a way that 'if this will happen, then do that'. For example, one of the fuzzy rules in an automatic car using the MFL model can be 'if a person is in the way, then stop the car'. The process of MFL consists of fuzzification, fuzzy logic operations by using if-then rules (inference engine), and defuzzification steps as illustrated in Figure 2.12.
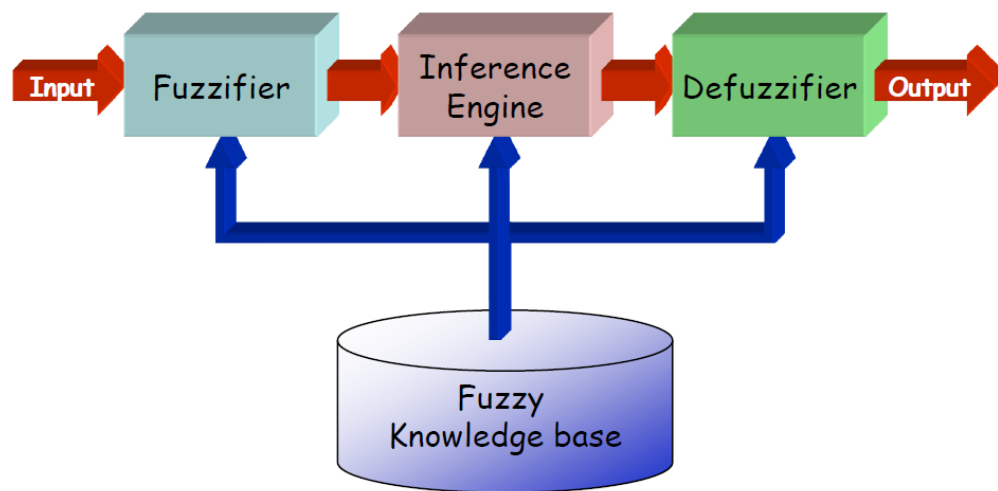
Figure 2.12. Structure of a fuzzy inference system

In fuzzification, all the input values are transformed into membership functions. All the possible if-then rules are executed in the fuzzy logic operations step, and the output functions are produced. For two input parameters (I_1 and I_2) and an output parameter (O),

the rule base (RB) model proposed by Mamdani (1976) can be presented as Equation (2.23). The fuzzy linguistic variables are presented by f_{1j}, f_{2j}, and f_{3j} for all j = 1, 2, 3, …, n. In the defuzzification step, all the fuzzy output values are transformed back into real values that are also known as crisp values. There are five different defuzzification methods available in the literature. Among these methods, the center of gravity (center of area or centroid) method is mostly accepted and used by different researchers (Lee, 1990; Sugeno, 1985) as illustrated in Equation (2.24). The membership function of fuzzy set 'A' w.r.t 'O' is denoted by $\mu_A(O)$.

$$\text{RB}^j = \text{if } I_1 \text{ is } f_{1j}, \text{ and/or } I_2 \text{ is } f_{2j}, \text{ then O is } f_{3j} \text{ for all } j = 1, 2, 3, \ldots, n \tag{2.23}$$

$$O_{COG} = \frac{\int \mu_A(O).ODO}{\int \mu_A(O)} \tag{2.24}$$

Fuzzy systems are gaining popularity because they can handle incorrect knowledge and data. Fuzzy systems are rule-based, by using fuzzy rules and inference. They are strong enough to handle confusing, subjective, and incorrect knowledge and data. Fuzzy systems are applied successfully in the fields of computer vision, decision analysis, data analysis, expert systems, and automation. Automatic washing machines, transmission control, and automatic camera focusing are some of the applications of these fuzzy systems (Shanmuganathan, 2016).

2.6.3. Hybrid Neural Fuzzy Inference System. Kim and Kasabov (1999) proposed the hybrid neural fuzzy inference system (HyFIS). All the details presented in this sub-section have been adopted from that paper. HyFIS is a neural network based on

the fuzzy system, consisting of five layers and its structure is shown in Figure 2.13. HyFIS uses a combination of both numerical data and fuzzy rules, thus exhibits the added advantage of both methods. Input nodes present the input states and output nodes present the output control-decision signals. The nodes in the hidden layers present the rules and membership functions (MFs). This is an advantage of HyFIS over the normal feedforward multi-layer network in which it is really difficult to understand and to make any change. The nodes in layer 1 are the input nodes, which represent input linguistic variables as crisp values. These nodes are used to transfer signals to layer 2 (MF layer). The nodes in layer 1 are linked to only those nodes of next layer that presents the linguistic values of variables.
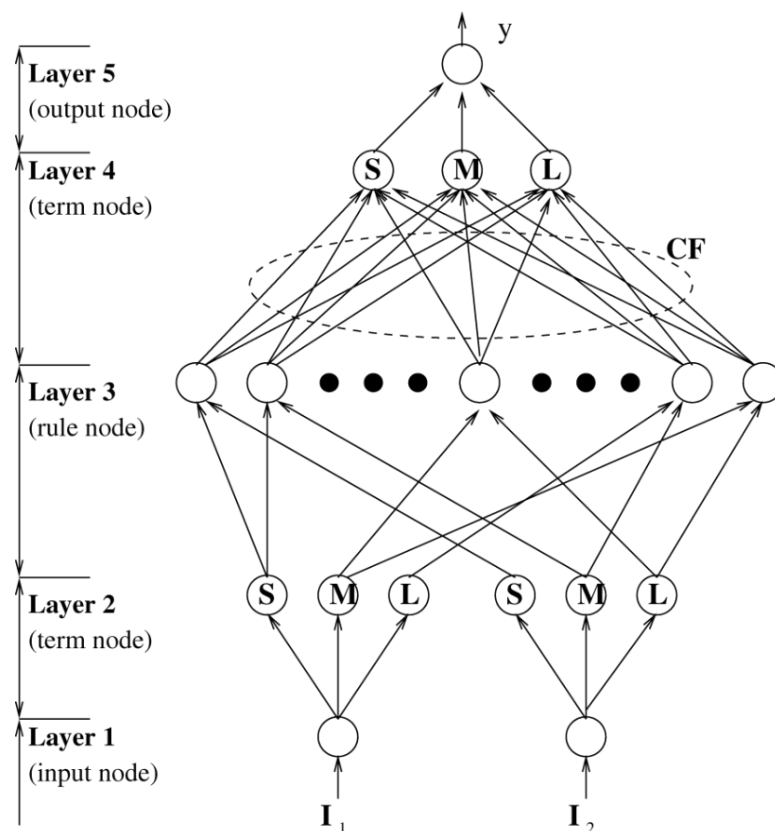
Figure 2.13. Structure of a hybrid neural fuzzy inference system

The nodes in layers 2 and 4 are given the name as 'term nodes (perform as MFs)' that are used to present input and output fuzzy linguistic variables. Nodes in layer 2 perform the duty of being MFs that are used to show the linguistic variables. The membership degrees are calculated by using the Gaussian (bell-shaped) function that is dependent on mean or center (c) and variance or width (σ) and is given by Equation (2.25). Any change in the values of these parameters results in the shape change of the bell MFs. The fuzzy sets defined in layers 2 and 4 of Figure 2.13 are small (S), medium (M), and large (L). The weights are unity at the start and the MFs are equally spaced over the entire area. The relation of the input to the MF is given as the output function of this layer as given by Equation (2.26). The parameters involved in this layer are known as precondition parameters.

Each node (rule node) in layer 3 represents the IF-part of a fuzzy rule. The weights are unity at the start and the nodes perform the 'AND' operation. All the nodes develop a fuzzy rule base and the output function is given by Equation (2.27). The output of node 'i' in layer 2 is denoted by y_i^2, I_j is the indices' set of layer 2 nodes and is connected to layer 3 via node j. Each node in layer 4 presents THEN-part of a fuzzy rule and the nodes perform the 'OR' operation. The nodes of layers 3 and 4 are connected with each other. The connection weights (w_{kj}) of 'k' nodes in layer 4 to 'j' nodes in layer 3 are in between the range [-1, +1]. The output function of layer 4 is given by Equation (2.28), where I_k is the indices' set of layer 3 nodes and are connected to layer 4 via node k. Finally, the nodes in layer 5 are the output nodes, which act as a defuzzifier. A node in layer 5 calculates a single crisp output. In the Centre of Gravity (COG) defuzzification method, the output signal is presented by the fuzzy centroid given by Equation (2.29). I_l is the indices' set of layer 4

nodes and is connected to layer 5 via node l. c_{lk} is the centroid and σ_{lk} is the width of the membership functions.

$$\mu_A(x) = \text{Gaussian}(x; c, \sigma) = e^{-((x-c)^2/\sigma^2)} \qquad (2.25)$$

$$y_i^2 = e^{-((x-c)^2/\sigma^2)} \qquad (2.26)$$

$$y_j^3 = \min_{i \in I_j}(y_i^2) \qquad (2.27)$$

$$y_k^4 = \max_{j \in I_k}(y_j^3 w_{kj}^2) \qquad (2.28)$$

$$y_l^5 = \frac{\sum_{k \in I_l} y_k^4 \sigma_{lk} c_{lk}}{\sum_{k \in I_k} y_k^{(4)} \sigma_k} \qquad (2.29)$$

Two phases are available in HyFIS during the learning process: structure learning phase for knowledge acquisition and parameter learning phase. In structure learning or rule finding phase, techniques proposed by Wang and Mendel (1992) are employed to determine the fuzzy rules from the required input-output pairs. These rules can further be used to establish the neuro-fuzzy structure. In parameter learning phase, a gradient descent learning scheme is employed to optimize the membership functions to achieve reasonable outputs. The error function is given by Equation (2.30). The number of nodes is presented by q, d_l presents the required output and y_l presents the actual output of the node l in layer 5 assuming $X = (x_1, x_2, x_3, \ldots\ldots, x_p)$ as an input vector. The weight (w_{kj}) can be adjusted

with respect to node *j* in layer 3 and node *k* in layer 4. The gradient descent-learning scheme uses a rule given by Equation (2.31), where $\eta > 0$ presents the learning rate. The chain rule in Equation (2.31) can be calculated by using Equation (2.32).

$$E = \frac{1}{2}\sum_X \sum_{l=1}^{q}(d_l - y_l^{(5)})^2 \qquad (2.30)$$

$$w_{kj}(t + 1) = w_{kj}(t) - \eta\left(\frac{\partial E}{\partial w_{kj}}\right) \qquad (2.31)$$

$$\frac{\partial E}{\partial w_{kj}} = \frac{\partial E}{\partial y_k^{(4)}}\frac{\partial y_k^{(4)}}{\partial w_{kj}} = \frac{\partial E}{\partial y_l^{(5)}}\frac{\partial y_l^{(5)}}{\partial y_k^{(4)}}\frac{\partial y_k^{(4)}}{\partial w_{kj}} \qquad (2.32)$$

2.7. RATIONALE FOR PHD RESEARCH

This research will serve as an effort towards enhancing the knowledge and frontiers in the field of numerical rock mechanics testing, artificial intelligence modeling, and cable shovel technology resulting in efficient and economic formation excavation.

The PFC models for the two rock formations (Sakesar limestone and Namal limestone) for the rock mechanics tests were developed. Different researchers have developed rock test models in the past using PFC, but according to the author's knowledge, no one have followed ISRM (1978a, b), ISRM (1979a, b), ASTM-D3967 (2008), and ASTM-D4543 (2008) standards. For the Brazilian tensile strength tests, it is recommended by these standards to have a sample that has a thickness to diameter ratio of 0.5. Researches have used cuboid samples for their rock test models. The size of the sample is expected to have an effect on the results of these numerical rock tests. It is expected to get reasonably

accurate rock strengths values that will save lot of time and money resources, especially for the feasibility studies.

This study is the first attempt to develop self-learning artificial intelligent models for the prediction of the selected formation material properties. These AI models include Artificial Neural Network (ANN), Mamdani Fuzzy Logic (MFL), Hybrid neural Fuzzy Inference System (HyFIS). The Multiple Linear Regression (MLR) method is also used for the predictive analysis, as it is one of the commonly used method. These models especially, HyFIS can be used to predict the desired formation material properties with reasonable accuracy. These properties include resilient modulus, Young's modulus, Poisson's ratio, shear modulus and friction coefficient.

It is further expected that the HyFIS can be used as a replacement for the PFC rock tests. This is the first attempt to look for an AI model as a replacement to PFC rock mechanics tests. This will allow researchers to use a cheap software, still getting comparable results. The system consisting of artificial intelligence model, capable of predicting the formation material properties, will allow engineers to save time, money and resources.

For the first time, DEM simulations for P&H 4800-XPC in PFC3D were performed to simulate, study and analyze the cable shovel digging phase. The models developed in PFC3D will expand the existing body of knowledge about the material behavior and how it will fail in advance of dipper movement. The research is expected to have immediate industry relevance. The developed simulator model can compare the performance of different excavation variables, and allow engineers to select optimum strategies to maximize excavation performance.

2.8. SUMMARY OF LITERATURE REVIEW

A thorough literature review has been carried out to determine the knowledge extent in the field of in-situ material properties, formation excavation modeling with primary focus on shovel excavation, numerical modeling, and artificial intelligence modeling. The section started with understanding the unique/complex nature of rocks and soils. According to Holtz et al. (2011), their heterogeneous nature, non-linear behavior, anisotropic condition and their good memory make them very complex engineering material.

Various soil cutting models have been reviewed and are presented in this section. Coulomb (1773) was the first to present a noteworthy theoretical model for describing soil failure and soil shear strength/resistive forces. Mohr (1914) presented a graphical technique (Mohr circle of stress) and mathematical equations to determine the stress condition at a point in equilibrium for any kind of material. Payne (1956), Osman (1964b), Reece (1964), Hettiaratchi et al. (1966), and Thakur and Godwin (1990) are some of the major studies that presented soil cutting models.

This section also reviews the available soil cutting resistance models. Dombrovskii and Pankratov (1961), Alekseeva et al. (1985), Balonev (1983), Zelenin et al. (1985), Perumpral et al. (1983), and Swick and Perumpral (1988) are some notable soil cutting resistance models. Hemami et al. (1994) proposed a model comprising of six forces that should be overcome for successful excavation. Takahashi et al. (1998) proposed a model comprising of five resistive forces that was almost similar to Hemami et al. (1994) model. A model to determine the six forces similar to the Hemami et al. (1994) model was proposed by Awuah-Offei and Frimpong (2004), Awuah-Offei (2006), and Awuah-Offei

et al. (2009). Raza and Frimpong (2017) used the Awuah-Offei (2006) model to determine the dynamic payload force.

Finite element method (FEM) is one of the main numerical methods used in the areas of soil-tool interaction and failure mechanism is also presented in this section. Yong and Hanna (1977) were the first to apply FEM technique to observe the soil-cutting process in front of the cutting tool, and to predict the displacement and stresses during the process. Kushwaha and Shen (1995), Rosa and Wulfsohn (1999), Chi and Kushwaha (1991) Mouazen and Nemenyi, (1999), Fielke (1999), and Plouffe et al. (1999) are some of the notable studies done using FEM.

Discrete element method (DEM) is one of the main numerical methods that is used in soil-tool interaction and failure mechanism studies and has gained great popularity in recent years. The DEM concept was first introduced by Cundall (1971) for rock mechanics analysis. Cundall and Strack (1979) extended the DEM use for the analysis of forces and motion in 2D discrete discs assemblies. Tanaka et al. (2000) used Cundall and Strack (1979) DEM to develop a mechanical model for analyzing the discontinuous nature of soil. Momozu et al. (2002) introduced the concept of soil clod and developed a modified DEM model. Ai et al. (2011) then proposed a modification in the Cundall and Strack (1979) DEM model and included the elastic-plastic spring-dashpot elements to account for rolling friction and rolling resistance. Rasimarzabadi and Joseph (2016) investigated the filling of a shovel dipper using PFC2D and calibrated their results by performing small-scale experiments.

Artificial intelligence (also known as machine intelligence) is the intelligence shown by machines. Three most commonly used AI models including Artificial Neural

Network (ANN), Mamdani Fuzzy Logic (MFL), and Hybrid neural Fuzzy Inference System (HyFIS) along with multiple linear regression (MLR) were discussed in this section. An artificial neural network (ANN) is a complex network that works similar to a human brain (Wang, 2003). An ANN consists of an input layer, hidden layers (one or more), and an output layer. An ANN model is developed in two phases: feedforward phase and gradient descent based error backpropagation phase. Mamdani fuzzy logic (MFL) is one of the first control systems that were developed using fuzzy set theory and is the most commonly used fuzzy logic models. The process of MFL consists of fuzzification, fuzzy logic operations by using if-then rules (inference engine), and defuzzification steps. Kim and Kasabov (1999) proposed the hybrid neural fuzzy inference system (HyFIS). HyFIS uses a combination of both numerical data and fuzzy rules, thus exhibits the added advantage of both methods. Two phases are available in HyFIS during the learning process: structure learning phase for knowledge acquisition and parameter learning phase. In structure learning or rule finding phase, techniques proposed by Wang and Mendel (1992) are employed to determine the fuzzy rules from the required input-output pairs. In parameter learning phase, a gradient descent learning scheme is employed to optimize the membership functions to achieve reasonable outputs. An MLR model is the advanced form of simple linear regression (SLR) model (Tranmer and Elliot, 2008). The coefficient of multiple determination (R^2) and the root mean square error (RMSE) are the two important parameter that shows the capability of the model predictions.

3. PARTICLE FLOW CODE

The mathematical formulation that captures the behavior of geomaterial to stress loading constitutes the geomaterial modeling. The behavior of the material is of prime importance in studying the failure mechanism of such material during the shovel digging process. In this process, the material cannot be modeled as a continuum. Instead it has to be modeled as distinct particles interacting with each other at specified contact points. This can be achieved with the discrete element modeling (DEM) technique, which deals with the modeling of geomaterials as distinct particles interacting with each other. This section covers a description of the DEM technique focusing on the details of the Particle Flow Code (PFC) software including PFC model components, available contacts and contact models with primary focus on the linear modeling theory.

3.1. DISCRETE ELEMENT MODELING

DEM is widely used to model the interaction between different independent bodies. It models each particle as an independent distinct body, which interacts with other distinct particles at specified contact points. DEM is a cyclic time-stepping process as shown in Figure 3.1 (Itasca, 2017). The DEM method requires a valid, finite time step to ensure the numerical stability of the model and that all contacts are created between pieces prior to the point that forces/moments develop between interacting bodies. The position and velocity of each body/piece is updated according to Newton's laws of motion using the current time step and the forces/moments calculated during the previous cycle (Ju et al., 2018). The model time is advanced by adding the current time step to the previous model

time. Contacts are dynamically created/deleted based on the current piece positions. By using the force – displacement law, the forces/moments at each contact are updated by the appropriate contact model using the current state of the pieces (Ju et al., 2018).
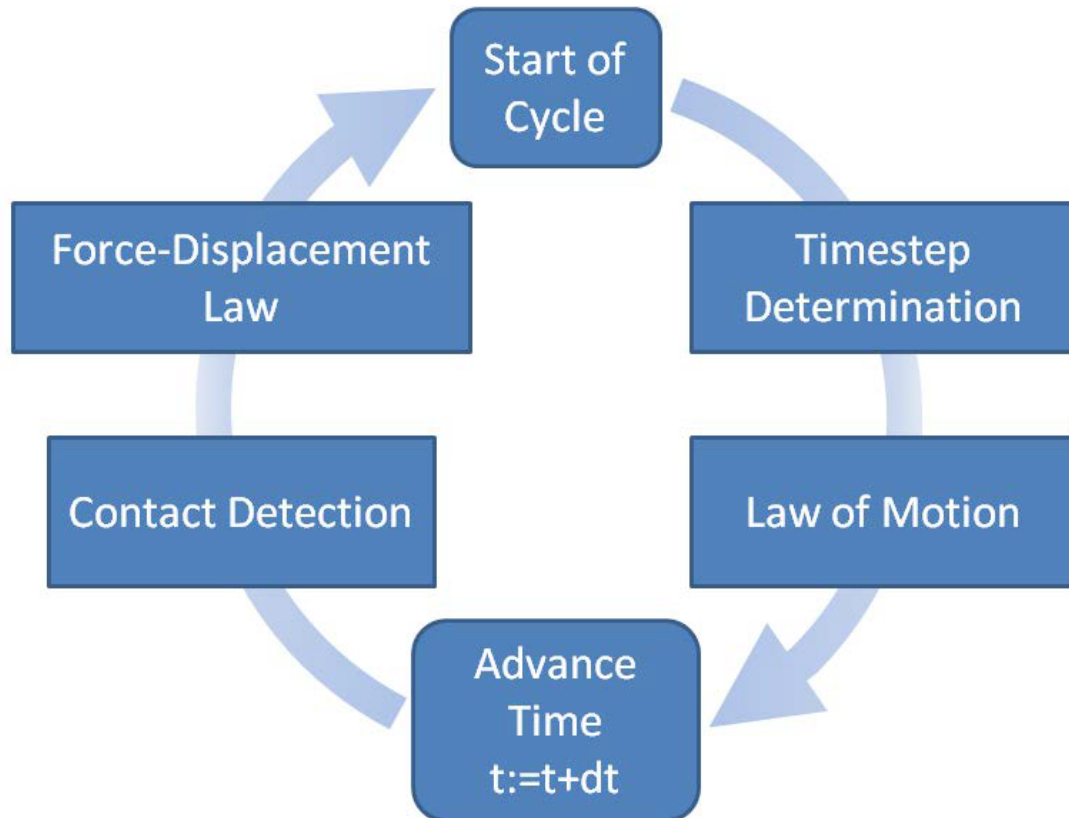
Figure 3.1. Sequence of primary operations during each cycle (Itasca, 2017)

Considering two bodies 'x' and 'y', with masses 'm_x' and 'm_y', respectively, moving towards each other with velocity 'v' (Figure 3.2). Within a defined time step ($t_n - t_{n-1}$), the incremental forces can be computed by using Equations (3.1) or (3.2). New

accelerations can be computed by using the Newton's second law of motion, as illustrated by Equation (3.3). By integrating the accelerations, new velocities can be obtained in Equation (3.4). New relative position from next time step (t_2) for both particles can then be computed by using Equations (3.5) and (3.6). Then, all the contact forces and moments are updated for each of the time step, as illustrated in Equation (3.7). The Equations from (3.1-3.7) are reproduced after Cundall and Strack (1979) with slight modifications.

$$F_x = k_x \times (Relative\ position)_x; \qquad F_y = k_y(Relative\ position)_y \qquad (3.1)$$

$$F_x = k_x \times \Delta\delta_x; \qquad F_y = k_y \times \Delta\delta_y \qquad (3.2)$$

$$\ddot{x} = \frac{F_x}{m_x}; \qquad \ddot{y} = \frac{F_y}{m_y} \qquad (3.3)$$

$$\dot{x} = \left(\frac{F_x}{m_x}\right) \times (t_n - t_{n-1}); \qquad \dot{y} = \left(\frac{F_y}{m_y}\right) \times (t_n - t_{n-1}) \qquad (3.4)$$

$$(\Delta\delta_x)_{t=n+1} = \left[v - \left(\frac{F_x}{m_x}\right)(t_n - t_{n-1})\right] \times (t_n - t_{n-1}) \qquad (3.5)$$

$$(\Delta\delta_y)_{t=n+1} = \left[v - \left(\frac{F_y}{m_y}\right)(t_n - t_{n-1})\right] \times (t_n - t_{n-1}) \qquad (3.6)$$

$$F^\Delta = \begin{cases} F^{n\Delta} = (F_l^n)_0 + k_n\Delta\delta_n; & Normal\ force \\ F^{s\Delta} = (F_l^s)_0 - k_s\Delta\delta_s; & Shear\ force \end{cases} \qquad (3.7)$$
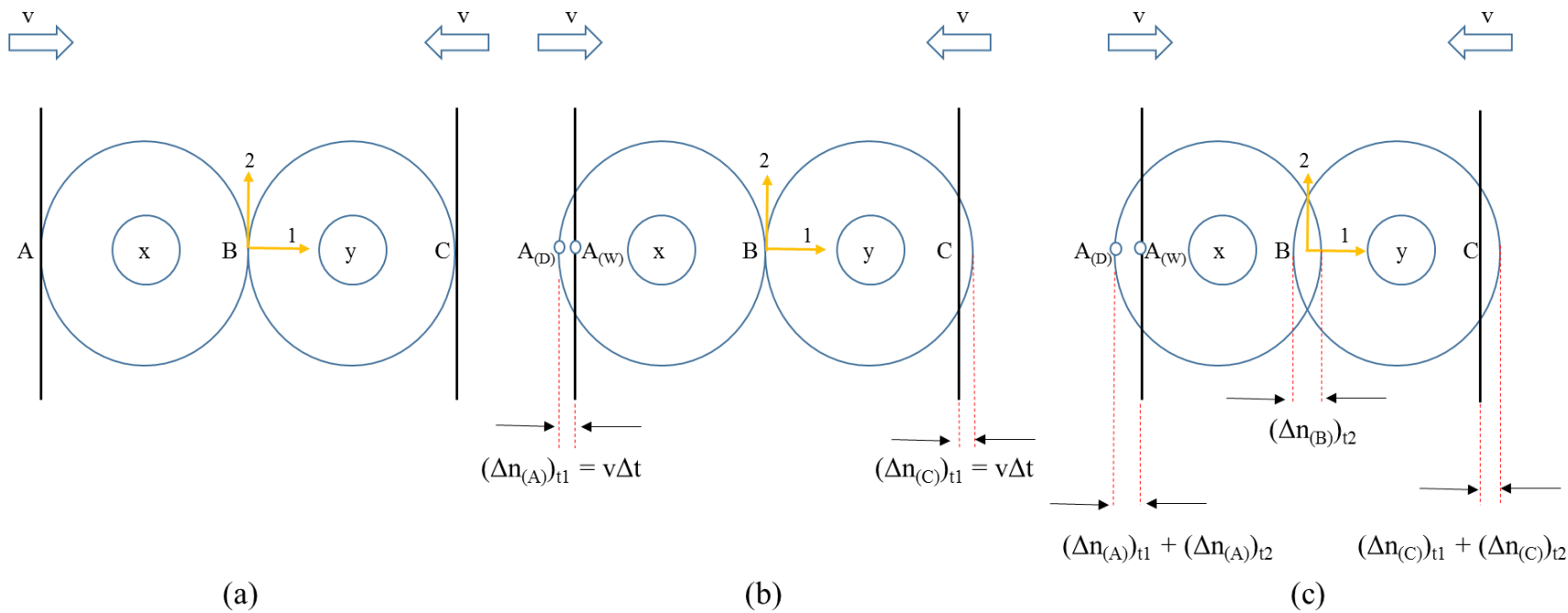
Figure 3.2. Two discs compressed between rigid walls (a) at $t = t_0$; (b) at $t = t_1 = t_0 + \Delta t$; (c) at $t = t_2 = t_0 + 2\Delta t$ (Reproduced after Cundall and Strack (1979))

3.2. THE PARTICLE FLOW CODE (PFC) OVERVIEW

The PFC offers a general purpose DEM modeling framework, which exhibits a graphical user interface, as well as a computational engine. The DEM technique is any modeling technique that allows finite displacements and rotations of discrete bodies, including complete detachment. The technique must also recognizes new contacts automatically as the simulation progresses (Cundall and Hart, 1992).

A PFC model (2D or 3D) is defined as a particular setup of a DEM model that can be used to simulate the movement and interaction of lot of small (finite) particles. These particles have some mass and are rigid bodies (circular in 2D, spherical in 3D), that can have independent translational and rotational motions. These particles interact and contact each other due to the presence of some internal forces and moments. Particle to particle interactions have been taken care of in the embodied laws and are used to change/update the forces and moments at each time step.

DEM is used to provide an explicit dynamic solution to the Newton's laws of motion. PFC is limited to the rigid bodies/particles contrary to the general DEM that can work well for the polygonal bodies/particles. The PFC model offers a synthetic material that includes both bonded and granular materials.

PFC can easily be customized and applied to a very broad range of numerical investigations into a variety of problems, where the discrete nature of the systems is of interest. The problems include soil-tool interactions, slope stability issues, fundamental research on soil and rock behavior, rock fall hazard mitigation, hydraulic fracturing, modeling a blast furnace, bulk flow, mixing, conveying and compaction of aggregates and powders (Zhou and Yang, 2017).

3.3. THE PARTICLE FLOW CODE (PFC) MODEL

The PFC model is used to simulate the mechanical behavior of a system comprising of thousands of various shaped particles. The following assumptions are made while developing a PFC model (Potyondy and Cundall, 2004).

- The particles are assumed to be rigid.

- The basic particle shape is a 'ball' (a disc in 2D having unit thickness, and a sphere in 3D).

- 'Pebbles' can be generated by rigidly joining the discs in 2D having unit thickness, and spheres in 3D. Pebbles can overlap with each other to obtain different complex shapes, having a deformable boundary and are known as 'clumps'.

- Particles interact at contacts due to the presence of internal forces and moments. These forces and moments are updated by the particle-interaction laws.

- The rigid particles can overlap each other at the contact points, and the magnitude of the overlap is related to the contact force.

- The contacts exist over a very small area (i.e., just a point).

- Bonds can develop between two or more particles at their contacts.

- Potential energy function can be used to develop the long range interactions.

The particle rigidity assumption is valid when the major portion of deformation is due to the movements along interfaces. The deformation of a complete particle assembly (packed) can be explained by this assumption. The opening and interlocking of the particles at their interfaces, and the sliding and rotation of the particles as rigid bodies are the main reasons of deformation. Precise modeling of such deformation is usually not required to achieve reasonable results of the mechanical behavior of such systems.

3.4. MODELING METHODOLOGY

The modeling of mechanical processes, such as those associated with geomaterials, requires distinctive design considerations. The strength properties for geomaterials change considerably over short distances. Thus, the detailed analyses for the structural designs or for any excavations must be developed, while having little site investigation data. This dilemma generally applies to applications that involve the interaction of many discrete particulate objects. In powder technology, contact behavior at high packing densities is generally unknown. In bulk flow of material, the effect on the flow of the distribution of irregularities in the flow material cannot easily be quantified. Because of the lack of data in such cases, a numerical model should be developed and used for analysis. A detailed design can be developed with given system behavior and acceptable preliminary results. If sufficient data and understanding of material behavior are available, PFC can directly be used for design purposes. The spectrum of modeling situations, in Figure 3.3, should be well understood by the modelers.

Typical situation	Complicated geology; Inaccessible; No testing budget	←——→		Simple geology; $$$$ spent on site investigation
Data	None	←——→		Complete
Approach	Investigation of mechanisms	Bracket field behavior by parameter studies		Predictive (direct use in design)

Figure 3.3. Spectrum of modeling situations (FLAC online manual, 2018)

PFC can either be used as a numerical laboratory tool (left side of Figure 3.3) or for the prediction purposes (right side of Figure 3.3). The type of use is usually characterized by the field situations and especially by the available budget. PFC can provide good estimations if enough quality data is available. The following steps should be followed to achieve efficient results from PFC.

- The objective of the model analysis should be clearly defined;

- The theoretical picture of the system should be created;

- Small scale models should be developed and tested;

- Acquire the specific data of the system under study;

- Develop and test the detailed models;

- Model calculations should be performed; as well as

- Data analysis or interpretation.

3.5. SOLUTION PROCEDURE

The detailed and generalized solution procedure used in PFC is presented in Figure 3.4. There are four vital components of a problem that should be mentioned in the PFC model to run a successful simulation.

- Defining the domain of the model;

- Generating the particles assembly;

- Defining the contact model and material properties; and

- Specifying initial and boundary conditions.

The size distribution and the locations of particles are characterized in particle assembly. The type of contact model and the assigned material properties controls the

model response to disturbance (e.g., deformation response due to excavation). The choice of appropriate energy dissipation mechanisms is crucial at this stage. The in-situ state of the particles is defined by the specified initial and boundary conditions.
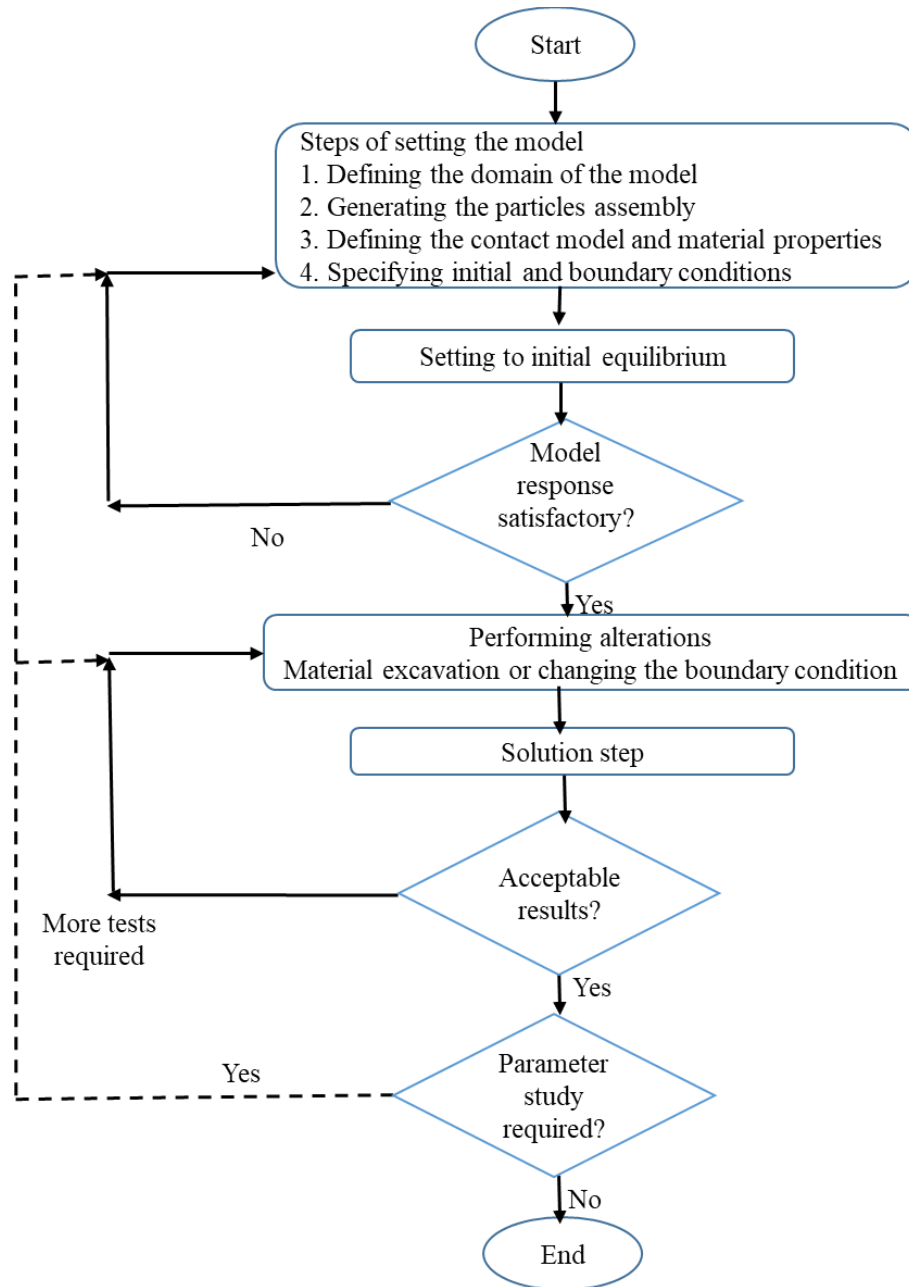
Figure 3.4. Generalized solution procedure in PFC

Once the problem is defined, the PFC model is allowed to achieve the initial equilibrium state. If the model response in not satisfactory, one can always go back to the definition of problem. In case of satisfactory results, alterations can be performed (e.g., material excavation or changing the boundary condition), to obtain the model solutions. As the PFC is an explicit distinct element program, it provides a different solution as compared to the conventional implicit methods. The algebraic equations are solved at each computational step to reach the solution. The number of steps needed to reach the final solution is controlled manually or by the code automatically. Other benefits of explicit program include requiring reasonably less computer memory to present large number of particles, because the matrices are not saved. As the failure mechanism shows the real material behavior, there is no difficulty in modeling the physical instability of the system.

3.6. MODEL COMPONENTS

Each particle in a PFC model is denoted as a body that is a discrete, rigid body which has finite extent and a well-defined surface. The PFC model is populated with bodies, pieces, and contacts as illustrated in Figure 3.5 (a). There are three types of bodies namely balls, clumps, and walls. Each body comprises one or more pieces. Bodies may have surface properties that can be assigned to each piece on the body surface. These surface properties may be used to determine the piece interactions. Bodies exist within the domain of the model, and cannot move outside of this region. The motion of balls and clumps obeys Newton's laws of motion, with user-specified motion of walls. Thus, only balls and clumps have mass properties (mass, centroid position, and inertia tensor) and

loading conditions (the force/moment applied from contacts, a body force arising from gravity, and an externally applied force/moment).

The generalized internal force consists of a force (F_c) and moment (M_c) that act at the contact location in an equal and opposite sense on the two pieces (Figure 3.5 (b)). An additional moment due to the application of the force at the contact location is added to each piece. Contact models that simulate surface-surface interactions update this force and these moment contributions. However, contact models that simulate interaction at a distance update the force and two internal moments that need not be equal and opposite.

(a)   (b)
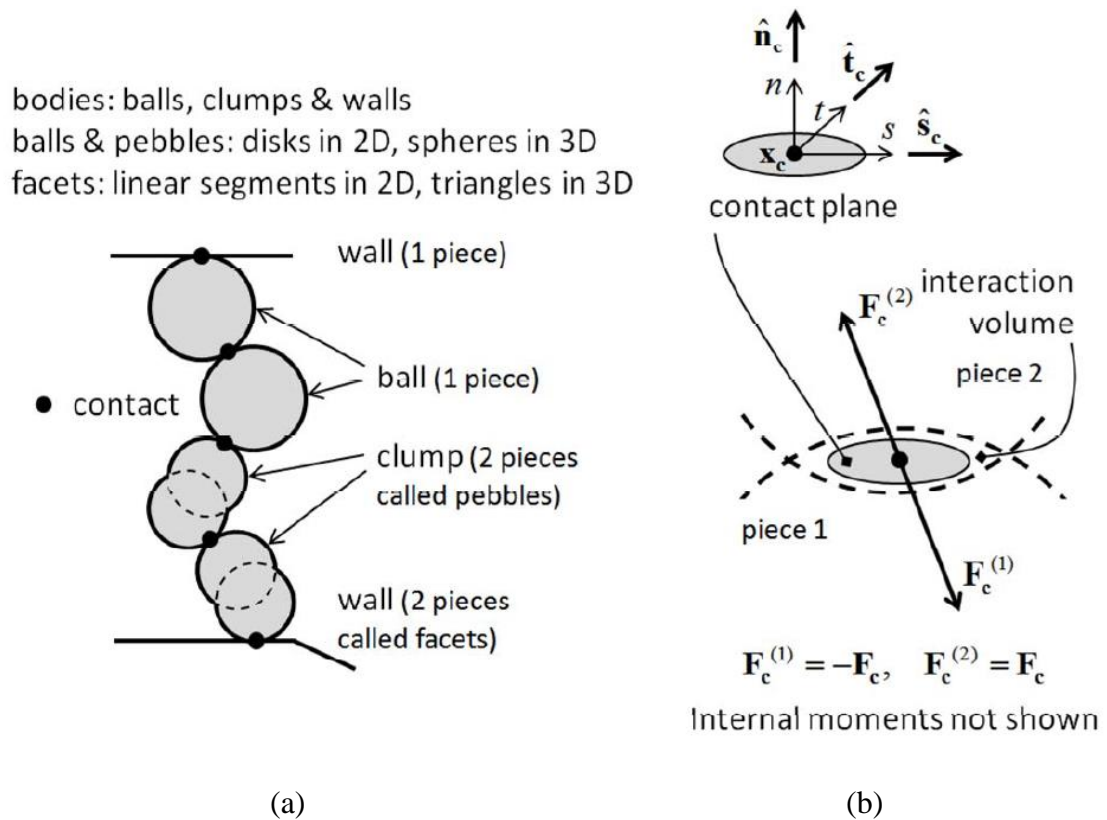
Figure 3.5. PFC model components; (a) bodies, pieces, and contacts; (b) the contact plane with the internal force (Potyondy, 2017)

3.6.1. Balls. A ball is defined as a rigid body (disc in 2D having unit thickness; a sphere in 3D). The sphere radius (R) defines the surface. A ball has a single set of surface properties. Balls can translate and rotate and are defined by the generalized velocity (v), and angular velocity or spin (w). Ball motion follows the equations of motion. This requires the existence of mass properties, loading and velocity conditions. Mass, centroid position, and inertia tensor (m, x, I) are the mass properties. Mass properties are defined by the density and radius. Loading conditions are defined by: (i) the force and moment resulting from interactions with other pieces; (ii) gravity; and (iii) an externally applied force and moment (defined by F_A and M_A). Velocity conditions are defined by velocity-fixities with (3 values in 2D; 6 values in 3D) (Shi et al., 2018).

Balls are inserted into the model domain in three ways: (i) by creating balls one at a time; (ii) by generating non-overlapping sets of balls; or (iii) by distributing overlapping balls to match a specified size distribution (Shi et al., 2018). The 'ball attribute' and 'ball property' commands are used in a PFC model to specify ball attributes and properties. The entire attribute/property lists can be listed with the 'ball list attribute' and 'ball list property' commands along with the values of specific attributes/properties.

3.6.2. Clumps. A clump is a rigid collection of 'n' rigid spherical pebbles. The pebble positions and radii ($\{x^i, R^i\}$, i = 1,2, 3 ……., n) defines the pebble surface. The surface properties of a clump can be specified independently for each pebble. Clumps can translate and rotate and are defined by the generalized velocity (v), and angular velocity or spin (w) of the clump centroid. Similar to a ball, a clump motion obeys the equations of motion. This requires the existence of mass properties, loading and velocity conditions (Shi et al., 2018). Loading and velocity conditions are exactly similar to balls.

Mass properties are mass, centroid position, and inertia tensor (m, x, I). Mass properties are defined by: (i) the reference configuration and clump density; (ii) the reference configuration and inertia tensor (m, x, I) for the reference configuration; or (iii) a closed surface and associated mass properties given by the clump density (Shi et al., 2018). The reference configuration defines the clump surface used for contact detection/resolution in all three cases.

A set of clump templates, which represent the desired particles should be defined at the start. Once the set of clump templates have been defined, the clumps can be inserted into the domain in three ways: (i) by replicating clumps one at a time; (ii) by generating non-overlapping sets of clumps; or (iii) by distributing overlapping clumps to match a specified size distribution (Shi et al., 2018).

Alternatively, one can create clumps that do not refer to clump templates with the 'clump create' command. The user may either specify the mass properties directly or calculate the actual mass properties based on the sphere distribution using the 'clump create calculate' command. The 'clump attribute' and 'clump property' commands are used to specify clump attributes and pebble properties. The entire attribute/property lists can be listed with the 'clump list attribute' and 'clump list property' commands along with the values of specific attributes/properties.

3.6.3. Walls. A wall is a manifold surface composed of (line segments in 2D; triangular facets in 3D) termed facets. The surface is defined by a mesh. The surface properties of a wall can be specified independently for each facet. Walls can translate and rotate defined by the generalized velocity (v) and angular velocity or spin (w) of the wall about the reference point. Wall motion does not obey the equations of motion. If

deformable, then independent translational velocities can be applied to each vertex ($\{v^k\}$, k = 1, 2, 3……, n - these values are specified directly). Wall deformation must preserve the manifold nature of the wall.

Walls may be created by using 'wall create' and facets may be added one at a time by using 'wall addfacet' commands. Alternatively, simple wall configurations can be generated with the 'wall generate' command (e.g., boxes, planes, spheres, cylinders, cones, etc.). The 'wall attribute' and 'wall property' commands are used to specify wall attributes and facet properties. The entire attribute/property lists can be listed with the 'wall list attribute' and 'wall list property' commands along with the values of specific attributes/properties.

3.7. BUILT-IN CONTACT MODELS (ITASCA, 2018)

There are two major types of built-in contact models available in PFC; linear-based models and bonded-particle materials and interfaces. The linear, linear contact bond, linear parallel bond, and rolling resistance linear models have some common characteristics and are known as linear-based models. The smooth joint, flat joint, linear contact bond, and linear parallel bond models use the bonding concept and can be categorized as the bonded-particle materials and interfaces.

The linear-based models offer two types of bonding behaviors included in both the contact bonds and parallel bonds. These bonds are available at ball-ball and ball-facet contacts. It can be said that both these bonds are joined with the help of a glue. The contact-bond glue exists over a small area (i.e., a point). On the other hand, the parallel-bond glue exists over some cross-section between the two or more pieces. The contact bond can

transfer the force, while the parallel bond can transfer the force, as well as the moment. Pieces are not bonded with each other. The type of bonds created are dependent upon the bond method. The bonds can break when their strength is exceeded or by applying the un-bonding method.

The bonded-particle modeling methodology explains materials and interfaces depending upon the used contact models. A linear contact bond model can be used to generate a granular assembly of contact-bonded material. A linear parallel bond model can be used to generate a granular assembly of parallel-bonded material. A flat-joint model can be used to produce a granular assembly of flat-jointed material. A smooth-jointed interface can be inserted into the contact-bonded, parallel-bonded and flat-jointed materials by identifying the contacts near the interface, and replacing their contact models with the smooth-joint model.

3.7.1. Linear Model. The linear model provides two components; linear and dashpot acting parallel to one another. The linear component provides linear elastic (no-tension) frictional behavior, while the dashpot component provides viscous behavior illustrated in Figure 3.6. Both components act over a vanishingly small area, and thus, transmit only a force. The linear model provides the behavior of an infinitesimal interface that does not resist relative rotation so that the contact moment (M_c) equals to zero as in Equation (3.8). The contact force (F_c) is resolved into linear (F_l) and dashpot (F_d) components as in Equation (3.8). The linear force is produced by linear springs with constant normal and shear stiffnesses, k_n and k_s as in Figure 3.6. The dashpot force is produced by dashpots with viscosity in terms of the normal and shear critical-damping ratios, β_n and β_s (Figure 3.6). The linear springs act in parallel with the dashpots. The

contact is active, if and only if, the surface gap (g_s) is less than or equal to zero and is illustrated in Figure 3.7.
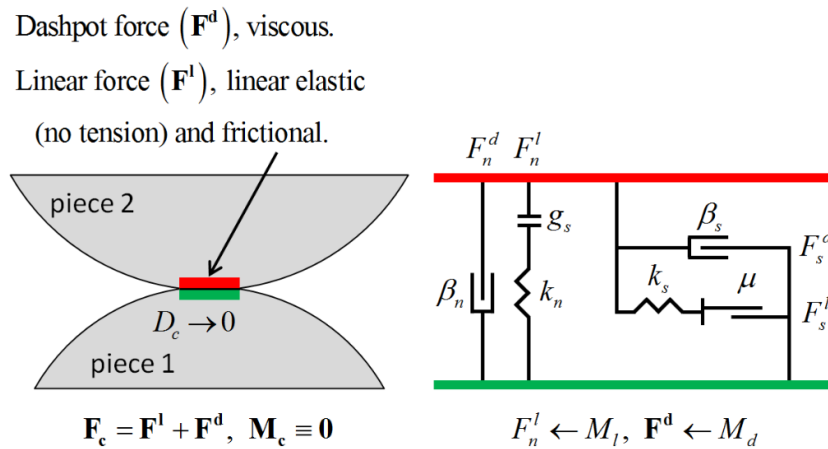
Figure 3.6. Linear model's components (Potyondy, 2017)

The linear model with inactive dashpots and a surface gap of zero corresponds with the model of Cundall and Strack (1979). It is a linear-based model that can be installed at both ball-ball and ball-facet contacts. The force-displacement law is skipped for inactive contacts. The linear springs cannot sustain tension, and slip is accommodated by imposing a Coulomb limit on the shear force using the friction coefficient (μ). Normal component of the linear force (F_{ln}) is updated either in an absolute sense based on the surface gap, or incrementally based on the surface-gap increments. The type of the update is controlled by the normal-force update mode, M_l as illustrated in Equations (3.9 (a)) and (3.9 (b)). Shear component of the linear force (F_{ls}) is always updated incrementally based on relative shear-displacement increments as illustrated in Equations (3.9 (a)) and (3.9 (b)).
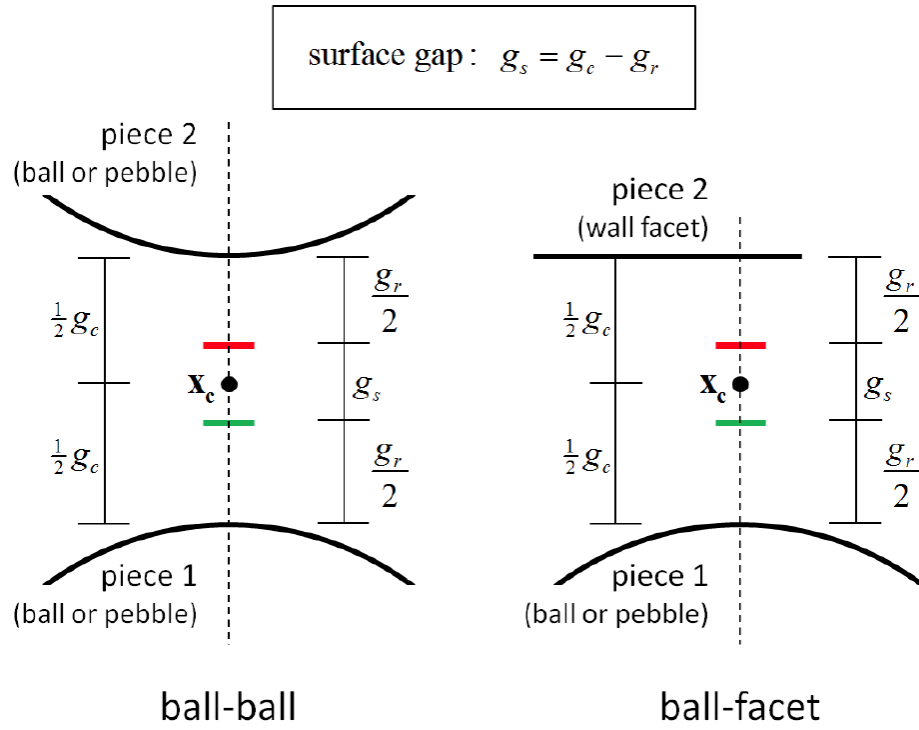
Figure 3.7. Surface gap for the linear-based models (Itasca, 2018)

$$F_c = F^l + F^d ; \qquad M_c = 0 \tag{3.8}$$

$$F^l = \begin{cases} F_n^l = \begin{cases} \begin{cases} k_n g_s; & g_s < 0 \\ 0; & otherwise \end{cases}; & M_l = 0 \ (absolute\ update) \\ \min[(F_n^l)_0 + k_n \Delta\delta_n, 0]; & M_l = 1 \ (incremental\ update) \end{cases} \\ F_s^l = \begin{cases} F_s^* = (F_s^l)_0 - k_s \Delta\delta_s; & ||F_s^*|| \le F_s^\mu \\ F_s^\mu \left(\frac{F_s^*}{||F_s^*||}\right); & otherwise \end{cases} \end{cases} \tag{3.9a}$$

$$F_s^\mu = -\mu F_n^l \tag{3.9b}$$

$$F^d = \begin{cases} F_n^d = \begin{cases} F^{n^*} = \left(2\beta_n\sqrt{m_c k_n}\right)\dot{\delta}_n; & (full\ normal) \\ \min[F^*, -F_n^l]; & (no-tension\ normal) \end{cases} \\ F_s^d = \begin{cases} F^{s^*} = \left(2\beta_s\sqrt{m_c k_s}\right)\dot{\delta}_s; & (Full\ shear) \\ 0; & (slip-cut) \end{cases} \end{cases} \quad (3.10a)$$

$$m_c = \begin{cases} \frac{m^1 m^2}{m^1 + m^2}; & Particle - Particle \\ m^1; & Particle - Dipper \end{cases} \quad (3.10b)$$

The dashpot force is affected by the dashpot mode (M_d), which provides four combinations of normal and shear behavior. The normal-behavior mode can be either full or no-tension. Full means that the entire dashpot load is assigned. No-tension means that the normal component of the dashpot force (F_{dn}) is capped to insure that the total normal force ($F_{ln} + F_{dn}$) does not become tensile as in Equations (3.10 (a)) and (3.10 (b)). The shear-behavior mode can be either full or slip-cut. Slip-cut means that the shear component of the dashpot force (F_{ds}) is set to zero if the linear spring is sliding as in Equations (3.10 (a)) and (3.10 (b)).

3.7.2. Linear Parallel Bond Model. The linear parallel bond contact model is present at all the grain-grain contacts in a parallel-bonded material. According to Potyondy (2017), this model provides the behavior of two interfaces. The first is an infinitesimal linear elastic having no tension and frictional interface, which carries a force. The second is finite sized linear elastic and bonded interface, which carries a force as well as moment (Figure 3.8). The first interface is similar to the linear model, as it doesn't resist relative rotation. The second interface is a parallel bond, as it works in parallel with the first interface. The second interface resists relative rotation until it is bonded. It behaves like

linear elastic material, until the bond breaks because of reaching strength limit. When the bond breaks, the second interface becomes equivalent to the linear model.
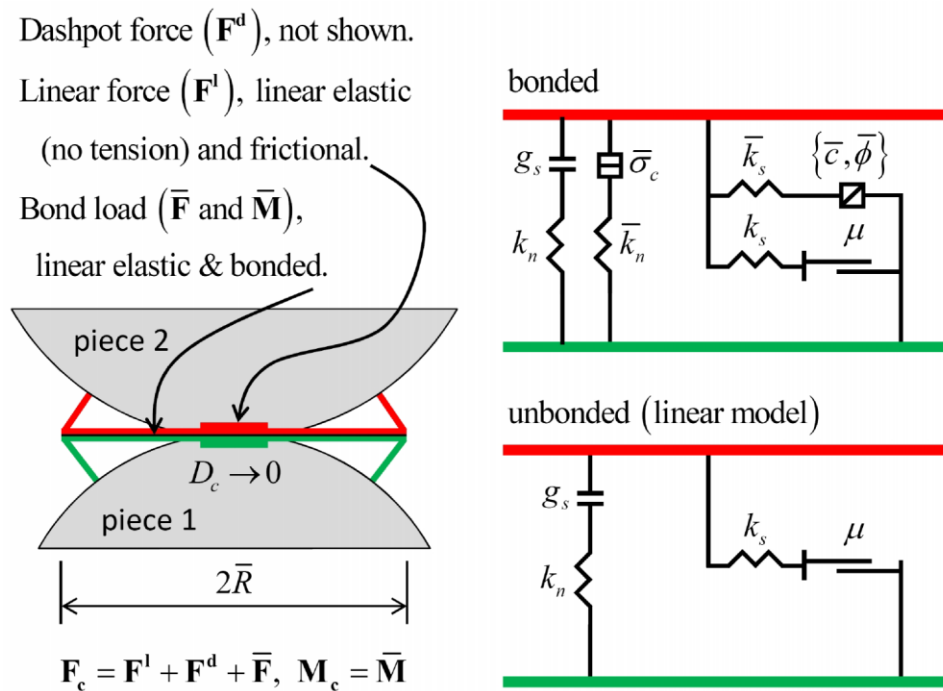
Figure 3.8. Linear parallel bond model's components (Potyondy, 2017)

3.8. SUMMARY

The mathematical formulation that captures the behavior of geomaterial to stress loading constitutes the geomaterial modeling. DEM is a cyclic time-stepping process that requires a valid, finite time step to ensure the numerical stability of the model. The PFC offers a general purpose DEM modeling framework, which exhibits a graphical user interface, as well as a computational engine. A PFC model (2D or 3D) is defined as a particular setup of a DEM model that can be used to simulate the movement and interaction

of lot of small (finite) particles. PFC has been successfully used around the world to solve a variety of problems. The problems include soil-tool interactions, slope stability issues, fundamental research on soil and rock behavior, rock fall hazard mitigation, hydraulic fracturing, modeling a blast furnace, bulk flow, mixing, conveying and compaction of aggregates and powders. Each particle in a PFC model is denoted as a body that is a discrete, rigid body which has finite extent and a well-defined surface. The PFC model is populated with bodies, pieces, and contacts. There are three types of bodies namely balls, clumps, and walls. There are two major types of built-in contact models available in PFC; linear-based models and bonded-particle materials and interfaces. The linear, linear contact bond, linear parallel bond, and rolling resistance linear models have some common characteristics and are known as linear-based models. The smooth joint, flat joint, linear contact bond, and linear parallel bond models use the bonding concept and can be categorized as the bonded-particle materials and interfaces.

4. NUMERICAL EXPERIMENTATION AND CALIBRATION

Rock tests are performed before the start of every mining or civil engineering project for the purpose of feasibility studies. It results in huge costs, comprising drilling, sample collection, sample handling and finally laboratory testing. Unconfined compressive strength (UCS), direct tension, and indirect Brazilian tests are common laboratory tests. In this section, the numerical tests (UCS, direct tension, Brazilian, and Triaxial) are conducted using the Particle Flow Code (PFC3D). The numerical results of these tests are calibrated using the data from literature.

4.1. BRIEF INTRODUCTION OF ROCK MECHANICS TESTS

UCS is the ability of a rock to sustain the maximum axial directed load. The Equation (4.1) can be used to determine the UCS of the sample. 'F' is the failure load (N) and A_0 is the initial cross-sectional area of the rock sample (m^2). The tensile strength is the ability of a rock to sustain the maximum tensile stress. A direct tensile strength test can be performed in a laboratory, but is difficult to perform. An indirect method known as Brazilian test is usually performed to determine the tensile strength. The Equation (4.2) can be used to determine the Brazilian tensile strength of the sample. 'F' is the failure load (N), 'd' is the diameter (m) and 't' is the thickness (m) of the rock sample (Goodman, 1989).

$$UCS = F/A_0 \tag{4.1}$$

$$\sigma_B = 2F/\pi dt \tag{4.2}$$

4.2. FORMATION MATERIAL MODELING IN PARTICLE FLOW CODE

The behavior of formation material is embodied in the contact model at the grain-grain contacts. The linear, parallel-bonded, flat-jointed, contact-bonded and user-defined PFC materials can be created by using the material-genesis procedure. These materials are made up of an isotropic, homogeneous and well-connected grain assembly having an indicated non-zero material pressure. The common properties of all the PFC materials are detailed in Table 4.1 (Potyondy, 2017). The material name is assigned for two purposes: to assign the title of the model corresponding to the current state, and to name the saved states. The type of the material can be selected from the four supported materials or the users can define it. Kinetic energy is dissipated by assigning a non-zero value to the local damping factor of each grain. By assigning a value of 0.7 to the local damping factor, quasi-static conditions can be modeled (Potyondy and Cundall, 2004, Eq. 3). The grain density can be assigned either directly or indirectly in the form of bulk density. The grain shape is assigned as either 'all balls' or 'all clumps'. The size distribution is allocated in terms of a finite number of separate size distribution. Each distribution can either be uniform or Gaussian (built-in distributions). The diameter range and volume fraction are assigned to each distribution. By changing the diameter multiplier, the size distribution can be altered.

The material can be produced in a vessel, which may be physical or a periodic space. To apply the boundary conditions, the material may be removed from the physical vessels. On the other hand, the material produced in the periodic space is converted into periodic bricks for the application of boundary conditions. To apply the boundary conditions, the material may be trimmed into a desirable shape. The material vessels and the material-genesis procedure are explained in the following subsections.

Table 4.1. Details of common parameters for all PFC materials (Potyondy, 2017)

Symbol	FISH	Range	Default	Description
N_m	cm_matName	NA	PFCmat	Name of the material

T_m	cm_matType	[0,4]	0	Material type code
				  0, linear
				  1, contact-bonded
				  2, parallel-bonded
				  3, flat-jointed
				  4, user-defined

A	cm_localDampFac	[0.0,0.7]	0.0	Local damping factor

C_ρ	cm_densityCode	{0,1}	0	Density code
				  0, grain
				  1, bulk

ρ_v	cm_densityVal	(0.0,∞)	NA	Grain density value $$\rho_g = \begin{cases} \rho_v, & C_\rho=0 \\ \frac{\rho_v V_v}{V_g}, & C_\rho=1 \end{cases}$$ V_v is vessel's volume V_g is total grain's volume
Grain shape and size distribution group:				

S_g	cm_shape	{0,1}	0	Grain shape code
				  0, all balls
				  1, all clumps

n_{SD}	cm_nSD	$n_{SD} \geq 1$	NA	Number of size distributions

T_{SD}	cm_typeSD (n_{SD})	{0,1}	0	Type of size distribution
				  0, uniform
				  1, Gaussian

$N_{ct}^{(j)}$	cm_ctName (n_{SD})	NA	NA	Clump template name ($S_g = 1$)
$D_l^{(j)}$	cm_Dlo (n_{SD})	(0.0,∞)	NA	Lower diameter value
$D_u^{(j)}$	cm_Dup (n_{SD})	$D_u^{(j)} \geq D_l^{(j)}$	NA	Upper diameter value
$\phi^{(j)}$	cm_Vfrac (n_{SD})	(0.0,1.0]	NA	Volume fraction $$\sum \phi^{(j)} = 1.0$$
D_{mult}	cm_Dmult	(0.0,∞)	1.0	Diameter multiplier (shifts the size distribution)

4.2.1. Material Vessels (Potyondy, 2017). The material can be generated in a physical vessel or a periodic space. The shape of the physical vessels can be cylindrical, polyaxial or spherical as is shown in Figure 4.1. A cylindrical vessel is made up of a cylinder wall and two planar walls. The planer walls of a polyaxial vessel form a rectangular cuboid (the angle between the adjacent faces is 90^0). A spherical vessel is made up of a sphere wall. During the compression tests, the vessel's walls can expand to stop the material particles to escape. The wall-wall overlap is not considered as the walls only interact with material particles. The material is generated in a rectangular cuboid in periodic space. Three spherical measurement sections are positioned symmetrically along the axis of the biggest vessel dimension (the spanning length of α_l times the biggest vessel dimension, and having a diameter of α_d times the smallest dimension).
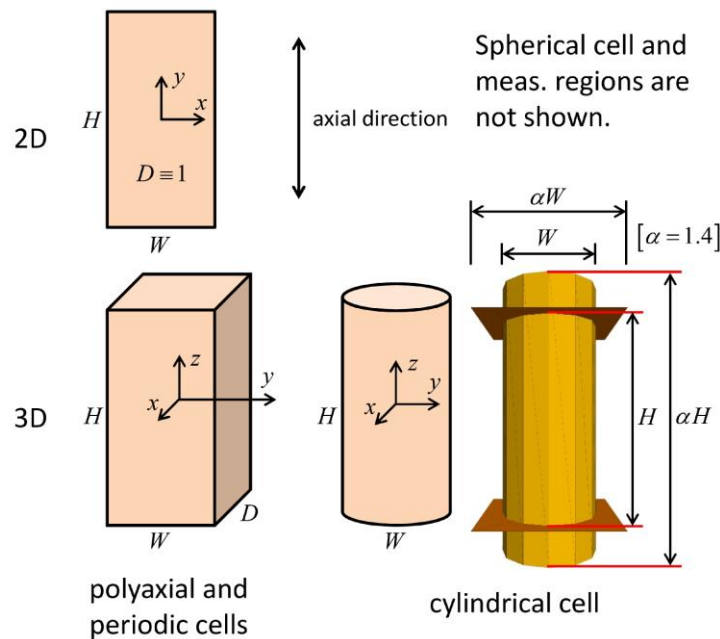
Figure 4.1. Different material vessels shapes having a centered global coordinate system (Potyondy, 2017)

The details of the material vessel parameters and the selected values for the numerical experiments are given in Table 4.2 (Potyondy, 2017). The linear contact model is available at the wall-grain contacts during the formation of a material in a physical vessel. The walls are frictionless. The wall-grain contact stiffness is allocated depending upon the specific contact deformability (E^*).

Table 4.2. Details of material vessels parameters (Potyondy, 2017)

Symbol	FISH	Range	Default	Description
T_v	mv_type	{0,1}	0	Vessel-type code 0, physical 1, periodic
S_v	mv_shape	{0,1,2}	0	Vessel-shape code 0, rectangular cuboid 1, cylinder 2, sphere $S_v \equiv 0$, for 2D model
{H,W,D}	mv_{H,W,D}	(0.0,∞)	NA	Height, width and, depth (sphere diameter is H; $D \equiv 0$, for 2D model)
α	mv_expandFac	[1.0,∞)	1.2	Expansion factor of physical vessel
{α_l, α_d)	mv_inset{L,D}Fac	(0.0,1.0]	{0.8, 0.8}	Inset factors of measurement regions
E_v^*	mv_emod	(0.0,∞)	NA	Effective modulus of physical vessel

4.2.2. Material-Genesis Procedure. The material-genesis procedure takes place in a physical vessel and consists of two phases: packing phase and finalization phase (Potyondy, 2015). These phases are explained in detail in the following subsections.

4.2.2.1. Packing phase. A packing procedure is applied to the grain assembly during the packing phase. A linear contact model behavior is present at all the grain-grain contacts. The properties of the linear model are deformability (effective modulus and stiffness ratio). The friction coefficient (μ_{CA}) is a packing parameter.

The boundary contraction and grain scaling are the two options during the packing procedure. A dense or loose packing of a granular material can be generated by using the boundary contraction procedure. On the other hand, only a dense packing of a granular material can be generated using the grain scaling procedure. The material generated using grain scaling procedure will ultimately become a bonded material during the finalization phase. A cloud of grains is produced during both procedures. Then under the condition of zero friction, the grain cloud is allowed to rearrange into a packed state. The pressure can be achieved during both procedures in a different way. Confinement can be applied by moving the walls of the vessel by using servomechanism (explained later in Section 4.3.3), during the boundary contraction procedure. The mean stress of the grains assembly is adjusted, by iteratively scaling the grain sizes during the grain scaling procedure. The friction coefficient is varied during the confinement application to obtain either dense or loose packing for the boundary contraction procedure. The friction coefficient remains zero during the grain scaling procedure to produce a dense packing. The details of the packing parameters are given in Table 4.3 (Potyondy, 2017). Different packing materials can be produced by using the same properties, with different seed of random-number generator.

Table 4.3. Details of the packing parameters (Potyondy, 2017)

Symbol	FISH	Range	Default	Description
S_{RN}	pk_seed	S_{RN} $\geq 10{,}000$	10,000	Seed of random-number generator (affects packing)
P_m	pk_Pm	$(0.0,\infty)$	NA	Material pressure
ε_p	pk_PTol	$(0.0,\infty)$	1×10^{-2}	Pressure tolerance $$\frac{|P - P_m|}{P_m} \leq \varepsilon_P$$ P is current pressure
ε_{lim}	pk_ARatLimit	$(0.0,\infty)$	8×10^{-3}	Equilibrium-ratio limit
n_{lim}	pk_stepLimit	$[1,\infty)$	2×10^6	Step limit
C_p	pk_procCode	$\{0,1\}$	0	Packing-procedure code 0, boundary contraction 1, grain scaling
n_c	pk_nc	$(0.0,1.0)$	$\begin{smallmatrix}0.58,3D\\0.25,2D\end{smallmatrix}, C_p = 0$ $\begin{smallmatrix}0.35,3D\\0.08,2D\end{smallmatrix}, C_p = 1$	Grain-cloud porosity
Boundary-contraction group ($C_p = 0$):				
μ_{CA}	pk_fricCA	$[0.0,\infty)$	0.0	Material friction coefficient during confinement application
υ_{lim}	pk_vLimit	$(0.0,\infty)$	NA	Servo velocity limit

McDowell et al. (2006) proposed the boundary contraction procedure that consists of three steps. The first step is to produce the grains cloud by using some value of porosity (n_c) illustrated in Equation (4.3). V_v is the vessel's volume and V_g is total grain's volume. The porosity does not consider the grains overlap. The grains are placed arbitrarily in different positions within the vessel. Normally, n_c is equal to the loose state porosity (n_l),

for which the grains are in contact at zero mean stress. For equal-sized particles in a linear model, $n_l = 0.58$ (3D) and $n_l = 0.25$ (2D) (Table 4.3).

$$n_c = (V_v - V_g)/V_g \qquad\qquad (4.3)$$

The second step of the boundary contraction procedure is to assign a zero value to the material friction coefficient. The grains are then allowed to settle, until either the mean stress reaches within 0.1% of material pressure (P_m) or static equilibrium is achieved. By setting the grain translational and rotational velocities equal to zero, the model is calmed. The calming process restricts the material grains from escaping through the walls of the vessel. The grains with centers outside the vessel are deleted at the end of this step. This provides an isotropic state by eliminating the large overlaps.

The third step of the boundary contraction procedure is to apply confinement by applying the material pressure (P_m) and assigning a value to material friction coefficient during confinement application (μ_{CA}). Confinement is applied by moving the walls of the vessel until the pressures are within the pressure tolerance and static equilibrium is achieved. The densest grain packing is obtained at $\mu_{CA} = 0$, and packing becomes looser with increasing values of μ_{CA}.

Potyondy and Cundall (2004) proposed the grain scaling procedure that also consists of three steps. The first step is almost similar to the first step of boundary contraction procedure. The difference is that the n_c value is normally taken equal to the dense state porosity (n_d). Therefore, the grains are in good contact, are well packed at a large mean stress, and have relatively small overlaps. It can be seen in the Table 4.3 that,

for equal-sized particles for a linear model, $n_d = 0.35$ (3D) and $n_d = 0.08$ (2D). The second step is exactly similar to the second step of boundary contraction procedure.

The third step of the grain scaling procedure is to adjust the mean stress of the grains assembly by iteratively scaling the grain sizes. This is done until the mean stress is within the pressure tolerance and static equilibrium is achieved. The material pressure is normally set to a small value compared to the material strength, for a bonded material.

4.2.2.2. Finalization phase. The material properties are allocated to the grain-grain contacts during this phase. Additional properties are also allocated to any new contact, which may develop during the grains motion. The first step of this phase is just for the bonded materials in which the presence of grain-grain contacts with a gap less than or equal to the installation gap is ensured (Potyondy, 2015). The installation gap and the material pressure control the grain connectivity. The installation gap plays a very important role in grain connectivity as it increases with increasing installation gap. The properties from Table 4.4 can be assigned to the grain-grain contact for linear materials. The properties from Table 4.4 can be assigned to the grain-grain contact for parallel-bonded materials as well, but only those contacts are bonded which has a gap of less than or equal to the installation gap (Potyondy, 2017). The corresponding model and material properties are allotted to the new contacts developed during succeeding motion.

By using the details of properties given in Tables 4.1–4.4, the base codes for the PFC materials were generated. By using the micro material properties in Tables 4.5 and 4.6, the samples for Sakersar limestone (Figure 4.2) and Namal limestone (Figure 4.3) are generated, respectively, for testing (Section 4.3). These samples were created in cylindrical

vessels of varying dimensions. By varying the properties, many PFC samples were produced to compare the results with the laboratory tests.

Table 4.4. Details of the linear and parallel bonded material parameters (Potyondy, 2017)

Symbol	FISH	Range	Default	Description
Parallel bonded material group:				
Linear group:				
E^*	pbm_emod	$[0.0,\infty)$	0.0	Effective modulus
k^*	pbm_krat	$[0.0,\infty)$	0.0	Stiffness ratio
μ	pbm_fric	$[0.0,\infty)$	0.0	Friction coefficient
Parallel bond group:				
g_i	pbm_igap	$[0.0,\infty)$	0.0	Installation gap
$\overline{\lambda}$	pbm_rmul	$(0.0,\infty)$	1.0	Radius multiplier
$\overline{E^*}$	pbm_bemod	$(0.0,\infty)$	0.0	Bond effective modulus
$\overline{k^*}$	pbm_bkrat	$[0.0,\infty)$	1.0	Bond stiffness ratio
$\overline{\beta}$	pbm_mcf	$[0.0,1.0]$	0.0	Moment contribution factor
$(\overline{\sigma_c})_{\{m,sd\}}$	pbm_ten_{m,sd}	$[0.0,\infty)$	{0.0,0.0}	Tensile strength (mean and standard deviation)
$(\overline{c})_{\{m,sd\}}$	pbm_coh_{m,sd}	$[0.0,\infty)$	{0.0,0.0}	Cohesion (mean and standard deviation)
$\overline{\phi}$	pbm_fa	$[0.0,90.0)$	0.0	Friction angle (degrees)
Linear material group:				
E_n^*	lnm_emod	$[0.0,\infty)$	0.0	Effective modulus
k_n^*	lnm_krat	$[0.0,\infty)$	0.0	Stiffness ratio
μ_n	lnm_fric	$[0.0,\infty)$	0.0	Friction coefficient

Table 4.5. Micro properties of Sakaser limestone

Micro Properties	Values
Common group:	
N_m , T_m , α, C_ρ , ρ_v (kg/m^3)	Sakesar_Limestone, 2, 0.7, 1, 2805
S_g , n_{SD}, T_{SD} , {$D_{\{l,u\}}$ (mm), ϕ}, D_{mult}	0, 1, 0, {3, 5, 1.0}, 1.0
Material vessel parameters:	
T_v , S_v , {H,W,D (mm)}, E_v^* (GPa)	0, 1, {27, 54, 54}, 70
Packing group:	
S_{RN} , P_m (GPa), ε_p , ε_{lim} , n_{lim}	10000, 1.7, 1 x 10^{-2}, 8 x 10^{-3}, 2 x 10^6
C_p , n_c	1, 0.30
Parallel bonded material group:	
Linear group:	
E^* (GPa), k^* , μ	35, 2.5, 0.5
Parallel bond group:	
g_i (mm), $\overline{\lambda}$, $\overline{E^*}$ (GPa), $\overline{k^*}$, $\overline{\beta}$	0, 1.0, 35, 2.5, 1.0
$(\overline{\sigma_c})_{\{m,sd\}}$ (MPa), $(\overline{c})_{\{m,sd\}}$ (MPa), $\overline{\phi}$ (degrees)	{15, 0}, {20, 0}, 35
Linear material group:	
E_n^* (GPa), k_n^*, μ_n	35, 2.5, 0.5

Figure 4.2. Sakesar limestone created in a cylindrical vessel for Brazilian test

Table 4.6. Micro properties of Namal limestone

Micro Properties	Values
Common group:	
N_m , T_m , α, C_ρ , ρ_v (kg/m^3)	Namal_Limestone, 2, 0.7, 1, 2700
S_g , n_{SD}, T_{SD} , {$D_{\{l,u\}}$ (mm), ϕ}, D_{mult}	0, 1, 0, {3, 5, 1.0}, 1.0
Material vessel parameters:	
T_v , S_v , {H,W,D (mm)}, $E_v{}^*$ (GPa)	0, 1, {130, 54, 54}, 70
Packing group:	
S_{RN} , P_m (GPa), ε_p , ε_{lim} , n_{lim}	30001, 2.7, 1 x 10^{-2}, 8 x 10^{-3}, 2 x 10^6
C_p , n_c	1, 0.30
Parallel bonded material group:	
Linear group:	
E^* (GPa), k^* , μ	35, 2.5, 0.5
Parallel bond group:	
g_i (mm), $\overline{\lambda}$, $\overline{E^*}$ (GPa), $\overline{k^*}$, $\overline{\beta}$	0, 1.0, 35, 2.5, 1.0
$(\overline{\sigma_c})_{\{m,sd\}}$ (MPa), $(\overline{c})_{\{m,sd\}}$ (MPa), $\overline{\phi}$ (degrees)	{15, 0}, {20, 0}, 35
Linear material group:	
$E_n{}^*$ (GPa), $k_n{}^*$, μ_n	35, 2.5, 0.5

Figure 4.3. Namal limestone created in a cylindrical vessel for compression test

4.3. LABORATORY TESTS IN PARTICLE FLOW CODE

The direct tension, Brazilian or diametral-compression, compression (confined, unconfined, and uniaxial strain), and fracture toughness tests can be performed in PFC (Figure 4.4). Tests are conducted on the samples created in physical vessels but the Brazilian test can be performed on any sample, which is centered at the origin. The axial direction presented in Figure 4.1 is the loading axis. After removing the samples from the vessels, they are loaded by surface grains in direct tension and fracture toughness tests, and by walls in the Brazilian and compression tests. The samples are pulled apart in the opposite directions (direct tension and fracture toughness tests) by assigning specified velocities to the surface grains in the axial direction. The axial walls in Brazilian test load the cylindrical or spherical shaped samples. The radial walls do not touch the sample in the unconfined test, and do not move in the uniaxial strain test. The velocities of the radial walls are controlled by a servomechanism to keep a constant confining pressure (P_c) in confined test (Wang et al., 2016).
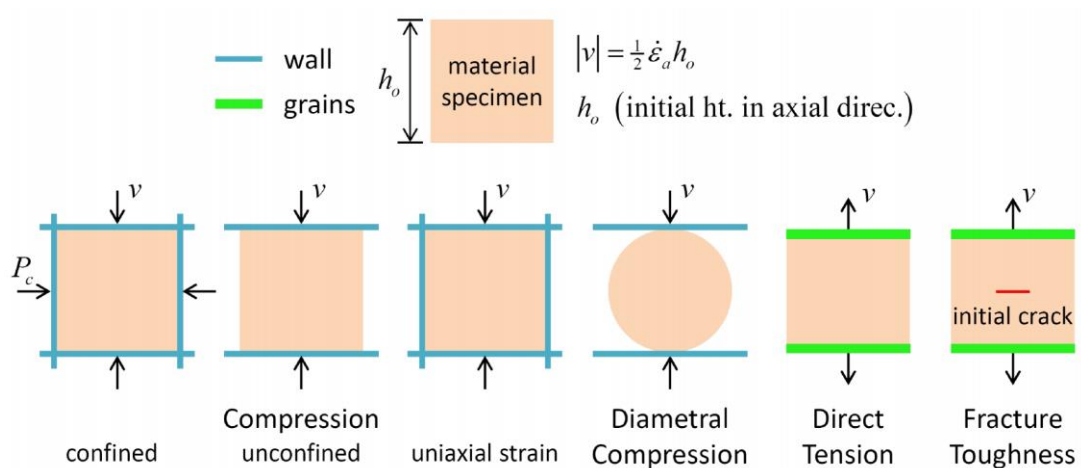
Figure 4.4. Loading conditions of different laboratory tests (Potyondy, 2017)

4.3.1. Stress, Strain, and Porosity Measurements.   Three methods can be used to determine stresses (σ_{xx} , σ_{yy} , σ_{zz} , σ_{xy} , σ_{xz} , σ_{yz}) and strains (ε_{xx} , ε_{yy} , ε_{zz} , ε_{xy} , ε_{xz} , ε_{yz}) of the samples ($\sigma_{ii} > 0$ is tension, and $\varepsilon_{ii} > 0$ is extension). These methods include the usage of measurement regions, walls, and gauge grains. The measurement-based values are determined as the average values of three spherical regions, which are symmetric along the axis of the largest vessel dimension. The wall-based method gives stress as wall force divided by the area of the sample, and strain depending upon the change in distance between two walls. The gauge-based method gives strain, depending upon the change in distance between opposite gauge grains. The gauge grain is a ball, which is closest to the center of the corresponding sample surface. The gauge grains may be disturbed by the damage formation in a bonded material. Therefore, the wall-based method gives a consistent response over the complete sample surface. Measurement regions and walls methods can be used to determine the porosity of a sample. Grain-grain overlap is considered in the measurement-based method, but is not considered in wall-based method.

Every type of material vessel is linked to an axial direction. In case of 3D modeling, the axial direction for cylindrical and polyaxial vessels is along the z-axis (Figure 4.1). Equations (4.4) and (4.5) are used to determine the axial and radial stresses, and strains, respectively. The deviator stresses and strains are determined from Equations (4.6) and (4.7). According to Engelder (1994), the deviator stress is different from deviatoric stress and should not be confused. In a Triaxial test, the value of axial stress departing from the confining pressure is known as the differential stress. Paterson and Wong (2005) used this definition while reporting results of Triaxial tests. The mean stress and volumetric strain can be determined from Equations (4.8) and (4.9), respectively.

$$\sigma_a = \sigma_{zz}, \quad \sigma_r = \frac{1}{2}(\sigma_{xx} + \sigma_{yy}) \tag{4.4}$$

$$\varepsilon_a = \varepsilon_{zz}, \quad \varepsilon_r = \frac{1}{2}(\varepsilon_{xx} + \varepsilon_{yy}) \tag{4.5}$$

$$\sigma_d = \sigma_a - \sigma_r \tag{4.6}$$

$$\varepsilon_d = \varepsilon_a - \varepsilon_r \tag{4.7}$$

$$\sigma_m = \frac{1}{3}(\sigma_{xx} + \sigma_{yy} + \sigma_{zz}) = \frac{1}{3}(\sigma_a + 2\sigma_r) \tag{4.8}$$

$$\varepsilon_v = \varepsilon_{xx} + \varepsilon_{yy} + \varepsilon_{zz} = \varepsilon_a + 2\varepsilon_r \tag{4.9}$$

4.3.2. Material Deformability. The deformability of a granular material is a measure of the resilient modulus (M_R), while the deformability of a bonded material is a measure of the effective isotropic elastic constants. Singh (2015) defined resilient modulus as the ratio of applied deviator stress to resilient strain (Figure 4.5). It is an important parameter to define a granular material and is dependent upon the stress. According to Han and Vanapalli (2016), the resilient modulus is "…the key soil property in the mechanistic pavement design methods to rationally characterize the resilient behavior of the pavement materials, analyze the fatigue failure of the surface layer, and dimension the multi-layer system of the pavement structure." According to Potyondy et al. (2016), layered elastic analysis (LEA) is a method to calculate the response of the pavement under loading. A pavement layer can be defined by its resilient modulus and Poisson's ratio.
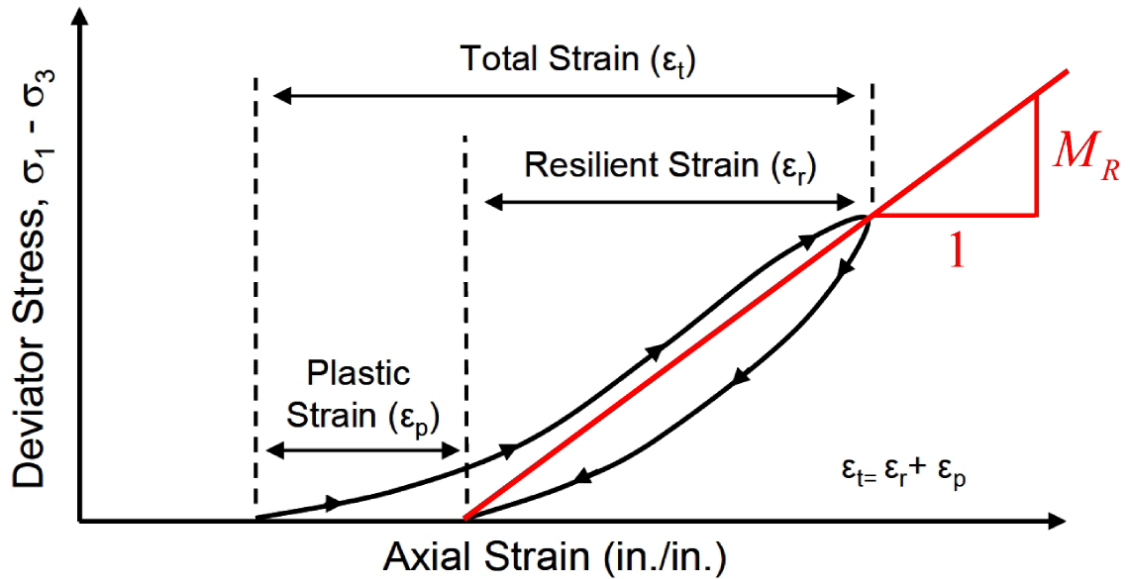
Figure 4.5. Determination of resilient modulus (Buchanan, 2007)

The Young's modulus (E) and Poisson's ratio (v) are known as the effective isotropic elastic constants for a linear elastic isotropic material. For the calibration of bonded material, E and v are compared with the elastic constants, measured during laboratory triaxial tests (Potyondy and Cundall, 2004). E and v for the PFC materials can be determined by performing a compression test and by doing the interpretation of the macroscopic force-displacement response. Equations (4.10) and (4.11) can be used to determine Young's modulus and Poisson's ratio.

$$E = \frac{\Delta\sigma_a}{\Delta\varepsilon_a} \tag{4.10}$$

$$v = -\frac{\Delta\varepsilon_r}{\Delta\varepsilon_a} \tag{4.11}$$

4.3.3. Servomechanism. The walls velocities of polyaxial and cylindrical vessels are controlled by a servomechanism. There are three pairs of opposing walls in a polyaxial vessel, a pair of opposing axial walls and a cylinder wall in a cylindrical vessel, and a sphere wall in a spherical vessel. Velocity or pressure is the boundary condition for all aforementioned walls. The velocity boundary condition assigns an equal and opposite velocity to the wall pair, and radial to the cylinder and sphere wall vertices. A pressure boundary condition triggers a servomechanism to retain the assigned pressure by controlling the wall velocities. The pressure acting on the opposing walls in the k-direction can be determined by using Equation (4.12).

$$P_k^w = -\sigma_k^w \,, (P_k^w > 0 \text{ is compression})$$

$$\text{with } k = \begin{cases} \{x, y, z\}, & \text{polyaxial vessel} \\ \{z, r\}, & \text{cylindrical vessel} \\ \{r\}, & \text{spherical vessel} \end{cases} \qquad (4.12)$$

4.3.4. Loading Rate. The response of a real or a PFC material is very sensitive to loading rate (Yue, 2015). To get a quasi-static response, a slow enough loading rate should be selected (Potyondy, 2017). The loading has to be slow enough, so that the system gets time to adjust the force redistribution that goes along with non-linear event (Bahrani, 2015). A strain-controlled test can be performed to obtain the quasi-static response, while the loading velocity is set to zero after each nonlinear event until a new static equilibrium is achieved (Banerjee, 2017). The stress-strain curve can be plotted to the peak value that presents the quasi-static response. The strain-controlled test should be performed at a series of constant loading velocities to obtain the same response.

The quasi-static response obtained from the PFC material can be compared with the response obtained from laboratory triaxial tests for calibration. If dynamic effects are disturbing the response of the real material, these should be included in the numerical model to match the dissipative mechanisms (Tamás, 2018). If the comparison is just for the quasi-static responses, then there is no need to repeat the dissipative mechanisms in the DEM model. The model can be approximated to quasi-static conditions by using the maximum (default) damping coefficient of 0.7 (Ding et al., 2014).

The axial strain rate ($\dot{\varepsilon}_a$) is the loading rate for the direct tension, Brazilian, and compression tests. The strain rate that can produce a quasi-static condition for a PFC sample of some length most probably cannot produce the quasi-static conditions for a sample of different length (Wang et al., 2016). The loading velocities can be equated for two samples of different length to obtain a good estimate of the strain rate.

4.3.5. Direct Tension Test.   The samples are gripped at both ends and are pulled slowly in opposite direction in a direct tension test, while tracking the axial force and strain (Raziperchikolaee et al., 2014). A thin layer of surface grains (grip grains) is recognized for gripping that is used to load the samples. The opposite sample surfaces can be pulled apart by setting the surface grains velocities in the axial direction. The translation and rotation of surface grains are not permitted during the test that is similar to the opposing surfaces being fixed to rigid and flat platens by some glue (Raziperchikolaee, 2014). The axial strain rate is used to define the velocity of the surface grains.

The set-up and loading phases are the two phases of a direct tension test. The motion of the grip grains is assigned and the strains are set to zero in the set-up phase. The PFC model state is saved at the end of the set-up phase. Grain displacements are reset to zero

after the set-up phase. The axial strain is applied by moving the grip grains at a specified strain rate, during the loading phase. The loading phase can be completed in a single stage that ends when the axial stress drops below a specified multiplier of its peak value, or in multiple stages in which the axial strain increments are assigned. The grip grain velocities are reset to zero at the end of each stage, and the model state is saved. The crack monitoring is performed during the test, and the sample behavior is observed to capture the required parameters. The observed parameters include axial stress, axial strain, axial displacement, and the number of cracks. Thirty-six (36) PFC experiments were conducted covering the range from soft soils to hard rocks. Figure 4.6 presents a direct tension test performed on Dolerite-1 sample taken from Majeed and Bakar (2016). The tensile strength is 22 MPa and is shown in negative on the y-axis to match with rock mechanics notations.
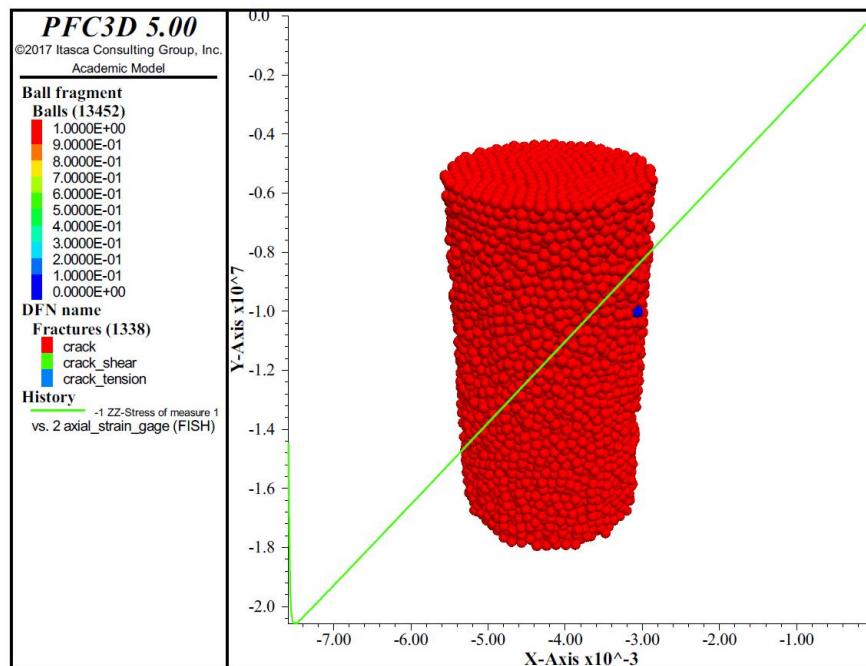
Figure 4.6. Direct tension test on Dolerite-1 sample

4.3.6. Brazilian Test.   Brazilian tests can be performed on the samples that are centered w.r.t. the origin. Axial walls are created in such a way that they are centered w.r.t. the origin, as well as the loading axis along the y-axis (Figure 4.7). The platens are set as frictionless, and effective modulus is assigned to set the grain-wall contact stiffness. Similar to the direct tension test, set-up and loading phases are the two phases of a Brazilian test. The walls are created, and the model equilibrium is achieved in the set-up phase. All the next steps are exactly similar to the direct tension test (explained earlier in Section 4.3.5). The only difference is that the axial strain is applied by moving the axial walls instead of grip grains.
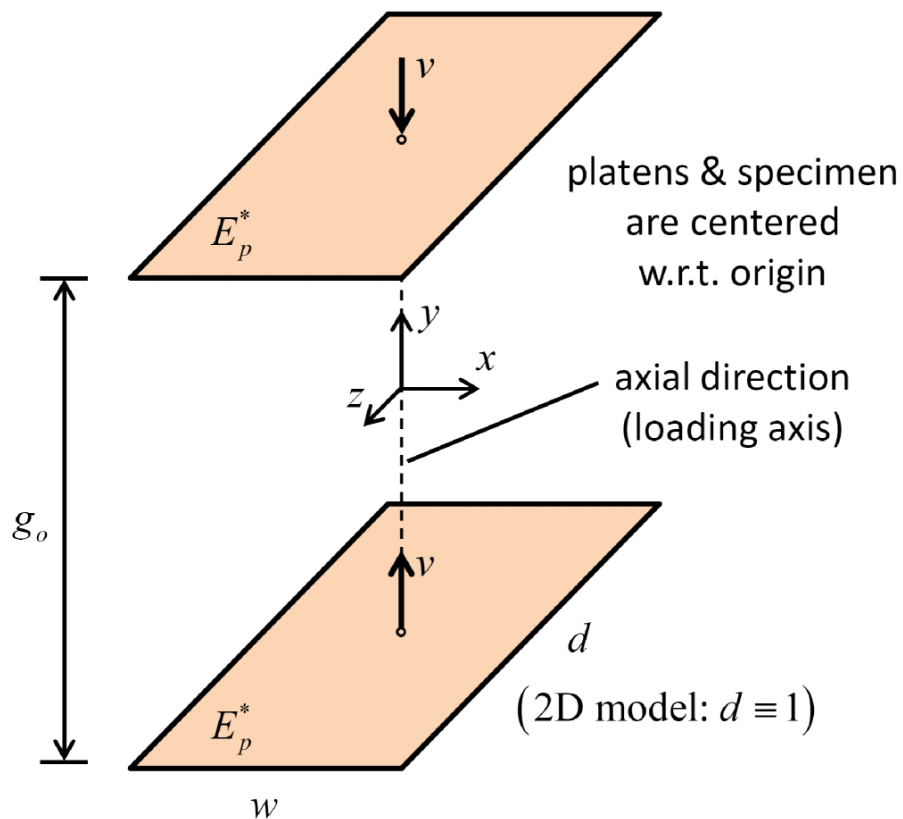
Figure 4.7. Loading configuration of Brazilian test (Potyondy, 2017)

The observed parameters include axial force, axial strain, axial displacement, and the number of cracks. The axial force is calculated by averaging the two forces working on the two opposing walls and is illustrated in Equation (4.13). $(F_y)^+$ and $(F_y)^-$ are the forces acting on top and bottom walls respectively. Based on the change in distance between the two opposing walls, the axial strain can be determined from Equation (4.14). The initial wall gap is denoted by 'g$_0$' and the wall gap is denoted by 'g'.

$$F_a = \frac{1}{2}((F_y)^- - (F_y)^+), \quad (F_a > 0 \text{ is tension})$$ (4.13)

$$\varepsilon_a = \frac{g - g_0}{g_0}, \quad (\varepsilon_a > 0 \text{ is extension})$$ (4.14)

Thirty-six (36) PFC single stage experiments were conducted covering the range from soft soils to hard rocks. Figure 4.8 presents a Brazilian test performed on a Sakesar limestone sample (presented earlier in Figure 4.2). It also presents the number of fractures created during the test. The fracture line is almost similar to the one obtained during the laboratory tests. The plot of axial force vs. axial strain is presented in Figure 4.9. The peak value of force is noted and by using Equation (4.2), the Brazilian tensile strength is determined for the PFC material. The plot of axial force vs. axial displacement is shown in Figure 4.10. The number of cracks vs. axial strain is shown in Figure 4.11 that presents the tensile, shear, and the total number of cracks generated during the test. As the strain rate increases, the number of tensile cracks increases but very little increase is seen in shear cracks. The contact force magnitude and the contact force chain are shown in Figure 4.12 and Figure 4.13, respectively (compression black, tension red).
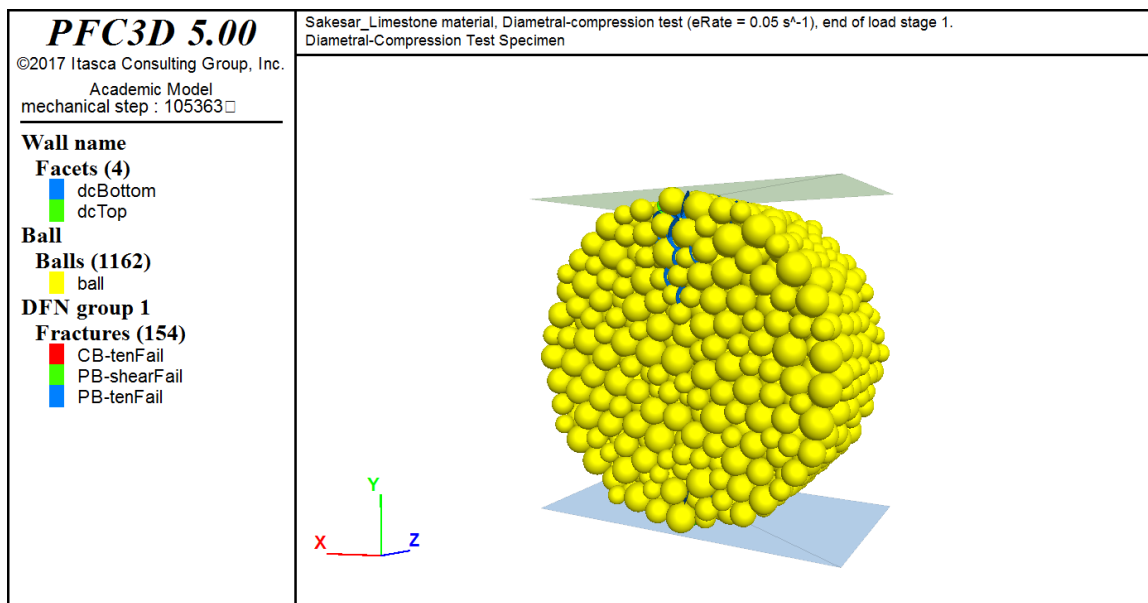
Figure 4.8. Sakesar limestone (PFC sample) after the Brazilian test
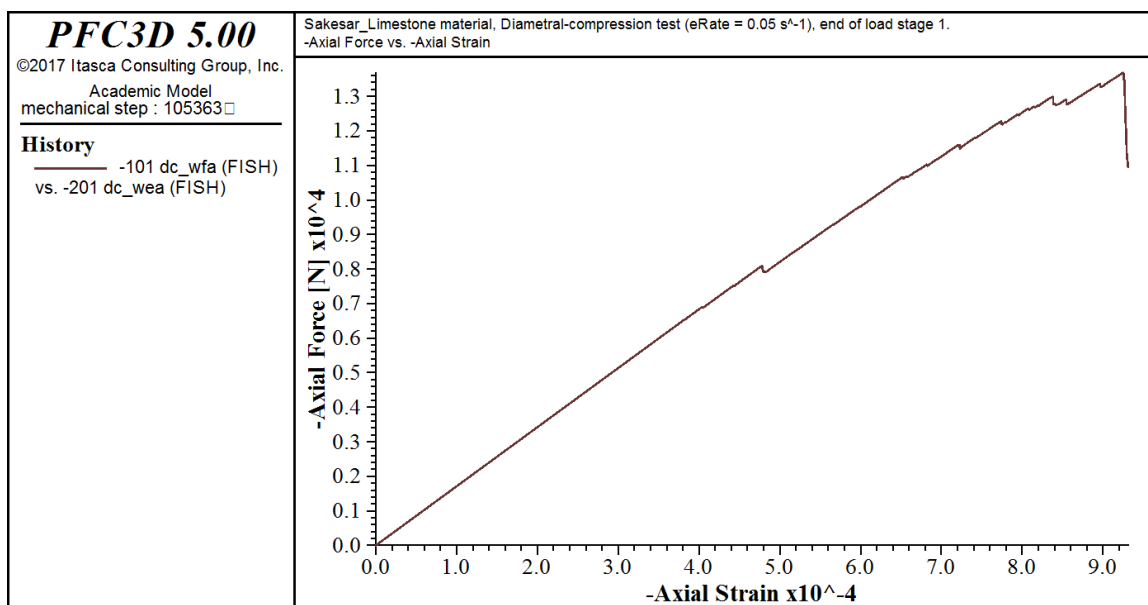
Figure 4.9. Axial force vs. axial strain after the Brazilian test
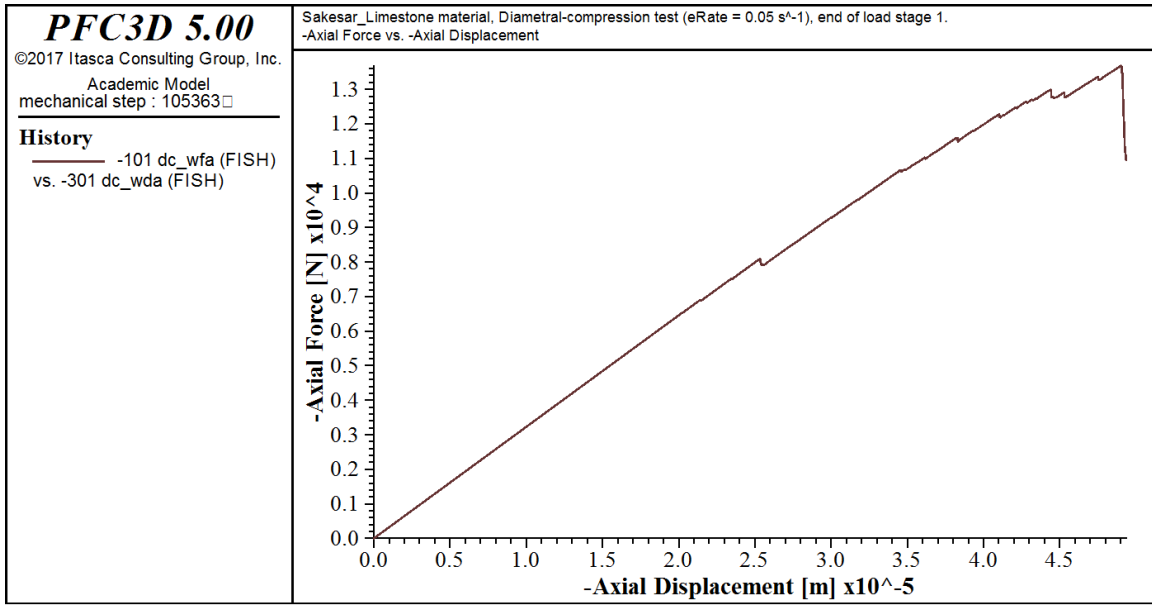
Figure 4.10. Axial force vs. axial displacement after the Brazilian test
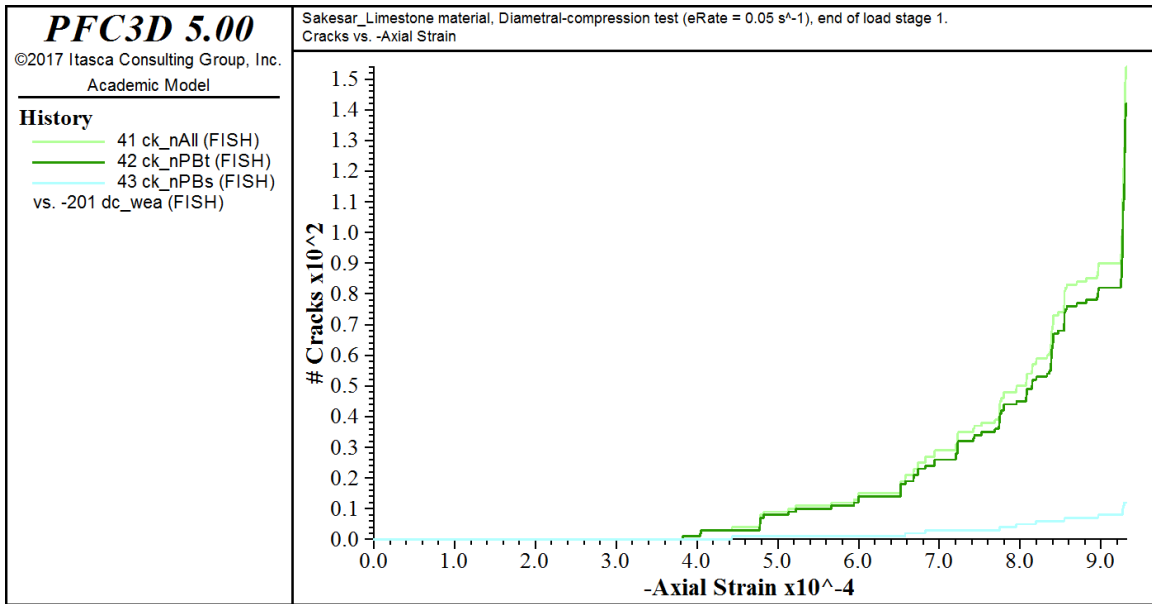
Figure 4.11. Number of cracks vs. axial strain after the Brazilian test
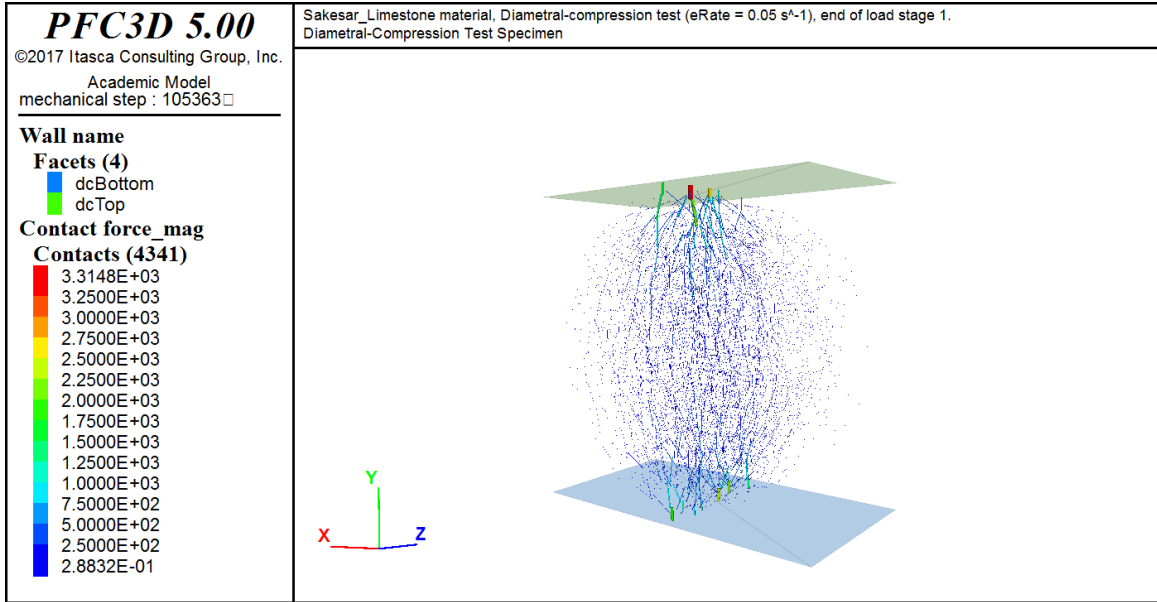
Figure 4.12. Contact force magnitudes after the Brazilian test
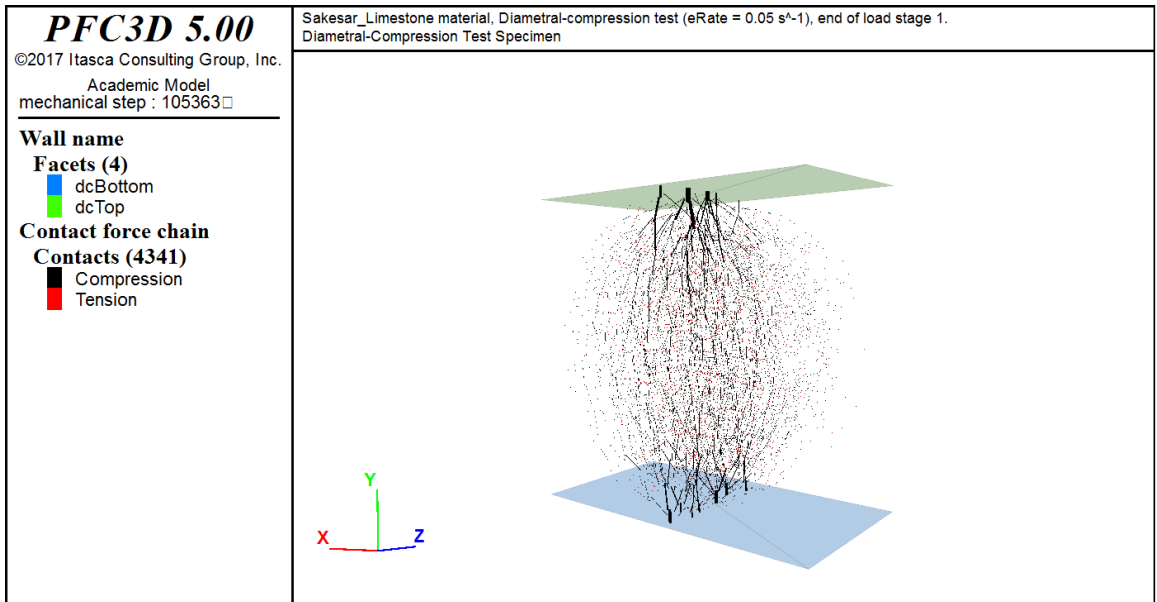
Figure 4.13. Contact force chain after the Brazilian test

4.3.7. Compression Test. Compression tests are conducted in either the polyaxial (polyaxial loading conditions) or cylindrical (triaxial loading conditions) vessels. The loading axis and loading conditions for the compression tests are presented earlier in Figures 4.1 and 4.4 respectively. The axial walls do the loading (Potyondy, 2017). The radial walls do not touch the sample in the unconfined test, and do not move in the uniaxial strain test. The velocities of the radial walls are controlled by a servomechanism to keep a constant confining pressure (P_c) in confined test (Wang et al., 2016).

Seating phase and loading phase are the two phases of a compression test. The strains are reset to zero during the seating phase. Confining pressure is applied in all directions in a confined test. The radial walls are moved away from the sample initially in an unconfined test, whereas the radial walls are motionless in uniaxial strain test. Then, an axial pressure is applied by the pressure boundary condition, and a zero velocity boundary condition in the radial direction. The PFC model state is saved at the end of the seating phase.

Grain displacements are reset to zero at the end of the seating phase and strains are reset to zero at the start of the loading phase. The axial walls are moved at a specified strain rate to keep a constant confining pressure for a confined test, or to keep radial walls motionless for an unconfined or uniaxial strain test (Jiang et al., 2013). The loading phase can be completed in a single stage that ends when the applied deviator stress drops below a specified multiplier of its peak value, or in multiple stages in which the axial strain increments are assigned. The wall velocities are reset to zero at the end of each stage, and the model state is saved. The crack monitoring is performed during the test, and the sample behavior is observed to capture axial stress, axial strain, axial displacement, and cracks.

4.3.7.1. Unconfined compression test in PFC. Thirty-six (36) experiments were conducted in PFC. Thirteen samples were Sakesar limestone, eleven samples were Namal limestone, and twelve samples were taken from Majeed and Bakar (2016) for calibration. Figure 4.14 presents an unconfined compression test performed on a Namal limestone sample. The compressive strength is 110 MPa.
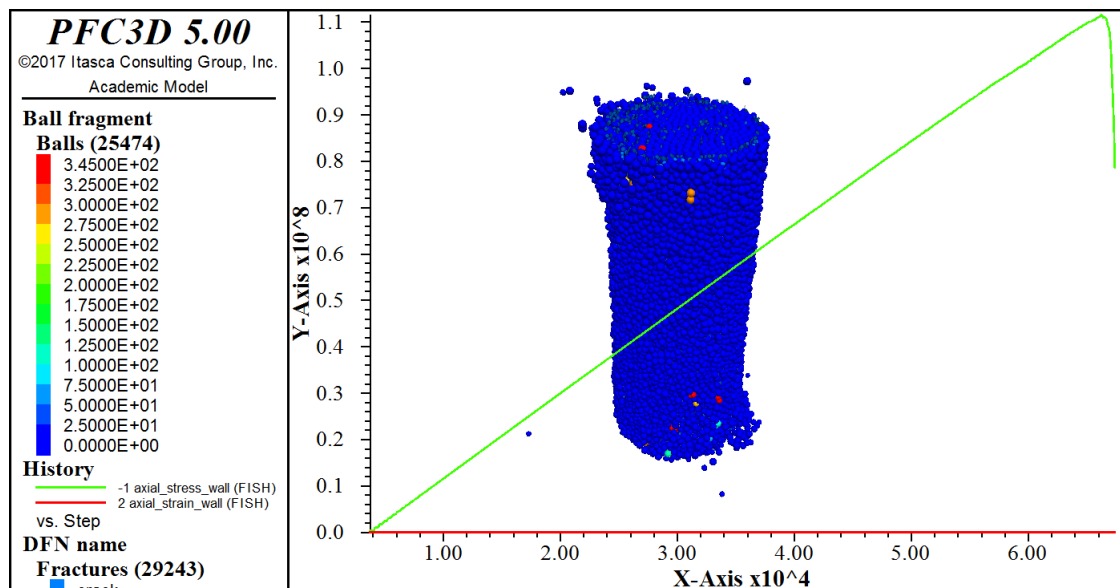
Figure 4.14. Unconfined compression test on Namal limestone sample

4.3.7.2. Confined compression test in PFC. About 1,800 confined compression tests were performed in PFC, using the linear model. Tests were performed on materials with density values ranging from 1800 to 3000 kg/m^3, and 196 tests were performed at a particular density value. All the tests were conducted in polyaxial vessels (76 x 38 x 38 mm^3) in three loading stages, at a confining pressure (P_c) of one MPa, and a strain rate of 0.1 s^{-1}. Figure 4.15 presents an overburden material in a polyaxial vessel at the end of the

second load stage. Three parameters including effective modulus (E*), normal-to-shear stiffness ratio (k*), and friction coefficient (μ) are varied to determine resilient modulus, Young's modulus, Poisson's ratio, shear modulus, and friction coefficient. The results of a confined compression test performed on a PFC sample with a density value of 2000 kg/m^3 are presented in Appendix A (Table A.3). These parameters are calibrated and validated using triaxial test data from PFC FISHTank (or fistPkg) which is developed and maintained by Itasca. FISHTank provides four well-defined materials and a user-defined material that can be used for practical applications and scientific inquiries (Itasca, 2017). Initial results were also calibrated using the results of Abdulhadi and Barghouthi (2012), Buchanan (2007), Coetzee and Els (2009a), Coetzee and Els (2009b), and Potyondy and Cundall (2004).
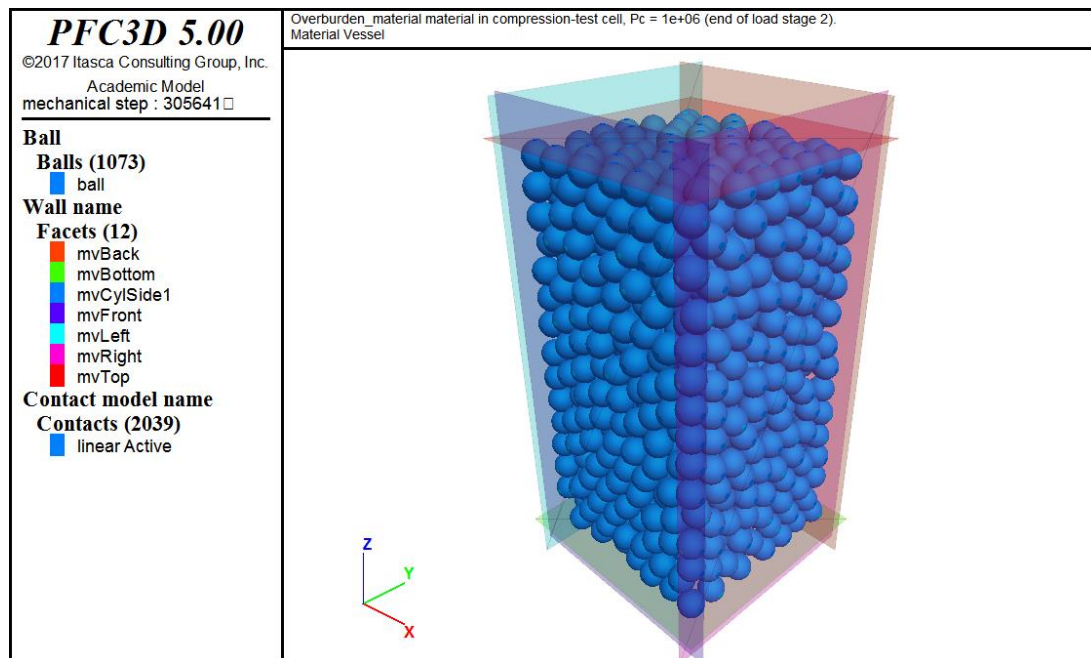
Figure 4.15. Overburden material in a polyaxial vessel at the end of second load stage during a confined compression test

4.4. SUMMARY

Laboratory rock tests (compression, direct tension, and Brazilian) are required for feasibility studies that result in huge costs. In the idealized world of numerical models, these tests are possible and provide reliable estimates of rock strength values. To perform the numerical experiments, samples were created using particle flow code (PFC3D) software. The PFC material is generated in a material vessel that can be cylindrical, polyaxial or spherical. To apply the boundary conditions, the material may be removed from the vessels and may be trimmed into a desirable shape. The material is generated in the vessel in two phases: packing and finalization phases. A cloud of grains is produced during the packing phase. Then under the condition of zero friction, the grain cloud is allowed to rearrange into a packed state. A dense or loose packing of a granular material can be generated by using the boundary contraction procedure. On the other hand, only a dense packing of a granular material can be generated using the grain scaling procedure. The material properties are allocated to the grain-grain contacts during the finalization phase. The installation gap and the material pressure plays a very important role in grain connectivity, as grain connectivity increases with increasing these parameters.

Tests are conducted on the samples created in physical vessels but the Brazilian test can be performed on any sample, which is centered at the origin. After removing the samples from the vessels, they are loaded by surface grains in direct tension tests, and by walls in the Brazilian and compression tests. Set-up and loading phases are the two phases for these tests. Thirty-six (36) PFC experiments were conducted each for direct tension, Brazilian, and unconfined compression tests, ranging from soft soils to hard rocks. About 1,800 confined compression tests were performed in PFC, using the linear model. Tests

were performed on materials with density values ranging from 1800 to 3000 kg/m^3, and 196 tests were performed at one density value. Three parameters including effective modulus (E^*), normal-to-shear stiffness ratio (k^*), and friction coefficient (μ) are varied to determine resilient modulus, Young's modulus, Poisson's ratio, shear modulus and friction coefficient. These parameters are calibrated and validated using triaxial test data from PFC FISHTank (or fistPkg) which is developed and maintained by Itasca. Initial results were also calibrated using the results of Abdulhadi and Barghouthi (2012), Buchanan (2007), Coetzee and Els (2009a), Coetzee and Els (2009b), and Potyondy and Cundall (2004).

5. ARTIFICIAL INTELLIGENCE EXPERIMENTATION

This section covers the details of experimentation performed using artificial intelligence (AI) models for the predictive analysis done in this study. These models include Artificial Neural Network (ANN), Mamdani Fuzzy Logic (MFL), and Hybrid neural Fuzzy Inference System (HyFIS). The multiple linear regression (MLR) method is also used for the predictions, as it is one of the most commonly used methods for the predictive analysis. The results of confined compression tests (presented in Appendix A) are used as input data for the predictive analysis. The purpose for using multiple linear regression and different AI models is to select the best model for the prediction of formation material properties. Based on cross-validation technique, eighty percent of data is used to train the AI models and twenty percent data is used to test the AI models (Fijani et al., 2013). This section includes the methods used in this study with justification, model formulation, verification and validation of the models, experimental design and experimentations, and finally ends with the summary of the section.

5.1. METHODS AND JUSTIFICATION

The multiple linear regression (MLR) method is one of the most commonly used methods for the predictive analysis. It has been used extensively and is known universally. Its success originates from its simple use and its ability to give predictive and illustrative outcomes that make it extremely interesting (Gevrey et al., 2003). To observe the predictive ability of MLR, a comparison to AI models was performed.

The ANN is a reliable method when the relationship between the variables is non-linear (Lek et al., 1996). ANNs are used to predict the performance of processes, because of their accuracy, adequacy, and wide range of engineering applications (Neelakantan et al., 2001). The ANN method has many applications in the real world. The ANN is an exceptionally helpful model and it can be used in critical thinking, problem solving, and machine learning. Their ability to learn by illustration makes them extremely adaptable and intense. Hence to best use the ANN for various problems, it is basic to comprehend the potentials and the limitations of Neural Networks (Team, 2017).

Fuzzy systems are gaining popularity because they can handle incorrect knowledge and data. Fuzzy systems are rule-based methods that use fuzzy rules and inference. They are strong enough to handle confusing, subjective, and incorrect knowledge and data. Fuzzy systems are applied successfully in the fields of computer vision, decision analysis, data analysis, expert systems, and automation. Automatic washing machines, transmission control, and automatic camera focusing are some of the applications of these fuzzy systems (Shanmuganathan, 2016).

5.2. APPLICATION TO RESEARCH AREA

The rock mechanics community has extensively used PFC to study the basic processes of brittle fracturing in rocks by using small-scale models (Lisjak and Grasselli, 2014). The calibrated model of Potyondy and Cundall (2004) for the confined compression test has been used in this research to determine resilient modulus, Young's modulus, Poisson's ratio, shear modulus and friction coefficient. Because PFC uses DEM during the analysis, thus, it is computationally too expensive as well as its initial cost is also high.

The purpose for using MLR and AI models is to look for the best alternative to PFC unconfined compression test results. Because of their wide range of applications, it is expected that one of these AI methods will provide reliable estimates of the formation properties within a short time. These models are developed in software R that is free (zero cost), which is an added advantage of AI models. The results of confined compression tests performed at different density values in this study are used to validate the AI models.

5.3. MODEL FORMULATION

The MLR analysis was performed in Microsoft Excel 2016. The values of the effective modulus (E^*), normal-to-shear stiffness ratio (k^*), and friction coefficient (μ) from Appendix A were used as input. Using the data analysis option, MLR analysis was performed separately for each of the five outputs (resilient modulus, Young's modulus, Poisson's ratio, shear modulus, and friction coefficient).

An ANN model with an input layer of three neurons (each neuron presents an input), a single hidden layer of six neurons (gave best prediction results by hit and trial method), and an output layer of five neurons (each neuron presents an output) was developed in two phases: feedforward phase and gradient descent based error backpropagation phase (Figure 5.1). The input data was processed and the weights were assigned by the neurons in the hidden and output layers. A bias (blue line in Figure 5.1) was also added to each neuron in hidden and output layers to obtain non-zero outputs. In phase two, ANN decision parameters were adjusted to optimize the problem and to get desired results. The error contribution of each neuron was determined, and by adjusting the weights and bias of the neurons, errors were brought within a specified tolerance (0.01).
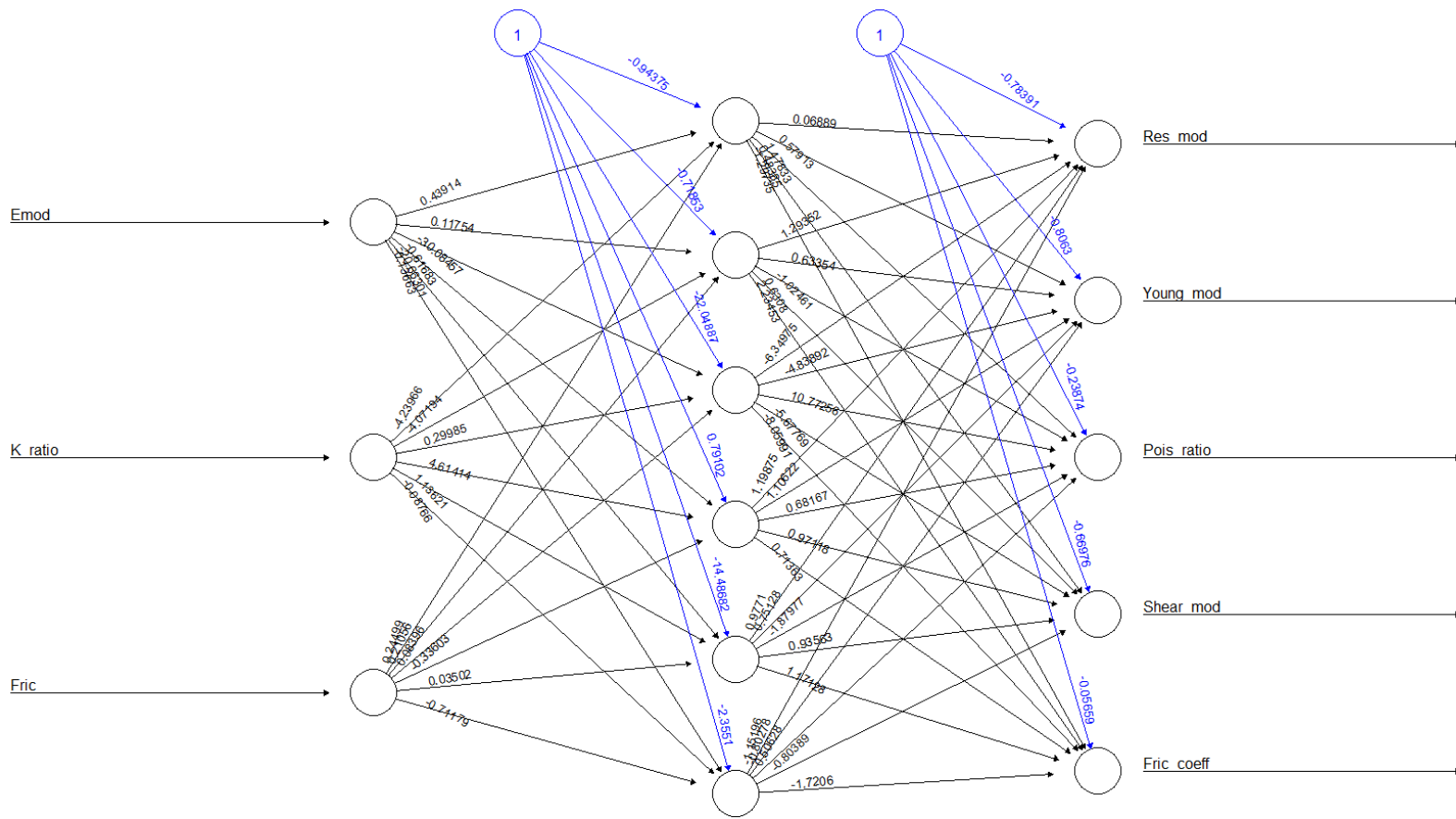
Figure 5.1. Artificial neural network with one hidden layer comprised of six hidden neurons. Black lines with numbers presenting the weights assigned and the blues lines are presenting the bias added to each neuron

The MFL process consists of fuzzification, fuzzy logic operations by using if-then rules, and defuzzification steps. In fuzzification, all the input values were transformed into the Gaussian membership functions that are used to relate each real variable to the fuzzy variable. All the possible if-then rules were executed in the fuzzy logic operations step, and the output functions were produced. In the defuzzification step, all the fuzzy output values were transformed back into real values by using the center of gravity (COG) method. The 'min' operator was used as an implication method (Mamdani and Assilian, 1975), and the 'max' operator was used for rule aggregation (Iancu, 2012).

HyFIS uses a combination of both numerical data and fuzzy rules. Thus it exhibits the added advantage of both methods. MFL method was used to develop and train the HyFIS model. Two phases are available in HyFIS during the learning process: structure learning phase for knowledge acquisition and parameter learning phase. In structure learning or rule finding phase, the techniques proposed by Wang and Mendel (1992) were employed to determine the fuzzy rules from the required input-output pairs. All the input values were transformed into the Gaussian membership functions during the fuzzification step. In parameter learning phase, a gradient descent learning scheme was employed to optimize the membership functions to achieve reasonable outputs. The center of gravity (COG) method was used as an aggregation function during the defuzzification step.

All the AI models were developed by using the software 'R' that is used for statistical computing. Linear mapping was used to scale the data between 0 and 1, as given by the Equation (5.1). At the end of the training phase, the data was unscaled to get the actual output values.

$$X_n = \frac{X - X_{min}}{X_{max} - X_{min}} \qquad\qquad (5.1)$$

5.4. VERIFICATION AND VALIDATION

Once the models are developed, the next logical step is to verify and validate those models. Verification assures that the model is working as designed whereas validation assures the model accurately works on real-world problems. One method is to compare the results produced by the model to known values. A simple and systematic approach was used for verification and validation of the AI models. The results of confined compression tests (Appendix A, Table A.3) performed in this study at a density value of 2000 kg/m^3 are used to verify and validate the AI models. Based on cross-validation technique, eighty percent of data (157 values) is used to train the AI models, and twenty percent data (39 values) is used to test the AI models (Fijani et al., 2013). The training dataset was first used to adjust the models, and then test data set was used to determine the best configuration (Geman et al., 1992). After the AI models were trained, de-normalization is carried out to get the unscaled output values.

5.4.1. Verification. The process of verification involves training of the developed AI and MLR models. The first 157 values from the Appendix A (Table A.3) were used to train the models. Effective modulus (E*), normal-to-shear stiffness ratio (k*), and friction coefficient (μ) are the three inputs that were varied to determine the five outputs that include resilient modulus, Young's modulus, Poisson's ratio, shear modulus, and friction coefficient. The variables defined in experimental design were varied to achieve the best possible results. Based on five outputs and four methods, the verification results are presented in Figures 5.2-5.21.
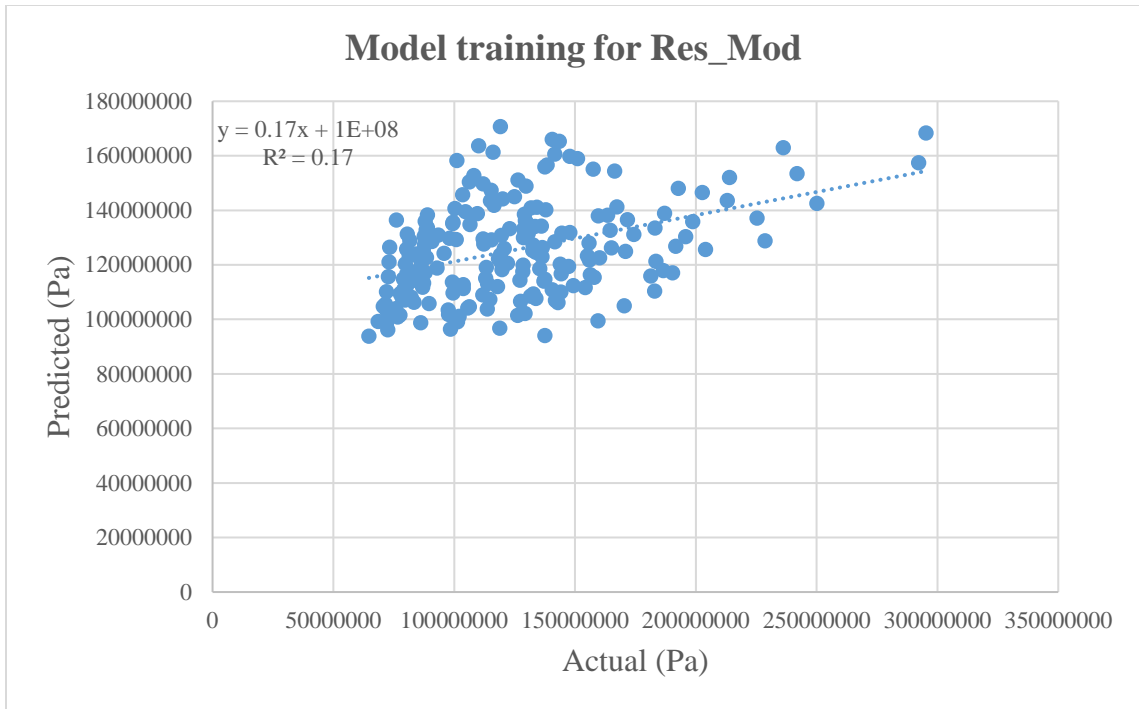
Figure 5.2. Actual versus predicted resilient modulus in the MLR training phase
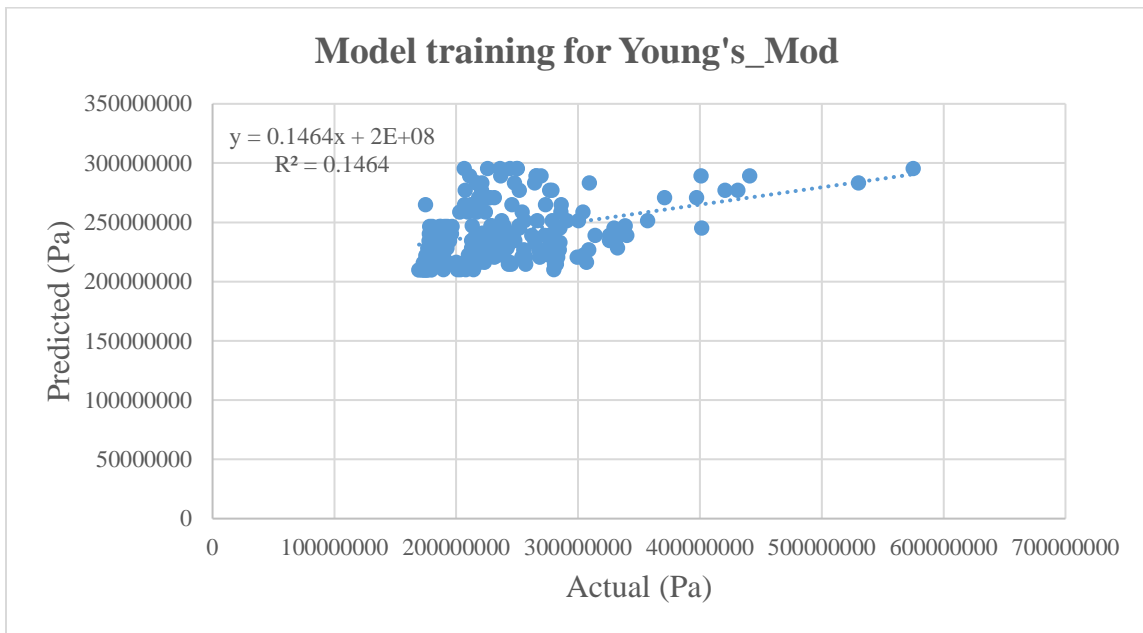
Figure 5.3. Actual versus predicted Young's modulus in the MLR training phase
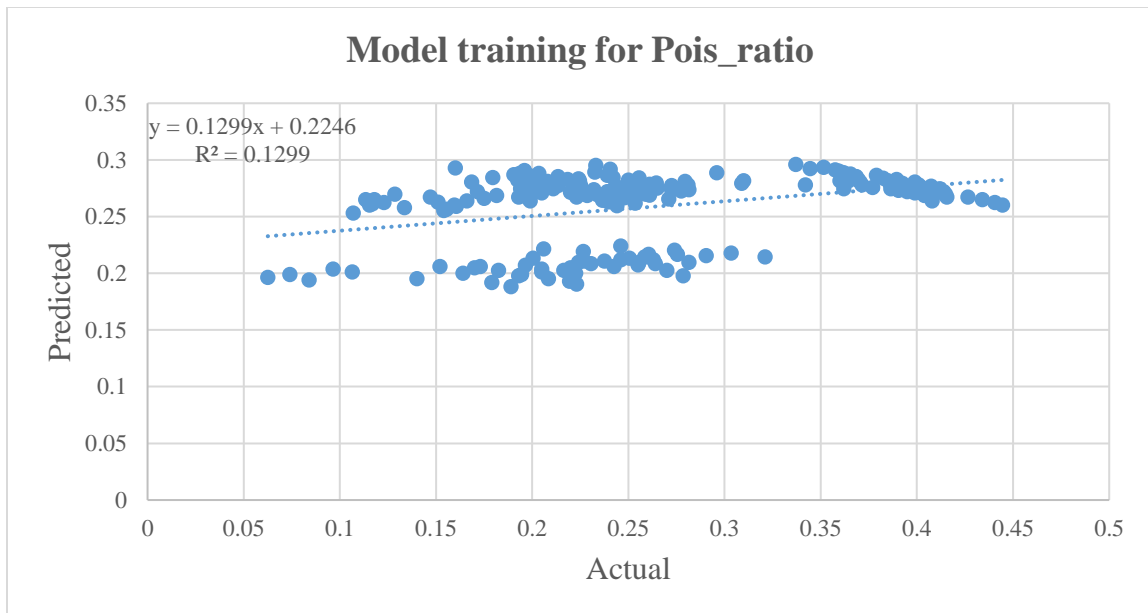
Figure 5.4. Actual versus predicted Poisson's ratio in the MLR training phase
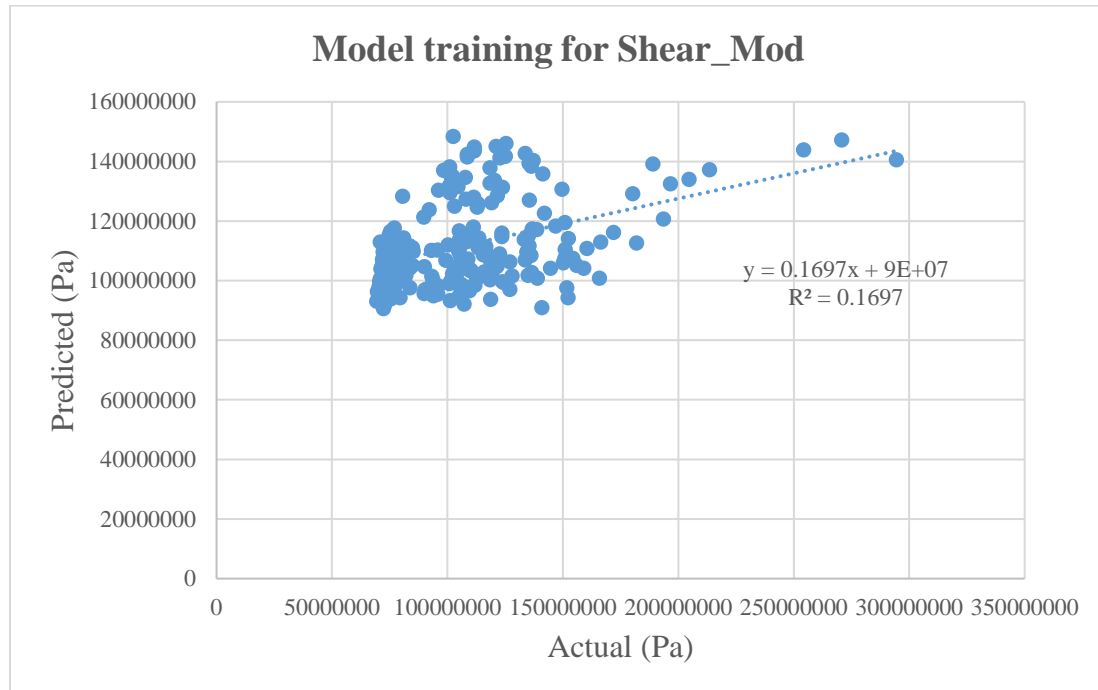
Figure 5.5. Actual versus predicted shear modulus in the MLR training phase
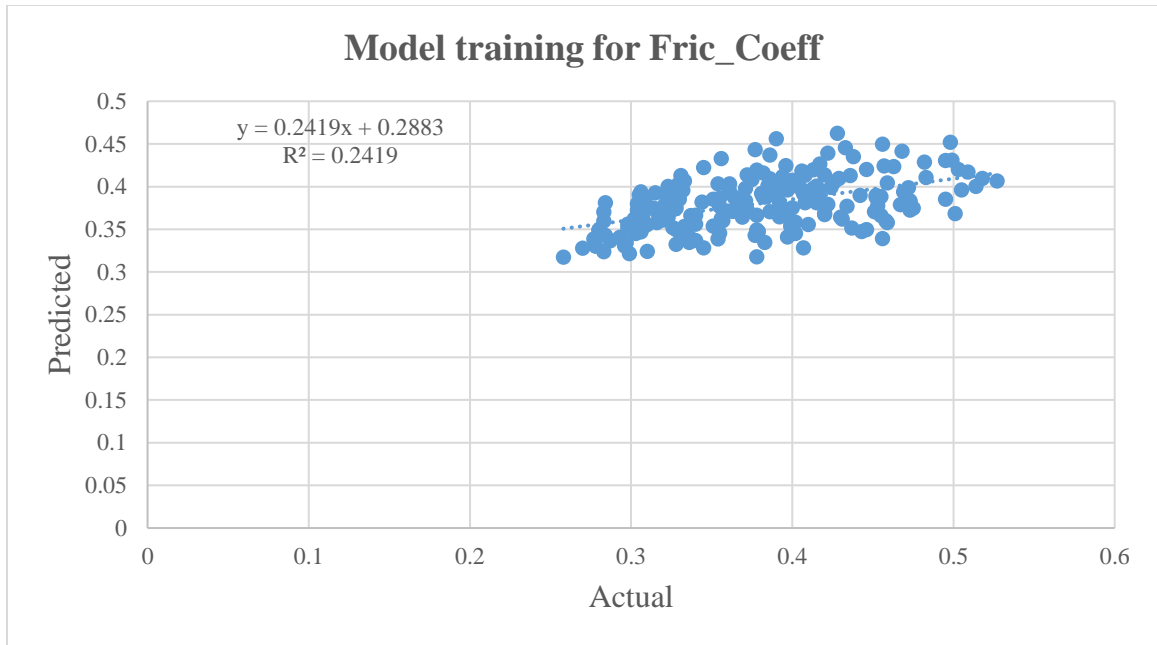
Figure 5.6. Actual versus predicted friction coefficient in the MLR training phase
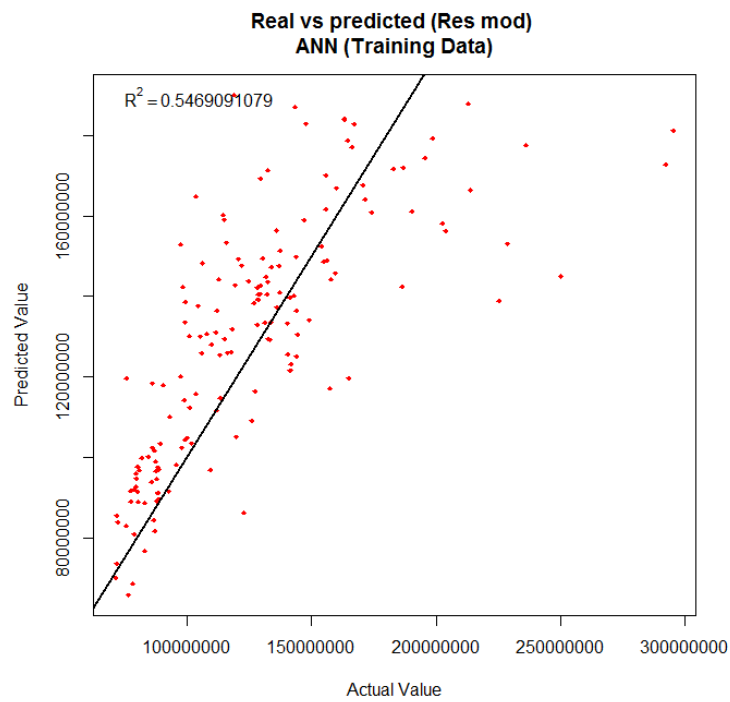
Figure 5.7. Actual versus predicted resilient modulus in the ANN training phase
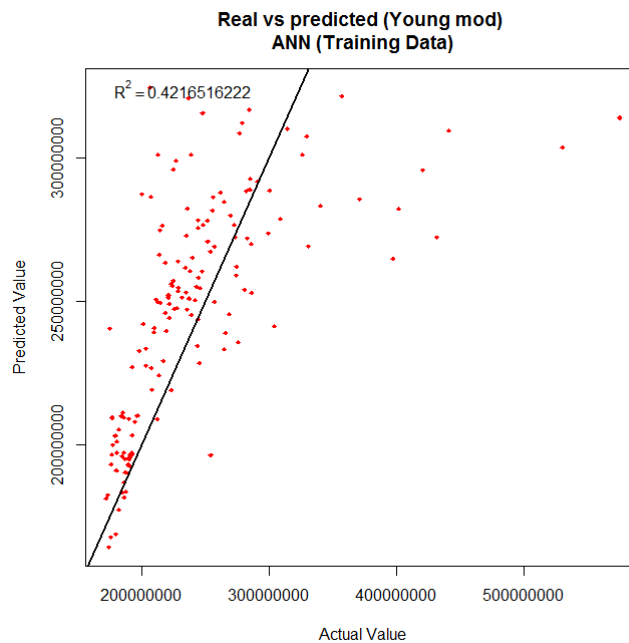
Figure 5.8. Actual versus predicted Young's modulus in the ANN training phase
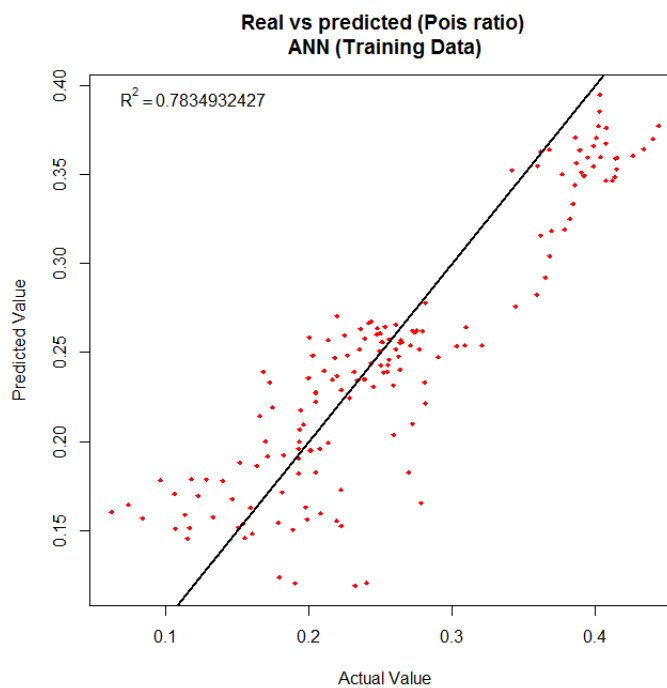
Figure 5.9. Actual versus predicted Poisson's ratio in the ANN training phase
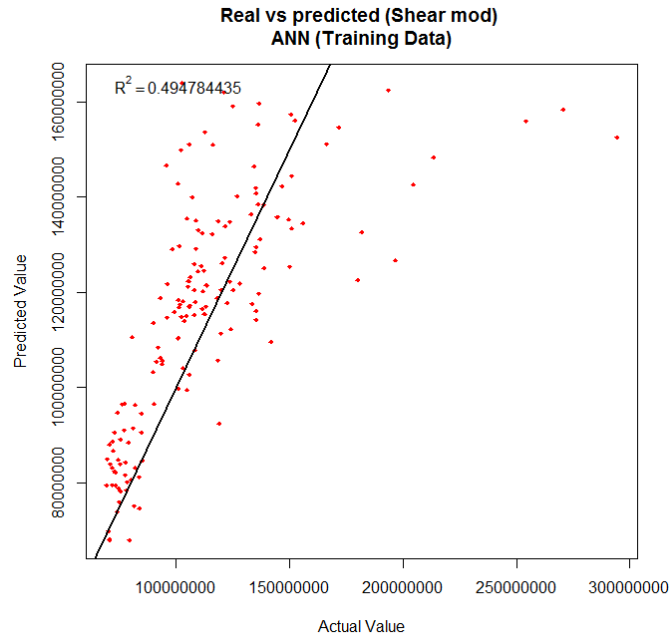
Figure 5.10. Actual versus predicted shear modulus in the ANN training phase
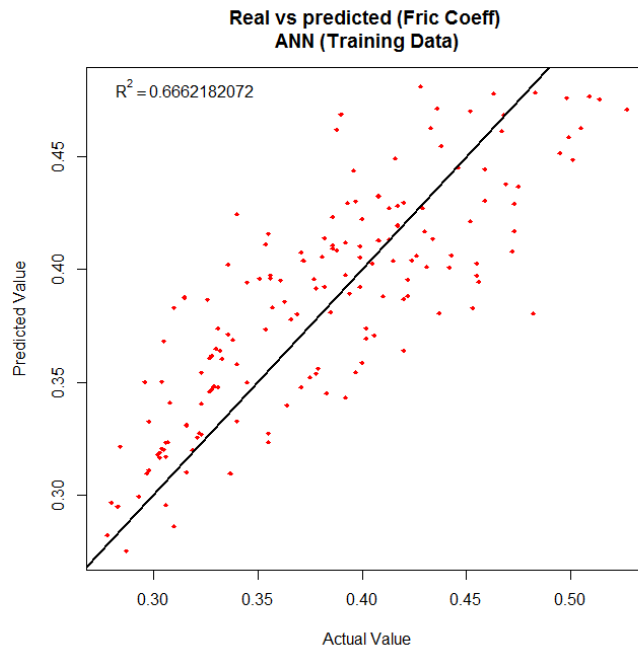
Figure 5.11. Actual versus predicted friction coefficient in the ANN training phase
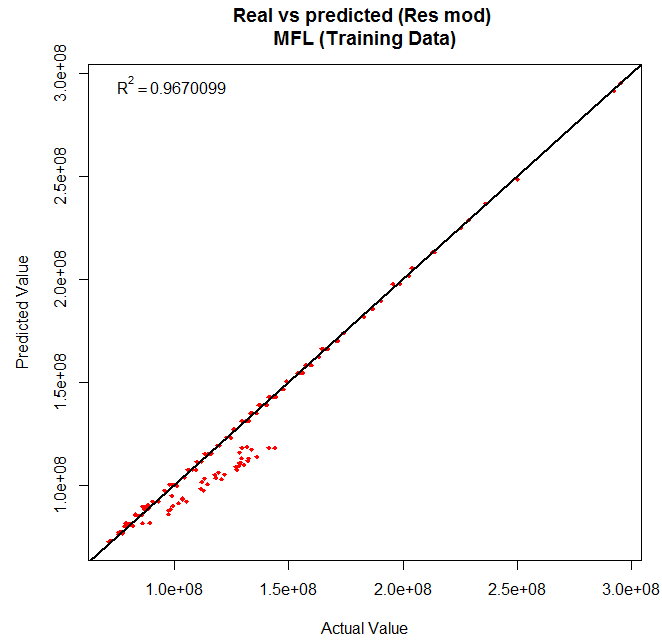
Figure 5.12. Actual versus predicted resilient modulus in the MFL training phase
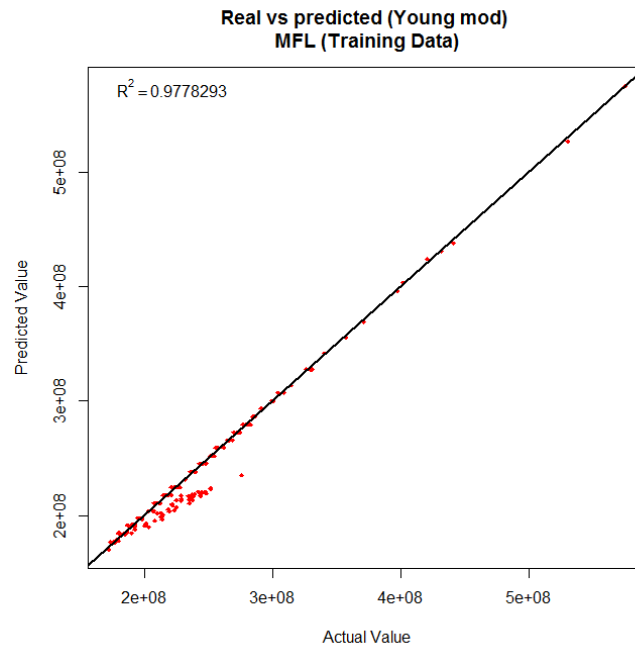
Figure 5.13. Actual versus predicted Young's modulus in the MFL training phase
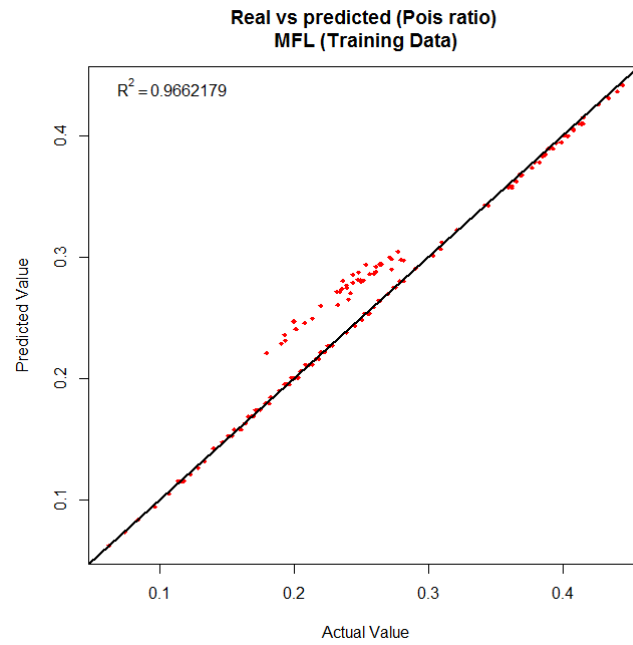
Figure 5.14. Actual versus predicted Poisson's ratio in the MFL training phase
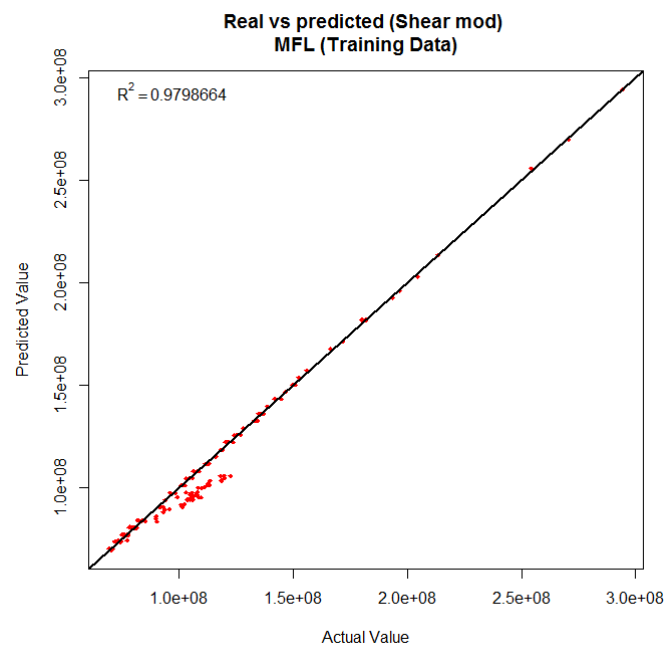
Figure 5.15. Actual versus predicted shear modulus in the MFL training phase
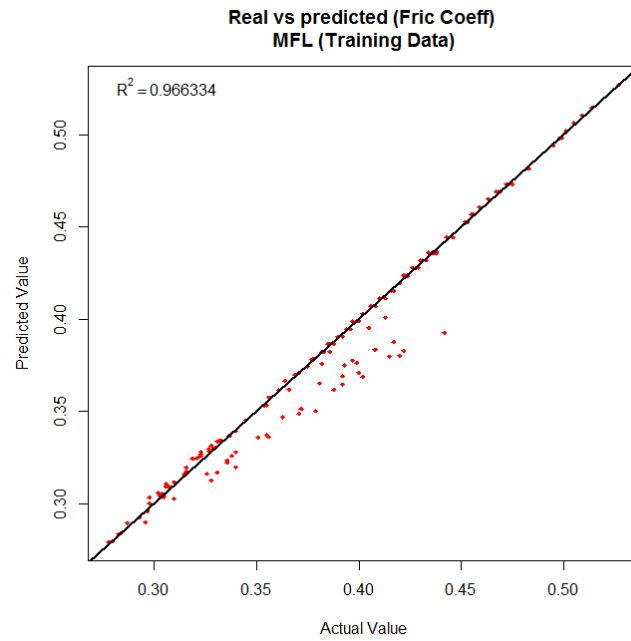
Figure 5.16. Actual versus predicted friction coefficient in the MFL training phase
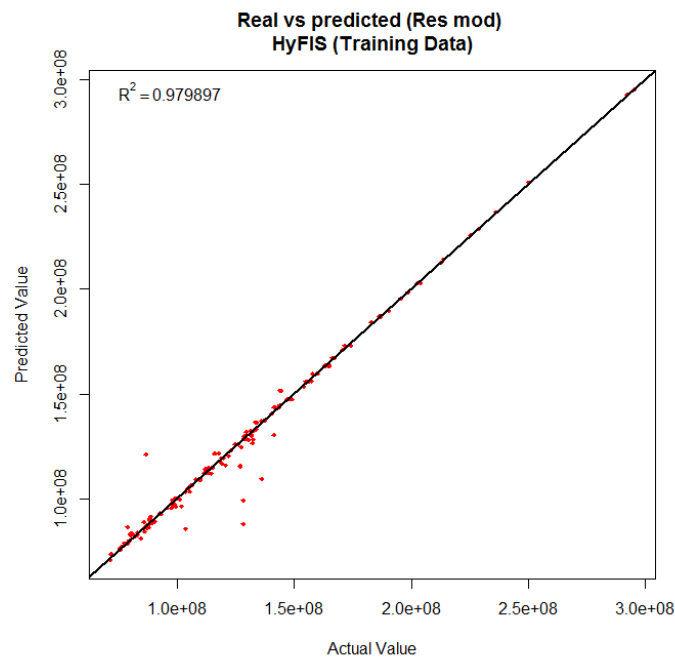
Figure 5.17. Actual versus predicted resilient modulus in the HyFIS training phase
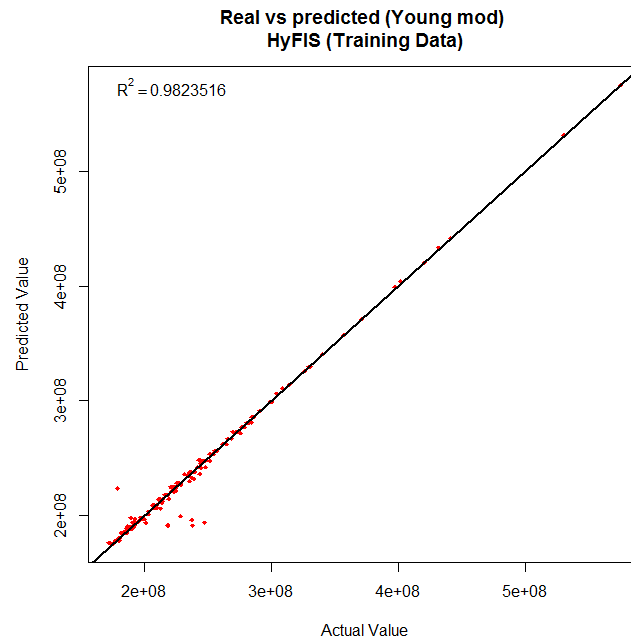
Figure 5.18. Actual versus predicted Young's modulus in the HyFIS training phase
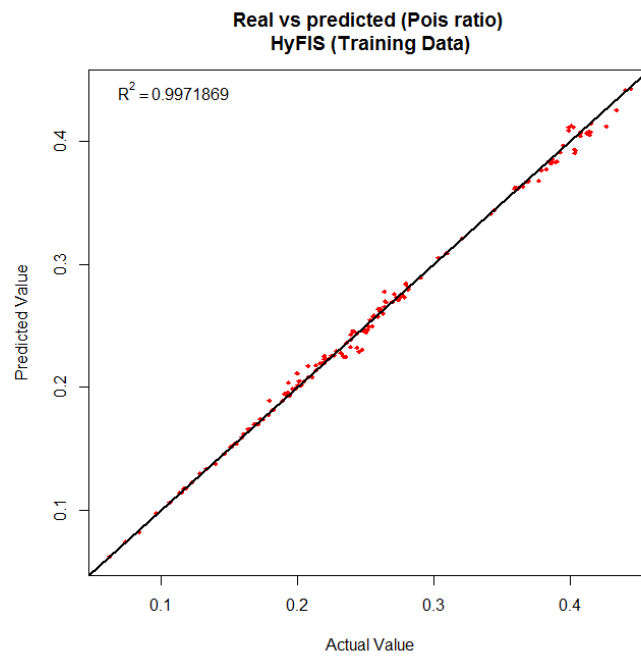
Figure 5.19. Actual versus predicted Poisson's ratio in the HyFIS training phase
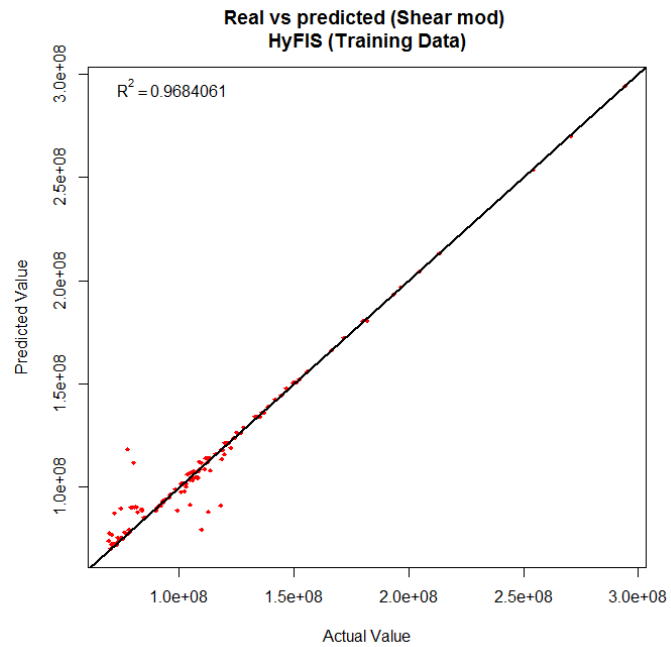
Figure 5.20. Actual versus predicted shear modulus in the HyFIS training phase
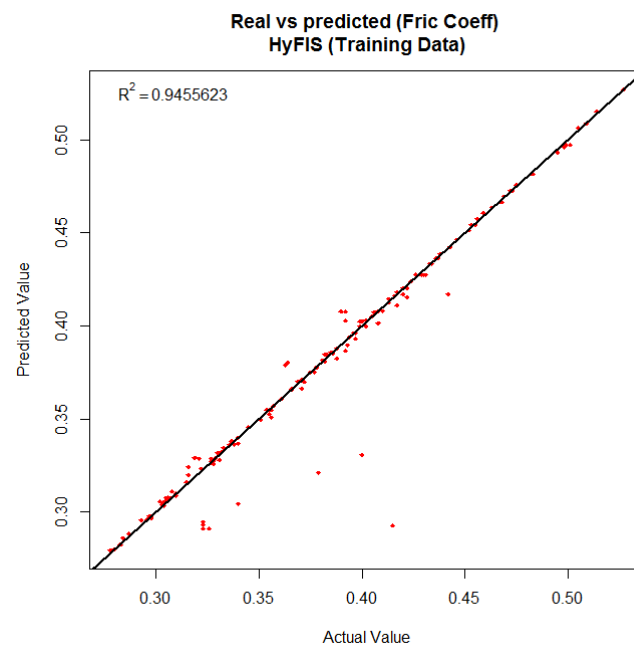
Figure 5.21. Actual versus predicted friction coefficient in the HyFIS training phase

5.4.2. Validation.   The last 39 values (twenty percent data) from the Appendix A-1 were used to test the predictive models. These models were run for many times until they gave reasonable statistical performance indicators (R^2 and RMSE). Parameters for each model explained in Section 5.5 were varied until the best possible results were obtained. R^2 values of 0.9857, 0.9717, 0.9871, 0.9703, and 0.9908 were obtained for resilient modulus, Young's modulus, Poisson's ratio, shear modulus, and friction coefficient respectively for the HyFIS method. The RMSE values of 4.98 MPa, 9.45 MPa, 0.007056, 5.16 MPa, and 0.006733 were obtained for resilient modulus, Young's modulus, Poisson's ratio, shear modulus, and friction coefficient respectively for the HyFIS method. Based on these statistical performance indicators determined for all the models, HyFIS was found to be the best predictive method. The results of models validation are presented in Section 7.3 (Figures 7.7 – 7.26).

5.5. EXPERIMENTAL DESIGN AND EXPERIMENTATION

One or more process variables are intentionally changed during an experiment to observe the effect on the output results. The design of experiments (DOE) is an effective method to plan the experiments in such a way so that the output data can be examined to achieve desired results (Sematech, 2006). DOE starts with setting the goals, and the process variables for the study. Before the actual experimentations, a DOE lays out the detailed experimental plan. In this study, the number of hidden neurons was set as a process variable for ANN model, and the number of linguistic variables as a process variable for MFL and HyFIS models.

The detailed experimental design used in this study for AI modeling is presented in Figure 5.22. The model was set up in four steps: reading the data from a CSV file, setting the training and testing datasets, training the model with inputs and corresponding outputs, and scaling the data. Then a loop was developed within the code to determine R^2 and root mean square error (RMSE) for the training dataset at different numbers of hidden neurons or linguistic variables. Once the model was able to predict the results reasonably close to the training dataset, the model was tested to predict the results of the testing dataset (AI models never saw that data before). If the results were not satisfied, the number of hidden neurons (in ANN) or linguistic variables (in MFL or in HyFIS) were changed to train the model. This process was repeated until the desirable prediction results were obtained.

The neuron is the basic component of an ANN model, and the number of hidden neurons is a major variable that affects the performance of an ANN model. To select the optimum number of hidden neurons is one of the major problems in any ANN model. Different researchers have proposed mathematical models to determine the optimum number of hidden neurons. The proposed model of Huang (2003) to determine the number of hidden neurons in a single hidden layer is given by Equation (5.2). 'N_h' presents the number of hidden neurons, the number of output neurons is presented by 'm', and 'N' presents the number of input samples. After testing a formula for the hidden number of neurons on forty different samples, Ke and Liu (2008) proposed the formula given by Equation (5.3). The number of hidden neurons is presented by 'N_h', the number of input neurons is presented by 'N_{in}', the number of input samples is presented by 'N_p', and the number of hidden layers is presented by 'L'. The proposed model of Mishra and Desai (2006) is given by Equation (5.4), in which 'N_h' and 'N_i' are the number of hidden and

input neurons, respectively. The proposed model of Trenn (2008) is given by Equation (5.5), in which 'n' and 'n_0' are the number of input and output neurons, respectively.
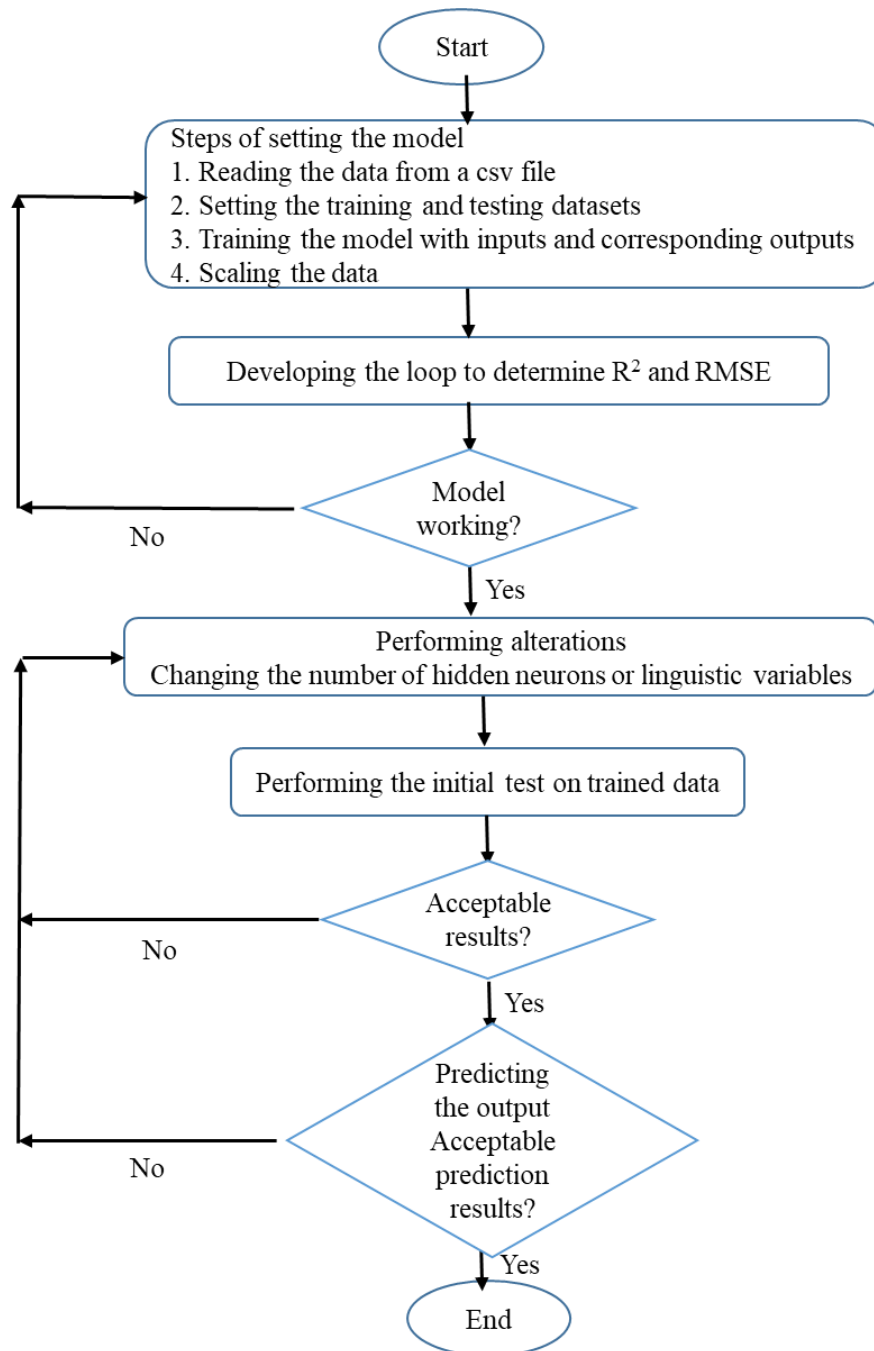
Figure 5.22. A detailed experimental design of AI modeling

$$N_h = \sqrt{(m+2)N} + 2\sqrt{N/(m+2)} \tag{5.2}$$

$$N_h = (N_{in} + \sqrt{N_p})/L \tag{5.3}$$

$$N_h = 2N_i + 1 \tag{5.4}$$

$$N_h = n + n_0 - 1/2 \tag{5.5}$$

The models presented above along with some others were used to determine the optimum number of hidden but none of them gave the satisfactory results (less error). The hit and trial method was used to determine the number of hidden neurons, which resulted in six hidden neurons. A loop was developed within the code to determine the number of hidden neurons that will produce the highest R^2 and the least error. The total number of iterations were kept constant at 500, and the error tolerance was kept constant at 0.01. The models proposed by Mishra and Desai (2006), and Trenn (2008), given in Equations (5.4) and (5.5), respectively gave close results to the hit and trial method.

In MFL and HyFIS methods, the total number of iterations were kept constant at 500, and the error tolerance was kept constant at 0.01 to be comparable with the ANN model. The number of linguistic variables is a major variable that affects the performance of fuzzy models. The number of linguistic variables was varied to get the best predictive results from these models. Loops were developed to determine the optimum number of linguistic variables. These models were run many times until the desired predictive results

were obtained. In MLR method, none of the variables was changed. The default regression analysis available in excel 2016 was used.

Once, all the predictive methods were evaluated on the same dataset, HyFIS was found to be the best method. HyFIS was further used on eight datasets (having 196 results in one dataset) and was able to predict the results quite accurately. The reason of being the best method is that the HyFIS uses a combination of both numerical data and fuzzy rules, thus exhibits the added advantage of both methods. Another advantage of HyFIS is that the fuzzy rule base is updated easily whenever new data become available (Wang and Mendel, 1992).

5.6. SUMMARY

Artificial Neural Network (ANN), Mamdani Fuzzy Logic (MFL), Hybrid neural Fuzzy Inference System (HyFIS) along with multiple linear regression (MLR) methods were used for the prediction analysis. The purpose for using multiple linear regression and different AI models was to select the best model for the prediction of formation material properties. MLR has been used extensively and is known universally because of its simple use and its ability to give prescient and illustrative outcomes. The ANN can be used in critical thinking, problem solving, and machine learning. Fuzzy systems are strong enough to handle confusing, subjective, and incorrect knowledge and data.

The purpose for using MLR and AI models is to look for the best alternative to PFC. All the AI models were developed by using the software 'R' that is used for statistical computing. A simple and systematic approach was used for verification and validation of the AI models. The results of confined compression tests performed in this study at a

density value of 2000 kg/m^3 are used to verify and validate the AI models. Based on cross-validation technique, eighty percent of data (157 values) is used to train the AI models, and twenty percent data (39 values) is used to test the AI models (Fijani et al., 2013). In this study, the number of hidden neurons was set as a process variable for ANN model and the number of linguistic variables as a process variable for MFL and HyFIS models.

Once, all the predictive methods were evaluated on the same dataset, HyFIS was found to be the best method. HyFIS was further used on eight datasets (having 196 results in one dataset) and was able to predict the results quite accurately. The reason of being the best method is that the HyFIS uses a combination of both numerical data and fuzzy rules, thus exhibits the added advantage of both methods.

6. NUMERICAL SIMULATIONS OF DIPPER FILLING

The 3D numerical simulations were performed in particle flow code (PFC) to observe the behavior of granular material flow into the shovel dipper. Virtual laboratory test simulations were done by writing FISH scripts in PFC3D software. The purpose of these simulations were to understand the behavior of material in front of a shovel dipper. This will allow engineers to select optimum strategies to maximize excavation performance. The verified and validated material properties determined in Sections 4 and 5 were used for the virtual simulations. This section covers the details of the virtual prototyping of shovel dipper-formation interaction, discrete element modeling of shovel dipper filling along with the summary.

6.1. VIRTUAL PROTOTYPING OF DIPPER-FORMATION INTERACTION

Figure 6.1 shows the complete flow diagram for virtual prototype simulation implementation in this study. The cable shovel dipper of the full scale P&H 4800-XPC by Wardeh and Frimpong (2016) was imported into Rhino 5. The full scale mining bench geometry (Table 6.1) was also created in Rhino 5 according to the general specification of 4800-XPC. The dipper, dipper door, eight teeth and the bench were imported into PFC3D. The complete shovel excavation process was then simulated using the PFC3D. The process started with defining the domain, creating the discrete particles that represent the formation, and then specifying the particle properties. The particles were allowed to settle down to achieve the equilibrium. The front and the top walls of the bench were then removed to present the real world mining bench. The model was again allowed to achieve

the equilibrium. The model was observed, and the parameters (slope angle and height) were varied until the desired parameters were close (within ±5 %) to the real values given in Table 6.1. Once the initial settlement was obtained, the model was saved for further analysis. In the next step, the dipper properties were assigned, the boundary conditions were defined, and the time step was defined to run the model. At the end of the simulation run, the dipper motion was initialized along the trajectory given by Equation (6.1). The trajectory was determined using the data from the handbook of P&H 4800-XPC (JOYGLOBAL, 2016). The data points (bench widths and bench heights) were used to develop a scatterplot in Microsoft Excel 2016, and a trend line was inserted to determine the trajectory given by Equation (6.1).
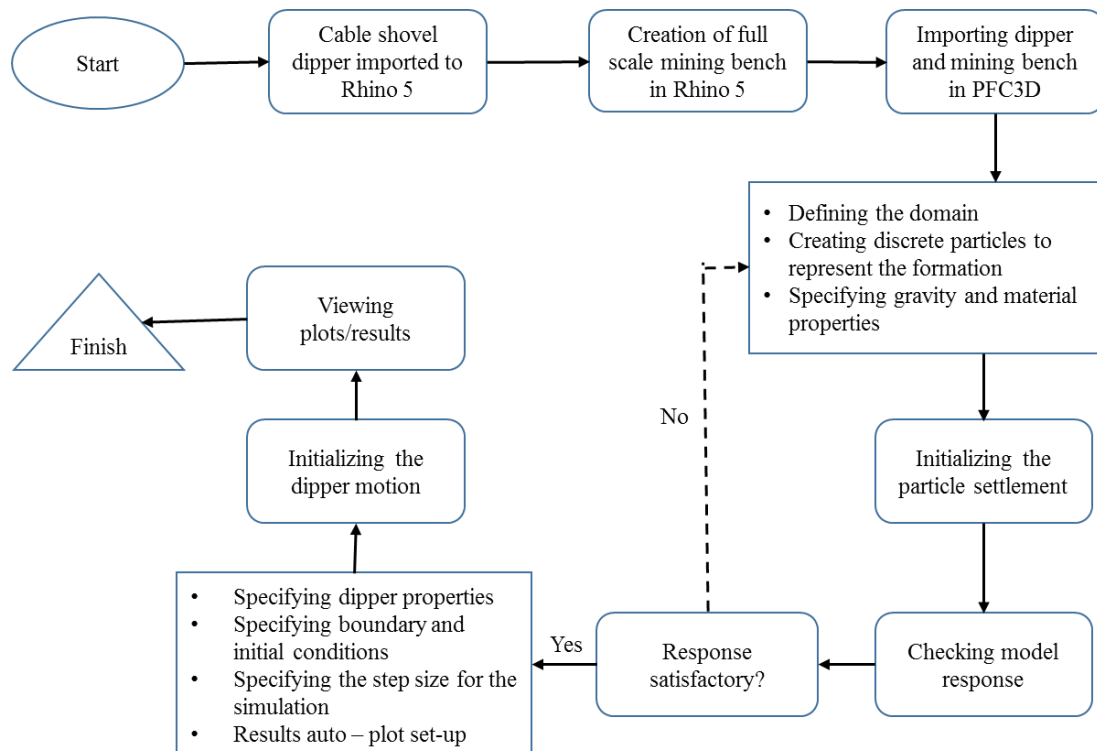
Figure 6.1. Complete flow chart illustrating the virtual prototyping in PFC3D

$$y = 5E\text{-}05x^6 - 0.0023x^5 + 0.0409x^4 - 0.3579x^3 + 1.598x^2 - 3.4702x + 1.9493 \qquad (6.1)$$

DEM analysis was carried out to observe the behavior of the discrete formation particles in front of the shovel dipper. Virtual simulations allowed the dipper filling procedure to be modeled and analyzed. A powerful computer is required to model the discrete element behavior of formations and their interactions with the shovel dipper. It was planned to vary the formation material properties to see the effect on the failure pattern in front of the dipper. However, very long computational times and occasional power outages resulted in running the base model successfully just for two times only. The time step and the cycle time of a PFC model controls the computational time (Dymond, 2007). Increasing the time step and reducing the cycle time can decrease the computational time, but the results may change drastically and the desired results may not be achieved (Dymond, 2007).

The time required to complete one cycle of a DEM is known as the cycle time. According to Dymond (2007), the cycle time can be decreased by decreasing the number of balls, clumps, and walls. Because the forces/moments are updated at each time step, the number of calculations in a cycle are decreased. A wide size distribution is another important factor that can reduce the cycle time. In this study, the spherical balls having radius range of 0.21 – 0.27 mm presented the real world formation particles. Majeed and Bakar (2016) reported the average particle size of Sakesar limestone as 0.485 mm. The other strategy for decreasing the computational time is to increase the time step. The time step in a linear contact model depends upon the size, density, and stiffness of the particles (Dymond, 2007). The calibration of these parameters values was performed in Section 5.

6.2. DISCRETE ELEMENT MODELING OF SHOVEL DIPPER FILLING

DEM was used to simulate, study and analyze the cable shovel excavation phase. Contacts between the bodies are essential components in DEM analysis. The linear model was used to model particle – particle and particle – dipper contacts. A detailed comprehension of the formation failure process is critical towards enhancing the whole digging cycle of the shovel dipper. A numerical model was developed in PFC3D to simulate the filling of the shovel dipper. Table 6.1 contains the virtual model having the validated material properties. A closed material bin was generated in Rhino 5 to serve as a mining bench. The shovel dipper was placed at the toe of the bench to present the real world scenario. The dipper and material bin were imported into the PFC3D model. The balls were generated using the properties given in Table 6.1, and the linear contact model properties were assigned, and the model was allowed to achieve equilibrium.

Table 6.1. Properties assigned during the shovel dipper filling

Properties	Symbols	Values
Balls radius	rad	0.21 – 0.27 mm
Density	dens	2000 kg/m^3
Porosity	poros	0.3
Young's modulus	emod	1.0e6 Pa
Stiffness ratio	kratio	1.0
Friction coefficient	fric	0.18
Damping	damp	0.7
Bench height	h	20 m
Bench width	w	16 m
Bench slope angle	θ	47.5^0

The dipper motion was initialized along the trajectory given by Equation (6.1), by assigning a fixed rotational speed. The snapshots were taken at different time steps to present the dipper movement through the formation particles as illustrated in Figure 6.2.
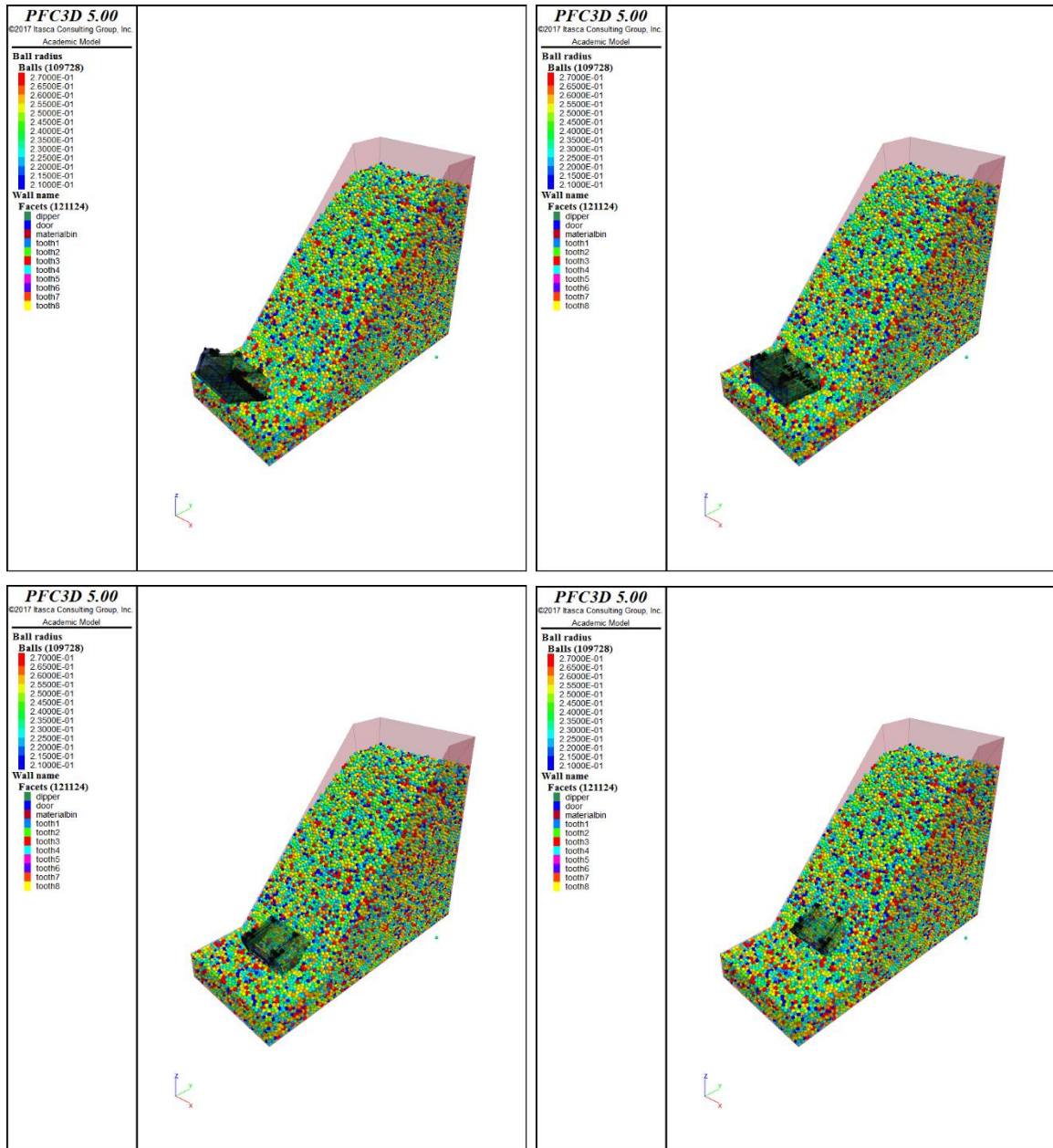
Figure 6.2. Simulation of shovel dipper filling using full-scale bench height
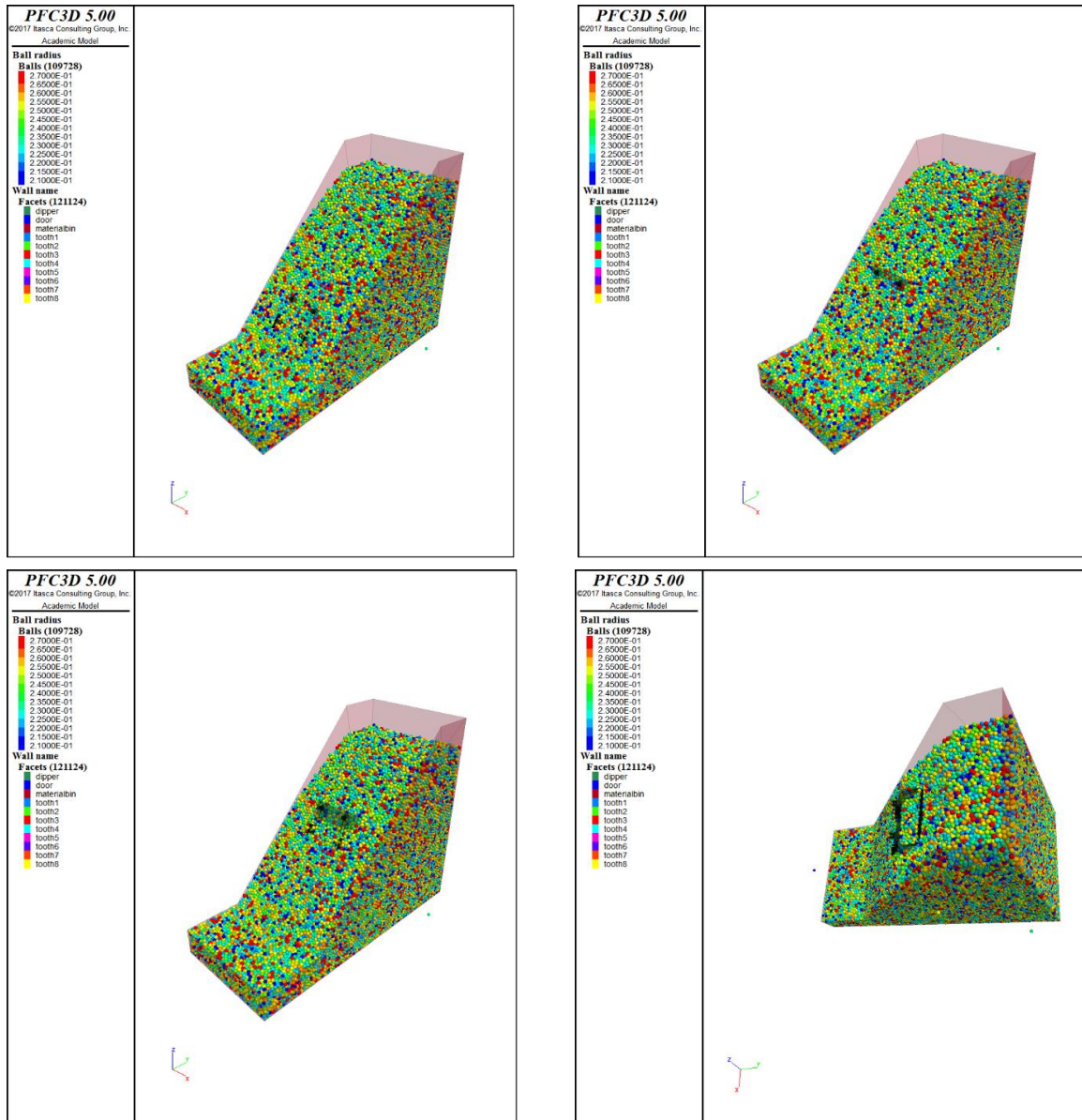
Figure 6.2. Simulation of shovel dipper filling using full-scale bench height (cont.)

For comparison purposes and to reduce the computational time, a smaller bench height of 14 m was also developed in Figure 6.3, while keeping the same properties of the formation material and the shovel dipper. The DEM was able to determine the filling procedure of the shovel dipper in both cases with no significance difference.
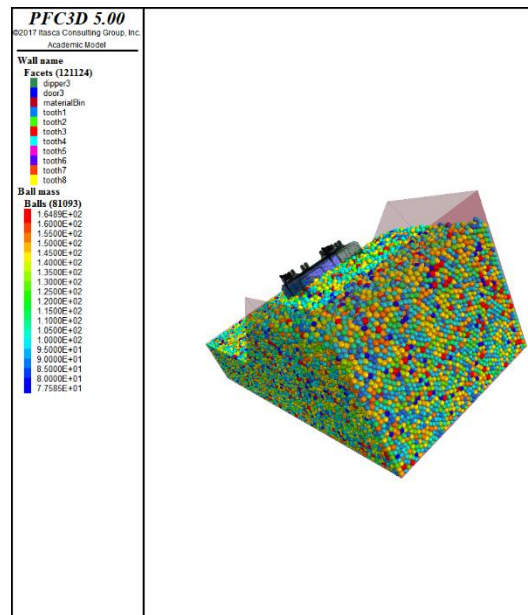
Figure 6.3. Simulation of shovel dipper filling using a smaller bench height

The movement of the formation material particles is defined by the friction coefficient of the particles. A small value of friction coefficient of particles can result in easy movement of particles. Also, the dipper can easily penetrate into the formation particles that offer small resistance. This is because of the low degree of compaction. In the numerical simulation, the formation particles were generated without any compaction. This low degree of compaction resulted in reduced interlocking of particles and reduced frictional resistance. This is one of the limitation of this numerical simulation as the material generated is not a true representative of the real world mining bench.

The purpose of doing these numerical simulations was to observe the behavior of granular material flow into the shovel dipper. The numerical model was verified and validated by using the data from the handbook of P&H 4800-XPC (JOYGLOBAL, 2016) for the shovel dipper and bench dimensions. The formation material is generated by using

the calibrated data from Sections 4 and 5. The data for shovel dipper, bench dimensions, and for material properties is already given in Table 6.1. It was planned to vary the formation material properties to see the effect on the material flow in front of the dipper. However, very long computational times and occasional power outages resulted in running the base model successfully just for two times only. Based on the two completed simulations, the dipper was able to move through the rock pile along a specified trajectory. A small value of friction coefficient resulted in easy movement of particles.

The simple linear contact model was used in this study which has its own limitations. More realistic contact model (rolling friction and rolling resistance) proposed by Ai et al. (2011) can be used to achieve better results. It is suggested to vary the formation material properties to see the effect on the failure pattern in front of the dipper. The 3D model developed will provide a base for further analysis. In future studies, the forces will be determined that are involved during the shovel-formation interactions.

6.3. SUMMARY

The 3D numerical simulations were performed in particle flow code (PFC) to observe the behavior of granular material flow into the shovel dipper. Virtual laboratory test simulations were done by writing FISH scripts in PFC3D software. DEM was used to simulate, study and analyze the cable shovel excavation phase. Contacts between the bodies are essential components in DEM analysis. The linear model is used to model particle – particle and particle – dipper contacts. Virtual simulations allowed the dipper filling procedure to be modeled and analyzed.

7. RESULTS AND DISCUSSIONS

This section presents the detailed results and analysis of the numerical experimentation performed in this study. Unconfined compression, direct tension, and indirect Brazilian tests, conducted on different rock formations were performed using particle flow code (PFC3D). About 1800 confined compression tests (9 datasets) were also performed using PFC3D. The results of nine datasets are presented in Appendices A-1 to A-9. These results were used for artificial intelligence (AI) modeling in Section 5, and are presented and discussed in detail. By using the calibrated properties, obtained in Chapters 4 and 5, DEM simulations of cable shovel dipper filling were performed in Chapter 6, and is discussed in detail. A summary of all the results is presented at the end.

7.1. RESULTS OF PARTICLE FLOW CODE EXPERIMENTS

The unconfined compression, direct tension, Brazilian, and confined compression tests were conducted in PFC3D. The samples were originally created in physical vessels by assigning the micro properties of Sakesar and Namal limestones given in Tables 4.5 and 4.6, respectively. After achieving equilibrium, these samples were removed from the vessels. They were then loaded by surface grains in direct tension tests, and by walls in the Brazilian and compression tests. The radial walls do not touch the sample in the unconfined test. The samples were pulled apart in the opposite directions in direct tension tests by assigning specified velocities to the surface grains in the axial direction. The axial walls in Brazilian test load the cylindrical or spherical shaped samples. The details of the experiments have already been discussed in Section 4.5.

To validate the PFC model to cover most of the rock types, the results of twenty-four rock samples were used from Rehman et al. (2013)[1] that were performed on Sakesar and Namal limestone formations. The results from rock mechanics tests on twelve different rock formations were also selected from Majeed and Bakar (2016).

7.1.1. Unconfined Compression Tests. These tests started with developing the un-bonded samples of Sakesar and Namal limestones in PFC according to the ASTM-D4543 (2008) standards and ISRM (1979a, b). Then the micro properties were assigned and the linear parallel contact bond model was assigned as well. Porosity and particle size values were adopted from Majeed and Bakar (2016). To minimize the computational cost, different particle size ranges were used. A particle size range of 3-5 mm with $D_{max}/D_{min} = 1.67$ gave reasonably good results, and are presented in Table 7.1.

From Table 7.1, the PFC UCS values ranged from 85 to 148 MPa for Sakesar limestone, whereas the UCS values ranged from 85 to 116 MPa for Namal limestone. The experiments were also replicated in PFC for twelve rock formations selected from Majeed and Bakar (2016), and the results are presented in Table 7.2. The lab UCS values ranged from 13.525 to 231.462 MPa, whereas the PFC UCS values ranged from 12 to 180 MPa. The comparison of experimental versus simulated values in Tables 7.1 and 7.2 were plotted, and are shown in Figures 7.1 and 7.2, respectively.

The numerical errors ranged from 10 to 19 % in Table 7.1. The sample N8 has the minimum error, while sample S3 has the maximum error. The numerical errors ranged from 6 to 22 % in Table 7.2. The 'Dolomite-1' sample has the minimum error while

---

[1] The permission to use their laboratory experimental data has been received for the calibration of numerical models developed in this study. The permission email is presented in Appendix B.

Table 7.1. Lab and PFC UCS values and associated errors

Sample	Lab. UCS[2] (MPa)	PFC UCS (MPa)	Error (%)
S1	111.44	96	-13.85
S2	124.26	105	-15.50
S3	140.29	114	-18.74
S4	117.58	100	-14.95
S5	155.61	132	-15.17
S6	98.4	85	-13.62
S7	136.8	118	-13.74
S8	120.04	105	-12.53
S9	155.88	136	-12.75
S10	114.79	101	-12.01
S11	124.26	107	-13.89
S12	147.42	129	-12.49
S13	167.42	148	-11.60
N1	127.94	113	-11.68
N2	113.62	101	-11.11
N3	125.19	111	-11.33
N4	102.92	90	-12.55
N5	98.212	85	-13.45
N7	107.67	96	-10.84
N8	121.73	109	-10.46
N9	103.68	91	-12.23
N10	122.84	107	-12.89
N11	131.53	116	-11.81
N12	113.43	99	-12.72

---

[2] This column data is used from Rehman et al. (2013) for the calibration of numerical results

Table 7.2. Lab and PFC UCS values and associated errors of selected rocks

Sample	Lab. UCS[3] (MPa)	PFC UCS (MPa)	Error (%)
Andesite	231.462	180	-22.23
Dolerite-1	214.5	172	-19.81
Granite-3	77.614	70	-9.81
Migmatite	56.76	52	-8.39
Granitic gneisse-1	69.22	62	-10.43
Phyllite	54.33	50	-7.97
Quartzite-1	56.39	50	-11.33
Siltstone-1	49.3	44	-10.75
Sandstone-1	39.8	36	-9.55
Chamositic siderite	51.715	48	-7.18
Dolomite-1	61.84	58	-6.21
Rock gypsum	13.525	12	-11.28

'Andesite' sample has the maximum error. Table 7.1 has less variability compared to the results in Table 7.2. The reason is that the results of only two rock formations (Sakesar and Namal limestone) are presented in Table 7.1, while Table 7.2 covers a variety of rock formations whose properties also varied accordingly. The percentage errors in Tables 7.1 and 7.2, and Figures 7.1 and 7.2 show that the PFC model underestimated the results. This underestimation is acceptable, because it will allow engineers to develop a more conservative design after the feasibility studies.

---

[3] This column data is used from Majeed and Bakar (2016) for the calibration of numerical results
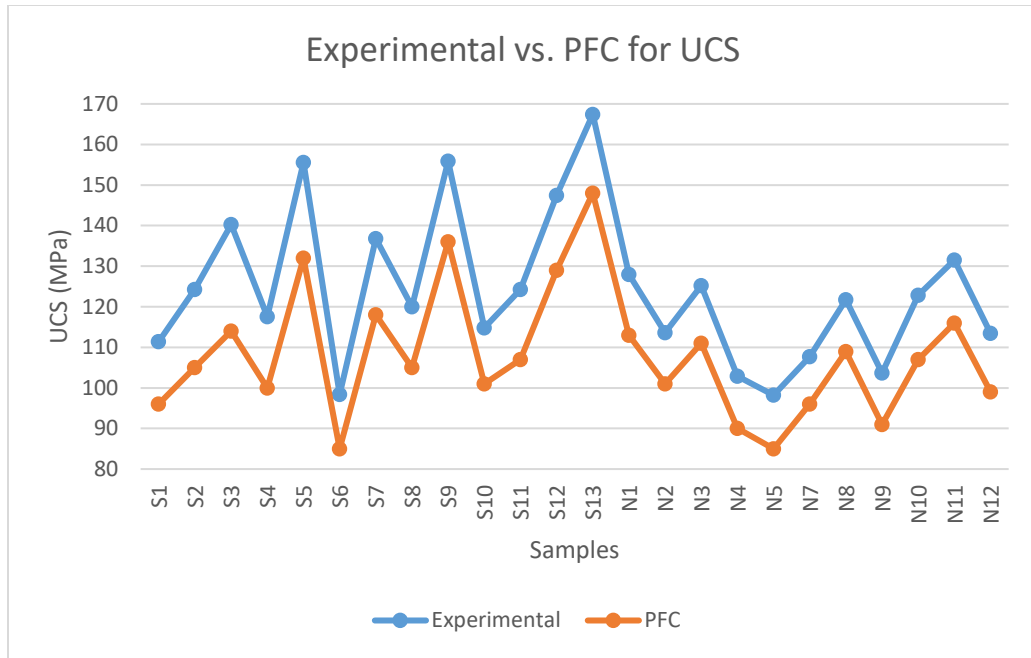
Figure 7.1. Experimental versus simulated values of UCS for the Sakesar and Namal limestone samples. The experimental data is used from Rehman et al. (2013) for the calibration of numerical results
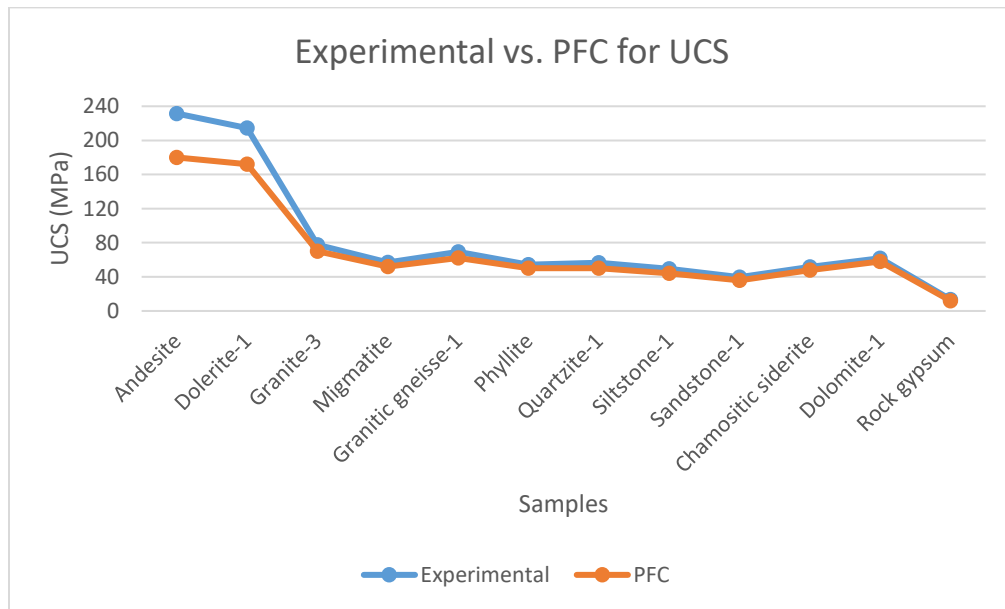
Figure 7.2. Experimental versus simulated values of UCS for the selected rock samples The experimental data is used from Majeed and Bakar (2016) for the calibration of numerical results

7.1.2. Direct Tension Tests.   A direct tensile strength test is difficult to perform in a laboratory, but the test is possible to perform by using numerical models. These tests started in exact same way as for unconfined compression tests. The only difference was the recognition of a thin layer of surface grains (grip grains). This layer was used to pull the sample surfaces apart from each other. A particle size range of 3-5 mm with D_{max}/D_{min} = 1.67 was used, similar to the unconfined compression tests. Similarly, thirty-six PFC experiments were performed on exactly the same rock samples and the results are presented in Tables 7.3 and 7.4. The PFC tensile strength values range from 6.6 to 9.4 MPa for Sakesar limestone, range from 7.4 to 9.2 MPa for Namal limestone, and range from 2.4 to 17 MPa for twelve different rock formations that were selected from Majeed and Bakar (2016).

The numerical errors ranged from 23 to 64 % in Table 7.3. The sample S8 has the minimum error, while sample S2 has the maximum error. The numerical errors ranged from 21 to 80 % in Table 7.4. The 'Andesite' sample has the minimum error while the 'Rock gypsum' sample has the maximum error. Table 7.3 has less variability compared to the results in Table 7.4, similar to the trend shown for UCS results because of the same reason. In the case of tensile strength results, larger errors were found. A possible reason is the use of balls to represent angular particles that don't have enough resistance to rotation. The other possibility is that the thin layer of grip grains don't have good bond with rest of the sample. It is well known that the tensile strength experiments are difficult to perform in laboratory. Similarly, the numerical models have their own limitations. The PFC tensile strength tests results were compared with the laboratory Brazilian tensile strength results of Rehman et al. (2013). Although these tests are reported to be almost

Table 7.3. Lab and PFC tensile strength values and associated errors

Sample	Lab. BTS[4] (MPa)	PFC TS (MPa)	Error (%)
S1	5.63	8.2	45.65
S2	5.36	8.8	64.18
S3	5.779	9.2	59.20
S4	4.93	7.6	54.16
S5	6.322	9.4	48.69
S6	4.975	6.6	32.66
S7	5.87	8	36.29
S8	6.32	7.8	23.42
S9	6.45	8.4	30.23
S10	4.975	7.4	48.74
S11	5.65	7.6	34.51
S12	5.486	8.2	49.47
S13	6.31	8.4	33.12
N1	6.32	8	26.58
N2	5.54	7.8	40.79
N3	6.272	8.6	37.12
N4	5.624	8.4	49.36
N5	5.72	8.2	43.36
N7	5.72	7.8	36.36
N8	5.956	7.6	27.60
N9	5.137	7.6	47.95
N10	6.78	9.2	35.69
N11	5.96	8.2	37.58
N12	5.54	7.4	33.57

---

[4] This column data is used from Rehman et al. (2013) for the calibration of numerical results

Table 7.4. Lab and PFC tensile strength values and associated errors of selected rocks

Sample	Lab. BTS[5] (MPa)	PFC TS (MPa)	Error (%)
Andesite	14.065	17	20.87
Dolerite-1	6.761	10.2	50.87
Granite-3	3.69	5.2	40.92
Migmatite	2.27	3.8	67.40
Granitic gneisse-1	4.07	6	47.42
Phyllite	4.1	6.2	51.22
Quartzite-1	4.35	6.4	47.13
Siltstone-1	7.36	9.2	25.00
Sandstone-1	1.846	3	62.51
Chamositic siderite	8.08	10.4	28.71
Dolomite-1	6.54	8.8	34.56
Rock gypsum	1.332	2.4	80.18

equivalent to each other, this might be another possible reason of larger errors. Itasca (2018) reported that the compressive to tensile strength ratio is expected to be in between 10 and 20. The PFC compressive strength and PFC tensile strength ratio values from Tables 7.1 to 7.4 fall within the range of 10 and 20.

The comparison of experimental versus simulated values in Tables 7.3 and 7.4 were plotted and are shown in Figures 7.3 and 7.4, respectively. The percentage errors in Tables 7.3 and 7.4 and Figures 7.3 and 7.4 show that the PFC model overestimated the results of tensile strength values.

---

[5] This column data is used from Majeed and Bakar (2016) for the calibration of numerical results
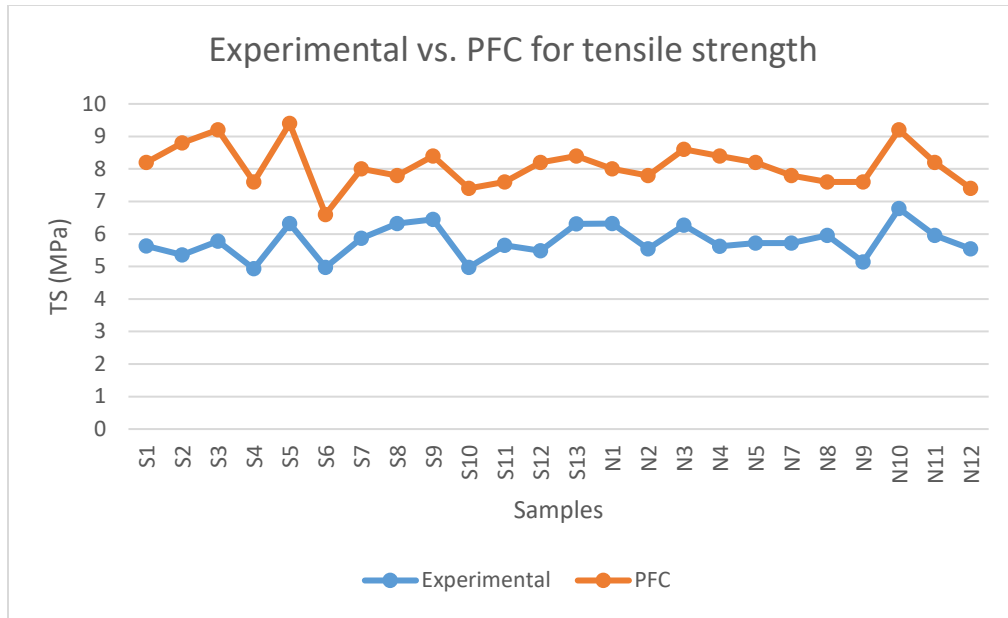
Figure 7.3. Experimental versus simulated values of tensile strength for the Sakesar and Namal limestone samples. The experimental data is used from Rehman et al. (2013) for the calibration of numerical results
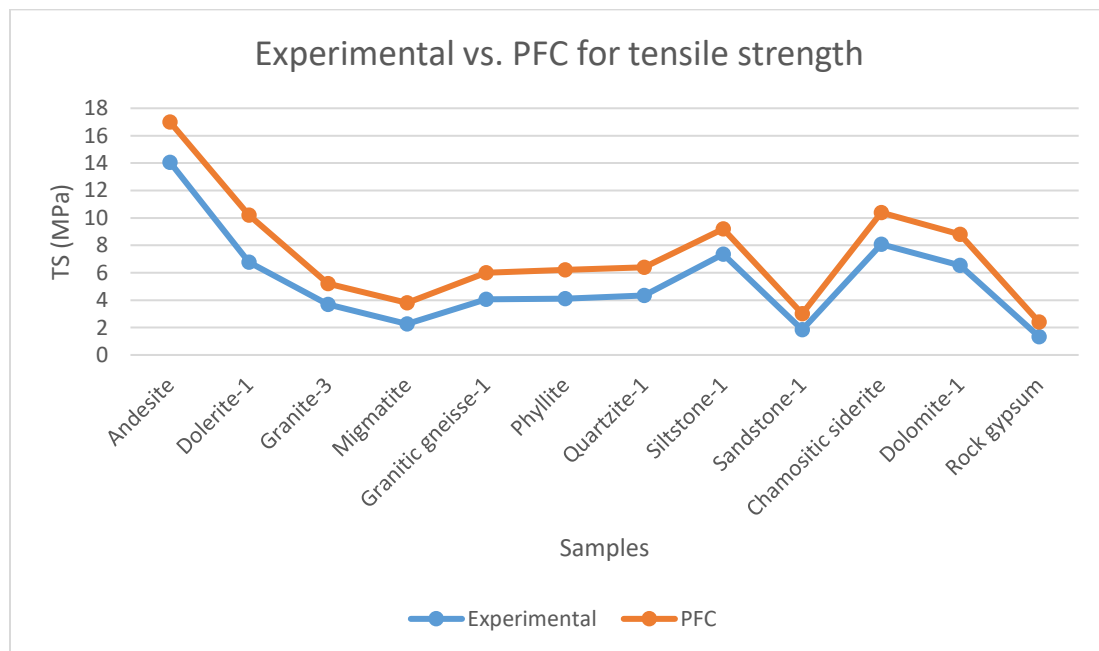
Figure 7.4. Experimental versus simulated values of tensile strength for the selected samples. The experimental data is used from Majeed and Bakar (2016) for the calibration of numerical results

7.1.3. Brazilian Tests. Thirty-six PFC single stage experiments were conducted according to the ASTM-D3967 (2008) standards and ISRM (1978a, b). New PFC samples were prepared, with thickness to diameter ratio of 0.5 as per the above mentioned standards. After assigning the properties, the samples were loaded diametrically by the loading platens, created in the PFC model. At the end of each experiment, failure load was noted and the Brazilian tensile strength values were determined and are presented in Tables 7.5 and 7.6. The PFC Brazilian tensile strength values ranged from 5.24 to 6.81 MPa for Sakesar limestone; from 5.59 to 7.25 MPa for Namal limestone; and from 1.46 to 15.14 MPa for twelve different rock formations that were selected from Majeed and Bakar (2016).

The numerical errors ranged from 5 to 10 % in Table 7.5. The sample N1 has the minimum error while the sample S7 has the maximum error. The numerical errors ranged from 5 to 10 % in Table 7.6. The 'Granitic gneisse-1' sample has the minimum error while the 'Dolerite-1' sample has the maximum error. Least variability has been seen in the Brazilian tensile strength results (Tables 7.5 and 7.6). It has been found that the compaction of the samples has a huge impact on the results. Higher compactions of PFC samples result in the samples to be close to the real world rock samples. The comparison of experimental vs simulated values in Tables 7.5 and 7.6 were plotted and are shown in Figures 7.5 and 7.6, respectively.

In this study, it was found that the compaction plays a vital role in these rock mechanics tests. It was also found that the particle size plays an important role on the computational cost, as well as on the numerical results. Different particle size ranges were tried and a particle size range of 3-5 mm with $D_{max}/D_{min} = 1.67$ gave reasonable results.

Table 7.5. Lab and PFC Brazilian tensile strengths and associated errors

Sample	Lab. BTS[6] (MPa)	PFC BTS (MPa)	Error (%)
S1	5.63	5.94	5.51
S2	5.36	5.68	5.97
S3	5.779	6.11	5.73
S4	4.93	5.33	8.11
S5	6.322	6.72	6.30
S6	4.975	5.24	5.33
S7	5.87	6.46	10.05
S8	6.32	6.68	5.70
S9	6.45	6.81	5.58
S10	4.975	5.41	8.74
S11	5.65	6.03	6.73
S12	5.486	5.94	8.28
S13	6.31	6.64	5.23
N1	6.32	6.64	5.06
N2	5.54	5.94	7.22
N3	6.272	6.64	5.87
N4	5.624	6.03	7.22
N5	5.72	6.2	8.39
N7	5.72	6.2	8.39
N8	5.956	6.38	7.12
N9	5.137	5.59	8.82
N10	6.78	7.25	6.93
N11	5.96	6.38	7.05
N12	5.54	5.85	5.60

---

[6] This column data is used from Rehman et al. (2013) for the calibration of numerical results

Table 7.6. Lab and PFC Brazilian tensile strengths and associated errors of selected rocks

Sample	Lab. BTS[7] (MPa)	PFC BTS (MPa)	Error (%)
Andesite	14.065	15.14	7.64
Dolerite-1	6.761	7.42	9.75
Granite-3	3.69	4.03	9.21
Migmatite	2.27	2.46	8.37
Granitic gneisse-1	4.07	4.28	5.16
Phyllite	4.1	4.36	6.34
Quartzite-1	4.35	4.62	6.21
Siltstone-1	7.36	7.78	5.71
Sandstone-1	1.846	1.98	7.26
Chamositic siderite	8.08	8.6	6.44
Dolomite-1	6.54	6.98	6.73
Rock gypsum	1.332	1.46	9.61

The effect of density was found to be very small. In an earlier study carried on Lac du Bonnet granite, Potyondy and Cundall (2004) reported that their model gave reasonable results for unconfined compression tests, and overestimated the Brazilian tensile strength by 3 times. In this study, the errors were reduced to a range between 6 and 22 % for UCS, obtained higher errors for tensile strength tests in a range between 21 and 80 %, and obtained most accurate results for Brazilian tensile strength in a range between 5 and 10 %. The reason for these better results is due to the fact that the samples were prepared according to the ASTM and ISRM standards.

---

[7] This column data is used from Majeed and Bakar (2016) for the calibration of numerical results
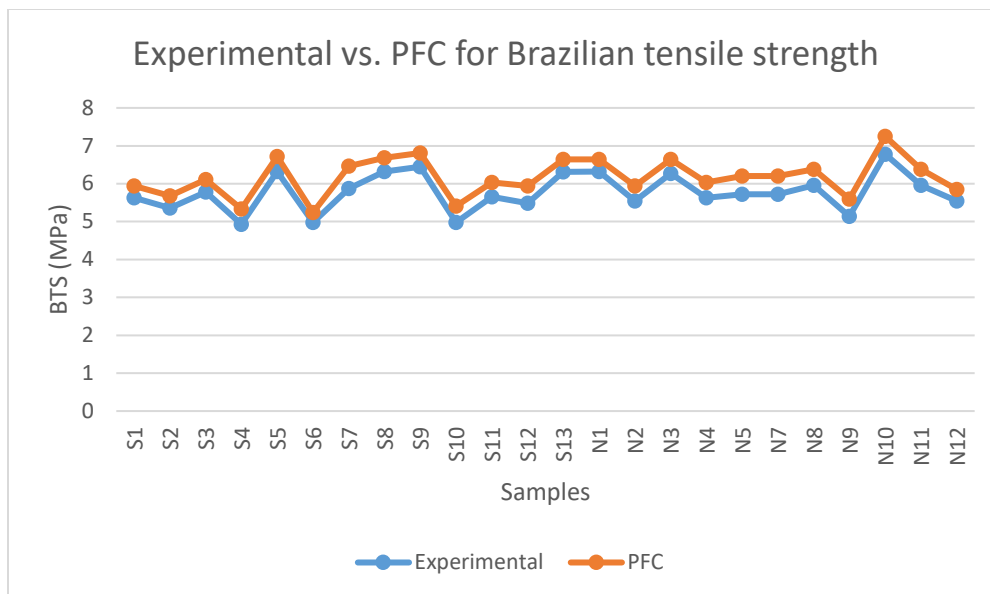
Figure 7.5. Experimental versus simulated Brazilian tensile strength for the Sakesar and Namal limestone samples. The experimental data is used from Rehman et al. (2013) for the calibration of numerical results
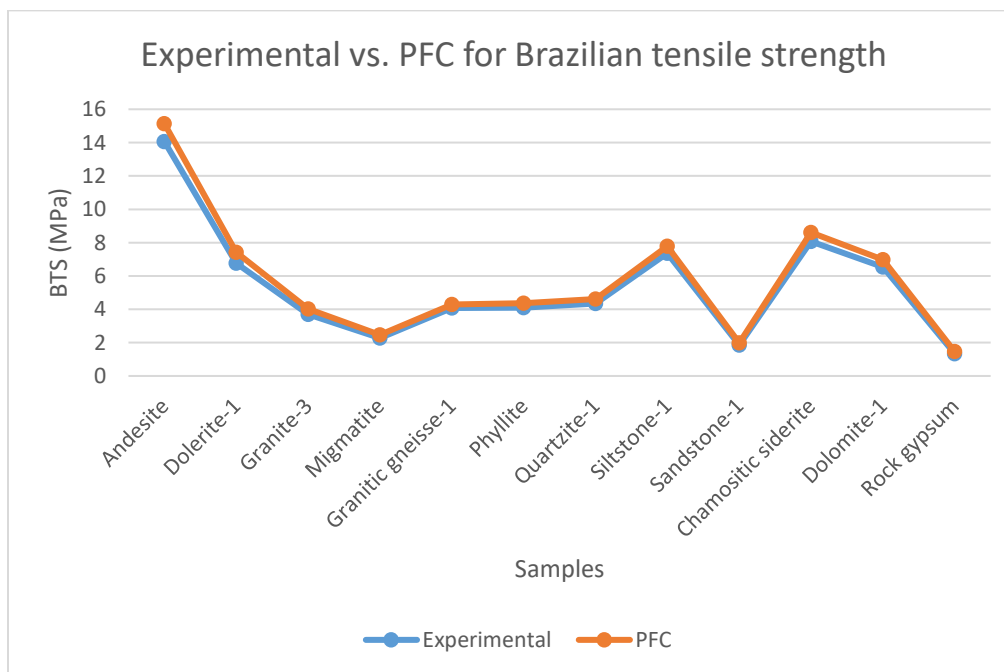
Figure 7.6. Experimental versus simulated Brazilian tensile strength for the selected rock samples. The experimental data is used from Majeed and Bakar (2016) for the calibration of numerical results

7.1.4. Confined Compression Tests. About 1,800 confined compression tests were performed in PFC, using the linear contact model of Potyondy and Cundall (2004). The basic purpose of these tests was to look for an alternative to PFC experiments. PFC, being a discrete element code takes a lot of time to complete the numerical tests. Tests were performed on materials with densities ranging from 1800 to 3000 kg/m^3. One hundred and ninety-six confined compression tests were performed, each on materials with density values of 1800, 1900, 2000, 2200, 2400, 2600, 2700, 2800, and 3000 kg/m^3. All the tests were conducted in polyaxial vessels (76 x 38 x 38 mm^3) in three loading stages, at a confining pressure (P_c) of one MPa, and a strain rate of 0.1 s^{-1}, and are presented in Appendix A (Table A-1 to Table A-9)

Three parameters including effective modulus (E*), normal-to-shear stiffness ratio (k*), and friction coefficient (μ) were varied to determine resilient modulus, Young's modulus, Poisson's ratio, shear modulus, and friction coefficient. These parameters are calibrated and validated using triaxial test data from PFC FISHTank (or fistPkg) which is developed and maintained by Itasca. FISHTank provides four well-defined materials and a user-defined material that can be used for practical applications and scientific inquiries (Itasca, 2017). Initial results were also calibrated using the results of Abdulhadi and Barghouthi (2012), Buchanan (2007), Coetzee and Els (2009a), Coetzee and Els (2009b), and Potyondy and Cundall (2004).

The results of a confined compression test performed on a PFC sample with a density value of 2000 kg/m^3 are represented in Appendix A (Table A.3). These results were used for predictive analysis in Section 5. The AI modeling results are presented in the next subsection.

7.2. RESULTS OF ARTIFICIAL INTELLIGENCE MODELING

Artificial intelligence models including Artificial Neural Network (ANN), Mamdani Fuzzy Logic (MFL), and Hybrid neural Fuzzy Inference System (HyFIS) were used for the predictive analysis in Section 5. The multiple linear regression (MLR) method, being a common method, was also used for the predictive analysis. The results of confined compression tests (in Appendix A) were used as input data for the predictive analysis. Based on cross validation, eighty percent of data was used to train the AI models and twenty percent data was used to test the AI models (Fijani et al., 2013). The purpose for using the MLR method and other AI models was to select the best model that can serve as an alternative to PFC experiments.

7.2.1. Multiple Linear Regression. Multiple linear regression method was used to predict the formation material properties. The results were plotted and are presented in Figures 7.7-7.11. The actual values in these figures are representing the results obtained from PFC in Appendix A. For the purpose of comparison with AI models, twenty percent of the data was used for prediction shown in Figures 7.7-7.11. The coefficient of multiple determination (R^2) and the root mean square errors (RMSE) are also presented. In general, the higher the value of R^2, the better is the prediction but it is not correct all the times. R^2 values of 0.0821, 0.0289, 0.0452, 0.0274, and 0.2466 were obtained for resilient modulus, Young's modulus, Poisson's ratio, shear modulus, and friction coefficient, respectively.

The RMSE values of 38.69 MPa, 58.13 MPa, 0.082067, 32.78 MPa, and 0.054912 were also obtained for resilient modulus, Young's modulus, Poisson's ratio, shear modulus, and friction coefficient, respectively. Overall, poor correlations were obtained, and thus the MLR method was not accurate in predicting the results in this study.
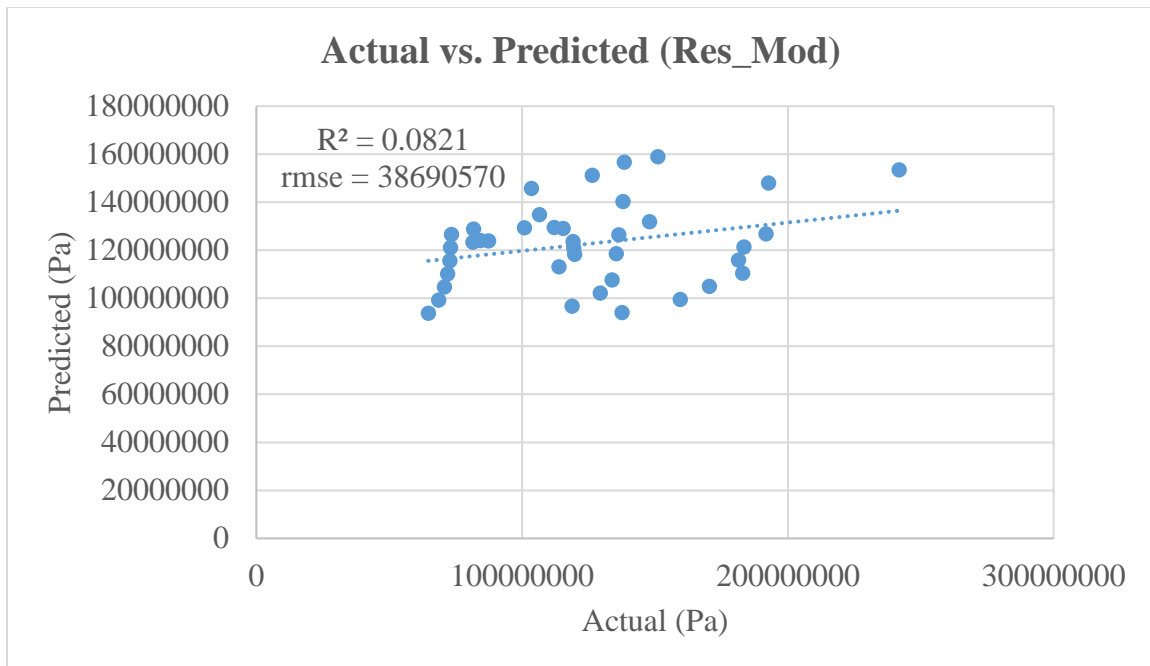
Figure 7.7. Prediction of resilient modulus values using multiple linear regression
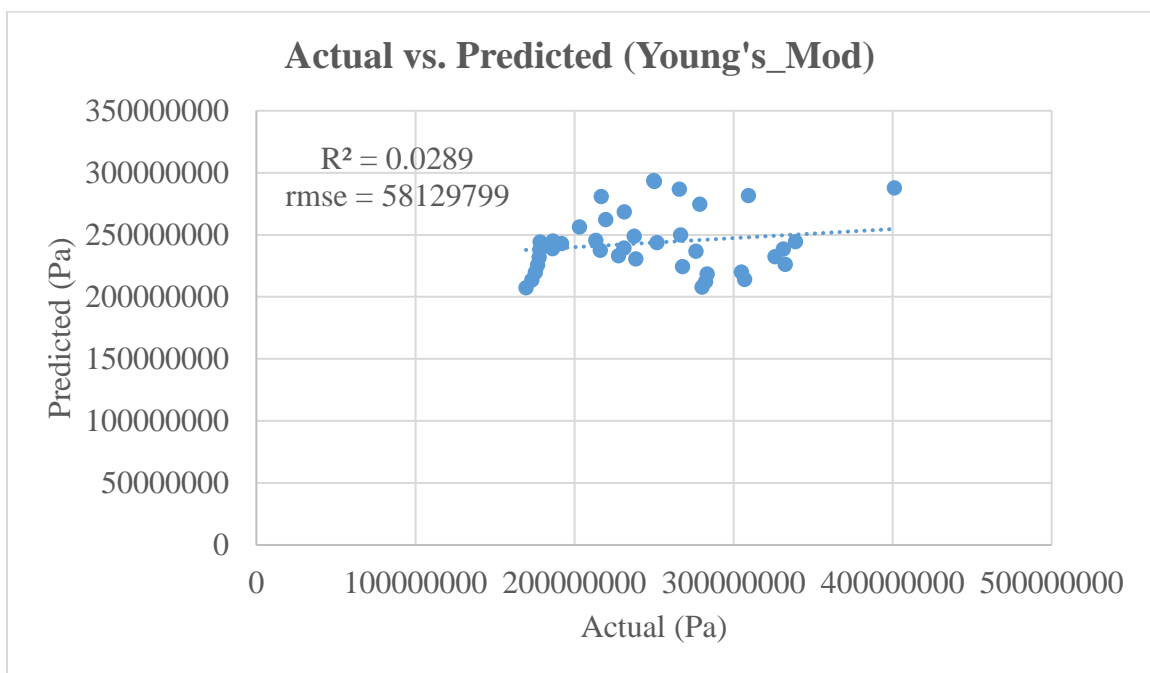
Figure 7.8. Prediction of Young's modulus values using multiple linear regression
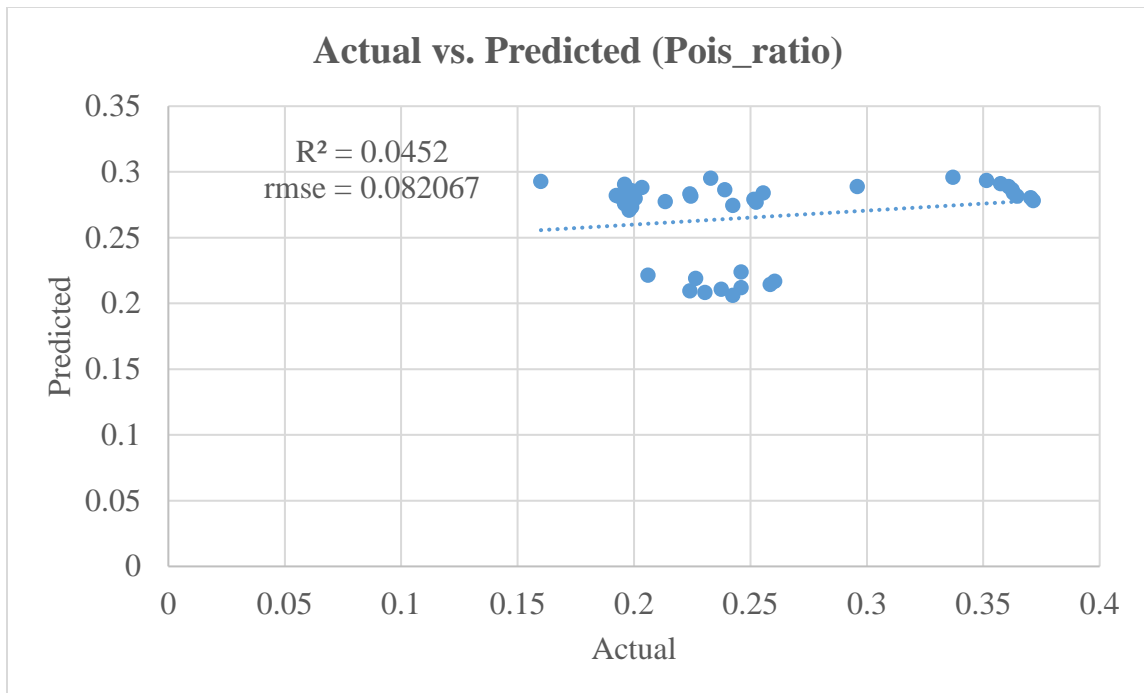
Figure 7.9. Prediction of Poisson's ratio values using multiple linear regression
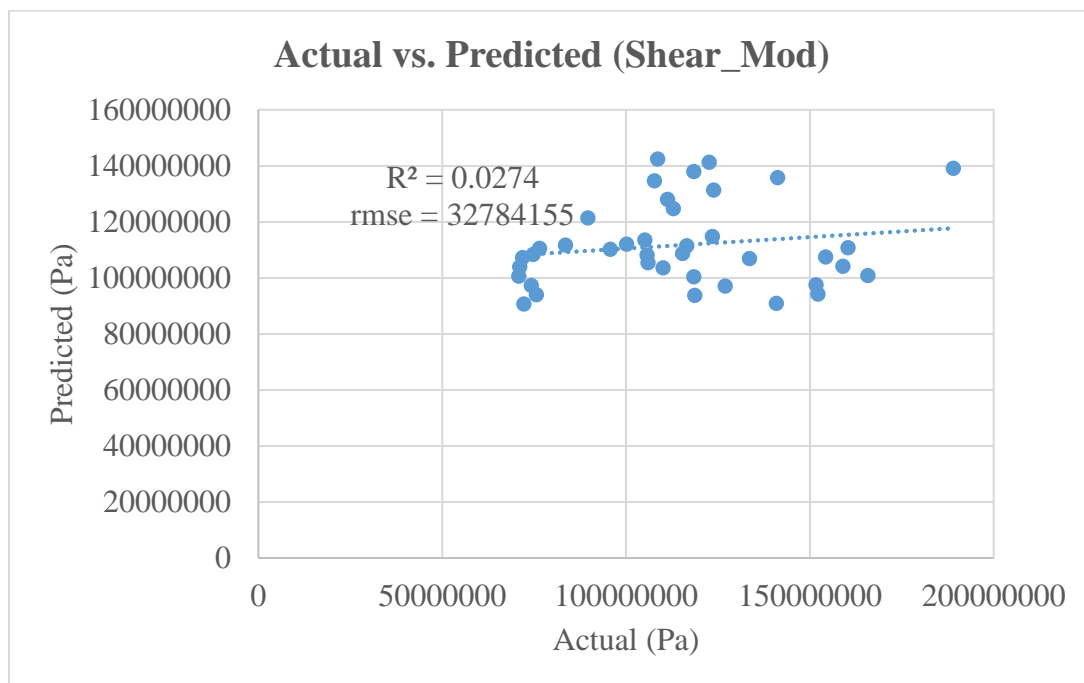
Figure 7.10. Prediction of shear modulus values using multiple linear regression
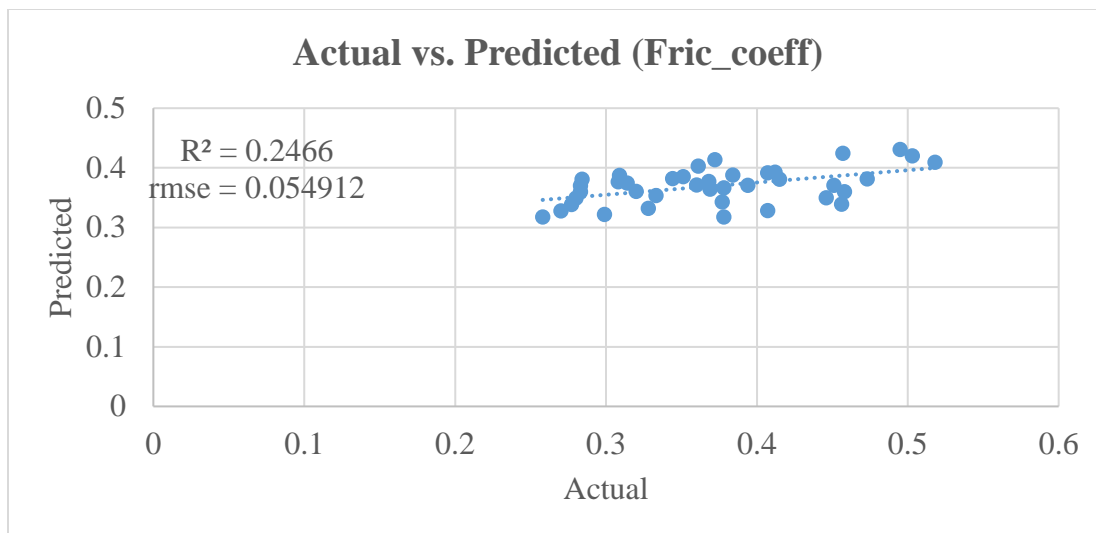
Figure 7.11. Prediction of friction coefficient values using multiple linear regression

7.2.2. Artificial Neural Network. The ANN method was used for the prediction of the same material properties as done by MLR method. By using the trial and error method, the best possible results were obtained and are presented in Figures 7.12-7.16. The actual values are representing the results obtained from Appendix A, while the predicted values are by the ANN method. Eighty percent data is shown in Figures 5.7-5.11, while twenty percent data is shown Figures 7.12-7.16. The coefficient of multiple determination (R^2) and root mean square errors (RMSE) are also presented. R^2 values of 0.2092, 0.0743, 0.1594, 0.2318, and 0.4132 were obtained for resilient modulus, Young's modulus, Poisson's ratio, shear modulus, and friction coefficient respectively. The RMSE values of 36.95 MPa, 54.11 MPa, 0.064822, 30.19 MPa, and 0.053848 were obtained for resilient modulus, Young's modulus, Poisson's ratio, shear modulus, and friction coefficient respectively. A little bit improvement can be seen from these numbers, as well as from the plots, but still these results are not acceptable for any predictive model.
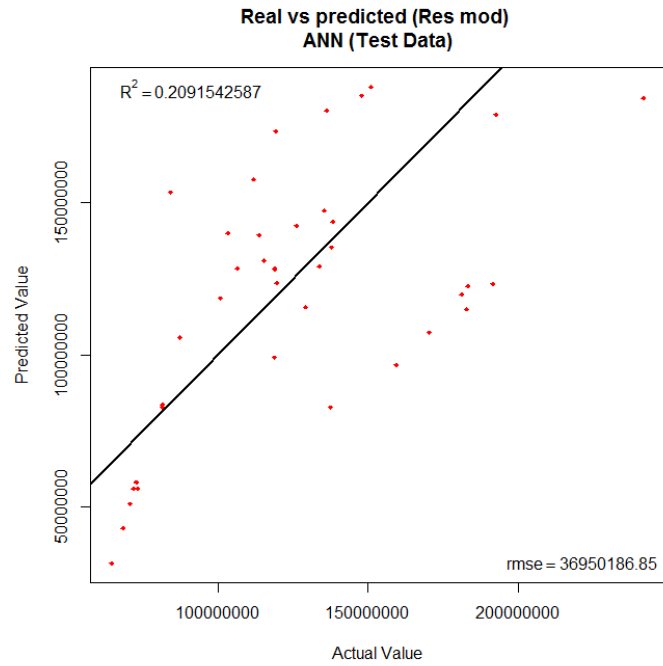
Figure 7.12. Actual versus predicted resilient modulus in the ANN test phase
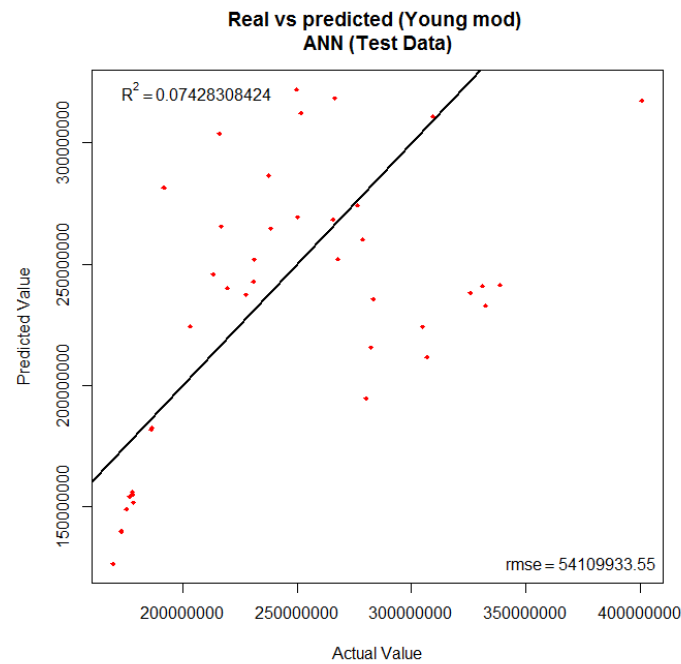
Figure 7.13. Actual versus predicted Young's modulus in the ANN test phase
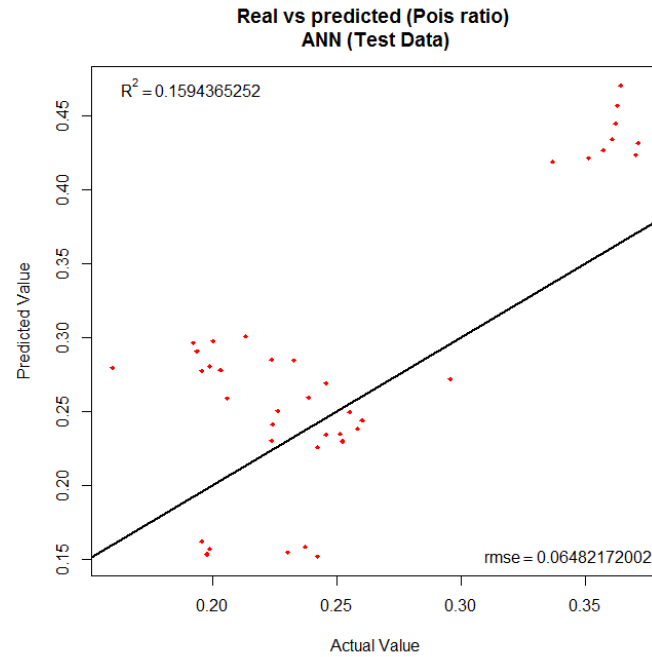
Figure 7.14. Actual versus predicted Poisson's ratio in the ANN test phase
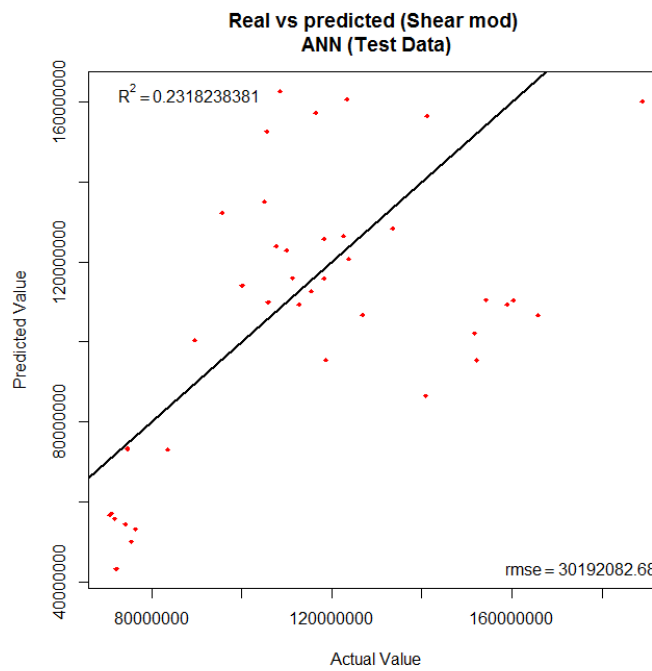
Figure 7.15. Actual versus predicted shear modulus in the ANN test phase
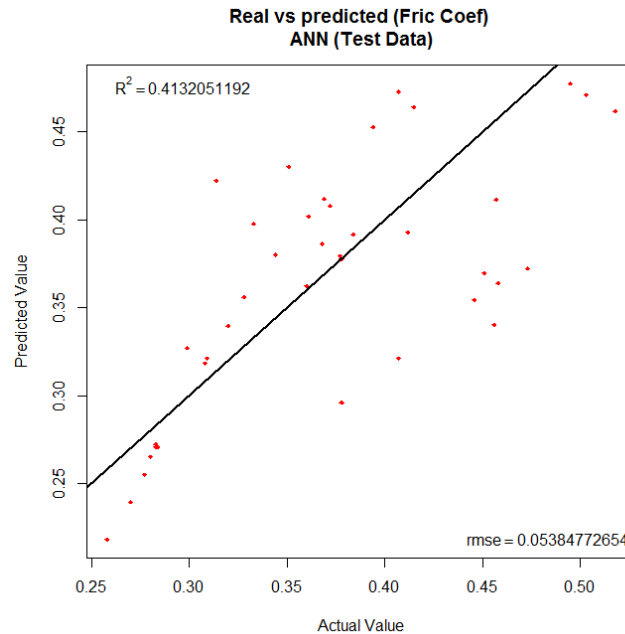
Figure 7.16. Actual versus predicted friction coefficient in the ANN test phase

7.2.3. Mamdani Fuzzy Logic. The MFL method was also used for the prediction of the same dataset. By using the trial and error method, the best possible results were obtained and are presented in Figures 7.17-7.21. The R^2 and the RMSE values are also presented. R^2 values of 0.7971, 0.7933, 0.9204, 0.8439, and 0.8878 were obtained for resilient modulus, Young's modulus, Poisson's ratio, shear modulus, and friction coefficient, respectively. The RMSE values of 18.71 MPa, 25.57 MPa, 0.017512, 11.82 MPa, and 0.023548 were obtained for resilient modulus, Young's modulus, Poisson's ratio, shear modulus, and friction coefficient, respectively. These numbers and the plots show a drastic improvement in the prediction, but it was thought that there are chances to achieve even better results. The MFL method is widely accepted because of its higher accuracy, even with less number of training data samples unlike the ANN method.
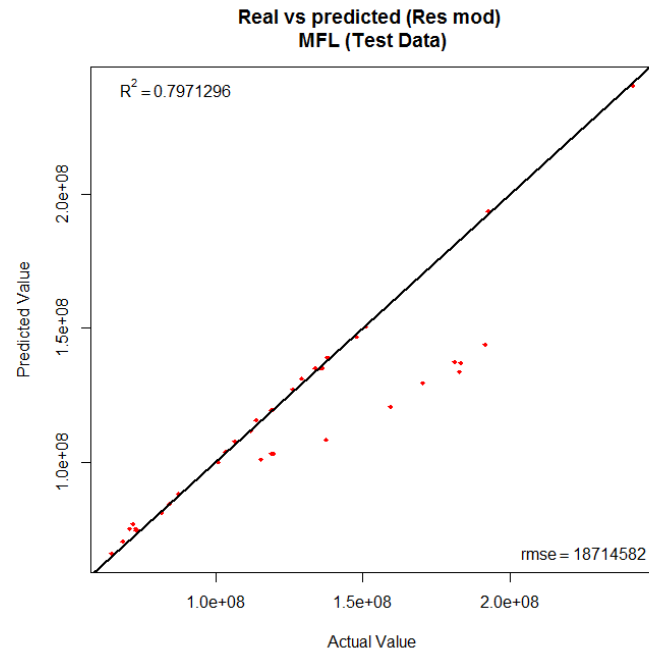
Figure 7.17. Actual versus predicted resilient modulus in the MFL test phase
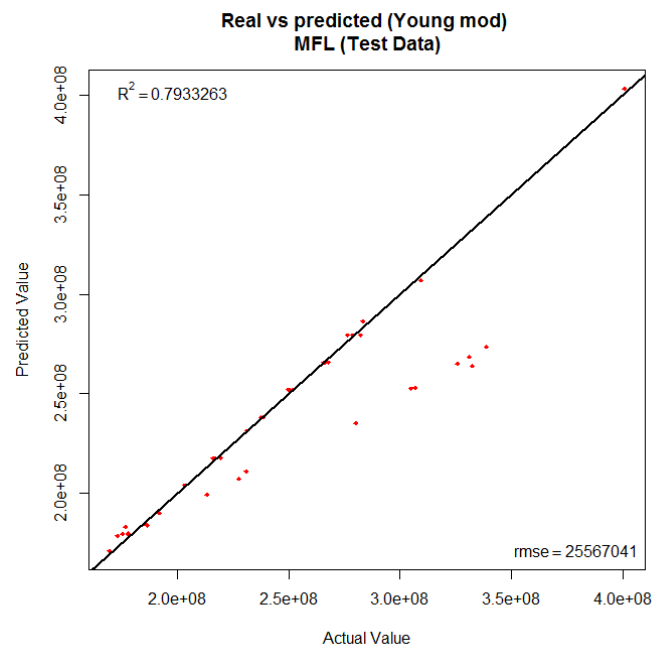
Figure 7.18. Actual versus predicted Young's modulus in the MFL test phase
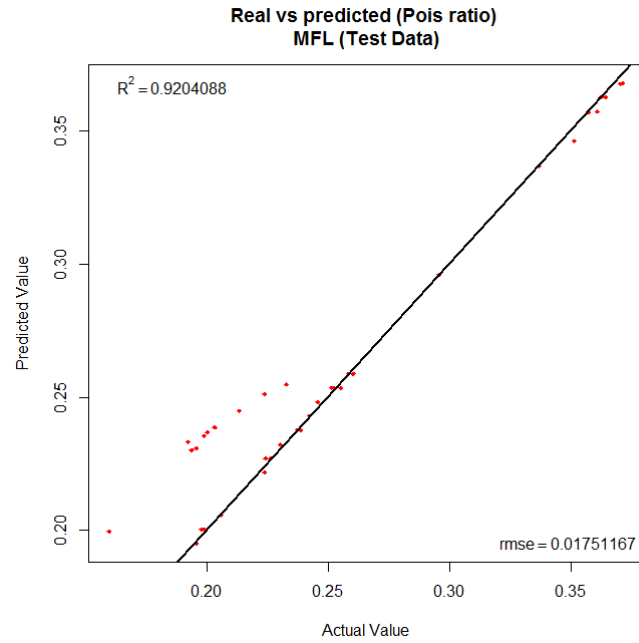
Figure 7.19. Actual versus predicted Poisson's ratio in the MFL test phase
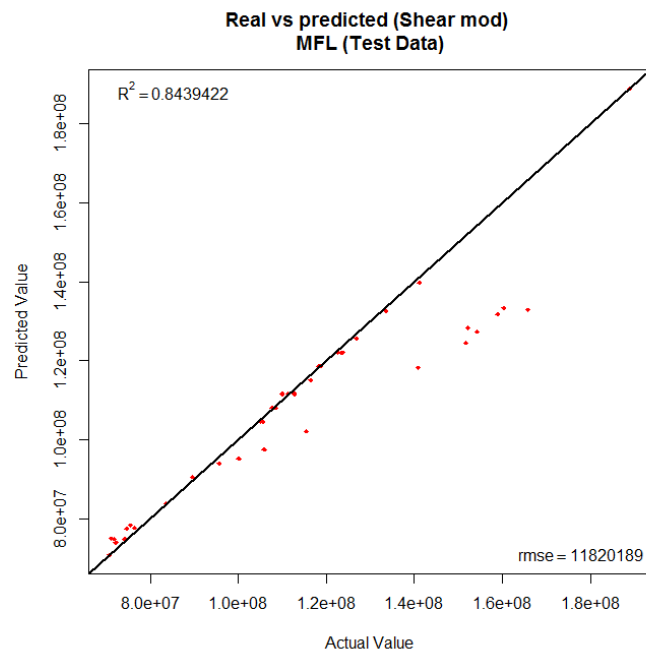
Figure 7.20. Actual versus predicted shear modulus in the MFL test phase
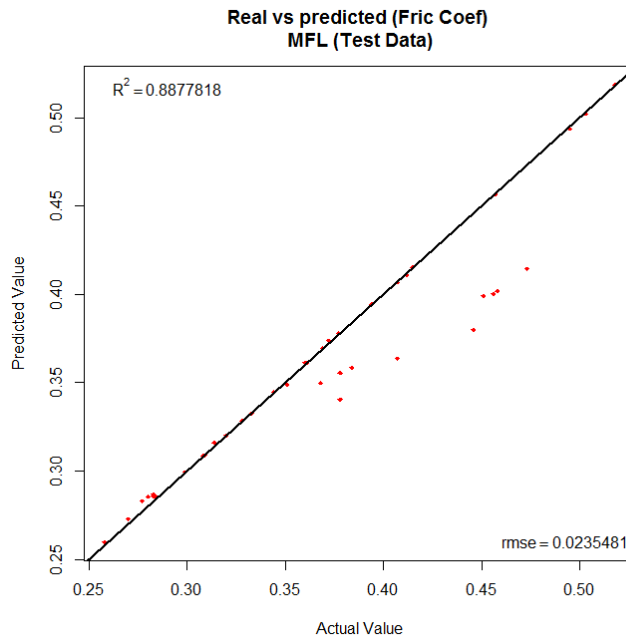
Figure 7.21. Actual versus predicted friction coefficient in the MFL test phase

7.2.4. Hybrid Neural Fuzzy Inference System. The HyFIS method was also used for the prediction, as it has many successful application in a variety of fields. By using the trial and error method, the best possible results were obtained and are presented in Figures 7.22-7.26. The R^2 and the RMSE values are also presented. R^2 values of 0.9857, 0.9717, 0.9871, 0.9703, and 0.9908 were obtained for resilient modulus, Young's modulus, Poisson's ratio, shear modulus, and friction coefficient, respectively. The RMSE values of 4.98 MPa, 9.45 MPa, 0.007056, 5.16 MPa, and 0.006733 were obtained for resilient modulus, Young's modulus, Poisson's ratio, shear modulus, and friction coefficient, respectively. These results and the plots show the best results. The reason is that the HyFIS method has the added advantage of both the ANN and the MFL methods.
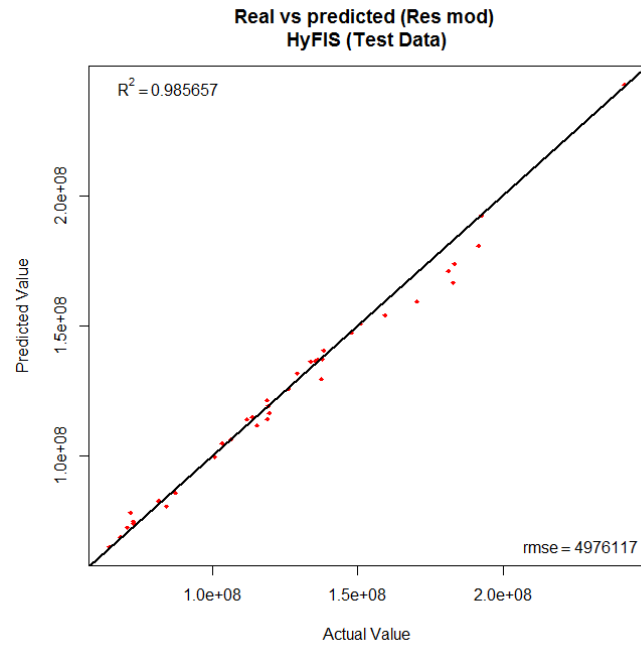
Figure 7.22. Actual versus predicted resilient modulus in the HyFIS test phase
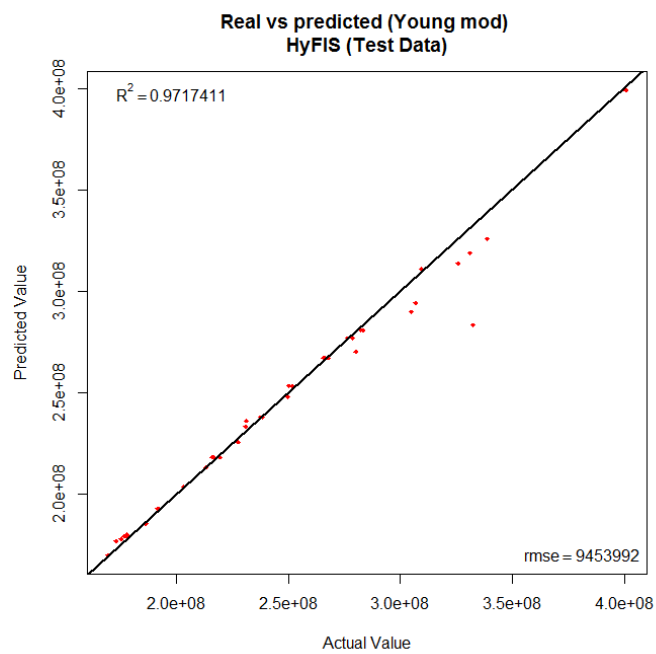
Figure 7.23. Actual versus predicted Young's modulus in the HyFIS test phase
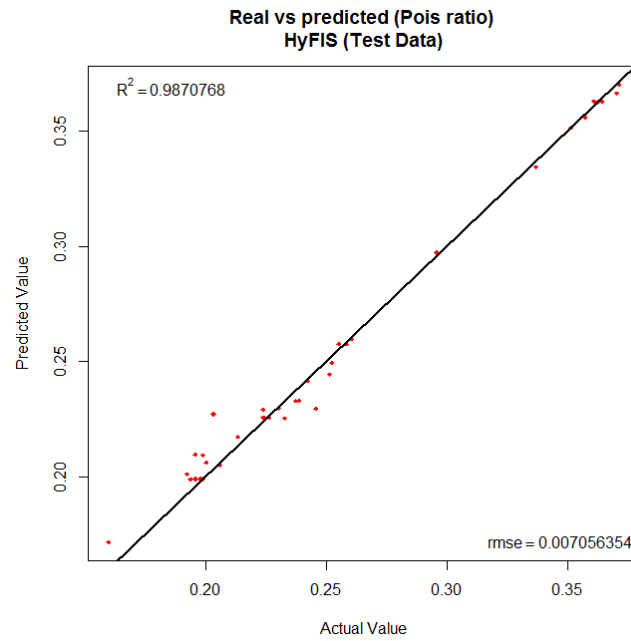
Figure 7.24. Actual versus predicted Poisson's ratio in the HyFIS test phase
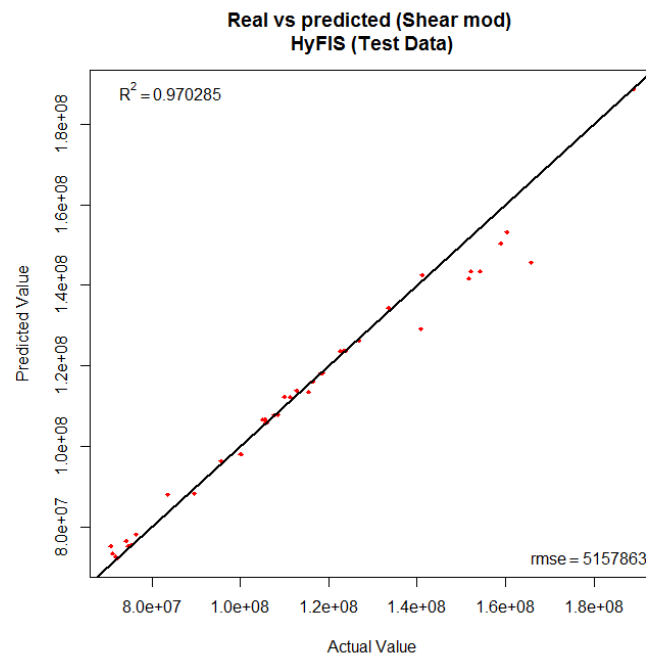
Figure 7.25. Actual versus predicted shear modulus in the HyFIS test phase
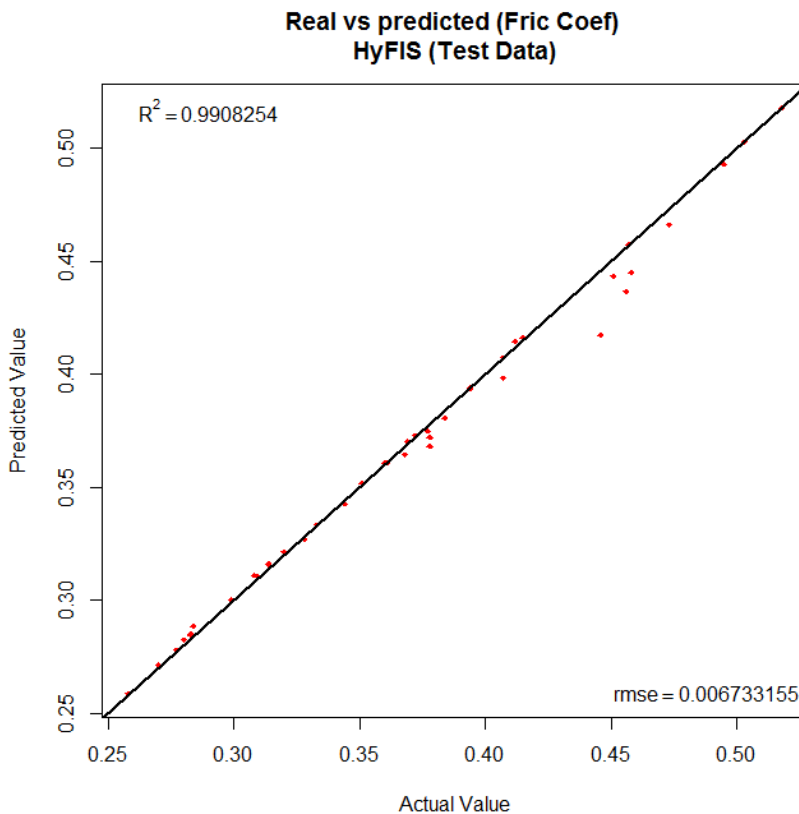
Figure 7.26. Actual versus predicted friction coefficient in the HyFIS test phase

In this subsection, the ANN, MFL, and HyFIS models were developed for the modeling and prediction of the formation material properties for an alternative to the PFC rock tests. Eighty percent of the data was used to train these models, and twenty percent data was used to test their performance. The MLR method is used as well for the predictions. The R^2 and RMSE values of the testing phase for each output, and for each of the above mentioned methods are presented in Table 7.7. The computational time (hours) taken by each method to complete one prediction test is also presented in Table 7.7. The RMSE values of resilient modulus, Young's modulus, and shear modulus are in MPa.

Table 7.7. Statistical performance indicators and the computational time taken by the MLR and AI models obtained after the testing phase for each output

Predictive Method	Statistical Performance Indicators	Comp time (Hrs)	Outputs				
			Res Mod	Young's Mod	Poisson's Ratio	Shear Mod	Fric Coeff
MLR	R²	0.1	0.0821	0.0289	0.0452	0.0274	0.2466
	RMSE		38.69	58.13	0.08207	32.78	0.05491
ANN	R²	168	0.2092	0.0743	0.1594	0.2318	0.4132
	RMSE		36.95	54.11	0.06482	30.19	0.05385
MFL	R²	48	0.7971	0.7933	0.9204	0.8439	0.8878
	RMSE		18.71	25.57	0.01751	11.82	0.02355
HyFIS	R²	60	0.9857	0.9717	0.9871	0.9703	0.9908
	RMSE		4.98	9.45	0.00706	5.16	0.00673

Based on these statistical performance indicators, it can be stated that the MLR and ANN models gave poor prediction results, whereas MFL and HyFIS models gave better predictions. The performance of these models can be put in decreasing order as; HyFIS > MFL > ANN > MLR. Based on the computational time, these models can be put in decreasing order as; ANN > HyFIS > MFL > MLR.

The HyFIS method was selected as the best predictive model for the current study, and thus, it was used for the remaining eight datasets (with 196 values in each dataset). By using the trial and error method, the best possible results were obtained. The R^2 and the RMSE values were recorded as given in Table 7.8. Based on these statistical performance indicators, it can be stated that the HyFIS can be used as a replacement for the PFC rock tests.

Table 7.8. Statistical performance indicators for the HyFIS method obtained after the testing phase for each output for materials with different densities

Material Density (kg/m³)	Statistical Performance Indicators	Outputs				
		Resilient Modulus	Young's Modulus	Poisson's Ratio	Shear Modulus	Friction Coefficient
1800	R²	0.9857	0.9717	0.9871	0.9703	0.9908
	RMSE	4.98	9.45	0.007056	5.16	0.006733
1900	R²	0.9574	0.9147	0.9513	0.8932	0.9083
	RMSE	7.84	10.22	0.009162	8.41	0.013237
2200	R²	0.9665	0.8649	0.9686	0.9251	0.9637
	RMSE	6.52	11.39	0.011914	7.39	0.008294
2400	R²	0.9020	0.9348	0.9739	0.9126	0.9712
	RMSE	8.68	9.95	0.010236	8.24	0.012055
2600	R²	0.9544	0.9724	0.9944	0.9683	0.9607
	RMSE	7.64	9.37	0.005128	9.22	0.009275
2700	R²	0.9429	0.9527	0.9952	0.9622	0.9879
	RMSE	7.98	8.22	0.004596	5.39	0.008565
2800	R²	0.9619	0.9699	0.9439	0.9923	0.9482
	RMSE	6.60	8.69	0.009265	4.59	0.011452
3000	R²	0.9736	0.9445	0.9571	0.9543	0.9539
	RMSE	5.82	9.26	0.005643	6.25	0.008566

7.3. SHOVEL DIPPER FILLING USING PARTICLE FLOW CODE

DEM analysis was carried out to observe the behavior of discrete formation particles in front of the shovel dipper. The 3D numerical simulations were performed in particle flow code (PFC) to observe the behavior of granular material flow into the shovel dipper. Virtual laboratory test simulations were done by writing FISH scripts in PFC3D

software. The calibrated input data for shovel dipper, bench dimensions, and for material properties is given in Table 6.1. The dipper motion was initialized along the trajectory given by Equation (6.1). The trajectory was determined using the data from the handbook of P&H 4800-XPC (JOYGLOBAL, 2016). The data points (bench widths and bench heights) were used to develop a scatterplot in Microsoft Excel 2016, and a trend line was inserted to determine the trajectory given by Equation (6.1).

Based on the two completed simulations, the dipper was able to move through the rock pile along a specified trajectory. A small value of friction coefficient resulted in easy movement of particles. In the numerical simulation, the formation particles were generated without any compaction. This low degree of compaction resulted in reduced interlocking of particles and reduced frictional resistance. With the use of more powerful computer, the developed simulator model can compare the performance of different excavation variables, and allow engineers to select optimum strategies to maximize excavation performance. In future studies, the forces involved during the shovel-formation interactions will be determined by using more realistic contact model (rolling friction and rolling resistance) proposed by Ai et al. (2011).

7.4. SUMMARY OF RESULTS

This section discusses the details of all the results obtained in this study. These include rock testing in particle flow code (PFC), artificial intelligence modeling, and the behavior of granular material flow into the shovel dipper. Unconfined compression, direct tension, Brazilian, and confined compression tests were conducted using the PFC3D software. Thirty-six PFC experiments were conducted each for UCS, tensile strength, and

Brazilian tensile strength. It was found that the compaction plays a vital role in these rock mechanics tests, as well as on the numerical results. It was also found that the particle size plays an important role on the computational cost. Different particle size ranges were tried and a particle size range of 3-5 mm with $D_{max}/D_{min} = 1.67$ gave reasonable results for rock strength values. The effect of density was found to be negligible. In this study, the errors obtained were in the range of 6 to 22 % for UCS, 21 to 80 % for tensile strength tests, and 5 to 10 % for Brazilian tensile strength tests, compared to the laboratory tests.

About 1,800 confined compression tests were performed in PFC, using the linear contact model of Potyondy and Cundall (2004) to obtain some of the formation material properties. The basic purpose of these tests was to look for an alternative to PFC experiments. PFC being a discrete element code takes a lot of time to complete the numerical tests. Artificial intelligence modeling was performed to predict the formation material properties (outputs of 1,800 confined compression tests) to look for an alternative of PFC. Artificial Neural Network (ANN), Mamdani Fuzzy Logic (MFL), Hybrid neural Fuzzy Inference System (HyFIS), along with the Multiple Linear Regression (MLR) methods were used for the predictive analysis. Based on the statistical performance indicators (R^2 and RMSE) determined for the testing phase (Table 7.7), it can be stated that the MLR and ANN models gave poor prediction results, whereas MFL and HyFIS models gave better predictions. The performance of these models can be put in decreasing order as; HyFIS > MFL > ANN > MLR. Based on the computational time, these models can be put in decreasing order as; ANN > HyFIS > MFL > MLR.

DEM analysis was carried out to observe the behavior of discrete formation particles in front of the shovel dipper. The 3D numerical simulations were performed in

particle flow code (PFC) to observe the behavior of granular material flow into the shovel dipper. Virtual laboratory test simulations were done by writing FISH scripts in PFC3D software. Virtual simulations allowed the dipper filling procedure to be modeled and analyzed.

8. CONCLUSIONS AND RECOMMENDATIONS

This sections covers the basic summary of this study, conclusions drawn from the results obtained, contributions of this study to the body of knowledge, and some recommendations for future studies. The summary provides the basic steps and methods to obtain the objectives of the study. The specific conclusions drawn on the basis of the test results have been discussed in detail. The research contributions subsection covers the highlights of the important contributions to the existing body of knowledge. Every study has its constraints and limitations that can somehow effect the results. At the end, recommendations for future studies have been discussed to take care of the limitations.

8.1. SUMMARY

Rock tests are performed before the start of every mining or civil engineering project for the purpose of feasibility studies. It results in huge costs, comprising drilling, sample collection, sample handling and finally laboratory testing. Unconfined compressive strength (UCS), direct tension, and indirect Brazilian tests are common laboratory tests. According to GEOLABS (2018), a UCS test costs $73 and an indirect Brazilian tensile strength test costs $86. According to Standard Laboratories. (2016), a UCS test costs $78 and an indirect Brazilian tensile strength test costs $35.50. In the idealized world of numerical models, these tests are possible and provide reliable estimates of rock strength values. The PFC3D offers a general purpose DEM framework, which was used to perform the above mentioned rock tests. The PFC3D software used numerical models to determine the rock strength values. The software allowed a combination of laboratory and numerical

estimations to lower the costs during the feasibility studies. Thirty-six PFC tests for each of UCS, direct tension, and indirect Brazilian tests were performed to cover different rock types. The validation of the numerical results was done by using the results of these tests from literature.

About 1,800 confined compression tests were performed in PFC, using the linear contact model of Potyondy and Cundall (2004) to obtain some of the formation material properties. The basic purpose of these tests was to look for an alternative to PFC experiments. PFC, being a discrete element code, takes a lot of time to complete the numerical tests. Artificial intelligence modeling was performed to predict the formation material properties (outputs of 1,800 confined compression tests) to look for an alternative of PFC. Artificial Neural Network (ANN), Mamdani Fuzzy Logic (MFL), Hybrid neural Fuzzy Inference System (HyFIS), along with the Multiple Linear Regression (MLR) methods were used for the predictive analysis.

In the last phase of this study, DEM analysis was carried out to observe the behavior of discrete formation particles in front of the shovel dipper. The numerical simulations were performed in PFC3D to observe the behavior of granular material flow into the shovel dipper. Virtual simulations modeled and analyzed the dipper filling procedure.

8.2. CONCLUSIONS

All the objectives of this study, stated in Section 1.3, have been achieved within the scope of the study. Thirty-six PFC experiments were conducted each for UCS, tensile strength, and Brazilian tensile strength. Based on these numerical rock tests, the following specific conclusions can be drawn:

1. The compaction of the PFC samples plays a vital role in obtaining the accurate numerical results. High compaction rate makes the sample much closer to the original compacted rock sample, so it results in more accuracy.

2. The particle size plays an important role on the computational cost, as well as on the accuracy of results. The smaller particle size results in high computational cost, so higher accuracy is expected.

3. A particle size range gives more accuracy as compared to using a single particle size, as in reality, the particle size is not the same throughout the rock sample. A particle size range will result in higher computational cost as compared to using a single particle size.

4. The effect of density on the rock strength values, as well as on the computational time is very small.

5. The sample size affects the rock strength values. Larger sample size results in higher strength values. The ASTM and ISRM standards must therefore be followed for sample preparation.

6. The numerical models underestimated the UCS values by 1.07 to 1.29 times, while they overestimated by 1.21 to 1.8 times for tensile strength values, and overestimated by 1.05 to 1.1 times for Brazilian tensile strength values.

7. The numerical models were able to find the crack growth.

8. The numerical models were able to determine the rock strength values with reasonable accuracy. The errors obtained were in the range of 6 and 22 % for UCS, 21 and 80 % for tensile strength tests, and 5 and 10 % for Brazilian tensile strength tests, compared to the laboratory tests.

About 1,800 confined compression tests were performed in PFC, using the linear contact model of Potyondy and Cundall (2004) to obtain formation material properties. PFC, being a discrete element code, takes a lot of time to complete the numerical tests, as well as it has high initial cost. Artificial intelligence models were developed and tested as alternative to perform the tests. Artificial Neural Network (ANN), Mamdani Fuzzy Logic (MFL), Hybrid neural Fuzzy Inference System (HyFIS), along with the Multiple Linear Regression (MLR) methods were used for the predictive analysis. All the AI models were developed by using the software 'R' that is used for statistical computing. From the AI modeling and analysis, the following specific conclusions can be drawn:

1. The AI models give results in reasonably less time compared to PFC.

2. The number of hidden neurons is a major variable that affects the performance of an ANN model.

3. The number of linguistic variables is a major variable that affects the performance of fuzzy models.

4. Based on the computational time taken (Table 7.7), these models can be put into the following sequence; ANN (168 hours) > HyFIS (60 hours) > MFL (48 hours) > MLR (0.1 hours).

5. Based on the statistical performance indicators (R^2 and RMSE) determined for the testing phase (Table 7.7) for five outputs, it can be stated that the MLR and ANN models gave poor prediction results, whereas MFL and HyFIS models gave good predictions. The performance of these models can be put into the following sequence; HyFIS > MFL > ANN > MLR.

6. The HyFIS method is clearly the best predictive model for the current study.

7. Based on the statistical performance indicators for the testing phase (Table 7.8), it is concluded that the HyFIS can be used as a replacement for the PFC rock tests.

DEM analysis was carried out to observe the behavior of discrete formation particles in front of the shovel dipper. Based on the 3D numerical simulations performed in PFC to observe the behavior of granular material flow into the shovel dipper, the following specific conclusions can be drawn:

1. The dipper was able to move through the rock pile along a specified trajectory.

2. A small value of friction coefficient resulted in easy movement of particles.

3. In the numerical simulation, the formation particles were generated without any compaction. This low degree of compaction resulted in reduced interlocking of particles and reduced frictional resistance.

8.3. RESEARCH CONTRIBUTIONS

All the objectives have been achieved for the research study. The notable contributions of this study are as follows:

1. The PFC models for the two rock formations (Sakesar limestone and Namal limestone) for the rock mechanics tests were developed. Different researchers have developed these models in the past, but improved results in terms of reduced errors were obtained in this study.

2. Rock tests are performed before the start of every mining or civil engineering project for the purpose of feasibility studies. It results in huge costs, comprising drilling, sample collection, sample handling and finally laboratory testing. The developed numerical models will help in reducing the time and cost.

3. The size of the sample is found to be a major factor affecting the results of these rock mechanics tests. According to the author's knowledge, no one have followed ISRM (1978a, b), ISRM (1979a, b), ASTM-D3967 (2008), and ASTM-D4543 (2008) standards. Researches have used cuboid samples for the tests. Especially for the Brazilian tensile strength tests, it is recommended by these standards to have a sample that has a thickness to diameter ratio of 0.5. These numerical models can be used to get reasonably accurate rock strengths. It will save a lot of time and costs, especially for the feasibility studies.

4. This study is the first attempt to develop self-learning artificial intelligent models for the prediction of the formation material properties. These AI models include Artificial Neural Network (ANN), Mamdani Fuzzy Logic (MFL), Hybrid neural Fuzzy Inference System (HyFIS). The Multiple Linear Regression (MLR) method was also used for the predictive analysis. These models especially, HyFIS can be used to predict the desired properties with reasonable accuracy.

5. HyFIS model was found to be the best AI model for the research problem under study. It was further used for the remaining eight datasets (having 196 values in each). Based on the statistical performance indicators (R^2 and RMSE), it is stated that the HyFIS can be used as a replacement for the PFC rock tests. This is the first attempt to look for an AI model as a replacement to PFC rock mechanics tests. This will allow researchers to use a cheap (computationally as well as initial cost) software, still getting comparable results.

6. For the first time, DEM simulations for P&H 4800-XPC in PFC3D were performed to simulate, study and analyze the cable shovel digging phase. The behavior of a

granular material in front of a shovel dipper was observed and understood. With the use of more powerful computer, the developed simulator model can compare the performance of different excavation variables, and allow engineers to select optimum strategies to maximize excavation performance.

8.4. RECOMMENDATIONS FOR FUTURE WORK

There is always room for improvement because of the assumptions made and limitations. Following recommendations are suggested to improve the quality of work.

1. The numerical rock mechanics test results can be improved by using more complex (angular) particles (clumps may be used in PFC). Because of more angularity, the particles will inter-lock and hence, will be closer to the real world rock samples.

2. The smaller particle size in PFC results in high computational cost, as well as high accuracy is obtained. A compromise between the computational cost, and the accuracy should be made.

3. Artificial intelligence is done by using trial and error method. Because of the time limitations, some errors were accepted. By using the trial and error method, future researchers may find more accurate results or develop a technique to replace the trial and error method.

4. One hidden layer was used for the ANN model in this study. Because the results were not good enough, it is recommended to use more than one hidden layer that may produce better results.

5. For the DEM simulations of cable shovel dipper filling, more powerful computers should be used to minimize to computational time.

6. The simple linear contact model was used in this study which has its own limitations. More realistic contact model (rolling friction and rolling resistance) proposed by Ai et al. (2011) can be used to achieve better results.

7. It is suggested to vary the formation material properties to see the effect on the failure pattern in front of the dipper.

8. The 3D model developed will provide a base for further analysis. In future studies, the forces will be determined that are involved during the shovel-formation interactions.

APPENDIX A.

PFC3D CONFINED COMPRESSION TEST RESULTS

Table A.1. Confined compression test results at a density value of 1800 kg/m^3

Emod (Pa)	K_ratio	Fric	Res_mod (Pa)	You_mod (Pa)	Poi_rat	She_mod (Pa)	Fri_Coe
1E+08	0.5	0.5	70370973	1.71E+08	0.3385	1.26E+08	0.28
1E+09	0.5	0.5	74887329	1.68E+08	0.276	1.52E+08	0.281
1E+10	0.5	0.5	1.1E+08	2.23E+08	0.246	2.27E+08	0.347
1E+11	0.5	0.5	1.09E+08	1.98E+08	0.247	2.01E+08	0.404
1E+08	0.5	0.75	81473453	1.81E+08	0.3795	1.19E+08	0.316
1E+09	0.5	0.75	1.04E+08	1.96E+08	0.2335	2.1E+08	0.345
1E+10	0.5	0.75	1.62E+08	3.41E+08	0.2625	3.24E+08	0.341
1E+11	0.5	0.75	1.27E+08	2.24E+08	0.2255	2.49E+08	0.44
1E+08	0.5	1	88718121	1.88E+08	0.402	1.17E+08	0.338
1E+09	0.5	1	97649127	1.86E+08	0.245	1.9E+08	0.342
1E+10	0.5	1	1.67E+08	3E+08	0.1285	5.85E+08	0.413
1E+11	0.5	1	1.7E+08	3.04E+08	0.197	3.86E+08	0.43
1E+08	0.5	1.25	92070136	1.91E+08	0.413	1.16E+08	0.348
1E+09	0.5	1.25	1.2E+08	2.13E+08	0.249	2.14E+08	0.391
1E+10	0.5	1.25	1.09E+08	2.13E+08	0.1805	2.96E+08	0.379
1E+11	0.5	1.25	1.45E+08	2.4E+08	0.2125	2.82E+08	0.472
1E+08	0.5	1.5	94294973	1.93E+08	0.4195	1.15E+08	0.355
1E+09	0.5	1.5	1.24E+08	2.18E+08	0.258	2.11E+08	0.389
1E+10	0.5	1.5	1.47E+08	2.63E+08	0.0845	7.77E+08	0.435
1E+11	0.5	1.5	1.49E+08	2.59E+08	0.1845	3.51E+08	0.45
1E+08	0.5	1.75	95881967	1.95E+08	0.4245	1.15E+08	0.359
1E+09	0.5	1.75	1.2E+08	2.21E+08	0.2335	2.37E+08	0.372
1E+10	0.5	1.75	1.68E+08	2.97E+08	0.1245	5.97E+08	0.439
1E+11	0.5	1.75	1.67E+08	2.76E+08	0.22	3.14E+08	0.502
1E+08	0.5	2	97029904	1.96E+08	0.429	1.14E+08	0.362
1E+09	0.5	2	1.46E+08	2.47E+08	0.2265	2.72E+08	0.422

Table A.1. Confined compression test results at a density value of 1800 kg/m³ (cont.)

Emod (Pa)	K_ratio	Fric	Res_mod (Pa)	You_mod (Pa)	Poi_rat	She_mod (Pa)	Fri_Coe
1E+10	0.5	2	1.79E+08	3.11E+08	0.1265	6.14E+08	0.456
1E+11	0.5	2	1.3E+08	2.22E+08	0.2165	2.56E+08	0.478
1E+08	0.75	0.5	69986178	1.72E+08	0.347	1.24E+08	0.278
1E+09	0.75	0.5	1.05E+08	2.29E+08	0.3145	1.82E+08	0.318
1E+10	0.75	0.5	1.18E+08	2.43E+08	0.2095	2.89E+08	0.382
1E+11	0.75	0.5	99478381	2.13E+08	0.194	2.74E+08	0.33
1E+08	0.75	0.75	79005500	1.81E+08	0.3785	1.19E+08	0.305
1E+09	0.75	0.75	1.29E+08	2.53E+08	0.2855	2.22E+08	0.358
1E+10	0.75	0.75	1.58E+08	3.13E+08	0.163	4.8E+08	0.389
1E+11	0.75	0.75	2.13E+08	4.46E+08	0.1845	6.05E+08	0.355
1E+08	0.75	1	83117849	1.85E+08	0.393	1.18E+08	0.318
1E+09	0.75	1	1.51E+08	2.9E+08	0.2105	3.44E+08	0.378
1E+10	0.75	1	1.54E+08	2.86E+08	0.1205	5.92E+08	0.433
1E+11	0.75	1	1.89E+08	3.6E+08	0.133	6.77E+08	0.405
1E+08	0.75	1.25	85250945	1.87E+08	0.4015	1.16E+08	0.324
1E+09	0.75	1.25	1.3E+08	2.54E+08	0.225	2.82E+08	0.371
1E+10	0.75	1.25	1.62E+08	2.96E+08	0.1315	5.64E+08	0.45
1E+11	0.75	1.25	2.03E+08	3.96E+08	0.1665	5.94E+08	0.398
1E+08	0.75	1.5	86581644	1.88E+08	0.407	1.16E+08	0.328
1E+09	0.75	1.5	1.17E+08	2.19E+08	0.2095	2.61E+08	0.383
1E+10	0.75	1.5	2.07E+08	3.4E+08	0.1	8.52E+08	0.524
1E+11	0.75	1.5	1.96E+08	3.4E+08	0.154	5.52E+08	0.472
1E+08	0.75	1.75	87470246	1.89E+08	0.41	1.15E+08	0.331
1E+09	0.75	1.75	1.74E+08	3.2E+08	0.22	3.64E+08	0.396
1E+10	0.75	1.75	1.94E+08	3.39E+08	0.101	8.4E+08	0.501
1E+11	0.75	1.75	1.66E+08	3.17E+08	0.1325	5.99E+08	0.411

Table A.1. Confined compression test results at a density value of 1800 kg/m^3 (cont.)

Emod (Pa)	K_ratio	Fric	Res_mod (Pa)	You_mod (Pa)	Poi_rat	She_mod (Pa)	Fri_Coe
1E+08	0.75	2	88110386	1.9E+08	0.4115	1.15E+08	0.332
1E+09	0.75	2	1.23E+08	2.22E+08	0.2345	2.36E+08	0.415
1E+10	0.75	2	1.95E+08	3.31E+08	0.125	6.61E+08	0.505
1E+11	0.75	2	1.46E+08	2.81E+08	0.112	6.25E+08	0.406
1E+08	1	0.5	73080659	1.73E+08	0.3645	1.19E+08	0.287
1E+09	1	0.5	1.05E+08	2.17E+08	0.3085	1.76E+08	0.338
1E+10	1	0.5	1.39E+08	2.38E+08	0.3005	1.98E+08	0.426
1E+11	1	0.5	95621953	1.9E+08	0.2385	1.99E+08	0.37
1E+08	1	0.75	79722202	1.8E+08	0.394	1.14E+08	0.31
1E+09	1	0.75	1.11E+08	2.23E+08	0.2835	1.96E+08	0.352
1E+10	1	0.75	1.42E+08	2.43E+08	0.185	3.28E+08	0.429
1E+11	1	0.75	84013860	1.79E+08	0.2015	2.22E+08	0.326
1E+08	1	1	81993828	1.81E+08	0.405	1.12E+08	0.318
1E+09	1	1	1.1E+08	2.22E+08	0.2505	2.21E+08	0.35
1E+10	1	1	1.53E+08	2.63E+08	0.16	4.12E+08	0.446
1E+11	1	1	1.57E+08	2.79E+08	0.1265	5.52E+08	0.44
1E+08	1	1.25	83053250	1.82E+08	0.41	1.11E+08	0.323
1E+09	1	1.25	1.15E+08	2.21E+08	0.2435	2.27E+08	0.371
1E+10	1	1.25	1.65E+08	2.64E+08	0.162	4.09E+08	0.488
1E+11	1	1.25	1.95E+08	3.58E+08	0.1555	5.76E+08	0.414
1E+08	1	1.5	83899091	1.82E+08	0.4125	1.1E+08	0.325
1E+09	1	1.5	1.14E+08	2.18E+08	0.262	2.08E+08	0.372
1E+10	1	1.5	1.89E+08	3.01E+08	0.187	4.03E+08	0.508
1E+11	1	1.5	1.22E+08	2.29E+08	0.1135	5.03E+08	0.405
1E+08	1	1.75	84475483	1.83E+08	0.4145	1.1E+08	0.327
1E+09	1	1.75	1.16E+08	2.16E+08	0.2485	2.17E+08	0.393

Table A.1. Confined compression test results at a density value of 1800 kg/m^3 (cont.)

Emod (Pa)	K_ratio	Fric	Res_mod (Pa)	You_mod (Pa)	Poi_rat	She_mod (Pa)	Fri_Coe
1E+10	1	1.75	2.69E+08	4.29E+08	0.2125	5.05E+08	0.519
1E+11	1	1.75	1.48E+08	2.78E+08	0.16	4.35E+08	0.414
1E+08	1	2	84899885	1.83E+08	0.4155	1.1E+08	0.329
1E+09	1	2	1.22E+08	2.19E+08	0.2205	2.48E+08	0.406
1E+10	1	2	2.17E+08	3.6E+08	0.206	4.36E+08	0.482
1E+11	1	2	1.88E+08	3.26E+08	0.182	4.47E+08	0.451
1E+08	1.25	0.5	76409213	1.79E+08	0.3725	1.2E+08	0.289
1E+09	1.25	0.5	89628528	1.94E+08	0.222	2.18E+08	0.308
1E+10	1.25	0.5	1.46E+08	2.7E+08	0.264	2.56E+08	0.387
1E+11	1.25	0.5	1.24E+08	2.81E+08	0.305	2.3E+08	0.325
1E+08	1.25	0.75	83387450	1.87E+08	0.393	1.19E+08	0.307
1E+09	1.25	0.75	1.19E+08	2.3E+08	0.208	2.76E+08	0.362
1E+10	1.25	0.75	1.15E+08	2.1E+08	0.216	2.43E+08	0.396
1E+11	1.25	0.75	93789185	2.08E+08	0.277	1.87E+08	0.321
1E+08	1.25	1	86303341	1.89E+08	0.402	1.18E+08	0.315
1E+09	1.25	1	1.24E+08	2.26E+08	0.2245	2.52E+08	0.407
1E+10	1.25	1	1.43E+08	2.57E+08	0.2045	3.14E+08	0.42
1E+11	1.25	1	1.17E+08	2.34E+08	0.2445	2.4E+08	0.361
1E+08	1.25	1.25	87630169	1.91E+08	0.406	1.17E+08	0.319
1E+09	1.25	1.25	1.65E+08	2.86E+08	0.2355	3.03E+08	0.428
1E+10	1.25	1.25	1.62E+08	2.6E+08	0.153	4.26E+08	0.471
1E+11	1.25	1.25	95042159	2.02E+08	0.2555	1.97E+08	0.33
1E+08	1.25	1.5	88180839	1.91E+08	0.4075	1.17E+08	0.321
1E+09	1.25	1.5	1.41E+08	2.49E+08	0.216	2.89E+08	0.428
1E+10	1.25	1.5	1.46E+08	2.49E+08	0.1105	5.63E+08	0.447
1E+11	1.25	1.5	1.29E+08	2.44E+08	0.235	2.59E+08	0.414

Table A.1. Confined compression test results at a density value of 1800 kg/m³ (cont.)

Emod (Pa)	K_ratio	Fric	Res_mod (Pa)	You_mod (Pa)	Poi_rat	She_mod (Pa)	Fri_Coe
1E+08	1.25	1.75	88481571	1.91E+08	0.4085	1.17E+08	0.322
1E+09	1.25	1.75	1.62E+08	2.78E+08	0.1895	3.66E+08	0.431
1E+10	1.25	1.75	1.37E+08	2.44E+08	0.1585	3.85E+08	0.411
1E+11	1.25	1.75	1.24E+08	2.69E+08	0.253	2.66E+08	0.336
1E+08	1.25	2	89304577	1.92E+08	0.4085	1.17E+08	0.325
1E+09	1.25	2	1.49E+08	2.56E+08	0.208	3.09E+08	0.447
1E+10	1.25	2	1.89E+08	3E+08	0.135	5.55E+08	0.486
1E+11	1.25	2	94695800	2.07E+08	0.193	2.68E+08	0.352
1E+08	1.5	0.5	75388891	1.79E+08	0.3485	1.29E+08	0.286
1E+09	1.5	0.5	1.03E+08	2.18E+08	0.2285	2.38E+08	0.333
1E+10	1.5	0.5	1.82E+08	3.62E+08	0.3885	2.33E+08	0.383
1E+11	1.5	0.5	1.34E+08	2.8E+08	0.236	2.96E+08	0.366
1E+08	1.5	0.75	79326786	1.83E+08	0.3665	1.25E+08	0.299
1E+09	1.5	0.75	1.1E+08	2.34E+08	0.1875	3.12E+08	0.334
1E+10	1.5	0.75	1.33E+08	2.52E+08	0.2875	2.19E+08	0.395
1E+11	1.5	0.75	1.06E+08	2.2E+08	0.257	2.14E+08	0.362
1E+08	1.5	1	80971532	1.84E+08	0.376	1.22E+08	0.306
1E+09	1.5	1	1.19E+08	2.4E+08	0.193	3.1E+08	0.362
1E+10	1.5	1	1.51E+08	2.94E+08	0.342	2.14E+08	0.375
1E+11	1.5	1	1.29E+08	2.53E+08	0.244	2.6E+08	0.414
1E+08	1.5	1.25	82109177	1.85E+08	0.38	1.22E+08	0.31
1E+09	1.5	1.25	1.19E+08	2.38E+08	0.2225	2.67E+08	0.367
1E+10	1.5	1.25	1.65E+08	2.98E+08	0.2205	3.39E+08	0.434
1E+11	1.5	1.25	1.05E+08	2.19E+08	0.229	2.4E+08	0.371
1E+08	1.5	1.5	82723003	1.85E+08	0.383	1.21E+08	0.313
1E+09	1.5	1.5	1.14E+08	2.23E+08	0.235	2.37E+08	0.373

Table A.1. Confined compression test results at a density value of 1800 kg/m^3 (cont.)

Emod (Pa)	K_ratio	Fric	Res_mod (Pa)	You_mod (Pa)	Poi_rat	She_mod (Pa)	Fri_Coe
1E+10	1.5	1.5	2.33E+08	4.03E+08	0.271	3.72E+08	0.472
1E+11	1.5	1.5	1.23E+08	2.55E+08	0.1815	3.51E+08	0.385
1E+08	1.5	1.75	83448699	1.86E+08	0.3855	1.2E+08	0.315
1E+09	1.5	1.75	1.15E+08	2.23E+08	0.185	3.02E+08	0.375
1E+10	1.5	1.75	1.65E+08	2.86E+08	0.205	3.49E+08	0.465
1E+11	1.5	1.75	2.14E+08	4.06E+08	0.2205	4.6E+08	0.43
1E+08	1.5	2	83829240	1.86E+08	0.387	1.2E+08	0.316
1E+09	1.5	2	1.34E+08	2.52E+08	0.2375	2.66E+08	0.398
1E+10	1.5	2	1.4E+08	2.51E+08	0.1785	3.51E+08	0.429
1E+11	1.5	2	1.9E+08	3.6E+08	0.1905	4.72E+08	0.455
1E+08	1.75	0.5	75301900	1.79E+08	0.3385	1.32E+08	0.291
1E+09	1.75	0.5	87181138	1.9E+08	0.254	1.87E+08	0.309
1E+10	1.75	0.5	1.07E+08	2.05E+08	0.2835	1.81E+08	0.362
1E+11	1.75	0.5	1.33E+08	2.4E+08	0.304	1.97E+08	0.41
1E+08	1.75	0.75	79744485	1.83E+08	0.354	1.29E+08	0.305
1E+09	1.75	0.75	92789584	1.96E+08	0.2355	2.08E+08	0.322
1E+10	1.75	0.75	1.13E+08	2.19E+08	0.257	2.13E+08	0.381
1E+11	1.75	0.75	1.39E+08	2.4E+08	0.264	2.28E+08	0.453
1E+08	1.75	1	82315761	1.85E+08	0.363	1.27E+08	0.313
1E+09	1.75	1	92892214	2E+08	0.2285	2.19E+08	0.315
1E+10	1.75	1	1.25E+08	2.41E+08	0.3175	1.9E+08	0.363
1E+11	1.75	1	1.68E+08	2.9E+08	0.208	3.48E+08	0.436
1E+08	1.75	1.25	84113468	1.87E+08	0.3675	1.27E+08	0.317
1E+09	1.75	1.25	96953673	1.97E+08	0.227	2.17E+08	0.346
1E+10	1.75	1.25	1.44E+08	2.79E+08	0.308	2.26E+08	0.367
1E+11	1.75	1.25	1.69E+08	3.07E+08	0.2905	2.65E+08	0.419

Table A.1. Confined compression test results at a density value of 1800 kg/m³ (cont.)

Emod (Pa)	K_ratio	Fric	Res_mod (Pa)	You_mod (Pa)	Poi_rat	She_mod (Pa)	Fri_Coe
1E+08	1.75	1.5	84864280	1.88E+08	0.37	1.27E+08	0.32
1E+09	1.75	1.5	98682091	1.99E+08	0.2375	2.09E+08	0.349
1E+10	1.75	1.5	1.45E+08	2.53E+08	0.2325	2.72E+08	0.427
1E+11	1.75	1.5	1.62E+08	2.78E+08	0.171	4.06E+08	0.439
1E+08	1.75	1.75	85199090	1.88E+08	0.3715	1.26E+08	0.321
1E+09	1.75	1.75	1.06E+08	2.07E+08	0.237	2.19E+08	0.359
1E+10	1.75	1.75	1.38E+08	2.51E+08	0.181	3.46E+08	0.405
1E+11	1.75	1.75	1.29E+08	2.28E+08	0.2045	2.79E+08	0.442
1E+08	1.75	2	85436594	1.88E+08	0.373	1.26E+08	0.322
1E+09	1.75	2	99603330	1.95E+08	0.227	2.15E+08	0.359
1E+10	1.75	2	1.15E+08	2.09E+08	0.1745	2.99E+08	0.395
1E+11	1.75	2	1.54E+08	2.53E+08	0.212	2.99E+08	0.503
1E+08	2	0.5	69287838	1.7E+08	0.3455	1.23E+08	0.273
1E+09	2	0.5	1.48E+08	3.04E+08	0.154	4.92E+08	0.372
1E+10	2	0.5	1.25E+08	3.27E+08	0.381	2.14E+08	0.263
1E+11	2	0.5	81698394	1.92E+08	0.282	1.71E+08	0.313
1E+08	2	0.75	73944211	1.75E+08	0.3645	1.2E+08	0.286
1E+09	2	0.75	1.52E+08	2.98E+08	0.186	4.01E+08	0.404
1E+10	2	0.75	1.16E+08	2.41E+08	0.2705	2.23E+08	0.348
1E+11	2	0.75	1.19E+08	2.64E+08	0.2655	2.48E+08	0.341
1E+08	2	1	76153602	1.78E+08	0.371	1.2E+08	0.292
1E+09	2	1	1.75E+08	3.24E+08	0.2135	3.8E+08	0.434
1E+10	2	1	1.13E+08	2.32E+08	0.242	2.4E+08	0.357
1E+11	2	1	1.25E+08	2.42E+08	0.267	2.27E+08	0.405
1E+08	2	1.25	77053338	1.79E+08	0.3735	1.2E+08	0.295
1E+09	2	1.25	1.8E+08	3.22E+08	0.1545	5.21E+08	0.454

Table A.1. Confined compression test results at a density value of 1800 kg/m^3 (cont.)

Emod (Pa)	K_ratio	Fric	Res_mod (Pa)	You_mod (Pa)	Poi_rat	She_mod (Pa)	Fri_Coe
1E+10	2	1.25	1.39E+08	2.94E+08	0.253	2.91E+08	0.352
1E+11	2	1.25	1.34E+08	2.81E+08	0.274	2.56E+08	0.368
1E+08	2	1.5	77476688	1.79E+08	0.3735	1.2E+08	0.296
1E+09	2	1.5	1.97E+08	3.55E+08	0.229	3.88E+08	0.455
1E+10	2	1.5	1.1E+08	2.18E+08	0.2585	2.11E+08	0.341
1E+11	2	1.5	84706294	1.88E+08	0.2185	2.15E+08	0.335
1E+08	2	1.75	77796795	1.79E+08	0.375	1.2E+08	0.297
1E+09	2	1.75	1.73E+08	3.02E+08	0.2145	3.52E+08	0.47
1E+10	2	1.75	1.22E+08	2.44E+08	0.26	2.35E+08	0.374
1E+11	2	1.75	1.02E+08	2.03E+08	0.2365	2.15E+08	0.387
1E+08	2	2	77975899	1.8E+08	0.375	1.2E+08	0.298
1E+09	2	2	1.93E+08	3.38E+08	0.2225	3.8E+08	0.472
1E+10	2	2	1.1E+08	2.17E+08	0.1855	2.92E+08	0.39
1E+11	2	2	1.14E+08	2.21E+08	0.215	2.57E+08	0.398

Table A.2. Confined compression test results at a density value of 1900 kg/m³

Emod (Pa)	K_ratio	Fric	Res_mod (Pa)	You_mod (Pa)	Poi_rat	She_mod (Pa)	Fri_Coe
1E+08	0.5	0.5	78491051	1.78E+08	0.3725	1.19E+08	0.312
1E+09	0.5	0.5	82955191	1.81E+08	0.266	1.7E+08	0.287
1E+10	0.5	0.5	1.22E+08	2.45E+08	0.2205	2.78E+08	0.341
1E+11	0.5	0.5	1.14E+08	2.13E+08	0.2705	1.97E+08	0.401
1E+08	0.5	0.75	87807557	1.86E+08	0.402	1.16E+08	0.342
1E+09	0.5	0.75	97648753	1.99E+08	0.234	2.13E+08	0.311
1E+10	0.5	0.75	1.47E+08	2.86E+08	0.162	4.41E+08	0.371
1E+11	0.5	0.75	1.3E+08	2.23E+08	0.243	2.29E+08	0.439
1E+08	0.5	1	93245978	1.91E+08	0.422	1.13E+08	0.359
1E+09	0.5	1	1.1E+08	2.07E+08	0.2605	1.98E+08	0.346
1E+10	0.5	1	1.35E+08	2.56E+08	0.192	3.33E+08	0.387
1E+11	0.5	1	1.48E+08	2.52E+08	0.231	2.73E+08	0.448
1E+08	0.5	1.25	97101774	1.95E+08	0.4345	1.12E+08	0.37
1E+09	0.5	1.25	1.23E+08	2.23E+08	0.228	2.44E+08	0.37
1E+10	0.5	1.25	1.53E+08	2.71E+08	0.143	4.74E+08	0.436
1E+11	0.5	1.25	1.4E+08	2.27E+08	0.221	2.57E+08	0.49
1E+08	0.5	1.5	99215268	1.97E+08	0.442	1.12E+08	0.377
1E+09	0.5	1.5	1.38E+08	2.41E+08	0.195	3.09E+08	0.387
1E+10	0.5	1.5	1.84E+08	3.38E+08	0.137	6.17E+08	0.407
1E+11	0.5	1.5	1.2E+08	2.11E+08	0.213	2.48E+08	0.425
1E+08	0.5	1.75	1.01E+08	1.99E+08	0.447	1.11E+08	0.381
1E+09	0.5	1.75	1.17E+08	2.18E+08	0.217	2.51E+08	0.365
1E+10	0.5	1.75	1.92E+08	3.38E+08	0.1375	6.15E+08	0.43
1E+11	0.5	1.75	1.63E+08	2.55E+08	0.236	2.71E+08	0.526
1E+08	0.5	2	1.01E+08	1.99E+08	0.451	1.1E+08	0.382
1E+09	0.5	2	1.28E+08	2.25E+08	0.1835	3.06E+08	0.401

Table A.2. Confined compression test results at a density value of 1900 kg/m^3 (cont.)

Emod (Pa)	K_ratio	Fric	Res_mod (Pa)	You_mod (Pa)	Poi_rat	She_mod (Pa)	Fri_Coe
1E+10	0.5	2	1.86E+08	3.22E+08	0.173	4.66E+08	0.458
1E+11	0.5	2	1.71E+08	2.87E+08	0.202	3.56E+08	0.488
1E+08	0.75	0.5	82426294	1.85E+08	0.361	1.28E+08	0.311
1E+09	0.75	0.5	1E+08	2.05E+08	0.2405	2.13E+08	0.335
1E+10	0.75	0.5	1.23E+08	2.52E+08	0.228	2.77E+08	0.381
1E+11	0.75	0.5	1.26E+08	2.75E+08	0.252	2.73E+08	0.331
1E+08	0.75	0.75	89902798	1.93E+08	0.3875	1.24E+08	0.333
1E+09	0.75	0.75	1.19E+08	2.25E+08	0.211	2.66E+08	0.376
1E+10	0.75	0.75	1.43E+08	2.87E+08	0.2275	3.16E+08	0.388
1E+11	0.75	0.75	1.16E+08	2.3E+08	0.2265	2.54E+08	0.369
1E+08	0.75	1	93993132	1.97E+08	0.4015	1.22E+08	0.345
1E+09	0.75	1	1.17E+08	2.26E+08	0.252	2.25E+08	0.353
1E+10	0.75	1	1.63E+08	2.95E+08	0.1525	4.84E+08	0.443
1E+11	0.75	1	1.38E+08	2.52E+08	0.1635	3.86E+08	0.427
1E+08	0.75	1.25	96519657	1.99E+08	0.4115	1.21E+08	0.353
1E+09	0.75	1.25	1.2E+08	2.31E+08	0.234	2.46E+08	0.365
1E+10	0.75	1.25	1.45E+08	2.68E+08	0.1485	4.52E+08	0.427
1E+11	0.75	1.25	1.34E+08	2.4E+08	0.1635	3.67E+08	0.415
1E+08	0.75	1.5	98036143	2E+08	0.416	1.2E+08	0.357
1E+09	0.75	1.5	1.33E+08	2.41E+08	0.238	2.54E+08	0.396
1E+10	0.75	1.5	1.96E+08	3.43E+08	0.139	6.17E+08	0.494
1E+11	0.75	1.5	1.54E+08	3.03E+08	0.1335	5.68E+08	0.401
1E+08	0.75	1.75	99164745	2.01E+08	0.4195	1.2E+08	0.36
1E+09	0.75	1.75	1.47E+08	2.57E+08	0.241	2.67E+08	0.417
1E+10	0.75	1.75	1.7E+08	3.01E+08	0.117	6.44E+08	0.487
1E+11	0.75	1.75	1.3E+08	2.37E+08	0.1025	5.79E+08	0.415

Table A.2. Confined compression test results at a density value of 1900 kg/m^3 (cont.)

Emod (Pa)	K_ratio	Fric	Res_mod (Pa)	You_mod (Pa)	Poi_rat	She_mod (Pa)	Fri_Coe
1E+08	0.75	2	1E+08	2.03E+08	0.4215	1.2E+08	0.362
1E+09	0.75	2	1.44E+08	2.53E+08	0.2315	2.73E+08	0.407
1E+10	0.75	2	1.62E+08	2.81E+08	0.138	5.1E+08	0.476
1E+11	0.75	2	1.66E+08	3.08E+08	0.1795	4.29E+08	0.442
1E+08	1	0.5	76329082	1.78E+08	0.3635	1.23E+08	0.293
1E+09	1	0.5	94043249	1.97E+08	0.301	1.64E+08	0.327
1E+10	1	0.5	1.24E+08	2.16E+08	0.23	2.35E+08	0.415
1E+11	1	0.5	1.29E+08	2.59E+08	0.305	2.12E+08	0.353
1E+08	1	0.75	82303567	1.84E+08	0.3895	1.18E+08	0.312
1E+09	1	0.75	1.14E+08	2.31E+08	0.24	2.4E+08	0.342
1E+10	1	0.75	1.61E+08	2.73E+08	0.2615	2.61E+08	0.441
1E+11	1	0.75	1.1E+08	2.05E+08	0.2665	1.92E+08	0.398
1E+08	1	1	84831107	1.86E+08	0.404	1.15E+08	0.322
1E+09	1	1	1.13E+08	2.15E+08	0.2175	2.47E+08	0.362
1E+10	1	1	1.53E+08	2.58E+08	0.173	3.74E+08	0.45
1E+11	1	1	1.34E+08	2.41E+08	0.187	3.22E+08	0.423
1E+08	1	1.25	86119778	1.86E+08	0.4105	1.13E+08	0.327
1E+09	1	1.25	1.25E+08	2.34E+08	0.239	2.45E+08	0.38
1E+10	1	1.25	1.8E+08	2.95E+08	0.1515	4.85E+08	0.472
1E+11	1	1.25	1.18E+08	2.21E+08	0.173	3.2E+08	0.413
1E+08	1	1.5	87220648	1.87E+08	0.4135	1.13E+08	0.331
1E+09	1	1.5	1.3E+08	2.33E+08	0.2235	2.61E+08	0.405
1E+10	1	1.5	1.64E+08	2.69E+08	0.1875	3.58E+08	0.504
1E+11	1	1.5	2E+08	3.75E+08	0.2065	4.55E+08	0.414
1E+08	1	1.75	87744321	1.87E+08	0.4155	1.13E+08	0.333
1E+09	1	1.75	1.32E+08	2.37E+08	0.2175	2.73E+08	0.404

Table A.2. Confined compression test results at a density value of 1900 kg/m³ (cont.)

Emod (Pa)	K_ratio	Fric	Res_mod (Pa)	You_mod (Pa)	Poi_rat	She_mod (Pa)	Fri_Coe
1E+10	1	1.75	1.4E+08	2.4E+08	0.151	3.97E+08	0.453
1E+11	1	1.75	1.8E+08	3.01E+08	0.2325	3.23E+08	0.481
1E+08	1	2	88137618	1.88E+08	0.417	1.13E+08	0.334
1E+09	1	2	1.27E+08	2.35E+08	0.2445	2.4E+08	0.397
1E+10	1	2	2.2E+08	3.45E+08	0.15	5.74E+08	0.522
1E+11	1	2	1.38E+08	2.45E+08	0.1705	3.59E+08	0.448
1E+08	1.25	0.5	76630679	1.81E+08	0.3685	1.23E+08	0.287
1E+09	1.25	0.5	1.06E+08	2.15E+08	0.211	2.55E+08	0.333
1E+10	1.25	0.5	1.47E+08	2.79E+08	0.228	3.06E+08	0.375
1E+11	1.25	0.5	1.24E+08	2.47E+08	0.2515	2.46E+08	0.38
1E+08	1.25	0.75	83247903	1.87E+08	0.391	1.19E+08	0.307
1E+09	1.25	0.75	1.26E+08	2.34E+08	0.223	2.63E+08	0.379
1E+10	1.25	0.75	1.72E+08	2.97E+08	0.236	3.15E+08	0.425
1E+11	1.25	0.75	80896884	1.88E+08	0.198	2.37E+08	0.307
1E+08	1.25	1	85997873	1.89E+08	0.4005	1.18E+08	0.315
1E+09	1.25	1	1.26E+08	2.41E+08	0.217	2.78E+08	0.38
1E+10	1.25	1	1.44E+08	2.49E+08	0.2	3.11E+08	0.445
1E+11	1.25	1	1.3E+08	2.74E+08	0.1865	3.67E+08	0.346
1E+08	1.25	1.25	87315190	1.91E+08	0.4035	1.18E+08	0.319
1E+09	1.25	1.25	1.27E+08	2.33E+08	0.231	2.53E+08	0.394
1E+10	1.25	1.25	1.52E+08	2.63E+08	0.186	3.53E+08	0.452
1E+11	1.25	1.25	1.52E+08	3.02E+08	0.2045	3.7E+08	0.389
1E+08	1.25	1.5	88232299	1.91E+08	0.405	1.18E+08	0.322
1E+09	1.25	1.5	1.4E+08	2.54E+08	0.202	3.14E+08	0.407
1E+10	1.25	1.5	1.71E+08	2.9E+08	0.1315	5.51E+08	0.453
1E+11	1.25	1.5	1.74E+08	3.49E+08	0.2105	4.15E+08	0.388

Table A.2. Confined compression test results at a density value of 1900 kg/m^3 (cont.)

Emod (Pa)	K_ratio	Fric	Res_mod (Pa)	You_mod (Pa)	Poi_rat	She_mod (Pa)	Fri_Coe
1E+08	1.25	1.75	88578899	1.91E+08	0.4055	1.18E+08	0.323
1E+09	1.25	1.75	1.38E+08	2.48E+08	0.2035	3.04E+08	0.41
1E+10	1.25	1.75	1.68E+08	2.8E+08	0.1875	3.74E+08	0.475
1E+11	1.25	1.75	1.46E+08	3.01E+08	0.195	3.85E+08	0.367
1E+08	1.25	2	88898175	1.92E+08	0.4055	1.18E+08	0.324
1E+09	1.25	2	1.87E+08	3.28E+08	0.243	3.37E+08	0.428
1E+10	1.25	2	3.13E+08	5.43E+08	0.182	7.45E+08	0.448
1E+11	1.25	2	1.16E+08	2.31E+08	0.1585	3.64E+08	0.378
1E+08	1.5	0.5	72810944	1.73E+08	0.346	1.25E+08	0.285
1E+09	1.5	0.5	1.03E+08	2.23E+08	0.193	2.89E+08	0.326
1E+10	1.5	0.5	1.39E+08	2.67E+08	0.363	1.84E+08	0.399
1E+11	1.5	0.5	1.24E+08	2.75E+08	0.305	2.25E+08	0.345
1E+08	1.5	0.75	77404522	1.77E+08	0.3635	1.22E+08	0.299
1E+09	1.5	0.75	1.15E+08	2.48E+08	0.203	3.05E+08	0.329
1E+10	1.5	0.75	1.36E+08	2.63E+08	0.32	2.05E+08	0.376
1E+11	1.5	0.75	97553392	1.96E+08	0.2575	1.9E+08	0.393
1E+08	1.5	1	79157736	1.79E+08	0.372	1.2E+08	0.306
1E+09	1.5	1	1.27E+08	2.65E+08	0.203	3.27E+08	0.343
1E+10	1.5	1	1.47E+08	2.77E+08	0.303	2.28E+08	0.412
1E+11	1.5	1	1.06E+08	2.15E+08	0.2755	1.95E+08	0.401
1E+08	1.5	1.25	80144631	1.8E+08	0.377	1.19E+08	0.309
1E+09	1.5	1.25	1.29E+08	2.6E+08	0.206	3.16E+08	0.366
1E+10	1.5	1.25	1.62E+08	3.2E+08	0.367	2.18E+08	0.377
1E+11	1.5	1.25	1.25E+08	2.7E+08	0.2635	2.57E+08	0.364
1E+08	1.5	1.5	80858273	1.81E+08	0.38	1.19E+08	0.311
1E+09	1.5	1.5	1.34E+08	2.68E+08	0.211	3.18E+08	0.368

Table A.2. Confined compression test results at a density value of 1900 kg/m^3 (cont.)

Emod (Pa)	K_ratio	Fric	Res_mod (Pa)	You_mod (Pa)	Poi_rat	She_mod (Pa)	Fri_Coe
1E+10	1.5	1.5	1.51E+08	2.73E+08	0.273	2.5E+08	0.424
1E+11	1.5	1.5	1.13E+08	2.31E+08	0.2485	2.33E+08	0.399
1E+08	1.5	1.75	81251808	1.81E+08	0.3825	1.18E+08	0.312
1E+09	1.5	1.75	1.39E+08	2.61E+08	0.1995	3.27E+08	0.404
1E+10	1.5	1.75	1.66E+08	3.04E+08	0.3015	2.52E+08	0.408
1E+11	1.5	1.75	2E+08	3.69E+08	0.233	3.96E+08	0.458
1E+08	1.5	2	81468358	1.81E+08	0.3845	1.18E+08	0.313
1E+09	1.5	2	1.42E+08	2.69E+08	0.196	3.42E+08	0.395
1E+10	1.5	2	1.57E+08	2.8E+08	0.264	2.65E+08	0.445
1E+11	1.5	2	1.21E+08	2.17E+08	0.243	2.23E+08	0.467
1E+08	1.75	0.5	73144542	1.81E+08	0.35	1.3E+08	0.283
1E+09	1.75	0.5	94905193	2.08E+08	0.239	2.18E+08	0.304
1E+10	1.75	0.5	1.18E+08	2.41E+08	0.2525	2.38E+08	0.336
1E+11	1.75	0.5	1.25E+08	2.36E+08	0.265	2.23E+08	0.399
1E+08	1.75	0.75	76767992	1.84E+08	0.3635	1.27E+08	0.296
1E+09	1.75	0.75	91613378	2.02E+08	0.2135	2.37E+08	0.301
1E+10	1.75	0.75	1.13E+08	2.2E+08	0.261	2.1E+08	0.347
1E+11	1.75	0.75	1.4E+08	2.45E+08	0.2225	2.75E+08	0.452
1E+08	1.75	1	78570673	1.86E+08	0.369	1.26E+08	0.302
1E+09	1.75	1	1.02E+08	2.23E+08	0.2295	2.43E+08	0.308
1E+10	1.75	1	1.37E+08	2.53E+08	0.285	2.22E+08	0.401
1E+11	1.75	1	2.08E+08	3.57E+08	0.229	3.89E+08	0.46
1E+08	1.75	1.25	79543884	1.87E+08	0.372	1.26E+08	0.304
1E+09	1.75	1.25	1.03E+08	2.14E+08	0.222	2.41E+08	0.33
1E+10	1.75	1.25	1.53E+08	2.9E+08	0.288	2.52E+08	0.38
1E+11	1.75	1.25	2.06E+08	3.4E+08	0.2155	3.94E+08	0.498

Table A.2. Confined compression test results at a density value of 1900 kg/m^3 (cont.)

Emod (Pa)	K_ratio	Fric	Res_mod (Pa)	You_mod (Pa)	Poi_rat	She_mod (Pa)	Fri_Coe
1E+08	1.75	1.5	80019405	1.88E+08	0.3745	1.25E+08	0.305
1E+09	1.75	1.5	1.04E+08	2.05E+08	0.2145	2.39E+08	0.35
1E+10	1.75	1.5	1.78E+08	3.2E+08	0.282	2.84E+08	0.421
1E+11	1.75	1.5	1.6E+08	2.69E+08	0.198	3.39E+08	0.496
1E+08	1.75	1.75	80358767	1.88E+08	0.3755	1.25E+08	0.306
1E+09	1.75	1.75	99255273	1.99E+08	0.215	2.32E+08	0.357
1E+10	1.75	1.75	1.23E+08	2.36E+08	0.2545	2.32E+08	0.395
1E+11	1.75	1.75	1.62E+08	2.63E+08	0.195	3.37E+08	0.497
1E+08	1.75	2	80553167	1.88E+08	0.3765	1.25E+08	0.307
1E+09	1.75	2	99396531	1.93E+08	0.2055	2.35E+08	0.366
1E+10	1.75	2	1.19E+08	2.16E+08	0.243	2.22E+08	0.414
1E+11	1.75	2	1.55E+08	2.52E+08	0.2005	3.14E+08	0.515
1E+08	2	0.5	69689944	1.68E+08	0.34	1.24E+08	0.279
1E+09	2	0.5	1.45E+08	2.98E+08	0.1765	4.22E+08	0.375
1E+10	2	0.5	95404041	2.14E+08	0.308	1.74E+08	0.304
1E+11	2	0.5	73262453	1.62E+08	0.316	1.29E+08	0.32
1E+08	2	0.75	73550961	1.73E+08	0.362	1.2E+08	0.29
1E+09	2	0.75	1.63E+08	3.02E+08	0.2075	3.64E+08	0.434
1E+10	2	0.75	1.22E+08	2.9E+08	0.279	2.6E+08	0.293
1E+11	2	0.75	93335820	1.87E+08	0.2325	2.02E+08	0.375
1E+08	2	1	76162095	1.76E+08	0.369	1.19E+08	0.297
1E+09	2	1	1.72E+08	3.07E+08	0.2	3.84E+08	0.459
1E+10	2	1	1.12E+08	2.21E+08	0.276	2E+08	0.362
1E+11	2	1	1.34E+08	2.84E+08	0.2665	2.66E+08	0.352
1E+08	2	1.25	77157254	1.77E+08	0.3715	1.19E+08	0.3
1E+09	2	1.25	1.76E+08	3.14E+08	0.2	3.92E+08	0.459

Table A.2. Confined compression test results at a density value of 1900 kg/m^3 (cont.)

Emod (Pa)	K_ratio	Fric	Res_mod (Pa)	You_mod (Pa)	Poi_rat	She_mod (Pa)	Fri_Coe
1E+10	2	1.25	1.55E+08	2.89E+08	0.189	3.83E+08	0.418
1E+11	2	1.25	1.21E+08	2.48E+08	0.2235	2.78E+08	0.391
1E+08	2	1.5	77712927	1.78E+08	0.3725	1.19E+08	0.301
1E+09	2	1.5	1.74E+08	3.08E+08	0.2375	3.24E+08	0.46
1E+10	2	1.5	1.34E+08	2.69E+08	0.2855	2.36E+08	0.359
1E+11	2	1.5	96272618	2.05E+08	0.2325	2.21E+08	0.355
1E+08	2	1.75	78059710	1.78E+08	0.3735	1.19E+08	0.302
1E+09	2	1.75	1.78E+08	3.18E+08	0.2135	3.72E+08	0.462
1E+10	2	1.75	1.2E+08	2.4E+08	0.211	2.85E+08	0.384
1E+11	2	1.75	1.27E+08	2.62E+08	0.2065	3.17E+08	0.381
1E+08	2	2	78121693	1.78E+08	0.374	1.19E+08	0.303
1E+09	2	2	1.84E+08	3.18E+08	0.2365	3.36E+08	0.476
1E+10	2	2	1.37E+08	2.7E+08	0.2455	2.75E+08	0.375
1E+11	2	2	1.46E+08	2.9E+08	0.2115	3.43E+08	0.406

Table A.3. Confined compression test results at a density value of 2000 kg/m³

Emod (Pa)	K_ratio	Fric	Res_mod (Pa)	You_mod (Pa)	Poi_rat	She_mod (Pa)	Fri_Coe
1E+08	0.5	0.5	7.8E+07	1.76E+08	0.362	7E+07	0.31
1E+09	0.5	0.5	8.2E+07	1.77E+08	0.2815	7.7E+07	0.298
1E+10	0.5	0.5	1.4E+08	2.81E+08	0.193	1.4E+08	0.357
1E+11	0.5	0.5	1.6E+08	2.86E+08	0.27	1.2E+08	0.424
1E+08	0.5	0.75	8.7E+07	1.85E+08	0.395	7.5E+07	0.337
1E+09	0.5	0.75	9.9E+07	1.93E+08	0.22	9.3E+07	0.34
1E+10	0.5	0.75	1.6E+08	2.99E+08	0.118	1.4E+08	0.386
1E+11	0.5	0.75	1.2E+08	2.07E+08	0.2225	1E+08	0.429
1E+08	0.5	1	9.3E+07	1.89E+08	0.4145	7.8E+07	0.355
1E+09	0.5	1	1.1E+08	2.1E+08	0.261	9E+07	0.366
1E+10	0.5	1	1.6E+08	2.85E+08	0.123	1.5E+08	0.408
1E+11	0.5	1	1.3E+08	2.27E+08	0.2785	1E+08	0.446
1E+08	0.5	1.25	9.6E+07	1.93E+08	0.4265	7.9E+07	0.364
1E+09	0.5	1.25	1.3E+08	2.42E+08	0.248	1.2E+08	0.382
1E+10	0.5	1.25	1.3E+08	2.39E+08	0.1595	1.2E+08	0.416
1E+11	0.5	1.25	1.7E+08	2.77E+08	0.2085	1.4E+08	0.499
1E+08	0.5	1.5	9.8E+07	1.95E+08	0.434	8.5E+07	0.371
1E+09	0.5	1.5	1.3E+08	2.25E+08	0.2365	1.1E+08	0.405
1E+10	0.5	1.5	1.6E+08	3.14E+08	0.1335	1.5E+08	0.388
1E+11	0.5	1.5	1.5E+08	2.48E+08	0.2195	1.3E+08	0.468
1E+08	0.5	1.75	9.9E+07	1.96E+08	0.4405	8.1E+07	0.375
1E+09	0.5	1.75	1.3E+08	2.34E+08	0.2535	1.1E+08	0.386
1E+10	0.5	1.75	1.6E+08	2.84E+08	0.154	1.4E+08	0.436
1E+11	0.5	1.75	1.4E+08	2.37E+08	0.223	1.2E+08	0.498
1E+08	0.5	2	1E+08	1.97E+08	0.4445	7.7E+07	0.378
1E+09	0.5	2	1.3E+08	2.29E+08	0.244	1.1E+08	0.413

Table A.3. Confined compression test results at a density value of 2000 kg/m^3 (cont.)

Emod (Pa)	K_ratio	Fric	Res_mod (Pa)	You_mod (Pa)	Poi_rat	She_mod (Pa)	Fri_Coe
1E+10	0.5	2	2.1E+08	3.57E+08	0.107	1.9E+08	0.463
1E+11	0.5	2	1.2E+08	2.07E+08	0.189	1E+08	0.428
1E+08	0.75	0.5	7.2E+07	1.74E+08	0.342	7.1E+07	0.28
1E+09	0.75	0.5	9E+07	1.9E+08	0.2725	9E+07	0.328
1E+10	0.75	0.5	1.3E+08	2.57E+08	0.205	1.2E+08	0.399
1E+11	0.75	0.5	9.9E+07	2.24E+08	0.152	1.1E+08	0.315
1E+08	0.75	0.75	7.9E+07	1.82E+08	0.377	8.1E+07	0.303
1E+09	0.75	0.75	1E+08	2.13E+08	0.2515	9.4E+07	0.338
1E+10	0.75	0.75	1.4E+08	2.54E+08	0.1815	1.2E+08	0.43
1E+11	0.75	0.75	1.3E+08	2.73E+08	0.0965	1.5E+08	0.354
1E+08	0.75	1	8.3E+07	1.86E+08	0.3905	7.8E+07	0.316
1E+09	0.75	1	1.4E+08	2.76E+08	0.2775	1.2E+08	0.363
1E+10	0.75	1	1.5E+08	2.56E+08	0.198	1.3E+08	0.475
1E+11	0.75	1	2E+08	3.71E+08	0.1065	2E+08	0.42
1E+08	0.75	1.25	8.6E+07	1.9E+08	0.399	8.2E+07	0.323
1E+09	0.75	1.25	1.2E+08	2.22E+08	0.2495	9.9E+07	0.392
1E+10	0.75	1.25	1.7E+08	2.85E+08	0.199	1.3E+08	0.495
1E+11	0.75	1.25	2.1E+08	4.21E+08	0.074	2.1E+08	0.396
1E+08	0.75	1.5	8.8E+07	1.91E+08	0.404	8.5E+07	0.327
1E+09	0.75	1.5	1.1E+08	2.13E+08	0.2355	9.3E+07	0.381
1E+10	0.75	1.5	2E+08	3.26E+08	0.117	1.7E+08	0.505
1E+11	0.75	1.5	2.9E+08	5.3E+08	0.0625	2.9E+08	0.438
1E+08	0.75	1.75	8.8E+07	1.92E+08	0.4075	7.4E+07	0.329
1E+09	0.75	1.75	1.3E+08	2.35E+08	0.271	1.1E+08	0.399
1E+10	0.75	1.75	2E+08	3.3E+08	0.1605	1.7E+08	0.527
1E+11	0.75	1.75	2.4E+08	4.41E+08	0.084	2.5E+08	0.433

Table A.3. Confined compression test results at a density value of 2000 kg/m^3 (cont.)

Emod (Pa)	K_ratio	Fric	Res_mod (Pa)	You_mod (Pa)	Poi_rat	She_mod (Pa)	Fri_Coe
1E+08	0.75	2	8.9E+07	1.93E+08	0.408	7.5E+07	0.331
1E+09	0.75	2	1.3E+08	2.29E+08	0.2395	1.1E+08	0.408
1E+10	0.75	2	1.7E+08	2.79E+08	0.1555	1.5E+08	0.509
1E+11	0.75	2	3E+08	5.75E+08	0.179	2.7E+08	0.39
1E+08	1	0.5	7.2E+07	1.72E+08	0.36	7.4E+07	0.284
1E+09	1	0.5	9.8E+07	2.03E+08	0.2795	9E+07	0.331
1E+10	1	0.5	1.4E+08	2.43E+08	0.194	1.1E+08	0.443
1E+11	1	0.5	1.2E+08	2.54E+08	0.2815	1.2E+08	0.355
1E+08	1	0.75	8E+07	1.8E+08	0.3925	7.2E+07	0.308
1E+09	1	0.75	1.1E+08	2.19E+08	0.261	1E+08	0.351
1E+10	1	0.75	1.5E+08	2.57E+08	0.1715	1.3E+08	0.459
1E+11	1	0.75	1.1E+08	2.12E+08	0.1965	1E+08	0.392
1E+08	1	1	8.5E+07	1.85E+08	0.4075	7.3E+07	0.323
1E+09	1	1	1.3E+08	2.36E+08	0.244	1E+08	0.392
1E+10	1	1	1.9E+08	3.09E+08	0.1285	1.6E+08	0.501
1E+11	1	1	1.2E+08	2.23E+08	0.17	1.2E+08	0.4
1E+08	1	1.25	8.6E+07	1.86E+08	0.412	7.2E+07	0.328
1E+09	1	1.25	1.3E+08	2.37E+08	0.232	1.1E+08	0.4
1E+10	1	1.25	1.6E+08	2.65E+08	0.147	1.4E+08	0.467
1E+11	1	1.25	1.1E+08	2.08E+08	0.1825	1E+08	0.406
1E+08	1	1.5	8.7E+07	1.87E+08	0.414	7.3E+07	0.33
1E+09	1	1.5	1.3E+08	2.37E+08	0.2	1.2E+08	0.417
1E+10	1	1.5	1.6E+08	2.62E+08	0.1135	1.4E+08	0.452
1E+11	1	1.5	1.6E+08	2.65E+08	0.164	1.4E+08	0.482
1E+08	1	1.75	8.8E+07	1.87E+08	0.415	7.3E+07	0.332
1E+09	1	1.75	1.2E+08	2.22E+08	0.234	1.1E+08	0.397

Table A.3. Confined compression test results at a density value of 2000 kg/m^3 (cont.)

Emod (Pa)	K_ratio	Fric	Res_mod (Pa)	You_mod (Pa)	Poi_rat	She_mod (Pa)	Fri_Coe
1E+10	1	1.75	1.8E+08	2.85E+08	0.151	1.4E+08	0.514
1E+11	1	1.75	1.4E+08	2.66E+08	0.193	1.3E+08	0.422
1E+08	1	2	8.8E+07	1.87E+08	0.4155	7.5E+07	0.333
1E+09	1	2	1.3E+08	2.39E+08	0.239	1.1E+08	0.393
1E+10	1	2	1.9E+08	3.01E+08	0.1155	1.5E+08	0.483
1E+11	1	2	1.4E+08	2.44E+08	0.14	1.3E+08	0.456
1E+08	1.25	0.5	7.7E+07	1.8E+08	0.368	7.9E+07	0.287
1E+09	1.25	0.5	1E+08	2.08E+08	0.242	1E+08	0.34
1E+10	1.25	0.5	1.1E+08	2.03E+08	0.225	9.1E+07	0.397
1E+11	1.25	0.5	9.3E+07	2.17E+08	0.2005	1E+08	0.304
1E+08	1.25	0.75	8.3E+07	1.86E+08	0.3895	8.4E+07	0.306
1E+09	1.25	0.75	1.3E+08	2.44E+08	0.25	1.1E+08	0.379
1E+10	1.25	0.75	1.3E+08	2.31E+08	0.203	1.1E+08	0.437
1E+11	1.25	0.75	7.6E+07	1.75E+08	0.227	8E+07	0.305
1E+08	1.25	1	8.7E+07	1.9E+08	0.399	7.5E+07	0.316
1E+09	1.25	1	1.2E+08	2.18E+08	0.2645	1E+08	0.402
1E+10	1.25	1	1.4E+08	2.4E+08	0.2525	1.1E+08	0.431
1E+11	1.25	1	1.2E+08	2.28E+08	0.264	1E+08	0.385
1E+08	1.25	1.25	8.8E+07	1.9E+08	0.401	8.4E+07	0.319
1E+09	1.25	1.25	1.3E+08	2.29E+08	0.264	1E+08	0.42
1E+10	1.25	1.25	1.4E+08	2.44E+08	0.2455	1.1E+08	0.473
1E+11	1.25	1.25	1.2E+08	2.21E+08	0.173	1E+08	0.394
1E+08	1.25	1.5	8.8E+07	1.91E+08	0.4025	7.8E+07	0.321
1E+09	1.25	1.5	1.4E+08	2.45E+08	0.265	1.2E+08	0.422
1E+10	1.25	1.5	2E+08	3.4E+08	0.2285	1.5E+08	0.473
1E+11	1.25	1.5	1.1E+08	2.21E+08	0.205	1E+08	0.345

Table A.3. Confined compression test results at a density value of 2000 kg/m^3 (cont.)

Emod (Pa)	K_ratio	Fric	Res_mod (Pa)	You_mod (Pa)	Poi_rat	She_mod (Pa)	Fri_Coe
1E+08	1.25	1.75	8.9E+07	1.91E+08	0.403	8E+07	0.322
1E+09	1.25	1.75	1.4E+08	2.47E+08	0.256	1.1E+08	0.442
1E+10	1.25	1.75	1.7E+08	2.82E+08	0.175	1.3E+08	0.469
1E+11	1.25	1.75	1E+08	2.11E+08	0.205	1.1E+08	0.356
1E+08	1.25	2	8.9E+07	1.91E+08	0.4035	7.8E+07	0.323
1E+09	1.25	2	1.3E+08	2.38E+08	0.2475	1.1E+08	0.415
1E+10	1.25	2	1.7E+08	2.91E+08	0.166	1.4E+08	0.459
1E+11	1.25	2	1.1E+08	2.26E+08	0.1945	1.1E+08	0.377
1E+08	1.5	0.5	7.2E+07	1.73E+08	0.362	6.9E+07	0.278
1E+09	1.5	0.5	8.6E+07	2.01E+08	0.1935	1E+08	0.296
1E+10	1.5	0.5	1.3E+08	2.45E+08	0.31	1.1E+08	0.383
1E+11	1.5	0.5	9.1E+07	2.1E+08	0.2755	9.2E+07	0.327
1E+08	1.5	0.75	7.6E+07	1.76E+08	0.379	7E+07	0.293
1E+09	1.5	0.75	1.1E+08	2.23E+08	0.193	1.1E+08	0.336
1E+10	1.5	0.75	1.4E+08	2.69E+08	0.309	1.2E+08	0.402
1E+11	1.5	0.75	1.3E+08	2.86E+08	0.321	1.4E+08	0.369
1E+08	1.5	1	7.8E+07	1.77E+08	0.3825	7.1E+07	0.298
1E+09	1.5	1	1E+08	2.14E+08	0.2015	1E+08	0.326
1E+10	1.5	1	1.5E+08	2.74E+08	0.256	1.4E+08	0.41
1E+11	1.5	1	1E+08	2.19E+08	0.263	9.6E+07	0.361
1E+08	1.5	1.25	7.9E+07	1.79E+08	0.385	7.6E+07	0.302
1E+09	1.5	1.25	1.1E+08	2.35E+08	0.208	1.1E+08	0.356
1E+10	1.5	1.25	1.9E+08	3.31E+08	0.211	1.5E+08	0.455
1E+11	1.5	1.25	1.2E+08	2.52E+08	0.2555	1.2E+08	0.426
1E+08	1.5	1.5	8E+07	1.8E+08	0.386	7.2E+07	0.304
1E+09	1.5	1.5	1.2E+08	2.48E+08	0.2135	1.2E+08	0.372

Table A.3. Confined compression test results at a density value of 2000 kg/m³ (cont.)

Emod (Pa)	K_ratio	Fric	Res_mod (Pa)	You_mod (Pa)	Poi_rat	She_mod (Pa)	Fri_Coe
1E+10	1.5	1.5	1.6E+08	2.73E+08	0.239	1.4E+08	0.434
1E+11	1.5	1.5	1.1E+08	2.16E+08	0.255	9.8E+07	0.382
1E+08	1.5	1.75	8E+07	1.8E+08	0.387	7.2E+07	0.305
1E+09	1.5	1.75	1.2E+08	2.44E+08	0.2595	1E+08	0.371
1E+10	1.5	1.75	2.3E+08	4.02E+08	0.259	1.8E+08	0.452
1E+11	1.5	1.75	1.4E+08	2.7E+08	0.22	1.4E+08	0.417
1E+08	1.5	2	8.1E+07	1.8E+08	0.3865	7.1E+07	0.306
1E+09	1.5	2	1.3E+08	2.52E+08	0.2725	1.1E+08	0.388
1E+10	1.5	2	1.4E+08	2.56E+08	0.223	1.2E+08	0.413
1E+11	1.5	2	1.2E+08	2.36E+08	0.2165	1.1E+08	0.386
1E+08	1.75	0.5	7.2E+07	1.76E+08	0.3445	7.3E+07	0.283
1E+09	1.75	0.5	9.8E+07	2.14E+08	0.2405	1.1E+08	0.31
1E+10	1.75	0.5	1E+08	1.98E+08	0.2135	9.4E+07	0.345
1E+11	1.75	0.5	1.7E+08	3.04E+08	0.274	1.4E+08	0.42
1E+08	1.75	0.75	7.8E+07	1.82E+08	0.3595	7.4E+07	0.297
1E+09	1.75	0.75	9.8E+07	2E+08	0.2325	9.6E+07	0.336
1E+10	1.75	0.75	1.1E+08	2.15E+08	0.2185	9.6E+07	0.354
1E+11	1.75	0.75	1.4E+08	2.46E+08	0.3035	1.1E+08	0.453
1E+08	1.75	1	8E+07	1.84E+08	0.3655	7.6E+07	0.303
1E+09	1.75	1	1.1E+08	2.25E+08	0.1905	1.1E+08	0.355
1E+10	1.75	1	1.4E+08	2.74E+08	0.1685	1.3E+08	0.378
1E+11	1.75	1	2.3E+08	3.97E+08	0.2905	1.8E+08	0.455
1E+08	1.75	1.25	8.1E+07	1.85E+08	0.3685	8.2E+07	0.306
1E+09	1.75	1.25	1E+08	2.13E+08	0.1795	1.1E+08	0.34
1E+10	1.75	1.25	1.6E+08	2.83E+08	0.281	1.2E+08	0.399
1E+11	1.75	1.25	2.5E+08	4.31E+08	0.2505	2E+08	0.472

Table A.3. Confined compression test results at a density value of 2000 kg/m^3 (cont.)

Emod (Pa)	K_ratio	Fric	Res_mod (Pa)	You_mod (Pa)	Poi_rat	She_mod (Pa)	Fri_Coe
1E+08	1.75	1.5	8.1E+07	1.86E+08	0.3695	8.5E+07	0.307
1E+09	1.75	1.5	1.2E+08	2.28E+08	0.1925	1.1E+08	0.378
1E+10	1.75	1.5	1.2E+08	2.16E+08	0.196	1.1E+08	0.394
1E+11	1.75	1.5	1.9E+08	3.09E+08	0.2375	1.4E+08	0.518
1E+08	1.75	1.75	8.1E+07	1.86E+08	0.3705	7.5E+07	0.308
1E+09	1.75	1.75	1.2E+08	2.31E+08	0.2005	1.2E+08	0.368
1E+10	1.75	1.75	1.4E+08	2.52E+08	0.199	1.2E+08	0.415
1E+11	1.75	1.75	2.4E+08	4.01E+08	0.2305	1.9E+08	0.503
1E+08	1.75	2	8.2E+07	1.86E+08	0.3715	8.4E+07	0.309
1E+09	1.75	2	1.2E+08	2.13E+08	0.2135	1E+08	0.384
1E+10	1.75	2	1.5E+08	2.67E+08	0.198	1.2E+08	0.407
1E+11	1.75	2	1.5E+08	2.5E+08	0.2425	1.1E+08	0.495
1E+08	2	0.5	6.5E+07	1.69E+08	0.337	7.2E+07	0.258
1E+09	2	0.5	1.4E+08	2.8E+08	0.233	1.4E+08	0.378
1E+10	2	0.5	1.2E+08	2.82E+08	0.296	1.2E+08	0.299
1E+11	2	0.5	8.7E+07	2.03E+08	0.246	9E+07	0.32
1E+08	2	0.75	6.9E+07	1.73E+08	0.3515	7.6E+07	0.27
1E+09	2	0.75	1.6E+08	3.07E+08	0.16	1.5E+08	0.407
1E+10	2	0.75	1.3E+08	2.83E+08	0.239	1.3E+08	0.328
1E+11	2	0.75	1E+08	2.2E+08	0.206	1.1E+08	0.36
1E+08	2	1	7.1E+07	1.75E+08	0.3575	7.4E+07	0.277
1E+09	2	1	1.7E+08	3.05E+08	0.196	1.5E+08	0.456
1E+10	2	1	1.3E+08	2.68E+08	0.2555	1.2E+08	0.377
1E+11	2	1	1.1E+08	2.31E+08	0.2265	1.1E+08	0.344
1E+08	2	1.25	7.2E+07	1.77E+08	0.361	7.1E+07	0.28
1E+09	2	1.25	1.8E+08	3.33E+08	0.2035	1.7E+08	0.446

Table A.3. Confined compression test results at a density value of 2000 kg/m^3 (cont.)

Emod (Pa)	K_ratio	Fric	Res_mod (Pa)	You_mod (Pa)	Poi_rat	She_mod (Pa)	Fri_Coe
1E+10	2	1.25	1.1E+08	2.39E+08	0.2245	1.1E+08	0.333
1E+11	2	1.25	1.4E+08	2.79E+08	0.2605	1.2E+08	0.412
1E+08	2	1.5	7.3E+07	1.78E+08	0.3625	7.1E+07	0.283
1E+09	2	1.5	1.8E+08	3.26E+08	0.199	1.6E+08	0.458
1E+10	2	1.5	1.4E+08	2.76E+08	0.2515	1.3E+08	0.369
1E+11	2	1.5	1E+08	2.17E+08	0.2585	1.1E+08	0.361
1E+08	2	1.75	7.3E+07	1.78E+08	0.363	7.2E+07	0.283
1E+09	2	1.75	1.8E+08	3.31E+08	0.224	1.5E+08	0.451
1E+10	2	1.75	8.4E+07	1.92E+08	0.2525	9.6E+07	0.314
1E+11	2	1.75	1.3E+08	2.66E+08	0.246	1.2E+08	0.372
1E+08	2	2	7.3E+07	1.78E+08	0.3645	7.6E+07	0.284
1E+09	2	2	1.9E+08	3.39E+08	0.194	1.6E+08	0.473
1E+10	2	2	1.1E+08	2.37E+08	0.2425	1.1E+08	0.351
1E+11	2	2	1.4E+08	2.5E+08	0.224	1.2E+08	0.457

Table A.4. Confined compression test results at a density value of 2200 kg/m^3

Emod (Pa)	K_ratio	Fric	Res_mod (Pa)	You_mod (Pa)	Poi_rat	She_mod (Pa)	Fri_Coe
1E+08	0.5	0.5	69188132	1.7E+08	0.355	1.2E+08	0.277
1E+09	0.5	0.5	79065482	1.76E+08	0.293	1.5E+08	0.277
1E+10	0.5	0.5	1.39E+08	2.69E+08	0.223	3.01E+08	0.375
1E+11	0.5	0.5	1E+08	1.85E+08	0.2255	2.05E+08	0.39
1E+08	0.5	0.75	80361888	1.79E+08	0.3885	1.15E+08	0.315
1E+09	0.5	0.75	1.16E+08	2.16E+08	0.252	2.14E+08	0.357
1E+10	0.5	0.75	1.04E+08	2E+08	0.1705	2.93E+08	0.349
1E+11	0.5	0.75	1.2E+08	2.13E+08	0.1825	2.92E+08	0.448
1E+08	0.5	1	87352455	1.86E+08	0.4125	1.13E+08	0.337
1E+09	0.5	1	1.05E+08	2.03E+08	0.244	2.07E+08	0.342
1E+10	0.5	1	1.49E+08	2.71E+08	0.204	3.32E+08	0.414
1E+11	0.5	1	1.36E+08	2.36E+08	0.161	3.67E+08	0.457
1E+08	0.5	1.25	91053994	1.9E+08	0.4215	1.13E+08	0.348
1E+09	0.5	1.25	1.11E+08	2.05E+08	0.216	2.37E+08	0.366
1E+10	0.5	1.25	1.58E+08	3.02E+08	0.212	3.56E+08	0.388
1E+11	0.5	1.25	1.5E+08	2.47E+08	0.185	3.34E+08	0.483
1E+08	0.5	1.5	93095373	1.92E+08	0.428	1.12E+08	0.354
1E+09	0.5	1.5	1.12E+08	2.01E+08	0.2125	2.36E+08	0.38
1E+10	0.5	1.5	1.7E+08	2.92E+08	0.137	5.33E+08	0.448
1E+11	0.5	1.5	1.6E+08	2.54E+08	0.1935	3.29E+08	0.531
1E+08	0.5	1.75	94040753	1.93E+08	0.432	1.12E+08	0.357
1E+09	0.5	1.75	1.27E+08	2.21E+08	0.2205	2.51E+08	0.4
1E+10	0.5	1.75	1.76E+08	3.17E+08	0.147	5.4E+08	0.432
1E+11	0.5	1.75	1.87E+08	3.23E+08	0.1755	4.6E+08	0.439
1E+08	0.5	2	94570385	1.94E+08	0.4345	1.11E+08	0.359
1E+09	0.5	2	1.13E+08	2.05E+08	0.2165	2.37E+08	0.384

Table A.4. Confined compression test results at a density value of 2200 kg/m^3 (cont.)

Emod (Pa)	K_ratio	Fric	Res_mod (Pa)	You_mod (Pa)	Poi_rat	She_mod (Pa)	Fri_Coe
1E+10	0.5	2	2.32E+08	4.35E+08	0.1485	7.32E+08	0.413
1E+11	0.5	2	1.39E+08	2.27E+08	0.188	3.02E+08	0.508
1E+08	0.75	0.5	77981704	1.82E+08	0.367	1.24E+08	0.297
1E+09	0.75	0.5	1.03E+08	2.1E+08	0.2325	2.26E+08	0.336
1E+10	0.75	0.5	1.37E+08	2.89E+08	0.1925	3.75E+08	0.36
1E+11	0.75	0.5	2.15E+08	4.86E+08	0.2775	4.38E+08	0.307
1E+08	0.75	0.75	84343341	1.88E+08	0.392	1.2E+08	0.318
1E+09	0.75	0.75	1.35E+08	2.57E+08	0.2145	2.99E+08	0.378
1E+10	0.75	0.75	1.89E+08	3.55E+08	0.174	5.1E+08	0.435
1E+11	0.75	0.75	2.03E+08	4.17E+08	0.159	6.55E+08	0.355
1E+08	0.75	1	88639238	1.92E+08	0.409	1.17E+08	0.331
1E+09	0.75	1	1.38E+08	2.68E+08	0.2265	2.96E+08	0.369
1E+10	0.75	1	1.6E+08	2.94E+08	0.197	3.73E+08	0.456
1E+11	0.75	1	1.64E+08	2.8E+08	0.1505	4.65E+08	0.447
1E+08	0.75	1.25	91209611	1.94E+08	0.4165	1.17E+08	0.339
1E+09	0.75	1.25	1.37E+08	2.62E+08	0.2275	2.88E+08	0.381
1E+10	0.75	1.25	1.69E+08	2.94E+08	0.129	5.69E+08	0.475
1E+11	0.75	1.25	2.56E+08	4.5E+08	0.0835	1.35E+09	0.448
1E+08	0.75	1.5	92429913	1.95E+08	0.421	1.16E+08	0.343
1E+09	0.75	1.5	1.42E+08	2.65E+08	0.214	3.09E+08	0.395
1E+10	0.75	1.5	1.67E+08	2.98E+08	0.142	5.24E+08	0.45
1E+11	0.75	1.5	1.84E+08	3.2E+08	0.075	1.07E+09	0.457
1E+08	0.75	1.75	93182704	1.96E+08	0.4235	1.16E+08	0.346
1E+09	0.75	1.75	1.33E+08	2.38E+08	0.2115	2.81E+08	0.408
1E+10	0.75	1.75	2.2E+08	3.74E+08	0.1085	8.61E+08	0.508
1E+11	0.75	1.75	1.99E+08	3.37E+08	0.082	1.03E+09	0.452

Table A.4. Confined compression test results at a density value of 2200 kg/m^3 (cont.)

Emod (Pa)	K_ratio	Fric	Res_mod (Pa)	You_mod (Pa)	Poi_rat	She_mod (Pa)	Fri_Coe
1E+08	0.75	2	94091001	1.96E+08	0.426	1.15E+08	0.349
1E+09	0.75	2	1.46E+08	2.58E+08	0.193	3.33E+08	0.421
1E+10	0.75	2	1.81E+08	3E+08	0.1425	5.27E+08	0.518
1E+11	0.75	2	1.51E+08	2.79E+08	0.1205	5.8E+08	0.413
1E+08	1	0.5	73447001	1.75E+08	0.3635	1.2E+08	0.29
1E+09	1	0.5	97503521	1.99E+08	0.286	1.73E+08	0.335
1E+10	1	0.5	1.44E+08	2.5E+08	0.2615	2.4E+08	0.436
1E+11	1	0.5	89559519	1.8E+08	0.257	1.75E+08	0.351
1E+08	1	0.75	79999779	1.8E+08	0.3875	1.16E+08	0.314
1E+09	1	0.75	1.13E+08	2.1E+08	0.2615	2E+08	0.372
1E+10	1	0.75	1.62E+08	2.86E+08	0.1735	4.11E+08	0.429
1E+11	1	0.75	92481123	1.82E+08	0.2015	2.25E+08	0.368
1E+08	1	1	83717581	1.83E+08	0.398	1.15E+08	0.326
1E+09	1	1	1.1E+08	2.1E+08	0.2205	2.38E+08	0.365
1E+10	1	1	1.49E+08	2.44E+08	0.197	3.11E+08	0.464
1E+11	1	1	1.15E+08	2.04E+08	0.1675	3.04E+08	0.417
1E+08	1	1.25	85696847	1.85E+08	0.4035	1.15E+08	0.331
1E+09	1	1.25	1.3E+08	2.35E+08	0.243	2.42E+08	0.394
1E+10	1	1.25	1.44E+08	2.44E+08	0.14	4.37E+08	0.453
1E+11	1	1.25	1.36E+08	2.42E+08	0.154	3.93E+08	0.431
1E+08	1	1.5	86743982	1.86E+08	0.4045	1.15E+08	0.334
1E+09	1	1.5	1.19E+08	2.22E+08	0.23	2.41E+08	0.382
1E+10	1	1.5	2.14E+08	3.72E+08	0.1745	5.33E+08	0.42
1E+11	1	1.5	1.34E+08	2.37E+08	0.143	4.13E+08	0.441
1E+08	1	1.75	87455986	1.86E+08	0.4055	1.15E+08	0.336
1E+09	1	1.75	1.26E+08	2.22E+08	0.2205	2.52E+08	0.405

Table A.4. Confined compression test results at a density value of 2200 kg/m^3 (cont.)

Emod (Pa)	K_ratio	Fric	Res_mod (Pa)	You_mod (Pa)	Poi_rat	She_mod (Pa)	Fri_Coe
1E+10	1	1.75	1.7E+08	2.73E+08	0.0825	8.25E+08	0.476
1E+11	1	1.75	1.32E+08	2.58E+08	0.171	3.77E+08	0.376
1E+08	1	2	87915370	1.87E+08	0.406	1.15E+08	0.338
1E+09	1	2	1.11E+08	2.1E+08	0.209	2.51E+08	0.37
1E+10	1	2	1.42E+08	2.4E+08	0.1595	3.76E+08	0.467
1E+11	1	2	1.25E+08	2.5E+08	0.1625	3.83E+08	0.39
1E+08	1.25	0.5	76320797	1.8E+08	0.3755	1.2E+08	0.286
1E+09	1.25	0.5	94125487	2.04E+08	0.242	2.11E+08	0.308
1E+10	1.25	0.5	1.61E+08	2.98E+08	0.3495	2.13E+08	0.389
1E+11	1.25	0.5	87157292	1.97E+08	0.2475	1.99E+08	0.312
1E+08	1.25	0.75	82666873	1.86E+08	0.396	1.18E+08	0.304
1E+09	1.25	0.75	1.13E+08	2.22E+08	0.275	2.02E+08	0.36
1E+10	1.25	0.75	1.44E+08	2.66E+08	0.284	2.34E+08	0.4
1E+11	1.25	0.75	1.1E+08	2.21E+08	0.2355	2.35E+08	0.368
1E+08	1.25	1	86406454	1.9E+08	0.404	1.18E+08	0.314
1E+09	1.25	1	1.25E+08	2.35E+08	0.2405	2.44E+08	0.381
1E+10	1.25	1	1.42E+08	2.41E+08	0.228	2.64E+08	0.457
1E+11	1.25	1	87749527	1.95E+08	0.217	2.25E+08	0.304
1E+08	1.25	1.25	87828559	1.91E+08	0.4075	1.17E+08	0.318
1E+09	1.25	1.25	1.43E+08	2.52E+08	0.249	2.53E+08	0.423
1E+10	1.25	1.25	1.37E+08	2.33E+08	0.174	3.35E+08	0.43
1E+11	1.25	1.25	1.3E+08	2.52E+08	0.214	2.94E+08	0.414
1E+08	1.25	1.5	88322045	1.92E+08	0.409	1.17E+08	0.32
1E+09	1.25	1.5	1.36E+08	2.54E+08	0.2245	2.83E+08	0.377
1E+10	1.25	1.5	1.34E+08	2.26E+08	0.161	3.52E+08	0.458
1E+11	1.25	1.5	1.52E+08	2.93E+08	0.2165	3.38E+08	0.409

Table A.4. Confined compression test results at a density value of 2200 kg/m^3 (cont.)

Emod (Pa)	K_ratio	Fric	Res_mod (Pa)	You_mod (Pa)	Poi_rat	She_mod (Pa)	Fri_Coe
1E+08	1.25	1.75	88619545	1.92E+08	0.4095	1.17E+08	0.321
1E+09	1.25	1.75	1.33E+08	2.38E+08	0.2215	2.68E+08	0.401
1E+10	1.25	1.75	1.58E+08	2.56E+08	0.194	3.3E+08	0.479
1E+11	1.25	1.75	1E+08	2.19E+08	0.2235	2.45E+08	0.347
1E+08	1.25	2	88824397	1.92E+08	0.4095	1.17E+08	0.322
1E+09	1.25	2	1.35E+08	2.44E+08	0.212	2.87E+08	0.409
1E+10	1.25	2	1.36E+08	2.37E+08	0.1855	3.2E+08	0.45
1E+11	1.25	2	1.11E+08	2.42E+08	0.232	2.61E+08	0.338
1E+08	1.5	0.5	73653914	1.76E+08	0.3555	1.24E+08	0.282
1E+09	1.5	0.5	98273425	2.14E+08	0.2265	2.37E+08	0.321
1E+10	1.5	0.5	1.33E+08	2.42E+08	0.346	1.75E+08	0.417
1E+11	1.5	0.5	97340886	2.21E+08	0.246	2.24E+08	0.339
1E+08	1.5	0.75	77292733	1.78E+08	0.371	1.2E+08	0.296
1E+09	1.5	0.75	1.03E+08	2.19E+08	0.1905	2.87E+08	0.335
1E+10	1.5	0.75	1.67E+08	3.24E+08	0.308	2.63E+08	0.387
1E+11	1.5	0.75	1.2E+08	2.69E+08	0.229	2.94E+08	0.328
1E+08	1.5	1	79571311	1.8E+08	0.377	1.2E+08	0.303
1E+09	1.5	1	1.11E+08	2.3E+08	0.2205	2.61E+08	0.344
1E+10	1.5	1	1.63E+08	2.96E+08	0.2615	2.83E+08	0.426
1E+11	1.5	1	1.07E+08	2.27E+08	0.241	2.35E+08	0.365
1E+08	1.5	1.25	80825907	1.82E+08	0.38	1.2E+08	0.307
1E+09	1.5	1.25	1.08E+08	2.21E+08	0.228	2.43E+08	0.351
1E+10	1.5	1.25	1.65E+08	3.18E+08	0.266	2.98E+08	0.401
1E+11	1.5	1.25	1.03E+08	2.2E+08	0.226	2.44E+08	0.355
1E+08	1.5	1.5	81775742	1.83E+08	0.3825	1.2E+08	0.309
1E+09	1.5	1.5	1.01E+08	2.13E+08	0.226	2.36E+08	0.345

Table A.4. Confined compression test results at a density value of 2200 kg/m^3 (cont.)

Emod (Pa)	K_ratio	Fric	Res_mod (Pa)	You_mod (Pa)	Poi_rat	She_mod (Pa)	Fri_Coe
1E+10	1.5	1.5	2.03E+08	3.96E+08	0.307	3.23E+08	0.404
1E+11	1.5	1.5	1.12E+08	2.14E+08	0.201	2.66E+08	0.393
1E+08	1.5	1.75	82065280	1.83E+08	0.3835	1.19E+08	0.31
1E+09	1.5	1.75	1.24E+08	2.43E+08	0.222	2.74E+08	0.375
1E+10	1.5	1.75	1.88E+08	3.41E+08	0.25	3.41E+08	0.465
1E+11	1.5	1.75	1.37E+08	2.71E+08	0.2075	3.27E+08	0.397
1E+08	1.5	2	82150301	1.83E+08	0.3855	1.19E+08	0.31
1E+09	1.5	2	1.21E+08	2.36E+08	0.2075	2.85E+08	0.381
1E+10	1.5	2	1.5E+08	2.69E+08	0.283	2.38E+08	0.435
1E+11	1.5	2	1.49E+08	2.64E+08	0.1855	3.56E+08	0.499
1E+08	1.75	0.5	72014260	1.73E+08	0.3565	1.22E+08	0.287
1E+09	1.75	0.5	80959641	1.8E+08	0.2645	1.7E+08	0.302
1E+10	1.75	0.5	1.28E+08	2.4E+08	0.3165	1.9E+08	0.373
1E+11	1.75	0.5	1.33E+08	2.32E+08	0.265	2.19E+08	0.429
1E+08	1.75	0.75	76701637	1.78E+08	0.3705	1.2E+08	0.301
1E+09	1.75	0.75	93899667	1.94E+08	0.242	2E+08	0.331
1E+10	1.75	0.75	1.38E+08	2.55E+08	0.254	2.51E+08	0.398
1E+11	1.75	0.75	1.38E+08	2.42E+08	0.214	2.83E+08	0.447
1E+08	1.75	1	78616031	1.8E+08	0.3775	1.19E+08	0.307
1E+09	1.75	1	82724997	1.81E+08	0.24	1.88E+08	0.306
1E+10	1.75	1	1.43E+08	2.56E+08	0.2055	3.11E+08	0.412
1E+11	1.75	1	1.66E+08	3.05E+08	0.233	3.28E+08	0.425
1E+08	1.75	1.25	79669160	1.81E+08	0.381	1.19E+08	0.311
1E+09	1.75	1.25	92932299	1.97E+08	0.19	2.59E+08	0.318
1E+10	1.75	1.25	1.12E+08	2.09E+08	0.227	2.3E+08	0.381
1E+11	1.75	1.25	1.75E+08	2.81E+08	0.192	3.66E+08	0.488

Table A.4. Confined compression test results at a density value of 2200 kg/m^3 (cont.)

Emod (Pa)	K_ratio	Fric	Res_mod (Pa)	You_mod (Pa)	Poi_rat	She_mod (Pa)	Fri_Coe
1E+08	1.75	1.5	80495921	1.82E+08	0.3825	1.19E+08	0.312
1E+09	1.75	1.5	98455915	1.99E+08	0.2135	2.33E+08	0.345
1E+10	1.75	1.5	2.07E+08	3.64E+08	0.212	4.3E+08	0.455
1E+11	1.75	1.5	1.45E+08	2.46E+08	0.217	2.83E+08	0.467
1E+08	1.75	1.75	81259716	1.83E+08	0.3825	1.19E+08	0.314
1E+09	1.75	1.75	93334330	1.92E+08	0.213	2.25E+08	0.34
1E+10	1.75	1.75	1.33E+08	2.48E+08	0.2335	2.66E+08	0.395
1E+11	1.75	1.75	1.85E+08	3.01E+08	0.2245	3.35E+08	0.522
1E+08	1.75	2	81488842	1.83E+08	0.384	1.19E+08	0.315
1E+09	1.75	2	1.04E+08	2.08E+08	0.201	2.59E+08	0.35
1E+10	1.75	2	1.4E+08	2.39E+08	0.137	4.36E+08	0.435
1E+11	1.75	2	1.32E+08	2.31E+08	0.1625	3.55E+08	0.458
1E+08	2	0.5	68846709	1.69E+08	0.335	1.26E+08	0.275
1E+09	2	0.5	1.44E+08	2.86E+08	0.178	4.01E+08	0.391
1E+10	2	0.5	1.1E+08	2.52E+08	0.28	2.24E+08	0.31
1E+11	2	0.5	83768039	1.9E+08	0.305	1.56E+08	0.314
1E+08	2	0.75	73153480	1.73E+08	0.357	1.22E+08	0.288
1E+09	2	0.75	1.69E+08	3.15E+08	0.185	4.26E+08	0.434
1E+10	2	0.75	1.05E+08	2.25E+08	0.2995	1.88E+08	0.34
1E+11	2	0.75	1.05E+08	2.22E+08	0.294	1.89E+08	0.361
1E+08	2	1	75842125	1.77E+08	0.363	1.22E+08	0.295
1E+09	2	1	1.69E+08	3.06E+08	0.2195	3.49E+08	0.444
1E+10	2	1	97812912	2.16E+08	0.2515	2.15E+08	0.326
1E+11	2	1	1.06E+08	2.04E+08	0.257	1.99E+08	0.419
1E+08	2	1.25	76934237	1.78E+08	0.366	1.21E+08	0.298
1E+09	2	1.25	1.86E+08	3.37E+08	0.2175	3.87E+08	0.449

Table A.4. Confined compression test results at a density value of 2200 kg/m^3 (cont.)

Emod (Pa)	K_ratio	Fric	Res_mod (Pa)	You_mod (Pa)	Poi_rat	She_mod (Pa)	Fri_Coe
1E+10	2	1.25	88501084	1.99E+08	0.221	2.25E+08	0.314
1E+11	2	1.25	1.06E+08	2.17E+08	0.268	2.03E+08	0.378
1E+08	2	1.5	77359724	1.78E+08	0.367	1.21E+08	0.299
1E+09	2	1.5	1.78E+08	3.14E+08	0.168	4.67E+08	0.468
1E+10	2	1.5	1.52E+08	3.15E+08	0.259	3.04E+08	0.362
1E+11	2	1.5	94104849	1.95E+08	0.2595	1.88E+08	0.375
1E+08	2	1.75	77467724	1.78E+08	0.368	1.21E+08	0.3
1E+09	2	1.75	1.77E+08	3.1E+08	0.2215	3.5E+08	0.471
1E+10	2	1.75	1.34E+08	2.49E+08	0.2625	2.37E+08	0.435
1E+11	2	1.75	93385728	1.94E+08	0.2815	1.73E+08	0.366
1E+08	2	2	77487031	1.78E+08	0.369	1.21E+08	0.3
1E+09	2	2	1.97E+08	3.32E+08	0.206	4.03E+08	0.504
1E+10	2	2	1.39E+08	2.65E+08	0.267	2.48E+08	0.421
1E+11	2	2	95170919	2.05E+08	0.2755	1.86E+08	0.364

Table A.5. Confined compression test results at a density value of 2400 kg/m^3

Emod (Pa)	K_ratio	Fric	Res_mod (Pa)	You_mod (Pa)	Poi_rat	She_mod (Pa)	Fri_Coe
1E+08	0.5	0.5	75030821	1.74E+08	0.366	1.19E+08	0.303
1E+09	0.5	0.5	80161729	1.76E+08	0.2645	1.66E+08	0.286
1E+10	0.5	0.5	1.47E+08	2.7E+08	0.2145	3.14E+08	0.407
1E+11	0.5	0.5	1.34E+08	2.51E+08	0.29	2.16E+08	0.392
1E+08	0.5	0.75	85115952	1.84E+08	0.399	1.15E+08	0.334
1E+09	0.5	0.75	1.1E+08	2.18E+08	0.2635	2.07E+08	0.32
1E+10	0.5	0.75	1.21E+08	2.31E+08	0.1925	3.01E+08	0.377
1E+11	0.5	0.75	1.26E+08	2.24E+08	0.274	2.05E+08	0.444
1E+08	0.5	1	91006038	1.9E+08	0.419	1.13E+08	0.353
1E+09	0.5	1	1.07E+08	2.01E+08	0.2375	2.11E+08	0.35
1E+10	0.5	1	1.33E+08	2.54E+08	0.213	2.98E+08	0.397
1E+11	0.5	1	1.63E+08	2.79E+08	0.2365	2.95E+08	0.459
1E+08	0.5	1.25	94627408	1.93E+08	0.431	1.12E+08	0.365
1E+09	0.5	1.25	1.03E+08	1.96E+08	0.2545	1.92E+08	0.344
1E+10	0.5	1.25	1.42E+08	2.51E+08	0.161	3.9E+08	0.421
1E+11	0.5	1.25	1.61E+08	2.79E+08	0.2125	3.28E+08	0.483
1E+08	0.5	1.5	97371411	1.95E+08	0.4385	1.11E+08	0.373
1E+09	0.5	1.5	1.24E+08	2.28E+08	0.195	2.92E+08	0.358
1E+10	0.5	1.5	1.29E+08	2.45E+08	0.1295	4.72E+08	0.37
1E+11	0.5	1.5	1.42E+08	2.34E+08	0.2175	2.69E+08	0.507
1E+08	0.5	1.75	99298020	1.97E+08	0.4435	1.11E+08	0.378
1E+09	0.5	1.75	1.46E+08	2.69E+08	0.237	2.84E+08	0.356
1E+10	0.5	1.75	1.6E+08	2.81E+08	0.0945	7.42E+08	0.439
1E+11	0.5	1.75	1.65E+08	2.7E+08	0.2275	2.97E+08	0.481
1E+08	0.5	2	1E+08	1.98E+08	0.4475	1.11E+08	0.381
1E+09	0.5	2	1.16E+08	2.14E+08	0.236	2.27E+08	0.361

Table A.5. Confined compression test results at a density value of 2400 kg/m^3 (cont.)

Emod (Pa)	K_ratio	Fric	Res_mod (Pa)	You_mod (Pa)	Poi_rat	She_mod (Pa)	Fri_Coe
1E+10	0.5	2	1.99E+08	3.53E+08	0.1315	6.73E+08	0.424
1E+11	0.5	2	1.59E+08	2.6E+08	0.1805	3.6E+08	0.5
1E+08	0.75	0.5	74752788	1.79E+08	0.3525	1.27E+08	0.287
1E+09	0.75	0.5	1.09E+08	2.19E+08	0.2685	2.04E+08	0.352
1E+10	0.75	0.5	1.19E+08	2.29E+08	0.228	2.51E+08	0.392
1E+11	0.75	0.5	1.04E+08	2.13E+08	0.1775	3E+08	0.345
1E+08	0.75	0.75	81636132	1.85E+08	0.3795	1.21E+08	0.311
1E+09	0.75	0.75	1.25E+08	2.36E+08	0.2295	2.57E+08	0.377
1E+10	0.75	0.75	1.25E+08	2.38E+08	0.1875	3.17E+08	0.405
1E+11	0.75	0.75	1.14E+08	2.42E+08	0.1985	3.05E+08	0.321
1E+08	0.75	1	85903446	1.89E+08	0.392	1.2E+08	0.324
1E+09	0.75	1	1.08E+08	2.09E+08	0.1895	2.76E+08	0.364
1E+10	0.75	1	1.65E+08	2.86E+08	0.1465	4.89E+08	0.471
1E+11	0.75	1	2.6E+08	4.93E+08	0.169	7.3E+08	0.41
1E+08	0.75	1.25	88251697	1.91E+08	0.3995	1.2E+08	0.331
1E+09	0.75	1.25	1.31E+08	2.3E+08	0.2395	2.4E+08	0.413
1E+10	0.75	1.25	1.89E+08	3.25E+08	0.128	6.35E+08	0.49
1E+11	0.75	1.25	2.09E+08	4.01E+08	0.18	5.57E+08	0.395
1E+08	0.75	1.5	89602365	1.93E+08	0.4035	1.19E+08	0.334
1E+09	0.75	1.5	1.37E+08	2.53E+08	0.2005	3.16E+08	0.387
1E+10	0.75	1.5	2.01E+08	3.44E+08	0.1375	6.26E+08	0.502
1E+11	0.75	1.5	2.18E+08	4E+08	0.156	6.41E+08	0.43
1E+08	0.75	1.75	90551443	1.94E+08	0.4055	1.19E+08	0.337
1E+09	0.75	1.75	1.42E+08	2.48E+08	0.216	2.87E+08	0.419
1E+10	0.75	1.75	2.97E+08	4.99E+08	0.17	7.35E+08	0.531
1E+11	0.75	1.75	3.38E+08	6.25E+08	0.2385	6.55E+08	0.432

Table A.5. Confined compression test results at a density value of 2400 kg/m³ (cont.)

Emod (Pa)	K_ratio	Fric	Res_mod (Pa)	You_mod (Pa)	Poi_rat	She_mod (Pa)	Fri_Coe
1E+08	0.75	2	91490650	1.94E+08	0.4075	1.19E+08	0.34
1E+09	0.75	2	1.46E+08	2.66E+08	0.1745	3.81E+08	0.389
1E+10	0.75	2	1.72E+08	3.06E+08	0.1295	5.91E+08	0.467
1E+11	0.75	2	1.74E+08	2.88E+08	0.1515	4.76E+08	0.473
1E+08	1	0.5	72530329	1.71E+08	0.356	1.2E+08	0.289
1E+09	1	0.5	92029201	1.9E+08	0.2945	1.61E+08	0.329
1E+10	1	0.5	1.41E+08	2.57E+08	0.185	3.47E+08	0.39
1E+11	1	0.5	89320139	1.85E+08	0.2595	1.78E+08	0.344
1E+08	1	0.75	79988628	1.79E+08	0.388	1.16E+08	0.31
1E+09	1	0.75	85961153	1.81E+08	0.249	1.81E+08	0.317
1E+10	1	0.75	1.3E+08	2.35E+08	0.205	2.87E+08	0.407
1E+11	1	0.75	1.16E+08	2.14E+08	0.2375	2.25E+08	0.416
1E+08	1	1	83142571	1.82E+08	0.4025	1.13E+08	0.321
1E+09	1	1	1.11E+08	2.09E+08	0.263	1.98E+08	0.378
1E+10	1	1	1.63E+08	2.7E+08	0.1175	5.73E+08	0.465
1E+11	1	1	1.21E+08	2.29E+08	0.195	2.94E+08	0.409
1E+08	1	1.25	85189550	1.84E+08	0.408	1.13E+08	0.327
1E+09	1	1.25	1.13E+08	2.1E+08	0.2235	2.35E+08	0.383
1E+10	1	1.25	1.78E+08	2.89E+08	0.122	5.93E+08	0.481
1E+11	1	1.25	1.39E+08	2.69E+08	0.1665	4.04E+08	0.371
1E+08	1	1.5	86651258	1.85E+08	0.4115	1.13E+08	0.331
1E+09	1	1.5	1.12E+08	2.07E+08	0.235	2.21E+08	0.385
1E+10	1	1.5	1.94E+08	2.99E+08	0.1355	5.52E+08	0.497
1E+11	1	1.5	1.54E+08	2.57E+08	0.1935	3.32E+08	0.485
1E+08	1	1.75	87259034	1.86E+08	0.4135	1.12E+08	0.333
1E+09	1	1.75	1.13E+08	2.08E+08	0.2105	2.47E+08	0.388

Table A.5. Confined compression test results at a density value of 2400 kg/m^3 (cont.)

Emod (Pa)	K_ratio	Fric	Res_mod (Pa)	You_mod (Pa)	Poi_rat	She_mod (Pa)	Fri_Coe
1E+10	1	1.75	2.11E+08	3.23E+08	0.177	4.56E+08	0.531
1E+11	1	1.75	1.28E+08	2.37E+08	0.1565	3.78E+08	0.39
1E+08	1	2	87592105	1.86E+08	0.4145	1.12E+08	0.334
1E+09	1	2	1.16E+08	2.11E+08	0.254	2.08E+08	0.395
1E+10	1	2	1.91E+08	2.97E+08	0.056	1.33E+09	0.515
1E+11	1	2	1.56E+08	2.79E+08	0.224	3.11E+08	0.435
1E+08	1.25	0.5	74189074	1.77E+08	0.3705	1.19E+08	0.284
1E+09	1.25	0.5	1.01E+08	2.07E+08	0.2575	2.01E+08	0.337
1E+10	1.25	0.5	1.21E+08	2.3E+08	0.2555	2.25E+08	0.378
1E+11	1.25	0.5	97558264	2.18E+08	0.2165	2.51E+08	0.32
1E+08	1.25	0.75	80204123	1.83E+08	0.3895	1.17E+08	0.303
1E+09	1.25	0.75	1.15E+08	2.26E+08	0.2485	2.27E+08	0.357
1E+10	1.25	0.75	1.69E+08	3E+08	0.204	3.68E+08	0.41
1E+11	1.25	0.75	1.04E+08	2.15E+08	0.1895	2.84E+08	0.35
1E+08	1.25	1	82972582	1.85E+08	0.3965	1.17E+08	0.311
1E+09	1.25	1	1.23E+08	2.32E+08	0.266	2.18E+08	0.395
1E+10	1.25	1	1.19E+08	2.08E+08	0.172	3.02E+08	0.425
1E+11	1.25	1	1.07E+08	2.09E+08	0.158	3.3E+08	0.376
1E+08	1.25	1.25	84364141	1.87E+08	0.3995	1.17E+08	0.315
1E+09	1.25	1.25	1.45E+08	2.55E+08	0.2195	2.9E+08	0.432
1E+10	1.25	1.25	1.35E+08	2.31E+08	0.184	3.15E+08	0.436
1E+11	1.25	1.25	1.16E+08	2.22E+08	0.1385	4.01E+08	0.39
1E+08	1.25	1.5	85199398	1.87E+08	0.401	1.17E+08	0.317
1E+09	1.25	1.5	1.44E+08	2.55E+08	0.229	2.79E+08	0.434
1E+10	1.25	1.5	1.47E+08	2.41E+08	0.149	4.04E+08	0.476
1E+11	1.25	1.5	1.14E+08	2.28E+08	0.1685	3.37E+08	0.369

Table A.5. Confined compression test results at a density value of 2400 kg/m^3 (cont.)

Emod (Pa)	K_ratio	Fric	Res_mod (Pa)	You_mod (Pa)	Poi_rat	She_mod (Pa)	Fri_Coe
1E+08	1.25	1.75	85760213	1.88E+08	0.4025	1.17E+08	0.319
1E+09	1.25	1.75	1.37E+08	2.4E+08	0.2225	2.7E+08	0.43
1E+10	1.25	1.75	1.48E+08	2.44E+08	0.157	3.89E+08	0.49
1E+11	1.25	1.75	1.28E+08	2.54E+08	0.162	3.93E+08	0.392
1E+08	1.25	2	86212364	1.88E+08	0.403	1.17E+08	0.32
1E+09	1.25	2	1.44E+08	2.42E+08	0.24	2.52E+08	0.456
1E+10	1.25	2	1.39E+08	2.3E+08	0.148	3.89E+08	0.456
1E+11	1.25	2	96151009	1.99E+08	0.153	3.25E+08	0.36
1E+08	1.5	0.5	74882690	1.79E+08	0.3465	1.29E+08	0.287
1E+09	1.5	0.5	85071491	1.95E+08	0.226	2.15E+08	0.307
1E+10	1.5	0.5	1.42E+08	2.75E+08	0.3335	2.06E+08	0.391
1E+11	1.5	0.5	93388060	2.14E+08	0.2465	2.17E+08	0.326
1E+08	1.5	0.75	79283108	1.82E+08	0.3655	1.24E+08	0.303
1E+09	1.5	0.75	94421633	2.1E+08	0.186	2.82E+08	0.32
1E+10	1.5	0.75	1.79E+08	3.36E+08	0.336	2.5E+08	0.401
1E+11	1.5	0.75	1.05E+08	2.16E+08	0.2585	2.09E+08	0.358
1E+08	1.5	1	81440436	1.84E+08	0.374	1.23E+08	0.311
1E+09	1.5	1	1.02E+08	2.25E+08	0.197	2.85E+08	0.319
1E+10	1.5	1	1.53E+08	2.72E+08	0.2735	2.49E+08	0.427
1E+11	1.5	1	1.15E+08	2.36E+08	0.2465	2.39E+08	0.395
1E+08	1.5	1.25	82306427	1.84E+08	0.378	1.22E+08	0.314
1E+09	1.5	1.25	1.14E+08	2.33E+08	0.178	3.28E+08	0.356
1E+10	1.5	1.25	1.44E+08	2.72E+08	0.254	2.67E+08	0.408
1E+11	1.5	1.25	2.09E+08	4.08E+08	0.2315	4.41E+08	0.417
1E+08	1.5	1.5	83283930	1.85E+08	0.3805	1.22E+08	0.317
1E+09	1.5	1.5	1.21E+08	2.48E+08	0.2255	2.76E+08	0.365

Table A.5. Confined compression test results at a density value of 2400 kg/m^3 (cont.)

Emod (Pa)	K_ratio	Fric	Res_mod (Pa)	You_mod (Pa)	Poi_rat	She_mod (Pa)	Fri_Coe
1E+10	1.5	1.5	2E+08	3.55E+08	0.264	3.36E+08	0.468
1E+11	1.5	1.5	1.56E+08	2.99E+08	0.234	3.19E+08	0.434
1E+08	1.5	1.75	83815663	1.86E+08	0.382	1.21E+08	0.318
1E+09	1.5	1.75	1.57E+08	3.25E+08	0.19	4.28E+08	0.348
1E+10	1.5	1.75	1.67E+08	2.96E+08	0.2195	3.38E+08	0.443
1E+11	1.5	1.75	1.58E+08	3.4E+08	0.219	3.88E+08	0.374
1E+08	1.5	2	84149127	1.86E+08	0.3825	1.21E+08	0.319
1E+09	1.5	2	1.3E+08	2.53E+08	0.208	3.04E+08	0.381
1E+10	1.5	2	1.41E+08	2.54E+08	0.2505	2.53E+08	0.429
1E+11	1.5	2	1.33E+08	2.52E+08	0.209	3.02E+08	0.419
1E+08	1.75	0.5	71650258	1.75E+08	0.3495	1.25E+08	0.284
1E+09	1.75	0.5	86375066	1.99E+08	0.276	1.8E+08	0.292
1E+10	1.75	0.5	2.07E+08	4.27E+08	0.2975	3.59E+08	0.336
1E+11	1.75	0.5	1.28E+08	2.35E+08	0.3355	1.75E+08	0.416
1E+08	1.75	0.75	75590610	1.79E+08	0.3625	1.23E+08	0.296
1E+09	1.75	0.75	83905525	1.87E+08	0.2125	2.19E+08	0.3
1E+10	1.75	0.75	1.28E+08	2.36E+08	0.2225	2.66E+08	0.395
1E+11	1.75	0.75	1.42E+08	2.53E+08	0.3005	2.1E+08	0.449
1E+08	1.75	1	77776111	1.81E+08	0.3705	1.22E+08	0.303
1E+09	1.75	1	86744565	1.85E+08	0.23	2.01E+08	0.324
1E+10	1.75	1	1.28E+08	2.52E+08	0.2555	2.46E+08	0.353
1E+11	1.75	1	1.34E+08	2.36E+08	0.214	2.75E+08	0.458
1E+08	1.75	1.25	78516589	1.82E+08	0.374	1.21E+08	0.305
1E+09	1.75	1.25	93404889	1.97E+08	0.2245	2.19E+08	0.334
1E+10	1.75	1.25	1.61E+08	2.98E+08	0.2525	2.96E+08	0.386
1E+11	1.75	1.25	1.6E+08	2.8E+08	0.284	2.46E+08	0.463

Table A.5. Confined compression test results at a density value of 2400 kg/m^3 (cont.)

Emod (Pa)	K_ratio	Fric	Res_mod (Pa)	You_mod (Pa)	Poi_rat	She_mod (Pa)	Fri_Coe
1E+08	1.75	1.5	78997876	1.82E+08	0.376	1.21E+08	0.307
1E+09	1.75	1.5	1.02E+08	2.14E+08	0.2385	2.24E+08	0.328
1E+10	1.75	1.5	1.72E+08	2.95E+08	0.2155	3.42E+08	0.452
1E+11	1.75	1.5	1.58E+08	2.59E+08	0.265	2.44E+08	0.465
1E+08	1.75	1.75	79457883	1.83E+08	0.378	1.21E+08	0.308
1E+09	1.75	1.75	1.08E+08	2.15E+08	0.235	2.28E+08	0.347
1E+10	1.75	1.75	2.26E+08	4.17E+08	0.256	4.07E+08	0.406
1E+11	1.75	1.75	1.37E+08	2.33E+08	0.238	2.45E+08	0.461
1E+08	1.75	2	79795453	1.83E+08	0.3795	1.21E+08	0.309
1E+09	1.75	2	1.04E+08	2.13E+08	0.229	2.32E+08	0.34
1E+10	1.75	2	1.53E+08	2.72E+08	0.1855	3.67E+08	0.436
1E+11	1.75	2	1.63E+08	2.74E+08	0.2375	2.89E+08	0.484
1E+08	2	0.5	68722351	1.69E+08	0.3365	1.25E+08	0.273
1E+09	2	0.5	1.4E+08	2.83E+08	0.1935	3.66E+08	0.383
1E+10	2	0.5	93157532	2.36E+08	0.325	1.81E+08	0.261
1E+11	2	0.5	79584066	1.93E+08	0.261	1.85E+08	0.306
1E+08	2	0.75	73179913	1.74E+08	0.3545	1.22E+08	0.286
1E+09	2	0.75	1.67E+08	3.16E+08	0.217	3.64E+08	0.429
1E+10	2	0.75	1.64E+08	3.39E+08	0.2465	3.43E+08	0.366
1E+11	2	0.75	79522184	1.7E+08	0.2635	1.61E+08	0.341
1E+08	2	1	76056425	1.77E+08	0.363	1.22E+08	0.293
1E+09	2	1	1.73E+08	3.18E+08	0.1935	4.11E+08	0.449
1E+10	2	1	2.04E+08	4.3E+08	0.2285	4.7E+08	0.359
1E+11	2	1	1.16E+08	2.32E+08	0.2365	2.45E+08	0.373
1E+08	2	1.25	77280467	1.79E+08	0.3665	1.22E+08	0.296
1E+09	2	1.25	1.63E+08	2.96E+08	0.214	3.45E+08	0.462

Table A.5. Confined compression test results at a density value of 2400 kg/m^3 (cont.)

Emod (Pa)	K_ratio	Fric	Res_mod (Pa)	You_mod (Pa)	Poi_rat	She_mod (Pa)	Fri_Coe
1E+10	2	1.25	1.68E+08	3.32E+08	0.2315	3.59E+08	0.386
1E+11	2	1.25	1.08E+08	2.2E+08	0.241	2.28E+08	0.397
1E+08	2	1.5	77761496	1.79E+08	0.368	1.22E+08	0.298
1E+09	2	1.5	1.76E+08	3.2E+08	0.2045	3.91E+08	0.459
1E+10	2	1.5	1.25E+08	2.46E+08	0.227	2.71E+08	0.388
1E+11	2	1.5	1.38E+08	2.43E+08	0.2315	2.62E+08	0.455
1E+08	2	1.75	78032354	1.8E+08	0.369	1.22E+08	0.298
1E+09	2	1.75	1.77E+08	3.09E+08	0.2285	3.38E+08	0.476
1E+10	2	1.75	1.49E+08	2.94E+08	0.2325	3.17E+08	0.381
1E+11	2	1.75	90895724	1.9E+08	0.2095	2.27E+08	0.363
1E+08	2	2	78166764	1.8E+08	0.3695	1.22E+08	0.299
1E+09	2	2	1.79E+08	3.23E+08	0.1985	4.07E+08	0.462
1E+10	2	2	1.08E+08	2.18E+08	0.212	2.57E+08	0.363
1E+11	2	2	1.42E+08	2.51E+08	0.187	3.36E+08	0.471

Table A.6. Confined compression test results at a density value of 2600 kg/m^3

Emod (Pa)	K_ratio	Fric	Res_mod (Pa)	You_mod (Pa)	Poi_rat	She_mod (Pa)	Fri_Coe
1E+08	0.5	0.5	75308136	1.74E+08	0.3585	1.21E+08	0.302
1E+09	0.5	0.5	1.03E+08	2.12E+08	0.279	1.9E+08	0.32
1E+10	0.5	0.5	1.24E+08	2.43E+08	0.198	3.07E+08	0.372
1E+11	0.5	0.5	1.22E+08	2.23E+08	0.287	1.94E+08	0.405
1E+08	0.5	0.75	83454427	1.82E+08	0.387	1.18E+08	0.328
1E+09	0.5	0.75	1.09E+08	2.09E+08	0.2325	2.25E+08	0.336
1E+10	0.5	0.75	1.68E+08	3.42E+08	0.236	3.62E+08	0.339
1E+11	0.5	0.75	1.78E+08	3.28E+08	0.249	3.29E+08	0.414
1E+08	0.5	1	90376462	1.88E+08	0.409	1.15E+08	0.349
1E+09	0.5	1	1.15E+08	2.11E+08	0.205	2.58E+08	0.363
1E+10	0.5	1	1.9E+08	3.99E+08	0.209	4.78E+08	0.356
1E+11	0.5	1	1.68E+08	2.82E+08	0.208	3.4E+08	0.483
1E+08	0.5	1.25	95071814	1.93E+08	0.425	1.13E+08	0.363
1E+09	0.5	1.25	1.29E+08	2.28E+08	0.228	2.51E+08	0.391
1E+10	0.5	1.25	1.33E+08	2.52E+08	0.123	5.13E+08	0.383
1E+11	0.5	1.25	1.37E+08	2.4E+08	0.22	2.73E+08	0.459
1E+08	0.5	1.5	98504996	1.96E+08	0.434	1.13E+08	0.373
1E+09	0.5	1.5	1.49E+08	2.69E+08	0.2685	2.5E+08	0.379
1E+10	0.5	1.5	1.67E+08	3E+08	0.127	5.91E+08	0.431
1E+11	0.5	1.5	1.9E+08	3.11E+08	0.176	4.41E+08	0.498
1E+08	0.5	1.75	1E+08	1.97E+08	0.4395	1.12E+08	0.378
1E+09	0.5	1.75	1.33E+08	2.33E+08	0.213	2.73E+08	0.4
1E+10	0.5	1.75	1.34E+08	2.42E+08	0.149	4.07E+08	0.4
1E+11	0.5	1.75	1.35E+08	2.39E+08	0.212	2.82E+08	0.458
1E+08	0.5	2	1.01E+08	1.98E+08	0.4425	1.12E+08	0.381
1E+09	0.5	2	1.34E+08	2.34E+08	0.251	2.33E+08	0.404

Table A.6. Confined compression test results at a density value of 2600 kg/m³ (cont.)

Emod (Pa)	K_ratio	Fric	Res_mod (Pa)	You_mod (Pa)	Poi_rat	She_mod (Pa)	Fri_Coe
1E+10	0.5	2	1.42E+08	2.46E+08	0.1135	5.42E+08	0.416
1E+11	0.5	2	2.13E+08	3.56E+08	0.198	4.5E+08	0.507
1E+08	0.75	0.5	69747683	1.72E+08	0.353	1.22E+08	0.276
1E+09	0.75	0.5	98425093	2.04E+08	0.2595	1.97E+08	0.335
1E+10	0.75	0.5	1.42E+08	2.74E+08	0.21	3.26E+08	0.415
1E+11	0.75	0.5	1.37E+08	2.7E+08	0.191	3.54E+08	0.366
1E+08	0.75	0.75	76470822	1.79E+08	0.3825	1.17E+08	0.297
1E+09	0.75	0.75	1.14E+08	2.21E+08	0.229	2.41E+08	0.365
1E+10	0.75	0.75	1.91E+08	3.49E+08	0.152	5.72E+08	0.455
1E+11	0.75	0.75	1.17E+08	2.54E+08	0.156	4.06E+08	0.343
1E+08	0.75	1	80144300	1.83E+08	0.398	1.15E+08	0.308
1E+09	0.75	1	1.28E+08	2.37E+08	0.219	2.71E+08	0.399
1E+10	0.75	1	1.75E+08	3.14E+08	0.153	5.13E+08	0.463
1E+11	0.75	1	1.91E+08	3.44E+08	0.1205	7.14E+08	0.453
1E+08	0.75	1.25	82435176	1.86E+08	0.4055	1.14E+08	0.315
1E+09	0.75	1.25	1.15E+08	2.14E+08	0.235	2.27E+08	0.399
1E+10	0.75	1.25	2.06E+08	3.77E+08	0.125	7.55E+08	0.438
1E+11	0.75	1.25	1.75E+08	3.25E+08	0.101	8.06E+08	0.412
1E+08	0.75	1.5	84208885	1.87E+08	0.4105	1.14E+08	0.32
1E+09	0.75	1.5	1.26E+08	2.32E+08	0.248	2.34E+08	0.397
1E+10	0.75	1.5	2.26E+08	3.74E+08	0.0435	2.14E+09	0.525
1E+11	0.75	1.5	2.12E+08	3.76E+08	0.0745	1.26E+09	0.443
1E+08	0.75	1.75	85609324	1.89E+08	0.4135	1.14E+08	0.324
1E+09	0.75	1.75	1.38E+08	2.47E+08	0.2005	3.08E+08	0.412
1E+10	0.75	1.75	1.88E+08	3.08E+08	0.127	6.07E+08	0.513
1E+11	0.75	1.75	2.2E+08	3.65E+08	0.0935	9.78E+08	0.503

Table A.6. Confined compression test results at a density value of 2600 kg/m^3 (cont.)

Emod (Pa)	K_ratio	Fric	Res_mod (Pa)	You_mod (Pa)	Poi_rat	She_mod (Pa)	Fri_Coe
1E+08	0.75	2	86951197	1.9E+08	0.4155	1.15E+08	0.327
1E+09	0.75	2	1.29E+08	2.32E+08	0.239	2.43E+08	0.413
1E+10	0.75	2	1.62E+08	2.9E+08	0.1975	3.67E+08	0.467
1E+11	0.75	2	2.55E+08	4.31E+08	0.1325	8.12E+08	0.471
1E+08	1	0.5	72588319	1.73E+08	0.359	1.2E+08	0.285
1E+09	1	0.5	90335897	1.88E+08	0.303	1.55E+08	0.326
1E+10	1	0.5	1.64E+08	3.02E+08	0.214	3.52E+08	0.391
1E+11	1	0.5	97892816	1.99E+08	0.255	1.96E+08	0.352
1E+08	1	0.75	79765917	1.8E+08	0.388	1.16E+08	0.307
1E+09	1	0.75	1.07E+08	2.11E+08	0.254	2.08E+08	0.353
1E+10	1	0.75	1.71E+08	2.83E+08	0.2105	3.36E+08	0.454
1E+11	1	0.75	1E+08	1.92E+08	0.2025	2.37E+08	0.384
1E+08	1	1	82921892	1.82E+08	0.403	1.13E+08	0.319
1E+09	1	1	1.22E+08	2.3E+08	0.2385	2.41E+08	0.384
1E+10	1	1	2.04E+08	3.23E+08	0.161	5.03E+08	0.497
1E+11	1	1	1.63E+08	2.86E+08	0.2005	3.57E+08	0.473
1E+08	1	1.25	84805081	1.84E+08	0.4085	1.13E+08	0.325
1E+09	1	1.25	1.23E+08	2.28E+08	0.2575	2.21E+08	0.388
1E+10	1	1.25	1.68E+08	2.74E+08	0.1225	5.59E+08	0.485
1E+11	1	1.25	1.1E+08	2.22E+08	0.146	3.8E+08	0.374
1E+08	1	1.5	85754658	1.85E+08	0.412	1.12E+08	0.327
1E+09	1	1.5	1.28E+08	2.43E+08	0.2295	2.64E+08	0.374
1E+10	1	1.5	1.61E+08	2.57E+08	0.108	5.93E+08	0.498
1E+11	1	1.5	1.09E+08	2.21E+08	0.1805	3.06E+08	0.368
1E+08	1	1.75	86237467	1.85E+08	0.414	1.12E+08	0.329
1E+09	1	1.75	1.34E+08	2.43E+08	0.2465	2.46E+08	0.41

Table A.6. Confined compression test results at a density value of 2600 kg/m³ (cont.)

Emod (Pa)	K_ratio	Fric	Res_mod (Pa)	You_mod (Pa)	Poi_rat	She_mod (Pa)	Fri_Coe
1E+10	1	1.75	1.7E+08	2.65E+08	0.1455	4.56E+08	0.508
1E+11	1	1.75	1.33E+08	2.55E+08	0.134	4.77E+08	0.407
1E+08	1	2	86592372	1.86E+08	0.415	1.12E+08	0.33
1E+09	1	2	1.36E+08	2.39E+08	0.246	2.43E+08	0.431
1E+10	1	2	2E+08	3.17E+08	0.129	6.15E+08	0.525
1E+11	1	2	1.46E+08	2.58E+08	0.1615	3.99E+08	0.437
1E+08	1.25	0.5	81096472	1.85E+08	0.3675	1.26E+08	0.296
1E+09	1.25	0.5	93754979	2.04E+08	0.242	2.1E+08	0.314
1E+10	1.25	0.5	1.19E+08	2.3E+08	0.2715	2.11E+08	0.365
1E+11	1.25	0.5	95633357	2.04E+08	0.2795	1.82E+08	0.343
1E+08	1.25	0.75	86466310	1.9E+08	0.3855	1.23E+08	0.313
1E+09	1.25	0.75	1.22E+08	2.36E+08	0.246	2.4E+08	0.37
1E+10	1.25	0.75	1.26E+08	2.24E+08	0.2135	2.62E+08	0.417
1E+11	1.25	0.75	1.04E+08	2.06E+08	0.2475	2.09E+08	0.362
1E+08	1.25	1	89252198	1.92E+08	0.3915	1.23E+08	0.321
1E+09	1.25	1	1.34E+08	2.56E+08	0.225	2.85E+08	0.378
1E+10	1.25	1	1.57E+08	2.82E+08	0.2245	3.14E+08	0.407
1E+11	1.25	1	1.34E+08	2.73E+08	0.2305	2.96E+08	0.368
1E+08	1.25	1.25	90178905	1.93E+08	0.394	1.22E+08	0.324
1E+09	1.25	1.25	1.32E+08	2.44E+08	0.1945	3.14E+08	0.392
1E+10	1.25	1.25	1.66E+08	2.72E+08	0.197	3.46E+08	0.468
1E+11	1.25	1.25	1.41E+08	2.74E+08	0.228	3E+08	0.378
1E+08	1.25	1.5	90900757	1.94E+08	0.396	1.22E+08	0.326
1E+09	1.25	1.5	1.37E+08	2.47E+08	0.22	2.8E+08	0.42
1E+10	1.25	1.5	1.38E+08	2.52E+08	0.227	2.77E+08	0.397
1E+11	1.25	1.5	1.64E+08	3.59E+08	0.2635	3.4E+08	0.342

Table A.6. Confined compression test results at a density value of 2600 kg/m^3 (cont.)

Emod (Pa)	K_ratio	Fric	Res_mod (Pa)	You_mod (Pa)	Poi_rat	She_mod (Pa)	Fri_Coe
1E+08	1.25	1.75	91471555	1.94E+08	0.3965	1.22E+08	0.328
1E+09	1.25	1.75	1.4E+08	2.46E+08	0.1915	3.21E+08	0.426
1E+10	1.25	1.75	1.46E+08	2.47E+08	0.177	3.48E+08	0.447
1E+11	1.25	1.75	1.08E+08	2.19E+08	0.1855	2.95E+08	0.342
1E+08	1.25	2	91657984	1.94E+08	0.397	1.22E+08	0.329
1E+09	1.25	2	1.48E+08	2.53E+08	0.2205	2.88E+08	0.446
1E+10	1.25	2	1.66E+08	2.92E+08	0.208	3.51E+08	0.437
1E+11	1.25	2	1.22E+08	2.45E+08	0.205	2.99E+08	0.364
1E+08	1.5	0.5	71851879	1.74E+08	0.3575	1.22E+08	0.278
1E+09	1.5	0.5	80816782	1.97E+08	0.2445	2.01E+08	0.285
1E+10	1.5	0.5	1.05E+08	2.04E+08	0.305	1.67E+08	0.38
1E+11	1.5	0.5	1.29E+08	2.72E+08	0.203	3.35E+08	0.378
1E+08	1.5	0.75	75635895	1.76E+08	0.3725	1.19E+08	0.292
1E+09	1.5	0.75	96983667	2.11E+08	0.2095	2.52E+08	0.314
1E+10	1.5	0.75	1.47E+08	2.79E+08	0.2875	2.43E+08	0.402
1E+11	1.5	0.75	1.42E+08	2.94E+08	0.2275	3.24E+08	0.367
1E+08	1.5	1	78090418	1.79E+08	0.379	1.18E+08	0.3
1E+09	1.5	1	1.05E+08	2.24E+08	0.2255	2.48E+08	0.336
1E+10	1.5	1	1.21E+08	2.38E+08	0.275	2.16E+08	0.379
1E+11	1.5	1	1.18E+08	2.37E+08	0.172	3.44E+08	0.409
1E+08	1.5	1.25	79021537	1.8E+08	0.382	1.18E+08	0.302
1E+09	1.5	1.25	1.21E+08	2.64E+08	0.231	2.85E+08	0.319
1E+10	1.5	1.25	1.9E+08	3.6E+08	0.2745	3.28E+08	0.422
1E+11	1.5	1.25	1.11E+08	2.21E+08	0.1965	2.82E+08	0.404
1E+08	1.5	1.5	79424481	1.8E+08	0.383	1.18E+08	0.303
1E+09	1.5	1.5	1.07E+08	2.24E+08	0.204	2.75E+08	0.342

Table A.6. Confined compression test results at a density value of 2600 kg/m^3 (cont.)

Emod (Pa)	K_ratio	Fric	Res_mod (Pa)	You_mod (Pa)	Poi_rat	She_mod (Pa)	Fri_Coe
1E+10	1.5	1.5	1.24E+08	2.34E+08	0.2025	2.89E+08	0.41
1E+11	1.5	1.5	1.28E+08	2.37E+08	0.2015	2.94E+08	0.445
1E+08	1.5	1.75	79860925	1.81E+08	0.385	1.17E+08	0.304
1E+09	1.5	1.75	1.19E+08	2.42E+08	0.2235	2.71E+08	0.362
1E+10	1.5	1.75	2.26E+08	4.18E+08	0.219	4.76E+08	0.434
1E+11	1.5	1.75	1.12E+08	2.19E+08	0.1615	3.39E+08	0.402
1E+08	1.5	2	80111157	1.81E+08	0.386	1.17E+08	0.305
1E+09	1.5	2	1.21E+08	2.42E+08	0.251	2.41E+08	0.36
1E+10	1.5	2	1.42E+08	2.64E+08	0.1895	3.48E+08	0.433
1E+11	1.5	2	2.05E+08	3.8E+08	0.104	9.13E+08	0.458
1E+08	1.75	0.5	73780702	1.74E+08	0.355	1.23E+08	0.291
1E+09	1.75	0.5	87834706	1.94E+08	0.2665	1.82E+08	0.303
1E+10	1.75	0.5	1.39E+08	2.85E+08	0.309	2.3E+08	0.344
1E+11	1.75	0.5	1.29E+08	2.42E+08	0.261	2.32E+08	0.416
1E+08	1.75	0.75	79397541	1.8E+08	0.372	1.21E+08	0.308
1E+09	1.75	0.75	92380164	1.95E+08	0.245	1.99E+08	0.328
1E+10	1.75	0.75	1.3E+08	2.46E+08	0.3425	1.8E+08	0.372
1E+11	1.75	0.75	1.47E+08	2.67E+08	0.2405	2.78E+08	0.422
1E+08	1.75	1	81606305	1.82E+08	0.3775	1.21E+08	0.315
1E+09	1.75	1	89796538	1.91E+08	0.237	2.02E+08	0.324
1E+10	1.75	1	1.39E+08	2.64E+08	0.2095	3.15E+08	0.372
1E+11	1.75	1	1.82E+08	3E+08	0.228	3.29E+08	0.496
1E+08	1.75	1.25	82835476	1.83E+08	0.3805	1.21E+08	0.318
1E+09	1.75	1.25	1.06E+08	2.1E+08	0.2065	2.53E+08	0.361
1E+10	1.75	1.25	1.52E+08	2.84E+08	0.22	3.22E+08	0.386
1E+11	1.75	1.25	1.7E+08	2.8E+08	0.206	3.4E+08	0.508

Table A.6. Confined compression test results at a density value of 2600 kg/m^3 (cont.)

Emod (Pa)	K_ratio	Fric	Res_mod (Pa)	You_mod (Pa)	Poi_rat	She_mod (Pa)	Fri_Coe
1E+08	1.75	1.5	83582902	1.84E+08	0.3825	1.2E+08	0.32
1E+09	1.75	1.5	1.04E+08	2.05E+08	0.2035	2.53E+08	0.36
1E+10	1.75	1.5	1.42E+08	2.65E+08	0.2475	2.68E+08	0.397
1E+11	1.75	1.5	1.65E+08	2.73E+08	0.242	2.83E+08	0.483
1E+08	1.75	1.75	84115539	1.85E+08	0.3835	1.2E+08	0.321
1E+09	1.75	1.75	1.13E+08	2.16E+08	0.2015	2.68E+08	0.383
1E+10	1.75	1.75	2.36E+08	4.16E+08	0.188	5.54E+08	0.416
1E+11	1.75	1.75	1.24E+08	2.24E+08	0.2485	2.25E+08	0.411
1E+08	1.75	2	84504850	1.85E+08	0.3845	1.2E+08	0.322
1E+09	1.75	2	1.14E+08	2.12E+08	0.2205	2.41E+08	0.388
1E+10	1.75	2	2.01E+08	3.44E+08	0.224	3.84E+08	0.44
1E+11	1.75	2	1.78E+08	2.96E+08	0.2355	3.14E+08	0.497
1E+08	2	0.5	68336082	1.68E+08	0.3365	1.25E+08	0.274
1E+09	2	0.5	1.5E+08	3.03E+08	0.18	4.2E+08	0.383
1E+10	2	0.5	1.4E+08	3.3E+08	0.284	2.9E+08	0.294
1E+11	2	0.5	86692996	1.84E+08	0.299	1.54E+08	0.353
1E+08	2	0.75	72343490	1.72E+08	0.3575	1.21E+08	0.286
1E+09	2	0.75	1.65E+08	3.24E+08	0.185	4.37E+08	0.406
1E+10	2	0.75	1.2E+08	2.51E+08	0.2305	2.73E+08	0.338
1E+11	2	0.75	1.15E+08	2.39E+08	0.2985	2E+08	0.359
1E+08	2	1	74768405	1.75E+08	0.3655	1.2E+08	0.293
1E+09	2	1	1.7E+08	3.15E+08	0.225	3.5E+08	0.443
1E+10	2	1	1.09E+08	2.29E+08	0.2105	2.72E+08	0.352
1E+11	2	1	1.47E+08	3.02E+08	0.256	2.95E+08	0.388
1E+08	2	1.25	76302566	1.77E+08	0.3685	1.2E+08	0.297
1E+09	2	1.25	1.88E+08	3.37E+08	0.202	4.18E+08	0.461

Table A.6. Confined compression test results at a density value of 2600 kg/m^3 (cont.)

Emod (Pa)	K_ratio	Fric	Res_mod (Pa)	You_mod (Pa)	Poi_rat	She_mod (Pa)	Fri_Coe
1E+10	2	1.25	1.14E+08	2.46E+08	0.212	2.91E+08	0.331
1E+11	2	1.25	1.14E+08	2.28E+08	0.2315	2.46E+08	0.386
1E+08	2	1.5	76780086	1.77E+08	0.3695	1.2E+08	0.299
1E+09	2	1.5	1.85E+08	3.32E+08	0.2145	3.87E+08	0.464
1E+10	2	1.5	1.63E+08	3.4E+08	0.1655	5.12E+08	0.347
1E+11	2	1.5	1.39E+08	2.8E+08	0.233	3.01E+08	0.389
1E+08	2	1.75	77005622	1.77E+08	0.37	1.2E+08	0.299
1E+09	2	1.75	2.04E+08	3.65E+08	0.1645	5.55E+08	0.465
1E+10	2	1.75	1.28E+08	2.5E+08	0.212	2.95E+08	0.398
1E+11	2	1.75	1.27E+08	2.31E+08	0.234	2.47E+08	0.428
1E+08	2	2	77103544	1.77E+08	0.371	1.19E+08	0.3
1E+09	2	2	1.84E+08	3.26E+08	0.175	4.65E+08	0.465
1E+10	2	2	1.23E+08	2.31E+08	0.186	3.1E+08	0.409
1E+11	2	2	98124700	1.99E+08	0.2255	2.2E+08	0.379

Table A.7. Confined compression test results at a density value of 2700 kg/m^3

Emod (Pa)	K_ratio	Fric	Res_mod (Pa)	You_mod (Pa)	Poi_rat	She_mod (Pa)	Fri_Coe
1E+08	0.5	0.5	74024600	1.73E+08	0.359	1.21E+08	0.299
1E+09	0.5	0.5	86170341	1.91E+08	0.3175	1.5E+08	0.283
1E+10	0.5	0.5	1.47E+08	2.9E+08	0.254	2.85E+08	0.366
1E+11	0.5	0.5	1.36E+08	2.61E+08	0.261	2.5E+08	0.388
1E+08	0.5	0.75	84582601	1.84E+08	0.3905	1.18E+08	0.33
1E+09	0.5	0.75	93623803	1.85E+08	0.2825	1.64E+08	0.329
1E+10	0.5	0.75	1.97E+08	3.91E+08	0.295	3.32E+08	0.359
1E+11	0.5	0.75	1.17E+08	2.16E+08	0.2125	2.55E+08	0.416
1E+08	0.5	1	91130811	1.91E+08	0.4105	1.16E+08	0.349
1E+09	0.5	1	1.03E+08	2.01E+08	0.225	2.24E+08	0.326
1E+10	0.5	1	1.37E+08	2.58E+08	0.1605	4.02E+08	0.406
1E+11	0.5	1	1.63E+08	2.68E+08	0.204	3.29E+08	0.474
1E+08	0.5	1.25	95914170	1.95E+08	0.425	1.15E+08	0.363
1E+09	0.5	1.25	1E+08	1.93E+08	0.218	2.21E+08	0.338
1E+10	0.5	1.25	1.5E+08	2.82E+08	0.1475	4.78E+08	0.386
1E+11	0.5	1.25	1.7E+08	2.99E+08	0.1815	4.11E+08	0.455
1E+08	0.5	1.5	98855972	1.98E+08	0.435	1.14E+08	0.371
1E+09	0.5	1.5	1.11E+08	2.09E+08	0.219	2.39E+08	0.351
1E+10	0.5	1.5	1.9E+08	3.46E+08	0.227	3.81E+08	0.414
1E+11	0.5	1.5	1.87E+08	3.16E+08	0.1705	4.64E+08	0.49
1E+08	0.5	1.75	1.01E+08	2E+08	0.442	1.13E+08	0.378
1E+09	0.5	1.75	1.25E+08	2.43E+08	0.2075	2.93E+08	0.333
1E+10	0.5	1.75	1.42E+08	2.65E+08	0.195	3.4E+08	0.403
1E+11	0.5	1.75	1.41E+08	2.47E+08	0.175	3.52E+08	0.473
1E+08	0.5	2	1.03E+08	2.02E+08	0.445	1.13E+08	0.382
1E+09	0.5	2	1.3E+08	2.39E+08	0.254	2.35E+08	0.367

Table A.7. Confined compression test results at a density value of 2700 kg/m^3 (cont.)

Emod (Pa)	K_ratio	Fric	Res_mod (Pa)	You_mod (Pa)	Poi_rat	She_mod (Pa)	Fri_Coe
1E+10	0.5	2	1.41E+08	2.43E+08	0.1075	5.66E+08	0.429
1E+11	0.5	2	1.7E+08	2.92E+08	0.191	3.82E+08	0.518
1E+08	0.75	0.5	78108246	1.81E+08	0.3595	1.26E+08	0.298
1E+09	0.75	0.5	1.17E+08	2.3E+08	0.2585	2.23E+08	0.366
1E+10	0.75	0.5	1.45E+08	2.9E+08	0.237	3.06E+08	0.398
1E+11	0.75	0.5	1.12E+08	2.45E+08	0.1905	3.22E+08	0.328
1E+08	0.75	0.75	85228926	1.88E+08	0.3875	1.21E+08	0.321
1E+09	0.75	0.75	1.1E+08	2.18E+08	0.227	2.4E+08	0.355
1E+10	0.75	0.75	1.64E+08	3.04E+08	0.211	3.6E+08	0.446
1E+11	0.75	0.75	1.61E+08	3.13E+08	0.1575	4.97E+08	0.398
1E+08	0.75	1	89577174	1.92E+08	0.4025	1.19E+08	0.333
1E+09	0.75	1	1.34E+08	2.4E+08	0.1915	3.13E+08	0.405
1E+10	0.75	1	1.49E+08	2.71E+08	0.2085	3.25E+08	0.438
1E+11	0.75	1	1.69E+08	3.19E+08	0.0925	8.6E+08	0.405
1E+08	0.75	1.25	92423547	1.95E+08	0.412	1.18E+08	0.341
1E+09	0.75	1.25	1.46E+08	2.53E+08	0.2195	2.89E+08	0.436
1E+10	0.75	1.25	1.84E+08	3.18E+08	0.174	4.57E+08	0.483
1E+11	0.75	1.25	1.78E+08	3.22E+08	0.1465	5.5E+08	0.438
1E+08	0.75	1.5	94024273	1.96E+08	0.418	1.17E+08	0.346
1E+09	0.75	1.5	1.41E+08	2.53E+08	0.207	3.06E+08	0.403
1E+10	0.75	1.5	2.01E+08	3.47E+08	0.1485	5.83E+08	0.49
1E+11	0.75	1.5	1.98E+08	3.51E+08	0.1	8.77E+08	0.422
1E+08	0.75	1.75	94840546	1.97E+08	0.4205	1.17E+08	0.348
1E+09	0.75	1.75	1.51E+08	2.56E+08	0.209	3.06E+08	0.441
1E+10	0.75	1.75	1.91E+08	3.21E+08	0.116	6.92E+08	0.5
1E+11	0.75	1.75	1.56E+08	2.8E+08	0.114	6.15E+08	0.44

Table A.7. Confined compression test results at a density value of 2700 kg/m^3 (cont.)

Emod (Pa)	K_ratio	Fric	Res_mod (Pa)	You_mod (Pa)	Poi_rat	She_mod (Pa)	Fri_Coe
1E+08	0.75	2	95504742	1.98E+08	0.4225	1.17E+08	0.35
1E+09	0.75	2	1.46E+08	2.55E+08	0.2125	3E+08	0.424
1E+10	0.75	2	1.89E+08	3.16E+08	0.155	5.1E+08	0.511
1E+11	0.75	2	1.52E+08	2.6E+08	0.1185	5.48E+08	0.456
1E+08	1	0.5	71985061	1.71E+08	0.359	1.19E+08	0.286
1E+09	1	0.5	93196325	1.99E+08	0.246	2.03E+08	0.314
1E+10	1	0.5	1.45E+08	2.55E+08	0.246	2.59E+08	0.422
1E+11	1	0.5	1.04E+08	2.17E+08	0.286	1.9E+08	0.339
1E+08	1	0.75	80667530	1.81E+08	0.3945	1.14E+08	0.31
1E+09	1	0.75	1.06E+08	2.16E+08	0.2225	2.43E+08	0.341
1E+10	1	0.75	1.71E+08	2.84E+08	0.1885	3.77E+08	0.454
1E+11	1	0.75	1.13E+08	2.13E+08	0.227	2.34E+08	0.394
1E+08	1	1	84992322	1.84E+08	0.409	1.13E+08	0.324
1E+09	1	1	1.1E+08	2.11E+08	0.2325	2.27E+08	0.359
1E+10	1	1	1.58E+08	2.63E+08	0.1825	3.61E+08	0.456
1E+11	1	1	1.26E+08	2.25E+08	0.223	2.53E+08	0.434
1E+08	1	1.25	86499336	1.85E+08	0.413	1.12E+08	0.33
1E+09	1	1.25	1.25E+08	2.38E+08	0.204	2.91E+08	0.375
1E+10	1	1.25	1.75E+08	2.74E+08	0.15	4.57E+08	0.515
1E+11	1	1.25	1.46E+08	2.55E+08	0.172	3.71E+08	0.435
1E+08	1	1.5	87424360	1.86E+08	0.416	1.12E+08	0.333
1E+09	1	1.5	1.39E+08	2.5E+08	0.1875	3.34E+08	0.415
1E+10	1	1.5	1.72E+08	2.84E+08	0.204	3.48E+08	0.47
1E+11	1	1.5	1.15E+08	2.24E+08	0.1835	3.05E+08	0.375
1E+08	1	1.75	88247117	1.87E+08	0.418	1.12E+08	0.335
1E+09	1	1.75	1.21E+08	2.25E+08	0.164	3.43E+08	0.387

Table A.7. Confined compression test results at a density value of 2700 kg/m^3 (cont.)

Emod (Pa)	K_ratio	Fric	Res_mod (Pa)	You_mod (Pa)	Poi_rat	She_mod (Pa)	Fri_Coe
1E+10	1	1.75	1.5E+08	2.45E+08	0.1665	3.68E+08	0.475
1E+11	1	1.75	1.45E+08	2.41E+08	0.1775	3.39E+08	0.48
1E+08	1	2	88559658	1.87E+08	0.419	1.12E+08	0.336
1E+09	1	2	1.36E+08	2.37E+08	0.1775	3.33E+08	0.417
1E+10	1	2	1.59E+08	2.56E+08	0.1015	6.3E+08	0.475
1E+11	1	2	1.61E+08	3.23E+08	0.214	3.77E+08	0.372
1E+08	1.25	0.5	77718946	1.77E+08	0.3675	1.2E+08	0.298
1E+09	1.25	0.5	92088597	1.97E+08	0.2555	1.93E+08	0.314
1E+10	1.25	0.5	1.62E+08	2.97E+08	0.2675	2.78E+08	0.4
1E+11	1.25	0.5	1.14E+08	2.48E+08	0.221	2.8E+08	0.335
1E+08	1.25	0.75	82499915	1.82E+08	0.3865	1.18E+08	0.312
1E+09	1.25	0.75	1.46E+08	2.77E+08	0.216	3.21E+08	0.378
1E+10	1.25	0.75	1.19E+08	2.1E+08	0.206	2.55E+08	0.419
1E+11	1.25	0.75	1.1E+08	2.24E+08	0.244	2.3E+08	0.358
1E+08	1.25	1	84855683	1.84E+08	0.3945	1.16E+08	0.319
1E+09	1.25	1	1.5E+08	2.68E+08	0.262	2.56E+08	0.418
1E+10	1.25	1	1.44E+08	2.52E+08	0.2175	2.89E+08	0.434
1E+11	1.25	1	1.7E+08	3.75E+08	0.262	3.58E+08	0.341
1E+08	1.25	1.25	86789507	1.86E+08	0.398	1.17E+08	0.325
1E+09	1.25	1.25	1.48E+08	2.65E+08	0.2345	2.83E+08	0.418
1E+10	1.25	1.25	1.63E+08	2.79E+08	0.257	2.72E+08	0.436
1E+11	1.25	1.25	1.02E+08	2.05E+08	0.245	2.09E+08	0.355
1E+08	1.25	1.5	87411134	1.86E+08	0.4005	1.16E+08	0.327
1E+09	1.25	1.5	1.41E+08	2.53E+08	0.2345	2.7E+08	0.423
1E+10	1.25	1.5	1.4E+08	2.3E+08	0.1885	3.05E+08	0.481
1E+11	1.25	1.5	1.39E+08	2.79E+08	0.2175	3.21E+08	0.367

Table A.7. Confined compression test results at a density value of 2700 kg/m^3 (cont.)

Emod (Pa)	K_ratio	Fric	Res_mod (Pa)	You_mod (Pa)	Poi_rat	She_mod (Pa)	Fri_Coe
1E+08	1.25	1.75	87782447	1.86E+08	0.4015	1.16E+08	0.329
1E+09	1.25	1.75	1.48E+08	2.58E+08	0.2395	2.7E+08	0.444
1E+10	1.25	1.75	2.01E+08	3.43E+08	0.1985	4.32E+08	0.438
1E+11	1.25	1.75	1.32E+08	2.82E+08	0.2115	3.33E+08	0.341
1E+08	1.25	2	88311312	1.87E+08	0.403	1.16E+08	0.33
1E+09	1.25	2	1.4E+08	2.43E+08	0.23	2.64E+08	0.444
1E+10	1.25	2	1.68E+08	2.72E+08	0.175	3.88E+08	0.498
1E+11	1.25	2	1.31E+08	2.5E+08	0.1935	3.24E+08	0.414
1E+08	1.5	0.5	73601119	1.76E+08	0.3515	1.25E+08	0.282
1E+09	1.5	0.5	90319996	2E+08	0.2095	2.39E+08	0.322
1E+10	1.5	0.5	1.36E+08	2.5E+08	0.282	2.22E+08	0.414
1E+11	1.5	0.5	91043405	1.99E+08	0.265	1.87E+08	0.353
1E+08	1.5	0.75	77318553	1.79E+08	0.3675	1.22E+08	0.296
1E+09	1.5	0.75	1.15E+08	2.43E+08	0.1755	3.45E+08	0.335
1E+10	1.5	0.75	1.93E+08	3.57E+08	0.2955	3.02E+08	0.417
1E+11	1.5	0.75	1.41E+08	2.94E+08	0.2745	2.68E+08	0.371
1E+08	1.5	1	79620469	1.81E+08	0.374	1.21E+08	0.303
1E+09	1.5	1	1.16E+08	2.4E+08	0.227	2.65E+08	0.352
1E+10	1.5	1	1.29E+08	2.36E+08	0.252	2.34E+08	0.397
1E+11	1.5	1	1.33E+08	2.59E+08	0.229	2.83E+08	0.419
1E+08	1.5	1.25	80491966	1.82E+08	0.377	1.21E+08	0.306
1E+09	1.5	1.25	1.14E+08	2.4E+08	0.194	3.09E+08	0.337
1E+10	1.5	1.25	1.5E+08	2.65E+08	0.261	2.53E+08	0.429
1E+11	1.5	1.25	1.24E+08	2.46E+08	0.243	2.52E+08	0.407
1E+08	1.5	1.5	80972654	1.82E+08	0.3785	1.2E+08	0.307
1E+09	1.5	1.5	1.11E+08	2.27E+08	0.187	3.03E+08	0.348

Table A.7. Confined compression test results at a density value of 2700 kg/m^3 (cont.)

Emod (Pa)	K_ratio	Fric	Res_mod (Pa)	You_mod (Pa)	Poi_rat	She_mod (Pa)	Fri_Coe
1E+10	1.5	1.5	1.55E+08	2.64E+08	0.2375	2.78E+08	0.466
1E+11	1.5	1.5	1.17E+08	2.35E+08	0.216	2.71E+08	0.41
1E+08	1.5	1.75	81362142	1.83E+08	0.38	1.2E+08	0.308
1E+09	1.5	1.75	1.16E+08	2.44E+08	0.1735	3.52E+08	0.34
1E+10	1.5	1.75	2.03E+08	3.41E+08	0.2065	4.12E+08	0.491
1E+11	1.5	1.75	1.66E+08	3.14E+08	0.2365	3.32E+08	0.43
1E+08	1.5	2	81612473	1.83E+08	0.3805	1.2E+08	0.309
1E+09	1.5	2	1.21E+08	2.37E+08	0.1825	3.25E+08	0.381
1E+10	1.5	2	1.74E+08	3.07E+08	0.2195	3.49E+08	0.459
1E+11	1.5	2	1.43E+08	2.55E+08	0.2255	2.82E+08	0.466
1E+08	1.75	0.5	75867275	1.8E+08	0.3435	1.31E+08	0.291
1E+09	1.75	0.5	79795615	1.8E+08	0.2475	1.82E+08	0.293
1E+10	1.75	0.5	1.04E+08	2.09E+08	0.305	1.71E+08	0.339
1E+11	1.75	0.5	1.68E+08	2.99E+08	0.3025	2.47E+08	0.423
1E+08	1.75	0.75	80393549	1.84E+08	0.3585	1.28E+08	0.306
1E+09	1.75	0.75	91701611	1.92E+08	0.2505	1.91E+08	0.325
1E+10	1.75	0.75	1.22E+08	2.33E+08	0.262	2.22E+08	0.358
1E+11	1.75	0.75	1.38E+08	2.45E+08	0.236	2.59E+08	0.434
1E+08	1.75	1	82432074	1.86E+08	0.365	1.27E+08	0.312
1E+09	1.75	1	1.01E+08	2E+08	0.246	2.03E+08	0.357
1E+10	1.75	1	2.85E+08	5.28E+08	0.2895	4.56E+08	0.393
1E+11	1.75	1	2.05E+08	3.6E+08	0.265	3.4E+08	0.443
1E+08	1.75	1.25	83707985	1.87E+08	0.369	1.27E+08	0.316
1E+09	1.75	1.25	1.03E+08	2.04E+08	0.245	2.09E+08	0.365
1E+10	1.75	1.25	1.25E+08	2.34E+08	0.1795	3.26E+08	0.387
1E+11	1.75	1.25	1.91E+08	3.32E+08	0.189	4.39E+08	0.465

Table A.7. Confined compression test results at a density value of 2700 kg/m^3 (cont.)

Emod (Pa)	K_ratio	Fric	Res_mod (Pa)	You_mod (Pa)	Poi_rat	She_mod (Pa)	Fri_Coe
1E+08	1.75	1.5	84541271	1.88E+08	0.3715	1.27E+08	0.318
1E+09	1.75	1.5	98517690	1.95E+08	0.253	1.93E+08	0.359
1E+10	1.75	1.5	1.7E+08	3.07E+08	0.224	3.43E+08	0.406
1E+11	1.75	1.5	1.8E+08	3.04E+08	0.2465	3.08E+08	0.457
1E+08	1.75	1.75	85150195	1.89E+08	0.373	1.26E+08	0.32
1E+09	1.75	1.75	1.04E+08	1.99E+08	0.2435	2.04E+08	0.377
1E+10	1.75	1.75	1.64E+08	2.83E+08	0.1425	4.96E+08	0.454
1E+11	1.75	1.75	1.6E+08	2.61E+08	0.2645	2.47E+08	0.494
1E+08	1.75	2	85501890	1.89E+08	0.374	1.26E+08	0.321
1E+09	1.75	2	1.07E+08	2.13E+08	0.214	2.49E+08	0.364
1E+10	1.75	2	1.63E+08	3.1E+08	0.2115	3.66E+08	0.394
1E+11	1.75	2	1.64E+08	2.78E+08	0.166	4.18E+08	0.469
1E+08	2	0.5	63065884	1.68E+08	0.3465	1.21E+08	0.254
1E+09	2	0.5	1.32E+08	2.72E+08	0.1935	3.52E+08	0.379
1E+10	2	0.5	1.26E+08	2.9E+08	0.3385	2.14E+08	0.313
1E+11	2	0.5	91312270	2.04E+08	0.2995	1.7E+08	0.344
1E+08	2	0.75	66914953	1.72E+08	0.358	1.2E+08	0.266
1E+09	2	0.75	1.7E+08	3.13E+08	0.2315	3.38E+08	0.446
1E+10	2	0.75	1.19E+08	2.51E+08	0.2565	2.44E+08	0.355
1E+11	2	0.75	83392938	1.9E+08	0.313	1.51E+08	0.317
1E+08	2	1	68718262	1.74E+08	0.365	1.19E+08	0.271
1E+09	2	1	1.77E+08	3.23E+08	0.1925	4.19E+08	0.447
1E+10	2	1	1.25E+08	2.47E+08	0.2355	2.62E+08	0.377
1E+11	2	1	1.3E+08	2.54E+08	0.2715	2.34E+08	0.397
1E+08	2	1.25	69625774	1.75E+08	0.3685	1.19E+08	0.274
1E+09	2	1.25	1.92E+08	3.4E+08	0.1905	4.46E+08	0.47

Table A.7. Confined compression test results at a density value of 2700 kg/m^3 (cont.)

Emod (Pa)	K_ratio	Fric	Res_mod (Pa)	You_mod (Pa)	Poi_rat	She_mod (Pa)	Fri_Coe
1E+10	2	1.25	1.37E+08	2.76E+08	0.2365	2.92E+08	0.381
1E+11	2	1.25	1.07E+08	2.36E+08	0.2765	2.14E+08	0.352
1E+08	2	1.5	70192244	1.76E+08	0.3705	1.18E+08	0.275
1E+09	2	1.5	1.95E+08	3.5E+08	0.2025	4.33E+08	0.465
1E+10	2	1.5	1.55E+08	2.78E+08	0.2495	2.78E+08	0.448
1E+11	2	1.5	1.37E+08	2.64E+08	0.261	2.53E+08	0.422
1E+08	2	1.75	70524878	1.76E+08	0.3725	1.18E+08	0.276
1E+09	2	1.75	1.85E+08	3.35E+08	0.22	3.81E+08	0.461
1E+10	2	1.75	1.38E+08	2.52E+08	0.1865	3.38E+08	0.413
1E+11	2	1.75	1.3E+08	2.71E+08	0.297	2.28E+08	0.38
1E+08	2	2	70695426	1.76E+08	0.373	1.18E+08	0.277
1E+09	2	2	1.93E+08	3.44E+08	0.209	4.11E+08	0.463
1E+10	2	2	1.26E+08	2.53E+08	0.2315	2.73E+08	0.369
1E+11	2	2	1.32E+08	2.48E+08	0.2585	2.4E+08	0.426

Table A.8. Confined compression test results at a density value of 2800 kg/m^3

Emod (Pa)	K_ratio	Fric	Res_mod (Pa)	You_mod (Pa)	Poi_rat	She_mod (Pa)	Fri_Coe
1E+08	0.5	0.5	75967497	1.76E+08	0.3735	1.18E+08	0.303
1E+09	0.5	0.5	93220193	2.01E+08	0.2655	1.89E+08	0.294
1E+10	0.5	0.5	1.36E+08	2.68E+08	0.2845	2.35E+08	0.358
1E+11	0.5	0.5	1.36E+08	2.65E+08	0.2475	2.67E+08	0.389
1E+08	0.5	0.75	84134790	1.84E+08	0.4	1.15E+08	0.329
1E+09	0.5	0.75	85765918	1.75E+08	0.246	1.78E+08	0.318
1E+10	0.5	0.75	1.6E+08	3.08E+08	0.22	3.5E+08	0.358
1E+11	0.5	0.75	1.49E+08	2.6E+08	0.2265	2.88E+08	0.462
1E+08	0.5	1	89687664	1.89E+08	0.42	1.13E+08	0.346
1E+09	0.5	1	1.18E+08	2.14E+08	0.255	2.1E+08	0.377
1E+10	0.5	1	1.66E+08	3.1E+08	0.2265	3.42E+08	0.396
1E+11	0.5	1	1.42E+08	2.51E+08	0.2075	3.02E+08	0.457
1E+08	0.5	1.25	93271174	1.93E+08	0.433	1.11E+08	0.357
1E+09	0.5	1.25	1.27E+08	2.25E+08	0.2065	2.72E+08	0.391
1E+10	0.5	1.25	1.36E+08	2.57E+08	0.2145	2.99E+08	0.389
1E+11	0.5	1.25	2.04E+08	3.72E+08	0.2255	4.12E+08	0.427
1E+08	0.5	1.5	95329173	1.95E+08	0.442	1.1E+08	0.363
1E+09	0.5	1.5	1.16E+08	2.18E+08	0.2435	2.23E+08	0.358
1E+10	0.5	1.5	1.72E+08	3.08E+08	0.1265	6.09E+08	0.408
1E+11	0.5	1.5	1.5E+08	2.42E+08	0.206	2.94E+08	0.506
1E+08	0.5	1.75	97508144	1.97E+08	0.448	1.1E+08	0.369
1E+09	0.5	1.75	1.35E+08	2.34E+08	0.22	2.66E+08	0.413
1E+10	0.5	1.75	1.57E+08	2.75E+08	0.149	4.62E+08	0.434
1E+11	0.5	1.75	1.82E+08	2.97E+08	0.1975	3.77E+08	0.511
1E+08	0.5	2	98544236	1.98E+08	0.4505	1.1E+08	0.372
1E+09	0.5	2	1.25E+08	2.18E+08	0.2145	2.53E+08	0.398

Table A.8. Confined compression test results at a density value of 2800 kg/m^3 (cont.)

Emod (Pa)	K_ratio	Fric	Res_mod (Pa)	You_mod (Pa)	Poi_rat	She_mod (Pa)	Fri_Coe
1E+10	0.5	2	1.71E+08	3.05E+08	0.084	9.07E+08	0.438
1E+11	0.5	2	1.45E+08	2.56E+08	0.219	2.92E+08	0.451
1E+08	0.75	0.5	78085062	1.82E+08	0.36	1.26E+08	0.295
1E+09	0.75	0.5	1E+08	2.05E+08	0.252	2.03E+08	0.341
1E+10	0.75	0.5	1.07E+08	2.33E+08	0.264	2.21E+08	0.345
1E+11	0.75	0.5	1.04E+08	2.19E+08	0.2	2.74E+08	0.337
1E+08	0.75	0.75	85719421	1.89E+08	0.3825	1.24E+08	0.317
1E+09	0.75	0.75	1.27E+08	2.4E+08	0.2425	2.47E+08	0.375
1E+10	0.75	0.75	1.66E+08	3.48E+08	0.237	3.67E+08	0.373
1E+11	0.75	0.75	1.66E+08	3.17E+08	0.187	4.23E+08	0.381
1E+08	0.75	1	89576736	1.93E+08	0.3975	1.21E+08	0.329
1E+09	0.75	1	1.29E+08	2.43E+08	0.2215	2.75E+08	0.379
1E+10	0.75	1	1.7E+08	2.83E+08	0.1625	4.36E+08	0.489
1E+11	0.75	1	1.64E+08	3.14E+08	0.1405	5.6E+08	0.414
1E+08	0.75	1.25	91629505	1.95E+08	0.408	1.2E+08	0.335
1E+09	0.75	1.25	1.43E+08	2.69E+08	0.2125	3.17E+08	0.386
1E+10	0.75	1.25	1.5E+08	2.87E+08	0.2	3.59E+08	0.41
1E+11	0.75	1.25	1.32E+08	2.42E+08	0.1025	5.89E+08	0.389
1E+08	0.75	1.5	93146350	1.97E+08	0.415	1.18E+08	0.34
1E+09	0.75	1.5	1.3E+08	2.34E+08	0.1905	3.07E+08	0.4
1E+10	0.75	1.5	1.71E+08	3.05E+08	0.1815	4.2E+08	0.452
1E+11	0.75	1.5	1.46E+08	2.67E+08	0.1045	6.38E+08	0.423
1E+08	0.75	1.75	94260391	1.98E+08	0.418	1.18E+08	0.343
1E+09	0.75	1.75	1.38E+08	2.44E+08	0.1865	3.27E+08	0.424
1E+10	0.75	1.75	1.6E+08	2.89E+08	0.1725	4.18E+08	0.457
1E+11	0.75	1.75	1.39E+08	2.67E+08	0.131	5.08E+08	0.413

Table A.8. Confined compression test results at a density value of 2800 kg/m^3 (cont.)

Emod (Pa)	K_ratio	Fric	Res_mod (Pa)	You_mod (Pa)	Poi_rat	She_mod (Pa)	Fri_Coe
1E+08	0.75	2	95363169	1.99E+08	0.4205	1.18E+08	0.345
1E+09	0.75	2	1.43E+08	2.49E+08	0.175	3.57E+08	0.424
1E+10	0.75	2	1.57E+08	2.82E+08	0.159	4.43E+08	0.44
1E+11	0.75	2	1.42E+08	2.5E+08	0.1515	4.13E+08	0.432
1E+08	1	0.5	71292365	1.71E+08	0.359	1.19E+08	0.283
1E+09	1	0.5	85495257	1.83E+08	0.2595	1.77E+08	0.315
1E+10	1	0.5	1.84E+08	3.29E+08	0.243	3.38E+08	0.405
1E+11	1	0.5	88740032	1.79E+08	0.282	1.59E+08	0.339
1E+08	1	0.75	78882594	1.79E+08	0.391	1.14E+08	0.306
1E+09	1	0.75	1.12E+08	2.15E+08	0.224	2.4E+08	0.366
1E+10	1	0.75	1.73E+08	2.93E+08	0.2305	3.18E+08	0.446
1E+11	1	0.75	83075722	1.82E+08	0.23	1.98E+08	0.312
1E+08	1	1	82397906	1.82E+08	0.406	1.12E+08	0.318
1E+09	1	1	1.35E+08	2.57E+08	0.2065	3.11E+08	0.367
1E+10	1	1	1.72E+08	2.71E+08	0.1035	6.55E+08	0.505
1E+11	1	1	1.29E+08	2.31E+08	0.2065	2.8E+08	0.422
1E+08	1	1.25	84610462	1.84E+08	0.412	1.12E+08	0.324
1E+09	1	1.25	1.32E+08	2.48E+08	0.22	2.82E+08	0.386
1E+10	1	1.25	2.25E+08	3.5E+08	0.125	7E+08	0.541
1E+11	1	1.25	1.06E+08	2.15E+08	0.233	2.31E+08	0.368
1E+08	1	1.5	85798482	1.85E+08	0.416	1.11E+08	0.327
1E+09	1	1.5	1.25E+08	2.37E+08	0.228	2.6E+08	0.391
1E+10	1	1.5	1.65E+08	2.7E+08	0.1875	3.6E+08	0.475
1E+11	1	1.5	1.14E+08	2.23E+08	0.209	2.67E+08	0.38
1E+08	1	1.75	86405123	1.86E+08	0.4175	1.11E+08	0.329
1E+09	1	1.75	1.26E+08	2.3E+08	0.2165	2.66E+08	0.401

Table A.8. Confined compression test results at a density value of 2800 kg/m^3 (cont.)

Emod (Pa)	K_ratio	Fric	Res_mod (Pa)	You_mod (Pa)	Poi_rat	She_mod (Pa)	Fri_Coe
1E+10	1	1.75	1.72E+08	2.73E+08	0.163	4.19E+08	0.521
1E+11	1	1.75	1.42E+08	2.53E+08	0.1685	3.76E+08	0.424
1E+08	1	2	86720542	1.86E+08	0.418	1.11E+08	0.329
1E+09	1	2	1.18E+08	2.18E+08	0.173	3.15E+08	0.392
1E+10	1	2	1.92E+08	3.03E+08	0.1205	6.28E+08	0.543
1E+11	1	2	1.22E+08	2.34E+08	0.1925	3.03E+08	0.402
1E+08	1.25	0.5	76799650	1.81E+08	0.3675	1.23E+08	0.289
1E+09	1.25	0.5	1.02E+08	2.12E+08	0.2335	2.27E+08	0.329
1E+10	1.25	0.5	1.05E+08	1.94E+08	0.192	2.53E+08	0.392
1E+11	1.25	0.5	1.03E+08	2.19E+08	0.23	2.38E+08	0.338
1E+08	1.25	0.75	81934740	1.86E+08	0.3855	1.2E+08	0.304
1E+09	1.25	0.75	1.34E+08	2.58E+08	0.2115	3.05E+08	0.374
1E+10	1.25	0.75	1.67E+08	3.04E+08	0.287	2.65E+08	0.402
1E+11	1.25	0.75	1.3E+08	2.45E+08	0.2195	2.79E+08	0.418
1E+08	1.25	1	84149446	1.87E+08	0.3925	1.19E+08	0.312
1E+09	1.25	1	1.39E+08	2.6E+08	0.2255	2.88E+08	0.404
1E+10	1.25	1	1.7E+08	2.84E+08	0.2135	3.32E+08	0.461
1E+11	1.25	1	1.36E+08	2.56E+08	0.215	2.98E+08	0.392
1E+08	1.25	1.25	85183635	1.88E+08	0.396	1.18E+08	0.316
1E+09	1.25	1.25	1.41E+08	2.53E+08	0.2385	2.65E+08	0.42
1E+10	1.25	1.25	2.56E+08	4.45E+08	0.2545	4.37E+08	0.447
1E+11	1.25	1.25	1.01E+08	2.04E+08	0.167	3.05E+08	0.362
1E+08	1.25	1.5	85883237	1.88E+08	0.398	1.18E+08	0.318
1E+09	1.25	1.5	1.45E+08	2.53E+08	0.216	2.92E+08	0.425
1E+10	1.25	1.5	1.4E+08	2.33E+08	0.2275	2.56E+08	0.467
1E+11	1.25	1.5	1.06E+08	2.12E+08	0.1905	2.78E+08	0.381

Table A.8. Confined compression test results at a density value of 2800 kg/m^3 (cont.)

Emod (Pa)	K_ratio	Fric	Res_mod (Pa)	You_mod (Pa)	Poi_rat	She_mod (Pa)	Fri_Coe
1E+08	1.25	1.75	86230252	1.88E+08	0.3995	1.18E+08	0.319
1E+09	1.25	1.75	1.52E+08	2.62E+08	0.1855	3.54E+08	0.442
1E+10	1.25	1.75	1.78E+08	2.78E+08	0.1305	5.33E+08	0.516
1E+11	1.25	1.75	1.2E+08	2.23E+08	0.209	2.66E+08	0.419
1E+08	1.25	2	86410595	1.89E+08	0.4	1.18E+08	0.32
1E+09	1.25	2	1.61E+08	2.72E+08	0.2015	3.37E+08	0.453
1E+10	1.25	2	1.48E+08	2.4E+08	0.1265	4.75E+08	0.505
1E+11	1.25	2	1.36E+08	2.57E+08	0.2115	3.04E+08	0.417
1E+08	1.5	0.5	73801323	1.77E+08	0.3515	1.26E+08	0.282
1E+09	1.5	0.5	89987281	2.04E+08	0.232	2.19E+08	0.306
1E+10	1.5	0.5	1.24E+08	2.45E+08	0.282	2.17E+08	0.366
1E+11	1.5	0.5	1.07E+08	2.29E+08	0.2545	2.25E+08	0.366
1E+08	1.5	0.75	77875973	1.8E+08	0.3675	1.22E+08	0.296
1E+09	1.5	0.75	94055754	2.06E+08	0.2445	2.11E+08	0.322
1E+10	1.5	0.75	1.56E+08	2.96E+08	0.3415	2.16E+08	0.412
1E+11	1.5	0.75	1.32E+08	2.64E+08	0.2375	2.78E+08	0.404
1E+08	1.5	1	80109889	1.82E+08	0.3735	1.22E+08	0.302
1E+09	1.5	1	1.11E+08	2.26E+08	0.253	2.23E+08	0.353
1E+10	1.5	1	1.55E+08	2.83E+08	0.241	2.94E+08	0.413
1E+11	1.5	1	1.48E+08	2.84E+08	0.227	3.13E+08	0.441
1E+08	1.5	1.25	80946550	1.83E+08	0.3765	1.22E+08	0.305
1E+09	1.5	1.25	1.03E+08	2.13E+08	0.2345	2.26E+08	0.344
1E+10	1.5	1.25	1.8E+08	3.17E+08	0.2545	3.11E+08	0.455
1E+11	1.5	1.25	1.71E+08	3.28E+08	0.2295	3.57E+08	0.424
1E+08	1.5	1.5	81588244	1.84E+08	0.3785	1.22E+08	0.306
1E+09	1.5	1.5	1.34E+08	2.66E+08	0.2235	2.98E+08	0.355

Table A.8. Confined compression test results at a density value of 2800 kg/m^3 (cont.)

Emod (Pa)	K_ratio	Fric	Res_mod (Pa)	You_mod (Pa)	Poi_rat	She_mod (Pa)	Fri_Coe
1E+10	1.5	1.5	1.81E+08	3.3E+08	0.2525	3.26E+08	0.43
1E+11	1.5	1.5	1.23E+08	2.4E+08	0.227	2.64E+08	0.412
1E+08	1.5	1.75	82098233	1.85E+08	0.3795	1.22E+08	0.308
1E+09	1.5	1.75	1.21E+08	2.3E+08	0.2575	2.24E+08	0.385
1E+10	1.5	1.75	1.84E+08	3.28E+08	0.1965	4.17E+08	0.45
1E+11	1.5	1.75	1.17E+08	2.3E+08	0.2205	2.61E+08	0.397
1E+08	1.5	2	82319418	1.85E+08	0.3805	1.22E+08	0.308
1E+09	1.5	2	1.22E+08	2.29E+08	0.215	2.67E+08	0.395
1E+10	1.5	2	1.61E+08	2.69E+08	0.203	3.31E+08	0.464
1E+11	1.5	2	1.17E+08	2.2E+08	0.228	2.41E+08	0.404
1E+08	1.75	0.5	73195678	1.78E+08	0.341	1.3E+08	0.285
1E+09	1.75	0.5	94855860	1.99E+08	0.2725	1.83E+08	0.323
1E+10	1.75	0.5	1.29E+08	2.44E+08	0.3335	1.83E+08	0.365
1E+11	1.75	0.5	1.44E+08	2.61E+08	0.2955	2.21E+08	0.42
1E+08	1.75	0.75	78489153	1.83E+08	0.3555	1.29E+08	0.299
1E+09	1.75	0.75	94610184	1.94E+08	0.271	1.79E+08	0.334
1E+10	1.75	0.75	1.4E+08	2.76E+08	0.309	2.23E+08	0.359
1E+11	1.75	0.75	1.91E+08	3.17E+08	0.2955	2.68E+08	0.495
1E+08	1.75	1	80302928	1.85E+08	0.363	1.28E+08	0.305
1E+09	1.75	1	94796580	1.9E+08	0.258	1.84E+08	0.346
1E+10	1.75	1	1.19E+08	2.2E+08	0.2665	2.06E+08	0.388
1E+11	1.75	1	1.44E+08	2.7E+08	0.2435	2.78E+08	0.412
1E+08	1.75	1.25	81398215	1.86E+08	0.366	1.27E+08	0.308
1E+09	1.75	1.25	91686167	1.88E+08	0.232	2.02E+08	0.343
1E+10	1.75	1.25	1.53E+08	2.74E+08	0.2545	2.69E+08	0.408
1E+11	1.75	1.25	1.52E+08	2.56E+08	0.2425	2.64E+08	0.492

Table A.8. Confined compression test results at a density value of 2800 kg/m^3 (cont.)

Emod (Pa)	K_ratio	Fric	Res_mod (Pa)	You_mod (Pa)	Poi_rat	She_mod (Pa)	Fri_Coe
1E+08	1.75	1.5	82102084	1.87E+08	0.3685	1.27E+08	0.31
1E+09	1.75	1.5	97642444	1.93E+08	0.225	2.15E+08	0.361
1E+10	1.75	1.5	1.37E+08	2.51E+08	0.3185	1.97E+08	0.401
1E+11	1.75	1.5	1.44E+08	2.45E+08	0.227	2.71E+08	0.473
1E+08	1.75	1.75	82473871	1.87E+08	0.3705	1.26E+08	0.312
1E+09	1.75	1.75	1.01E+08	1.96E+08	0.2485	1.97E+08	0.363
1E+10	1.75	1.75	1.63E+08	2.92E+08	0.243	3.01E+08	0.406
1E+11	1.75	1.75	1.31E+08	2.26E+08	0.2105	2.68E+08	0.474
1E+08	1.75	2	82815245	1.88E+08	0.371	1.26E+08	0.313
1E+09	1.75	2	97417913	1.93E+08	0.256	1.88E+08	0.357
1E+10	1.75	2	1.45E+08	2.58E+08	0.232	2.78E+08	0.403
1E+11	1.75	2	1.48E+08	2.44E+08	0.189	3.24E+08	0.488
1E+08	2	0.5	70360174	1.72E+08	0.335	1.29E+08	0.274
1E+09	2	0.5	1.39E+08	2.86E+08	0.145	4.93E+08	0.377
1E+10	2	0.5	92246482	2.19E+08	0.344	1.59E+08	0.3
1E+11	2	0.5	82059487	1.84E+08	0.294	1.57E+08	0.34
1E+08	2	0.75	75196946	1.78E+08	0.355	1.25E+08	0.288
1E+09	2	0.75	1.85E+08	3.48E+08	0.1755	4.96E+08	0.422
1E+10	2	0.75	1.02E+08	2.21E+08	0.2725	2.03E+08	0.323
1E+11	2	0.75	1.05E+08	2.36E+08	0.273	2.17E+08	0.34
1E+08	2	1	77453436	1.8E+08	0.3625	1.24E+08	0.294
1E+09	2	1	1.88E+08	3.3E+08	0.2095	3.94E+08	0.469
1E+10	2	1	1.36E+08	2.57E+08	0.289	2.22E+08	0.416
1E+11	2	1	1.22E+08	2.43E+08	0.2335	2.6E+08	0.405
1E+08	2	1.25	78435450	1.81E+08	0.3655	1.24E+08	0.297
1E+09	2	1.25	1.94E+08	3.41E+08	0.2215	3.85E+08	0.479

Table A.8. Confined compression test results at a density value of 2800 kg/m^3 (cont.)

Emod (Pa)	K_ratio	Fric	Res_mod (Pa)	You_mod (Pa)	Poi_rat	She_mod (Pa)	Fri_Coe
1E+10	2	1.25	1.77E+08	3.4E+08	0.2215	3.84E+08	0.422
1E+11	2	1.25	1.56E+08	3.17E+08	0.23	3.44E+08	0.377
1E+08	2	1.5	78871108	1.82E+08	0.3665	1.24E+08	0.298
1E+09	2	1.5	1.81E+08	3.23E+08	0.212	3.81E+08	0.462
1E+10	2	1.5	1.66E+08	3.49E+08	0.2385	3.66E+08	0.352
1E+11	2	1.5	1.3E+08	2.56E+08	0.23	2.79E+08	0.407
1E+08	2	1.75	79142046	1.82E+08	0.3675	1.24E+08	0.299
1E+09	2	1.75	1.77E+08	3.15E+08	0.195	4.04E+08	0.459
1E+10	2	1.75	1.57E+08	2.92E+08	0.213	3.43E+08	0.419
1E+11	2	1.75	1.14E+08	2.27E+08	0.232	2.44E+08	0.401
1E+08	2	2	79300517	1.82E+08	0.3675	1.24E+08	0.3
1E+09	2	2	2.07E+08	3.47E+08	0.2015	4.31E+08	0.502
1E+10	2	2	1.19E+08	2.5E+08	0.2425	2.58E+08	0.387
1E+11	2	2	1.13E+08	2.3E+08	0.2095	2.74E+08	0.378

Table A.9. Confined compression test results at a density value of 3000 kg/m^3

Emod (Pa)	K_ratio	Fric	Res_mod (Pa)	You_mod (Pa)	Poi_rat	She_mod (Pa)	Fri_Coe
1E+08	0.5	0.5	77453806	1.76E+08	0.359	1.22E+08	0.306
1E+09	0.5	0.5	85818677	1.76E+08	0.2875	1.53E+08	0.313
1E+10	0.5	0.5	1.25E+08	2.59E+08	0.2395	2.7E+08	0.337
1E+11	0.5	0.5	1.23E+08	2.2E+08	0.2565	2.14E+08	0.434
1E+08	0.5	0.75	87802413	1.87E+08	0.396	1.18E+08	0.336
1E+09	0.5	0.75	83939179	1.7E+08	0.227	1.87E+08	0.31
1E+10	0.5	0.75	1.26E+08	2.45E+08	0.2205	2.77E+08	0.383
1E+11	0.5	0.75	1.19E+08	2.12E+08	0.1955	2.71E+08	0.435
1E+08	0.5	1	93480043	1.92E+08	0.417	1.15E+08	0.353
1E+09	0.5	1	89064079	1.7E+08	0.2765	1.54E+08	0.34
1E+10	0.5	1	1.8E+08	3.3E+08	0.182	4.54E+08	0.393
1E+11	0.5	1	1.47E+08	2.63E+08	0.22	2.99E+08	0.442
1E+08	0.5	1.25	97260661	1.95E+08	0.43	1.13E+08	0.365
1E+09	0.5	1.25	1.01E+08	1.86E+08	0.242	1.92E+08	0.366
1E+10	0.5	1.25	1.62E+08	3.06E+08	0.158	4.84E+08	0.403
1E+11	0.5	1.25	1.64E+08	2.77E+08	0.1835	3.78E+08	0.479
1E+08	0.5	1.5	99908733	1.98E+08	0.4405	1.12E+08	0.373
1E+09	0.5	1.5	1.01E+08	1.82E+08	0.234	1.94E+08	0.378
1E+10	0.5	1.5	1.46E+08	2.62E+08	0.1355	4.83E+08	0.419
1E+11	0.5	1.5	1.39E+08	2.28E+08	0.243	2.35E+08	0.514
1E+08	0.5	1.75	1.01E+08	1.99E+08	0.4475	1.11E+08	0.378
1E+09	0.5	1.75	1.12E+08	2.07E+08	0.247	2.1E+08	0.374
1E+10	0.5	1.75	1.95E+08	3.46E+08	0.205	4.22E+08	0.432
1E+11	0.5	1.75	1.6E+08	2.61E+08	0.1875	3.48E+08	0.477
1E+08	0.5	2	1.02E+08	2E+08	0.4515	1.11E+08	0.381
1E+09	0.5	2	1.35E+08	2.38E+08	0.2505	2.37E+08	0.396

Table A.9. Confined compression test results at a density value of 3000 kg/m^3 (cont.)

Emod (Pa)	K_ratio	Fric	Res_mod (Pa)	You_mod (Pa)	Poi_rat	She_mod (Pa)	Fri_Coe
1E+10	0.5	2	2.52E+08	4.67E+08	0.164	7.12E+08	0.412
1E+11	0.5	2	1.44E+08	2.4E+08	0.223	2.69E+08	0.498
1E+08	0.75	0.5	71816173	1.74E+08	0.3445	1.26E+08	0.283
1E+09	0.75	0.5	1.05E+08	2.09E+08	0.2835	1.84E+08	0.352
1E+10	0.75	0.5	1.26E+08	2.5E+08	0.193	3.24E+08	0.379
1E+11	0.75	0.5	94969737	2.09E+08	0.2095	2.5E+08	0.317
1E+08	0.75	0.75	79365666	1.82E+08	0.372	1.22E+08	0.306
1E+09	0.75	0.75	1.27E+08	2.4E+08	0.2265	2.64E+08	0.379
1E+10	0.75	0.75	1.51E+08	2.94E+08	0.175	4.2E+08	0.423
1E+11	0.75	0.75	1.38E+08	2.73E+08	0.1515	4.51E+08	0.377
1E+08	0.75	1	83917996	1.87E+08	0.3885	1.2E+08	0.318
1E+09	0.75	1	1.36E+08	2.46E+08	0.2405	2.55E+08	0.404
1E+10	0.75	1	1.81E+08	3.39E+08	0.1275	6.64E+08	0.436
1E+11	0.75	1	1.23E+08	2.47E+08	0.1515	4.07E+08	0.358
1E+08	0.75	1.25	86232426	1.89E+08	0.3985	1.19E+08	0.325
1E+09	0.75	1.25	1.33E+08	2.41E+08	0.22	2.74E+08	0.406
1E+10	0.75	1.25	2.13E+08	3.84E+08	0.1005	9.54E+08	0.463
1E+11	0.75	1.25	1.6E+08	3.01E+08	0.138	5.44E+08	0.411
1E+08	0.75	1.5	87657406	1.91E+08	0.403	1.18E+08	0.33
1E+09	0.75	1.5	1.48E+08	2.61E+08	0.2225	2.93E+08	0.424
1E+10	0.75	1.5	1.68E+08	2.92E+08	0.132	5.53E+08	0.482
1E+11	0.75	1.5	2.02E+08	3.4E+08	0.1545	5.51E+08	0.467
1E+08	0.75	1.75	88698587	1.92E+08	0.4065	1.18E+08	0.332
1E+09	0.75	1.75	1.35E+08	2.35E+08	0.236	2.5E+08	0.427
1E+10	0.75	1.75	1.93E+08	3.17E+08	0.1265	6.25E+08	0.536
1E+11	0.75	1.75	2.24E+08	4.14E+08	0.1135	9.13E+08	0.409

Table A.9. Confined compression test results at a density value of 3000 kg/m^3 (cont.)

Emod (Pa)	K_ratio	Fric	Res_mod (Pa)	You_mod (Pa)	Poi_rat	She_mod (Pa)	Fri_Coe
1E+08	0.75	2	89702376	1.93E+08	0.409	1.18E+08	0.335
1E+09	0.75	2	1.35E+08	2.43E+08	0.234	2.59E+08	0.416
1E+10	0.75	2	1.73E+08	3.08E+08	0.1305	5.91E+08	0.493
1E+11	0.75	2	2.3E+08	4.34E+08	0.1055	1.03E+09	0.413
1E+08	1	0.5	71848891	1.7E+08	0.359	1.19E+08	0.286
1E+09	1	0.5	1.11E+08	2.22E+08	0.287	1.93E+08	0.343
1E+10	1	0.5	1.5E+08	2.69E+08	0.2495	2.7E+08	0.417
1E+11	1	0.5	89348412	1.87E+08	0.2475	1.89E+08	0.349
1E+08	1	0.75	79713744	1.8E+08	0.3915	1.15E+08	0.309
1E+09	1	0.75	1.15E+08	2.23E+08	0.233	2.4E+08	0.362
1E+10	1	0.75	1.32E+08	2.29E+08	0.179	3.2E+08	0.416
1E+11	1	0.75	1.12E+08	2.04E+08	0.2605	1.95E+08	0.418
1E+08	1	1	83284228	1.83E+08	0.406	1.13E+08	0.32
1E+09	1	1	1.3E+08	2.45E+08	0.203	3.02E+08	0.377
1E+10	1	1	1.7E+08	2.96E+08	0.2055	3.6E+08	0.434
1E+11	1	1	1.59E+08	2.76E+08	0.218	3.17E+08	0.448
1E+08	1	1.25	85280993	1.84E+08	0.411	1.12E+08	0.327
1E+09	1	1.25	1.32E+08	2.41E+08	0.2125	2.84E+08	0.392
1E+10	1	1.25	2.03E+08	3.16E+08	0.1385	5.71E+08	0.522
1E+11	1	1.25	1.38E+08	2.36E+08	0.232	2.54E+08	0.441
1E+08	1	1.5	86277482	1.85E+08	0.414	1.12E+08	0.33
1E+09	1	1.5	1.32E+08	2.45E+08	0.209	2.93E+08	0.393
1E+10	1	1.5	1.95E+08	3.08E+08	0.1695	4.55E+08	0.501
1E+11	1	1.5	1.91E+08	3.39E+08	0.2415	3.51E+08	0.438
1E+08	1	1.75	86640300	1.86E+08	0.415	1.12E+08	0.331
1E+09	1	1.75	1.42E+08	2.56E+08	0.2125	3.01E+08	0.4

Table A.9. Confined compression test results at a density value of 3000 kg/m^3 (cont.)

Emod (Pa)	K_ratio	Fric	Res_mod (Pa)	You_mod (Pa)	Poi_rat	She_mod (Pa)	Fri_Coe
1E+10	1	1.75	1.94E+08	3.2E+08	0.1445	5.53E+08	0.485
1E+11	1	1.75	1.83E+08	3.15E+08	0.2055	3.84E+08	0.46
1E+08	1	2	86921788	1.86E+08	0.416	1.12E+08	0.332
1E+09	1	2	1.43E+08	2.54E+08	0.2045	3.11E+08	0.407
1E+10	1	2	1.88E+08	2.94E+08	0.1475	4.98E+08	0.528
1E+11	1	2	1.61E+08	2.86E+08	0.1775	4.03E+08	0.456
1E+08	1.25	0.5	74635455	1.74E+08	0.3635	1.19E+08	0.29
1E+09	1.25	0.5	94756682	2.04E+08	0.256	2E+08	0.316
1E+10	1.25	0.5	1.13E+08	2.13E+08	0.2505	2.13E+08	0.378
1E+11	1.25	0.5	97183523	2.19E+08	0.242	2.27E+08	0.331
1E+08	1.25	0.75	80322428	1.79E+08	0.3835	1.17E+08	0.306
1E+09	1.25	0.75	98631420	1.97E+08	0.275	1.79E+08	0.342
1E+10	1.25	0.75	1.19E+08	2.13E+08	0.21	2.54E+08	0.408
1E+11	1.25	0.75	1.02E+08	2.18E+08	0.207	2.64E+08	0.341
1E+08	1.25	1	82704380	1.81E+08	0.3915	1.16E+08	0.314
1E+09	1.25	1	1.18E+08	2.2E+08	0.2455	2.24E+08	0.381
1E+10	1.25	1	1.43E+08	2.35E+08	0.1815	3.23E+08	0.478
1E+11	1.25	1	1.25E+08	2.46E+08	0.243	2.52E+08	0.399
1E+08	1.25	1.25	84193220	1.82E+08	0.395	1.15E+08	0.319
1E+09	1.25	1.25	1.11E+08	2.18E+08	0.2125	2.56E+08	0.352
1E+10	1.25	1.25	1.33E+08	2.23E+08	0.1835	3.04E+08	0.46
1E+11	1.25	1.25	1.39E+08	2.92E+08	0.234	3.12E+08	0.363
1E+08	1.25	1.5	84915817	1.83E+08	0.3965	1.15E+08	0.322
1E+09	1.25	1.5	1.38E+08	2.54E+08	0.2365	2.69E+08	0.407
1E+10	1.25	1.5	1.64E+08	2.77E+08	0.1825	3.8E+08	0.447
1E+11	1.25	1.5	1.23E+08	2.59E+08	0.218	2.97E+08	0.362

Table A.9. Confined compression test results at a density value of 3000 kg/m^3 (cont.)

Emod (Pa)	K_ratio	Fric	Res_mod (Pa)	You_mod (Pa)	Poi_rat	She_mod (Pa)	Fri_Coe
1E+08	1.25	1.75	85396289	1.83E+08	0.3975	1.15E+08	0.323
1E+09	1.25	1.75	1.35E+08	2.3E+08	0.205	2.8E+08	0.435
1E+10	1.25	1.75	1.52E+08	2.38E+08	0.12	4.96E+08	0.505
1E+11	1.25	1.75	1.45E+08	2.98E+08	0.2135	3.49E+08	0.362
1E+08	1.25	2	85628555	1.83E+08	0.3985	1.15E+08	0.324
1E+09	1.25	2	1.34E+08	2.36E+08	0.192	3.08E+08	0.425
1E+10	1.25	2	2.11E+08	3.5E+08	0.21	4.16E+08	0.463
1E+11	1.25	2	1.7E+08	3.42E+08	0.2195	3.89E+08	0.379
1E+08	1.5	0.5	73698108	1.77E+08	0.3505	1.26E+08	0.281
1E+09	1.5	0.5	91810949	2.01E+08	0.213	2.36E+08	0.324
1E+10	1.5	0.5	1.12E+08	2.21E+08	0.293	1.89E+08	0.369
1E+11	1.5	0.5	1.37E+08	2.83E+08	0.303	2.34E+08	0.383
1E+08	1.5	0.75	77979689	1.8E+08	0.3695	1.22E+08	0.297
1E+09	1.5	0.75	1.14E+08	2.38E+08	0.181	3.29E+08	0.34
1E+10	1.5	0.75	1.44E+08	2.82E+08	0.3225	2.19E+08	0.37
1E+11	1.5	0.75	1.29E+08	2.76E+08	0.2785	2.48E+08	0.375
1E+08	1.5	1	80070143	1.82E+08	0.3755	1.21E+08	0.304
1E+09	1.5	1	1.42E+08	2.91E+08	0.2025	3.59E+08	0.346
1E+10	1.5	1	1.49E+08	2.65E+08	0.3405	1.95E+08	0.426
1E+11	1.5	1	1.95E+08	3.98E+08	0.284	3.51E+08	0.409
1E+08	1.5	1.25	81167371	1.83E+08	0.379	1.21E+08	0.307
1E+09	1.5	1.25	1.16E+08	2.33E+08	0.198	2.94E+08	0.355
1E+10	1.5	1.25	1.63E+08	2.81E+08	0.2735	2.57E+08	0.45
1E+11	1.5	1.25	94479396	2.03E+08	0.248	2.04E+08	0.367
1E+08	1.5	1.5	81894354	1.84E+08	0.3805	1.21E+08	0.309
1E+09	1.5	1.5	1.32E+08	2.48E+08	0.1985	3.13E+08	0.391

Table A.9. Confined compression test results at a density value of 3000 kg/m^3 (cont.)

Emod (Pa)	K_ratio	Fric	Res_mod (Pa)	You_mod (Pa)	Poi_rat	She_mod (Pa)	Fri_Coe
1E+10	1.5	1.5	1.36E+08	2.38E+08	0.3045	1.96E+08	0.452
1E+11	1.5	1.5	1.19E+08	2.53E+08	0.246	2.57E+08	0.377
1E+08	1.5	1.75	82308089	1.84E+08	0.3825	1.2E+08	0.31
1E+09	1.5	1.75	1.36E+08	2.55E+08	0.176	3.62E+08	0.39
1E+10	1.5	1.75	1.42E+08	2.65E+08	0.296	2.24E+08	0.44
1E+11	1.5	1.75	2.31E+08	4.65E+08	0.237	4.91E+08	0.402
1E+08	1.5	2	82629313	1.84E+08	0.383	1.2E+08	0.311
1E+09	1.5	2	1.33E+08	2.49E+08	0.1885	3.3E+08	0.391
1E+10	1.5	2	1.32E+08	2.49E+08	0.3005	2.07E+08	0.421
1E+11	1.5	2	1.55E+08	3.02E+08	0.22	3.44E+08	0.446
1E+08	1.75	0.5	73426314	1.78E+08	0.3495	1.27E+08	0.285
1E+09	1.75	0.5	97914930	2.08E+08	0.287	1.81E+08	0.324
1E+10	1.75	0.5	1.21E+08	2.26E+08	0.309	1.83E+08	0.352
1E+11	1.75	0.5	1.33E+08	2.54E+08	0.294	2.16E+08	0.381
1E+08	1.75	0.75	78423132	1.83E+08	0.363	1.26E+08	0.299
1E+09	1.75	0.75	95691156	2.1E+08	0.2015	2.61E+08	0.315
1E+10	1.75	0.75	1.26E+08	2.32E+08	0.269	2.15E+08	0.388
1E+11	1.75	0.75	1.66E+08	2.86E+08	0.2655	2.69E+08	0.468
1E+08	1.75	1	80444847	1.85E+08	0.3685	1.26E+08	0.304
1E+09	1.75	1	1.09E+08	2.21E+08	0.2025	2.73E+08	0.342
1E+10	1.75	1	1.47E+08	2.74E+08	0.3055	2.24E+08	0.397
1E+11	1.75	1	1.34E+08	2.4E+08	0.231	2.6E+08	0.425
1E+08	1.75	1.25	81552702	1.86E+08	0.372	1.25E+08	0.308
1E+09	1.75	1.25	1.2E+08	2.28E+08	0.221	2.58E+08	0.379
1E+10	1.75	1.25	1.47E+08	2.49E+08	0.1815	3.42E+08	0.439
1E+11	1.75	1.25	2.43E+08	4.42E+08	0.297	3.71E+08	0.445

Table A.9. Confined compression test results at a density value of 3000 kg/m^3 (cont.)

Emod (Pa)	K_ratio	Fric	Res_mod (Pa)	You_mod (Pa)	Poi_rat	She_mod (Pa)	Fri_Coe
1E+08	1.75	1.5	82091370	1.87E+08	0.377	1.24E+08	0.31
1E+09	1.75	1.5	1.16E+08	2.3E+08	0.199	2.89E+08	0.365
1E+10	1.75	1.5	2E+08	3.7E+08	0.2005	4.62E+08	0.384
1E+11	1.75	1.5	1.99E+08	3.4E+08	0.214	3.97E+08	0.463
1E+08	1.75	1.75	82568450	1.87E+08	0.377	1.24E+08	0.311
1E+09	1.75	1.75	1.17E+08	2.26E+08	0.2025	2.79E+08	0.377
1E+10	1.75	1.75	1.66E+08	3.01E+08	0.243	3.1E+08	0.406
1E+11	1.75	1.75	1.89E+08	3.56E+08	0.1995	4.46E+08	0.398
1E+08	1.75	2	83036437	1.88E+08	0.377	1.25E+08	0.312
1E+09	1.75	2	1.16E+08	2.29E+08	0.175	3.28E+08	0.36
1E+10	1.75	2	1.42E+08	2.53E+08	0.2255	2.8E+08	0.433
1E+11	1.75	2	1.59E+08	2.82E+08	0.167	4.23E+08	0.455
1E+08	2	0.5	70231383	1.7E+08	0.333	1.27E+08	0.279
1E+09	2	0.5	1.43E+08	2.88E+08	0.179	4.02E+08	0.384
1E+10	2	0.5	1.03E+08	2.47E+08	0.2835	2.18E+08	0.298
1E+11	2	0.5	92999490	2.05E+08	0.258	1.99E+08	0.355
1E+08	2	0.75	74712888	1.75E+08	0.356	1.23E+08	0.293
1E+09	2	0.75	1.76E+08	3.21E+08	0.2265	3.54E+08	0.452
1E+10	2	0.75	1.52E+08	3.14E+08	0.2225	3.52E+08	0.362
1E+11	2	0.75	1.18E+08	2.37E+08	0.2575	2.3E+08	0.372
1E+08	2	1	77359606	1.78E+08	0.362	1.23E+08	0.3
1E+09	2	1	1.81E+08	3.28E+08	0.2355	3.48E+08	0.457
1E+10	2	1	1.25E+08	2.57E+08	0.31	2.07E+08	0.374
1E+11	2	1	87962493	1.89E+08	0.226	2.09E+08	0.342
1E+08	2	1.25	78816690	1.79E+08	0.364	1.23E+08	0.303
1E+09	2	1.25	1.83E+08	3.26E+08	0.1955	4.16E+08	0.466

Table A.9. Confined compression test results at a density value of 3000 kg/m^3 (cont.)

Emod (Pa)	K_ratio	Fric	Res_mod (Pa)	You_mod (Pa)	Poi_rat	She_mod (Pa)	Fri_Coe
1E+10	2	1.25	1.39E+08	2.59E+08	0.2175	2.98E+08	0.415
1E+11	2	1.25	1.18E+08	2.31E+08	0.2	2.89E+08	0.406
1E+08	2	1.5	79219940	1.8E+08	0.366	1.23E+08	0.305
1E+09	2	1.5	1.82E+08	3.21E+08	0.2275	3.53E+08	0.469
1E+10	2	1.5	1.5E+08	2.87E+08	0.2555	2.81E+08	0.411
1E+11	2	1.5	1.03E+08	2.11E+08	0.237	2.23E+08	0.36
1E+08	2	1.75	79248811	1.8E+08	0.3675	1.22E+08	0.305
1E+09	2	1.75	1.83E+08	3.3E+08	0.216	3.83E+08	0.463
1E+10	2	1.75	1.15E+08	2.23E+08	0.221	2.53E+08	0.403
1E+11	2	1.75	1.2E+08	2.25E+08	0.234	2.41E+08	0.413
1E+08	2	2	79373091	1.8E+08	0.368	1.22E+08	0.305
1E+09	2	2	1.81E+08	3.21E+08	0.1985	4.05E+08	0.466
1E+10	2	2	1.44E+08	2.73E+08	0.2465	2.77E+08	0.409
1E+11	2	2	1.85E+08	3.46E+08	0.219	3.94E+08	0.442

APPENDIX B.

PERMISSION LETTER FROM REHMAN ET AL. (2013)

Figure B.1. Permission letter from Rehman et al. (2013) to use their laboratory experimental data to calibrate the numerical models developed in this study

BIBLIOGRAPHY

Abdulhadi, N., & Barghouthi, A. (2012). Measurement of stiffness of rock from laboratory and field tests. In *Proceedings of the 5th Jordanian international civil engineering conference*.

Ai, J., Chen, J. F., Rotter, J. M., & Ooi, J. Y. (2011). Assessment of rolling resistance models in discrete element simulations. *Powder Technology*, *206*(3), 269-282.

Alekseeva, T. V. (1985). *Machines for earthmoving work: theory and calculations* (Vol. 30). Intl Public Service.

Ali, D., & Frimpong, S. (2018). Artificial intelligence models for predicting the performance of hydro-pneumatic suspension struts in large capacity dump trucks. *Journal of Ergonomics*, (Under review).

Alramahi, B. A., Alshibli, K. A., & Attia, A. M. (2005). Influence of Grain Size and Consolidation Pressure on Porosity of Rocks. In *Site Characterization and Modeling* (pp. 1-13).

ASTM-D3967 (2008) Standard test method for splitting tensile strength of intact rock core specimens. *Amer Soc Test Mater Int* 1–4.

ASTM-D4543 (2008) Standard practices for preparing rock core as cylindrical test specimens and verifying conformance to dimensional and shape tolerances. *Amer Soc Test Mater Int* 1–9. doi:10.1520/D4543-08

Awuah-Offei, K. (2006). Dynamic modeling of cable shovel-formation interactions for efficient oil sands excavation.

Awuah-Offei, K., & Frimpong, S. (2004). Geometric simulation of material weight resistance in cable shovel loading.

Awuah-Offei, K., & Frimpong, S. (2006). Numerical simulation of cable shovel resistive forces in oil sands excavation. *International Journal of Surface Mining, Reclamation and Environment*, *20*(3), 223-238.

Awuah-Offei, K., Frimpong, S., & Askari-Nasab, H. (2009). Formation excavation resistance modelling for shovel dippers. *International Journal of Mining and Mineral Engineering*, *1*(2), 127-146.

Bahrani, N. (2015). *Estimation of confined peak strength for highly interlocked jointed rockmasses* (Doctoral dissertation, Laurentian University of Sudbury).

Balovnev, V. I. (1983). New methods for calculating resistance to cutting of soil: Amerind Publishing, New Delhi, India.

Banerjee, A. (2017). *Response of unsaturated soils under monotonic and dynamic loading over moderate suction states* (Doctoral dissertation).

Blouin, S., Hemami, A., & Lipsett, M. (2001). Review of resistive force models for earthmoving processes. *Journal of Aerospace Engineering*, *14*(3), 102-111.

Brown, O. F., & Frimpong, S. (2012). Nonlinear finite element analysis of blade-formation interactions in excavation. *Mining Engineering*, *64*(11).

Buchanan, S. (2007). Resilient Modulus: What, Why, and How. *Vulcan Materials Company*, *8*(31), 07.

CDC. (2015). CDC - Mining - Statistics: Metal Operators - NIOSH [WWW Document].

CDC. (2015a). CDC - Mining - Statistics: Nonmetal Operators - NIOSH [WWW Document].

Chi, L., & Kushwaha, R. L. (1991). Three-dimensional, finite element interaction between soil and simple tillage tool. *Transactions of the ASAE*, *34*(2), 361-0366.

Coetzee, C. J., & Els, D. N. J. (2009a). Calibration of granular material parameters for DEM modelling and numerical verification by blade–granular material interaction. *Journal of Terramechanics*, *46*(1), 15-26.

Coetzee, C. J., & Els, D. N. J. (2009b). Calibration of discrete element parameters and the modelling of silo discharge and bucket filling. *Computers and electronics in agriculture*, *65*(2), 198-212.

Coulomb, C. A. (1773). Essai sur une application des regles de maximis et minimis a quelques problemes de statique relatifs a l'architecture (essay on maximums and minimums of rules to some static problems relating to architecture).

Cundall, P. A. (1971). A computer model for simulating progressive, large scale movement in blocky rock systems. In *Symp. ISRM, Nancy, France, Proc.* (Vol. 2, pp. 129-136).

Cundall, P. A., & Hart, R. D. (1992). Numerical modelling of discontinua. *Engineering computations*, *9*(2), 101-113.

Cundall, P. A., & Strack, O. D. (1979). A discrete numerical model for granular assemblies. *geotechnique*, *29*(1), 47-65.

Cundall, P. A., & Strack, O. D. L. (2008). A discrete numerical model for granular assemblies. In *The Essence of Geotechnical Engineering: 60 years of Géotechnique* (pp. 305-329). Thomas Telford Publishing.

De Blasio, F. V. (2011). *Introduction to the physics of landslides: lecture notes on the dynamics of mass wasting*. Springer Science & Business Media.

Dechao, Z., & Yusu, Y. (1991). Investigation on the relationship between soil shear strength and shear rate. *Journal of terramechanics*, *28*(1), 1-10.

Ding, X., Zhang, L., Zhu, H., & Zhang, Q. (2014). Effect of model scale and particle size distribution on PFC3D simulation results. *Rock mechanics and rock engineering*, *47*(6), 2139-2156.

Dombrovskii, N. G., & Pankratov, S. A. (1961). Zemleroinye Mashiny, Ch. 1 Odnokovshovye Ekskavatory (Earthmoving Machines, Part 1 Single-Bucket Shovels).

Dymond, G. F. D. (2007). *Creation, optimization and verification of a three dimensional numerical model to simulate a dragline bucket during the digging cycle using modern DEM software* (Doctoral dissertation, Stellenbosch: University of Stellenbosch).

Engelder, T. (1994). Deviatoric stressitis: A virus infecting the Earth Science community. *EOS, Transactions American Geophysical Union*, *75*(18), 209-212.

Electric rope shovels | Komatsu Mining Corp. (2017). Retrieved November 29, 2017, from https://mining.komatsu/surface-mining/electric-rope-shovels

EPA, U. S. (2005). U.S. Surface Mines Emissions Assessment. Retrieved from https://www.epa.gov/sites/production/files/2016-03/documents/us_surface_coal_mines_markets-update_feb2015.pdf

Fielke, J. M. (1999). Finite element modelling of the interaction of the cutting edge of tillage implements with soil. *Journal of Agricultural Engineering Research*, *74*(1), 91-101.

Fijani, E., Nadiri, A. A., Moghaddam, A. A., Tsai, F. T. C., & Dixon, B. (2013). Optimization of DRASTIC method by supervised committee machine artificial intelligence to assess groundwater vulnerability for Maragheh–Bonab plain aquifer, Iran. *Journal of hydrology*, *503*, 89-100.

FLAC. Fast Lagrangian Analysis of Continua. *Online Manual.* Retrieved June 22, 2018, from http://www.civil.utah.edu/~bartlett/CVEEN6920/FLAC%20manual.pdf

Frimpong, S., & Hu, Y. (2004). Parametric simulation of shovel-oil sands interactions during excavation. *International Journal of Surface Mining, Reclamation and Environment*, *18*(3), 205-219.

Frimpong, S., & Hu, Y. (2008). Intelligent cable shovel excavation modeling and simulation. *International Journal of Geomechanics*, *8*(1), 2-10.

Frimpong, S., Hu, Y., & Awuah-Offei, K. (2005). Mechanics of cable shovel-formation interactions in surface mining excavations. *Journal of Terramechanics, 42*(1), 15-33.

Geman, S., Bienenstock, E., & Doursat, R. (1992). Neural networks and the bias/variance dilemma. *Neural computation*, *4*(1), 1-58.

GEOLABS. (2018). Retrieved June 19, 2018, from https://geolabs.co.uk/rock-testing/#tab-id-1

Gevrey, M., Dimopoulos, I., & Lek, S. (2003). Review and comparison of methods to study the contribution of variables in artificial neural network models. *Ecological modelling*, *160*(3), 249-264.

Godwin, R., & Spoor, G. (1977). Soil failure with narrow tines. *Journal of Agricultural Engineering Research, 22*(3), 213-228.

Goodman, R. E. (1989). *Introduction to rock mechanics* (Vol. 2). New York: Wiley.

Han, Z., & Vanapalli, S. K. (2016). State-of-the-Art: Prediction of resilient modulus of unsaturated subgrade soils. *International Journal of Geomechanics*, *16*(4), 04015104.

Hemami, A. (1994). An approximation of the weight of the loaded material during the scooping operation of a mechanical loader. *Transactions of the Canadian Society for Mechanical Engineering*, *18*(3), 191-205.

Hemami, A., Goulet, S., & Aubertin, M. (1994). Resistance of particulate media to excavation: Application to bucket loading. *International Journal of Surface Mining and Reclamation*, *8*(3), 125-129.

Hendricks, C., Daneshmend, L., Wu, S., & Scoble, M. (1993). Design of a simulator for productivity analysis of electric mining shovels. In *Proc., 2nd Int. Symp. on Mine Mechanization and Automation* (pp. 329-336).

Hettiaratchi, D., Witney, B., & Reece, A. (1966). The calculation of passive pressure in two-dimensional soil failure. *Journal of Agricultural Engineering Research, 11*(2), 89-107.

Holtz, R. D., Kovacs, W. D., & Sheahan, T. C. (2011). *An Introduction to Geotechnical Engineering*. Upper Saddle River, New Jersey: Prentice-Hall.

Huang, G. B. (2003). Learning capability and storage capacity of two-hidden-layer feedforward networks. *IEEE Transactions on Neural Networks*, *14*(2), 274-281.

Hustrulid, W. A. (1999). *Blasting principles for open pit mining: general design concepts*. Balkema.

Iancu, I. (2012). A Mamdani type fuzzy logic controller. In *Fuzzy Logic-Controls, Concepts, Theories and Applications*. InTech.

ISRM (1978a) Suggested methods for determining tensile strength of rock materials. *Int J Rocks Mech Min Sci Geomech 15*:99–103

ISRM (1978b) Suggested methods for determining sound velocity. *Int J Rocks Mech Min Sci Geomech 15*:53–58

ISRM (1979a) Suggested methods for determining the uniaxial compressive strength and deformability of rock materials. *Int J Rocks Mech Min Sci Geomech 16*:135–140

ISRM (1979b) Suggested methods for determining water content, porosity, density, absorption and related properties and swelling and slake-durability index properties. *Int J Rocks Mech Min Sci Geomech 16*:141–156

Itasca. (2017). *PFC 5.0 Documentation*. Itasca Consulting Group, Inc.

Itasca. (2018). *PFC 5.0 Documentation*. Itasca Consulting Group, Inc.

Jiang, M. J., Liu, J., Sun, Y., & Yin, Z. (2013). Investigation into macroscopic and microscopic behaviors of bonded sands using distinct element method. *Soils and foundations*, *53*(6), 804-819.

Johnson, R. B., & DeGraff, J. V. (1988). *Principles of engineering geology*. Wiley.

Joseph, T. G., Rasimarzabadi, R., & Curley, M. (2018). Visual interpretation of DEM fill mechanisms for a rope shovel dipper in dry broken rock. *Civil Engineering Research Journal*, *3*(3), 1-11.

JOYGLOBAL. (2016). 4800XPC, Electric Mining Shovel Product Overview. 1-7.

Ju, L., Vassalos, D., Wang, Q., Wang, Y., & Liu, Y. (2018). Numerical investigation of solid bulk cargo liquefaction. *Ocean Engineering*, *159*, 333-347.

Kasabov, N. K. (1996). *Foundations of neural networks, fuzzy systems, and knowledge engineering*. Marcel Alencar.

Ke, J., & Liu, X. (2008, December). Empirical analysis of optimal hidden neurons in neural network modeling for stock prediction. In *Computational Intelligence and Industrial Application, 2008. PACIIA'08. Pacific-Asia Workshop on* (Vol. 2, pp. 828-832). IEEE.

Kim, J., & Kasabov, N. (1999). HyFIS: adaptive neuro-fuzzy inference systems and their application to nonlinear dynamical systems. *Neural Networks*, *12*(9), 1301-1319.

Knights, P. F. (2009). Optimal replacement intervals for shovel dipper teeth. *International Journal of Mining, Reclamation and Environment*, *23*(3), 157-167.

Kushwaha, R. L., & Shen, J. (1995). Finite element analysis of the dynamic interaction between soil and tillage tool. *Transactions of the ASAE*, *38*(5), 1315-1319.

Lee, C. C. (1990). Fuzzy logic in control systems: fuzzy logic controller. I. *IEEE Transactions on systems, man, and cybernetics*, *20*(2), 404-418.

Lek, S., Delacoste, M., Baran, P., Dimopoulos, I., Lauga, J., & Aulagnier, S. (1996). Application of neural networks to modelling nonlinear relationships in ecology. *Ecological modelling*, *90*(1), 39-52.

Lipsett, M. G., & Moghaddam, Y. R. (2011). Bifurcations, Instabilities and Degradation in Geomaterials, SSGG. *Modeling Excavator-Soil Interaction*, 347-366.

Lisjak, A., & Grasselli, G. (2014). A review of discrete modeling techniques for fracturing processes in discontinuous rock masses. *Journal of Rock Mechanics and Geotechnical Engineering*, *6*(4), 301-314.

Majeed, Y., & Bakar, M. A. (2016). Statistical evaluation of CERCHAR Abrasivity Index (CAI) measurement methods and dependence on petrographic and mechanical properties of selected rocks of Pakistan. *Bulletin of Engineering Geology and the Environment*, *75*(3), 1341-1360.

Mamdani, E. H. (1976). Advances in the linguistic synthesis of fuzzy controllers. *International Journal of Man-Machine Studies*, *8*(6), 669-678.

Mamdani, E. H., & Assilian, S. (1975). An experiment in linguistic synthesis with a fuzzy logic controller. *International journal of man-machine studies*, *7*(1), 1-13.

McDowell, G. R., Harireche, O., Konietzky, H., Brown, S. F., & Thom, N. H. (2006). Discrete element modelling of geogrid-reinforced aggregates. *Proceedings of the Institution of Civil Engineers-Geotechnical Engineering*, *159*(1), 35-48.

McKyes, E. (Ed.). (1985). *Soil cutting and tillage* (Vol. 7). Elsevier.

McKyes, E., & Ali, O. S. (1977). The cutting of soil by narrow blades. *Journal of Terramechanics*, *14*(2), 43-58.

Mishra, A. K., & Desai, V. R. (2006). Drought forecasting using feed-forward recursive neural network. *ecological modelling*, *198*(1-2), 127-138.

Mohr, O. (1914). *Die Elastizitatsgrenze und Bruch eines Materials* (Vol. 44): Z. Ver. Dtsch. Ing.

Momozu, M., Oida, A., Yamazaki, M., & Koolen, A. J. (2002). Simulation of a soil loosening process by means of the modified distinct element method. *Journal of Terramechanics*, *39*(4), 207-220.

Mouazen, A. M., & Neményi, M. (1999). Finite element analysis of subsoiler cutting in non-homogeneous sandy loam soil. *Soil and Tillage Research*, *51*(1-2), 1-15.

Neelakantan, T. R., Brion, G. M., & Lingireddy, S. (2001). Neural network modelling of Cryptosporidium and Giardia concentrations in the Delaware River, USA. *Water Science and Technology*, *43*(12), 125-132.

Osman, M. S. (1964a). The measurement of soil shear strength. *Journal of Terramechanics, 1*(3), 54-60.

Osman, M. S. (1964b). The mechanics of soil cutting blades. *Journal of Agricultural Engineering Research, 9*(4), 313-328.

Paterson, M. S., & Wong, T. F. (2005). *Experimental rock deformation-the brittle field*. Springer Science & Business Media.

Payne, P. (1956). The relationship between the mechanical properties of soil and the performance of simple cultivation implements. *Journal of Agricultural Engineering Research, 1*(1), 23-50.

PBCo | Electric Shovel Population | Mining Equipment Database & amp; Mining Market Research. (2017). Retrieved October 12, 2017, from http://parkerbaymining.com/mining-equipment/electric-shovels.htm

Perumpral, J. V., Grisso, R. D., & Desai, C. S. (1983). A soil-tool model based on limit equilibrium analysis. *Transactions of the ASAE*, *26*(4), 991-995.

Plouffe, C., Laguë, C., Tessier, S., Richard, M. J., & McLaughlin, N. B. (1999). Moldboard plow performance in a clay soil: simulations and experiment. *Transactions of the ASAE*, *42*(6), 1531.

Potyondy, D. O. (2015). The bonded-particle model as a tool for rock mechanics research and application: current trends and future directions. *Geosystem Engineering*, *18*(1), 1-28.

Potyondy, D. O. (2017). *Material modeling support in PFC* [fistPkg25]. Itasca Consulting Group, Inc., Technical Memorandum distributed with *PFC3D* 5.0 executable (March 16, 2017), Minneapolis, Minnesota.

Potyondy, D. O., & Cundall, P. A. (2004). A bonded-particle model for rock. *International journal of rock mechanics and mining sciences*, *41*(8), 1329-1364.

Potyondy, D., Siekmeier, J., & Petersen, L. (2016). *Aggregate-geogrid interaction model incorporating moisture effects* (No. 16-6085).

Qinsen, Y., & Shuren, S. (1994). A soil-tool interaction model for bulldozer blades. *Journal of terramechanics*, *31*(2), 55-65.

Rasimarzabadi, R. (2016). *Granular material flow into cable shovel dippers* (Doctoral dissertation, University of Alberta).

Rasimarzabadi, R., & Joseph, T. G. (2016). Particle flow mechanism into cable shovel dippers. *Journal of Terramechanics*, *64*, 10-22.

Raza, M. A. (2016). Cable shovel dipper stress and fatigue failure modeling in formation excavation engineering.

Raza, M. A., & Frimpong, S. (2013). Cable Shovel Stress & Fatigue Failure Modeling-Causes and Solution Strategies Review. *J Powder Metall Min S*, *1*, 2.

Raza, M. A., & Frimpong, S. (2017). Mechanics of electric rope shovel performance and reliability in formation excavation. In *Lagrangian mechanics*. InTech.

Raziperchikolaee, S. (2014). *Studying physical properties of deformed intact and fractured rocks by micro-scale hydro-mechanical-seismicity model*. (Doctoral dissertation).

Raziperchikolaee, S., Alvarado, V., & Yin, S. (2014). Microscale modeling of fluid flow-geomechanics-seismicity: Relationship between permeability and seismic source response in deformed rock joints. *Journal of Geophysical Research: Solid Earth*, *119*(9), 6958-6975.

Reece, A. R. (1964, June). Paper 2: The fundamental equation of earth-moving mechanics. In *Proceedings of the Institution of Mechanical Engineers, Conference Proceedings* (Vol. 179, No. 6, pp. 16-22). Sage UK: London, England: SAGE Publications.

Rehman, A. U., Saleem, A., Mustafa, N. (Project Members), & Hayat, M. B. (Project Advisor) (2013). *Study of relationship between destructive and non-destructive tests in predicting uniaxial compressive strength and tensile strength*. Unpublished, Department of Mining Engineering, University of Engineering and Technology, Lahore, Pakistan.

Rosa, U. A., & Wulfsohn, D. (1999). Constitutive model for high speed tillage using narrow tools. *Journal of Terramechanics*, *36*(4), 221-234.

Roy, S. K., Bhattacharyya, M. M., & Naikan, V. N. A. (2001). Maintainability and reliability analysis of a fleet of shovels. *Mining Technology*, *110*(3), 163-171.

Sematech, N. I. S. T. (2006). Engineering statistics handbook. *NIST SEMATECH*. Retrieved May 9, 2018, from https://www.itl.nist.gov/div898/handbook/pri/section1/pri11.htm

Shanmuganathan, S. (2016). Artificial Neural Network Modelling: An Introduction. In *Artificial Neural Network Modelling* (pp. 1-14). Springer, Cham.

Shi, X., Liu, Z., & Liu, J. (Eds.). (2018). *Proceedings of GeoShanghai 2018 International Conference: Transportation Geotechnics and Pavement Engineering*. Springer.

Singh, P. (2015). *Resilient modulus of recycled aggregates as road pavement materials*. Southern Illinois University at Carbondale.

Standard Laboratories, Inc. (2016). *Rock Mechanics Price Guide.* Retrieved June 19, 2018, from http://www.standardlabs.com/pdf/Rock%20Mechanics%20011316.pdf

Sugeno, M. (1985). An introductory survey of fuzzy control. *Information sciences*, *36*(1-2), 59-83.

Suministrado, D. C., Koike, M., Konaka, T., Yuzawa, S., & Kuroishi, I. (1990a). A model to determine the trajectory of soil motion on a moldbroad plow surface. *Journal of Terramechanics*, *27*(3), 207-218.

Suministrado, D. C., Koike, M., Konaka, T., Yuzawa, S., & Kuroishi, I. (1990b). Prediction of soil reaction forces on a moldboard plow surface. *Journal of Terramechanics*, *27*(4), 307-320.

Swick, W. C., & Perumpral, J. V. (1988). A model for predicting soil-tool interaction. *Journal of Terramechanics*, *25*(1), 43-56.

Takahashi, H., Hasegawa, M., & Nakano, E. (1998). Analysis on the resistive forces acting on the bucket of a Load-Haul-Dump machine and a wheel loader in the scooping task. *Advanced robotics*, *13*(2), 97-114.

Tamás, K. (2018). The role of bond and damping in the discrete element model of soil-sweep interaction. *Biosystems Engineering*, *169*, 57-70.

Tanaka, H., Momozu, M., Oida, A., & Yamazaki, M. (2000). Simulation of soil deformation and resistance at bar penetration by the distinct element method. *Journal of Terramechanics*, *37*(1), 41-56.

Team, D. F. (2017). Artificial neural network applications in the real world. *Machine Learning Tutorials*. Retrieved May 1, 2018, from https://data-flair.training/blogs/artificial-neural-network-applications/

Terzaghi, K. (1943). *Theoretical soil mechanics*. New York; London: J. Wiley and Sons, Inc.; Chapman and Hall, Limited.

Thakur, T. C., & Godwin, R. J. (1990). The mechanics of soil cutting by a rotating wire. *Journal of Terramechanics*, *27*(4), 291-305.

Trenn, S. (2008). Multilayer perceptrons: Approximation order and necessary number of hidden units. *IEEE Transactions on Neural Networks*, *19*(5), 836-844.

U.S. Geological Survey. (2017). *Mineral Commodity Summaries 2017*. *U.S. Geological Survey* (Vol. 1). https://doi.org/http://dx.doi.org/10.3133/70140094.

Wang, L. X., & Mendel, J. M. (1992). Generating fuzzy rules by learning from examples. *IEEE Transactions on systems, man, and cybernetics*, *22*(6), 1414-1427.

Wang, S. C. (2003). Artificial neural network. In *Interdisciplinary computing in java programming* (pp. 81-100). Springer, Boston, MA.

Wang, T., Xu, D., Elsworth, D., & Zhou, W. (2016). Distinct element modeling of strength variation in jointed rock masses under uniaxial compression. *Geomechanics and Geophysics for Geo-Energy and Geo-Resources*, *2*(1), 11-24.

Wardeh, M., & Frimpong, S. (2016). Virtual prototype modeling and simulation of an electric shovel for efficient excavation. *SME Annual Conference and Expo*, Feb 21-24, 214-215.

Wei, B., & Gao, F. (2012, August). Digging trajectory optimization for a new excavating mechanism of electric mining shovel. In *ASME 2012 International Design Engineering Technical Conferences and Computers and Information in Engineering Conference* (pp. 1033-1039). American Society of Mechanical Engineers.

Wyllie, D. C., Mah, C. W., & Hoek, E. (2004). *Rock slope engineering: civil and mining* (Vol. 4th). New York; London: Spon Press.

Xiang, J., & Saperstein, L. W. (1988).   Numerical analysis of rock failure during drag bit cutting. *Mineral Resources Engineering, Vol. 1(3)*, Imperial College Press, UK pp. 249-261.

Yong, R. N., & Hanna, A. W. (1977). Finite element analysis of plane soil cutting. *Journal of Terramechanics*, *14*(3), 103-125.

Yue, K. (2015). *Study of brittle/ductile layering effect on fracture geometry and mechanical behavior by tri-axial testing* (Doctoral dissertation).

Zadeh, L. A. (1965a). Information and control. *Fuzzy sets*, *8*(3), 338-353.

Zadeh, L. A. (1973b). Outline of a new approach to the analysis of complex systems and decision processes. *IEEE Transactions on systems, Man, and Cybernetics*, (1), 28-44.

Zelenin, A. N., Balovnev, V. I., & Kerov, I. P. (1985). *Machines for moving the earth*: Amerind Publishing New Delhi, India.

Zhang, L. (2016). *Engineering properties of rocks*. Butterworth-Heinemann.

Zhou, L. Q., & Yang, B. (2017). Simulation of A Hot-rolled H-section Steel Beam Subject to Static Loading Based on Discrete Element Method. *Procedia Engineering*, *210*, 312-319.

VITA

Mr. Muhammad Waqas was born in Sargodha, Pakistan. He completed his BS and MS in Mining Engineering from 'University of Engineering and Technology (UET), Lahore' in 2009 and 2013, respectively. After completing his BS degree, his passion and profound interest in academia led him to work as a Lecturer in the Department of Mining Engineering at UET Lahore, where he was involved in teaching and research. He was later promoted to the rank of Assistant Professor in December 2013. He joined Missouri University of Science and Technology (Missouri S&T) in August 2013 as a PhD student under the supervision of Dr. Samuel Frimpong. He served as a 'Teaching Fellow' for Missouri S&T at Saudi Mining Polytechnic (SMP), Arar, Saudi Arabia. He also worked as a Graduate Teaching Assistant in the Department of Mining and Nuclear Engineering at Missouri S&T. He completed the PFC2D/PFC3D course offered by Itasca Consulting Group, Inc. in March 2016. He completed his 2nd MS in Mechanical Engineering and a Graduate certificate in 'Engineering Mechanics' from Missouri S&T in May, 2017. He won the 'Graduate Teaching Award' from the Department of Mining and Nuclear Engineering in April 2018. He completed the requirements for the PhD degree in Mining Engineering in December 2018.